

ELECTRONIC STRUCTURE, SURFACE REACTIVITY AND
SITE ANALYSIS OF TRANSITION METAL COMPLEXES
AND METALLOPROTEINS BY X-RAY PHOTOELECTRON
SPECTROSCOPY

Thesis By

Frank John Grunthaner

In Partial Fulfillment of the Requirements
for the Degree of
Doctor of Philosophy

California Institute of Technology
Pasadena, California

1974

(Submitted December 21, 1973)

ACKNOWLEDGEMENTS

As this period of my life draws to a close, it is appropriate to remember those who have contributed so much professionally and personally during this time and work. The understanding and patience of my thesis advisor, Dr. Harry B. Gray, is gratefully acknowledged. His perception, creativity, and imagination were a constant stimulation and encouragement.

I am deeply indebted to Dr. Paul Pietrokowsky who introduced me to electron spectroscopy and steadfastly resisted my initial pessimism with his intuitive belief in the future promise of this field.

Dr. Jay A. Young who initiated my education so many years ago, must be remembered for the considerable influence of his teachings on my present and past.

My years at Caltech have been memorable and deeply satisfying due in large measure to the wealth of my friendships with Mr. John Swanson, Dr. Jurg Waser, Dr. Joe Gordon, and Mr. Bob Nixon. Particular mention must be made of the exhilarating experience of having been able to teach and work with that unique breed of scholar, the Caltech undergraduate. My students in Chem 1 and 3 taught me far more than I was able to impart to them. The considerable assistance of two of these students, Mr. Lou Scheffer and Miss Paula Clendening, who worked long and hard with me during the last hours of this work, is gratefully acknowledged.

Dr. Lee Scharpen, Dr. John Wood, Dr. Paul Larsen, and Dr. Bill Riggs made this thesis and research possible through their advice and counsel. In particular, the long hours of instrumental time given by Dr. Scharpen of Hewlett-Packard and Dr. John Wood of Utah State University were crucial

to the progress of this work.

My colleagues at Caltech in our research group, Dana Powers, Bob Holwerda, Jill Rawlings, and Dr. Diane Guttermann gave invaluable experimental assistance and endured the development of the ideas projected in this thesis. Jim Wurzback has been a source of considerable technical assistance and has taught me much.

Dr. Sten Samson has labored for many long hours trying to translate my crude writing into passable communication so that others could read this thesis. His selfless determination and patience with my illiteracy have put me deeply in his debt.

Lastly my feelings concerning the patience and understanding of my mother and father through all these years of study cannot adequately be expressed. Through the long hours of assistance in the preparation of this thesis, the years of compassion, understanding, and strength she has given me, my wife, Eileen, has made this all possible. But, it's to our children, Angela and Mary Jennifer, who have brought us so much happiness and to whom the future belongs, that this work, so imperfect, should be dedicated.

ABSTRACT

High resolution x-ray photoelectron core level spectra for a variety of transition metal complexes and metalloproteins are presented and related to questions of surface reactivity, electronic structure and metal ion valency. Core level spectra of VOSO_4 , VB_2 , V_2O_3 , V_2O_5 , V, VN, Na_3VO_4 , B_2O_3 , B, H_3BO_3 , $\text{Na}_2\text{B}_4\text{O}_7 \cdot 10\text{H}_2\text{O}$, Au, Laccase, Stellacyanin, Plastocyanin, Hemocyanin, Spinach Ferredoxin, High Potential Iron Protein, $\text{Fe}_4\text{S}_4(\text{SEt})_4^{2-}$, $\text{Fe}_2(\text{SCH}_2\text{CH}_2\text{S})_4^{2-}$, $\text{Fe}(\text{SP}\phi_2\text{N P}\phi_2\text{S})_2$, $\text{Fe}(\text{SP}\phi_2\text{NP}\phi_2\text{O})_3$, $\text{Fe}(\text{SP}\phi_2\text{NC}(\text{NC}_4\text{H}_8)\text{S})_3$, $\text{Cu}(\text{BuSCH}_2\text{CO}_2)_2$, $\text{Cu}_3(\text{SC}(\text{CH}_3)_2\text{CH}(\text{NH}_2)\text{CO}_2)_2$, $\text{Cu}(\text{O}_2\text{CCH}_2\text{S}(\text{CH}_2)_2\text{SCH}_2\text{CO}_2)$, $\text{CuCl}_2(\text{n-Bu S}(\text{CH}_2)_2\text{S-n-Bu})$, $\text{Cu}(\text{n-Pr}(\text{C}_4\text{H}_4\text{N}_2\text{OH})_5)$ are reported.

Electron binding energies correlated by internal referencing are tabulated for the species studied.

Charging effects in insulating chemical species are quantified and used to examine the electronic and chemical properties of the compounds studied. It is demonstrated that charge neutralization in electron spectroscopy is primarily due to capture of secondary electrons in the sample chamber with average kinetic energies below 6 eV.

Data handling methods for noise removal based on Fourier methods are presented. Treatment of the observed photoelectron line shape is given and spectral deconvolution is employed in data analysis.

Passivation reactions on vanadium diboride in carboxylic acid attack are attributed to the formation of surface vanadium oxides. Quantitative aspects of the electron spectra are developed, together with observed charging phenomenon, to show the unperturbed observation of adsorbed species on catalytic vanadium oxides.

The valency of copper in Laccase is studied by means of new copper sulfo-complexes and the well-defined proteins Stellacyanin and Plastocyanin. Type 1 and Type 2 copper is observed and Type 3 copper is described by a $\text{Cu}^{\text{I}}\text{-S-S-Cu}^{\text{I}}$ model. Oxyhemocyanin is also studied and assigned in terms of a cupric model.

The $\text{Fe}_4\text{S}_4(\text{Set})_4^{2-}$ cluster complex is examined and the mercaptyl and sulfido sulfurs are assigned. Only one iron state is observed, Fe^{III} , supporting the delocalized model of this species. It is suggested that the oxidized and reduced cluster species can be stabilized in the electron spectrometer. By comparison of the photoelectron spectra, the cluster complex is shown to be a reasonable model for 2-Fe and 4-Fe Ferredoxins and a discussion of the spectral differences is given.

The experimental parameters necessary for the successful study of metallo-proteins by photoelectron spectroscopy are developed in terms of elemental sensitivity, decomposition profiling, photoreduction, energy reference standards, sample preparation and thermal effects.

TABLE OF CONTENTS

	<u>Page</u>
I. <u>INTRODUCTION</u>	1
II. <u>GENERAL THEORETICAL CONSIDERATIONS</u>	
A. <u>Theory of Photoelectric Emission</u>	5
1. General Einsteinian Equation	
2. Work Function Treatment	
3. V_C Effects	
B. <u>Core Electron Binding Energy Shifts</u>	9
1. Free Atom Description	
2. Approximate Molecular Models	
3. Solid State Complications	
4. Reference Level	
C. <u>Second Order Effects</u>	11
1. Multiplet Splitting	
2. Electrostatic Splitting	
3. Satellite Transitions	
D. <u>Quantitative Aspects</u>	14
1. Transition Probabilities	
2. Empirical Relationships	
III. <u>EXPERIMENTAL METHODS</u>	
A. <u>General Experimental Description</u>	22
1. Basic System	
2. Vacuum Requirements	
3. X-ray Contributions	
4. Observed Line Width Contributions	
B. <u>Instrumental Characteristics</u>	25
1. <u>USU Spectrometer</u>	
a. Vacuum Level	
b. Magnetic Shielding	
c. Multiple Image Processes	

2.	<u>McPherson ESCA 36</u>	
	a. High Resolution Analyzer	
	b. Sample Chamber Configuration	
C.	<u>Voltaic Potential Effects</u>	31
	1. Flood Gun Experiments	
	2. Bias-Potential Method	
D.	<u>Sample Preparation</u>	40
	1. Observational Depth	
	a. Surface Effect	
	b. Contamination	
	c. Oxidation-Reduction	
	d. Success of Anaerobic Conditions	
	e. Reproducibility	
	2. Mounting Methods	43
	a. Metals	
	b. Solids	
	1. Powders on Adhesive Tape	
	2. Powder Pelletizing on Graphite Substrates	
	3. Physical Abrasion on Soft Coarse Metal Substrates	
	4. Compression on Metal Grids	
	5. Slurry Deposition	
	6. Thin Films from Solution Deposition	
	a. Amorphous	
	b. Single Crystals	
	c. Liquids	
	1. Frozen Solutions	
	a. Freeze Drying	
	b. Thermal Variation of Work Function with Temperatures	
	2. Liquid Beams	
	3. Particle Size Effects	45
IV.	<u>DATA ANALYSIS</u>	
A.	<u>Description of Data Characteristics</u>	46
	1. N(E) Distribution	
	2. Channel Sampling	
	3. Time-Averaging	
	4. Observed Line Widths	

B.	<u>Standard Smoothing Methods</u>	50
	1. Moving Average	
	2. Triangular Weighting Functions	
	3. Least Squares Convolution Functions	
C.	<u>Fourier Noise Filtration Methods</u>	51
	1. Frequency Analysis of Signal	
	2. Power Spectral Density of Noise	
	3. Frequency of Instrumentally Generated Noise	
	4. Truncation of Higher Order Terms	
	a. Sin (x)/x Convolution in real domain	
	b. Ringing Oscillations	
	5. Optimal Resolution Filtration	55
	a. Estimation Methods - Wiener Filter	
	1. Derivation	
	2. Application	
	3. Noise/Signal Sample	
	b. Detection Methods - Matched Filter	
D.	<u>Deconvolution</u>	
	1. Experimental Basis	72
	2. Instrumental Broadening Functions	
	3. Preliminary Results	
V.	<u>SURFACE STUDIES OF VANADIUM DIBORIDE</u>	
A.	<u>Introduction</u>	74
	1. Preparation of Vanadium Carboxylate Dimers	
	2. V ₂ O ₅ Catalysis	
	3. Charging Effect Experiments	
B.	<u>Experimental</u>	75
	1. Source of Vanadium Compounds	
	a. VB ₂ Samples	
	b. Vanadium Model Compounds	
	2. Mounting of Samples	
	a. Graphite Pellets	
	b. Abrasion into Coarse Al Plate	
	3. Flood Gun Experiments	
	4. Bias Potential Results	

C. <u>Results and Discussion</u>	81
1. Spectral Analysis of VB ₂ spectra	
a. Charging Experiments	
b. Oxidation Effects	
c. Passivation Differences	
d. Quantitative Analysis of Surface Composition	
e. Differential Analysis of Sample Charging Behavior	
2. Model Compound Studies	93
a. This work	
1. Oxide Overlayer	
2. Charging Variations	
b. Previous Studies	113
VI. <u>COPPER METALLOPROTEINS</u>	120
A. <u>Introduction</u>	124
1. General Problem of Valency in Metalloproteins	
2. Previous ESCA Protein Studies	
B. <u>Experimental</u>	128
1. Sample Source	
a. Buffered Solutions	
b. Freeze-dried Specimens	
2. ESCA Sample Preparation	
a. Air Dried Thin Films	
b. Frozen Solutions	
c. Variable Temperature	
d. Charging	
3. Radiation Decomposition	
4. Photo Reduction	
5. Energy Reference Standards	
6. Curve Analysis	
C. <u>Results and Discussion</u>	147
1. Model Complex Studies	
a. Binding Energies	
b. Satellite Observations	
c. Photo Reduction	160
2. Model Copper Proteins	165
a. Stellacyanin	
b. Plastocyanin	
c. Reference Energy Charge with Internal Standard	

3.	Laccase	172
	a. Binding Energies	
	b. Quantitative Analysis of Photo Reduction Products	
	c. Satellite Observation	
	d. Decomposition of Protein	
	e. Sulfur Electron Spectra	183
	f. Difference Analysis of Model Complex Data	
	g. Valency Assignments	
4.	Hemocyanin	187
	a. Binding Energies	
	b. Satellite Observations	
	c. Copper Spectra	
	d. Oxygen Spectra	
	e. Valency Assignments	
D.	<u>Conclusions</u>	188

VII. STUDIES OF THE IRON-SULFUR MOIETY IN 2-IRON AND 4-IRON FERREDOXINS

A.	<u>Introduction</u>	192
	1. Iron in Proteins	
	2. Electron Spectroscopy of Sulfur Containing Compounds	
B.	<u>Experimental</u>	196
	1. Sample Sources	
	2. Anaerobic Preparation	
	3. Energy Reference Standard	
	4. Curve Analysis	
C.	<u>Results and Discussions</u>	201
	1. Model Complex Studies	
	a. Cluster Complexes	
	1. Holm's Compound	
	2. Other	
	3. Oxidation Effects	
	4. Difference Analysis	
	b. Iron-Sulfur Complexes	225
	1. Fe Spectra	
	2. Sulfur 2p Region	
	3. Other Spectral Regions	
	2. Ferredoxin Spectra	252
	a. Iron Spectral Region	
	1. Binding Energies	
	2. Multiplet Splitting	
	3. Magnetic Broadening	

b. Sulfur Spectra	258
1. Oxidation Effects	
2. Labile Sulfur Assignments	
D. <u>Conclusions</u>	263
1. Iron Spin State	
2. Sulfur Protein Environments	
3. Future work	
VIII. <u>CONCLUSIONS</u>	266
A. Application of ESCA to a Variety of Fundamental Problems	
B. Experimental Design Criterion	
C. Passivation Studies of VB ₂	
D. Valency in Copper Metalloproteins	
E. Studies of Sulfur Environments in Proteins	
F. Iron Cluster Complexes as Models of Iron-Sulfur Proteins	
G. Data Handling Methods	
IX. <u>APPENDICES</u>	
A. Index of Spectra	280
B. Electron Energy Diagrams	283
C. General ESCA Data Analysis Program	289
X. <u>PROPOSITIONS</u>	301

I. INTRODUCTION

The application of spectroscopic techniques, which profile the interaction of electromagnetic radiation with matter has yielded information about the electronic structure. Generally, these techniques measure relationships between species in the ground state and in the bound excited states.

A few years ago, K. Siegbahn's ESCA monograph¹ excited new interest in a spectroscopic method which made possible the direct study of the energy distribution of bound electrons in atoms, molecules and solids.

This method required the illumination of a sample with electromagnetic radiation and the analysis of the kinetic energy or momentum distribution of the photoelectrons emitted. A considerable number of reviews of the theory^{2,3,4}, experiment^{5,6} and application^{7,8} of electron spectroscopy have appeared since the pioneering work of the Uppsala group.

-
1. Siegbahn, Kai; Nordling, Carl; Fahlman, Anders; Nordberg, Ragnar; Hamrin, Kjell; Hedman, Jan; Johansson, Gunnilla; Bergmark, Torsten; Karlsson, Sven; Lindgren, Ingvar; Lindberg, Bernt; Electron Spectroscopy for Chemical Analysis - Atomic, Molecular and Solid State Studies by Means of Electron Spectroscopy, Almqvist & Wiksells Boktryckeri AB, Stockholm, Sweden, 1967.
 2. Hollander, J.M., and Shirley, D.A., Ann. Rev. Nucl.Sci., 20, 435 (1970).
 3. Siegbahn, et. al., ESCA Applied to Free Molecules, North Holland, Amsterdam, 1969.
 4. Gelius, U., Molecular Orbitals and Line Intensities in ESCA Spectra Uppsala University, Institute of Physics, Publication #753, November 1971.
 5. Fadley, C.S., Thesis, University of California, Berkeley, 1970.
 6. Pollak, R.A., Thesis, University of California, Berkeley, 1972.
 7. Bremser, W., Xray Photoelectron Spectroscopy, in Topics in Current Chemistry, 36, *Springer-Verlag, Berlin, 1973.
 8. Hercules, D.M., Analytical Chemistry, 42, 20A, 1970.

The electrons of interest escape from a depth of 4 to 120 Å inside the solid sample and are not perturbed by collision. The observed energy of the photo-emitted electron is related to the atomic number of the emitting atom as well as the principal quantum number of the bound electron, the angular momentum and the chemical environment. The discovery of the chemical shift of the core electron binding energies promised considerable information about chemical structure.

Initial enthusiasm for this new form of spectroscopy was dampened because of experimental and instrumental difficulties: (1) The chemical shift is small in relation to the natural X-ray line widths and instrumental resolution. (2) Surface contamination of samples gave rise to data which was not representative of the bulk material. (3) The sample often decomposed in the vacuum or suffered radiation damage. (4) Charge built up on the sample altered the energy of emitted electrons in a non-reproducible manner.

Because of the great potential of this method as an analytical tool, the author decided to overcome these difficulties and to study the electronic structure of transition-metal complexes. Also, it seemed important to apply ESCA to bio-inorganic chemistry, incorporating transition metals. Here enzymatic activity at specific sites⁹ (often called active sites) can be studied, especially as regards oxygen and electron transport.

9. Gray, H.B., Structural Models for Iron and Copper Proteins Based on Spectroscopic and Magnetic Properties in Bioinorganic Chemistry, Advances in Chemistry, 100, American Chemical Soc., Washington, D.C., 1971.

Model complexes have been developed, which approximate the metal-protein environment. To such systems standard spectroscopic techniques as well as magnetic and electrochemical methods have already been applied^{9,10,11}. Metal ions at active sites of enzymes have unusual ligand configurations probably as a result of their unique electronic structure. To devise a model requires knowledge of the identity of ligands, their coordination, and their physical accessibility.

The present work has concerned itself with a series of copper and iron metalloproteins for which well-characterized model complexes were available. The valency and site environment of the metal were determined in laccase and hemocyanin. Concurrently, sulfur environments in metalloproteins were studied. A similar study of the iron-sulfur clusters in ferredoxins was carried out.

In this thesis emphasis is placed mainly on the experimental aspects as regards ESCA and metalloproteins. Radiation damage, dehydration in vacuum and thermal decomposition were monitored. An energy referencing system was devised for the comparison of model complex and protein spectra.

-
10. Tsibris, J.C.M., and Woody, R.W., Coordination Chemistry Reviews, Elsevier Publishing, Amsterdam, 1970.
 11. Williams, R.J.P., Role of Transition Metal Ions in Biological Processes, R.I.C. Reviews, 1, 13 (1968).

Special sections of this thesis are devoted to the description of experiments concerning charging effects and to removal of noise through data-handling methods.

X-ray photoelectron spectroscopy is limited to the examination of only the first few angstroms of the surface of a solid and seems to be an ideal tool for the study of the passivation of vanadium diboride. In this case, the study of charging effects leads to increased structural information. The results of this study are compared with data recently obtained elsewhere on catalysts consisting of vanadium oxide and vanadium-molybdenum oxides.

II. GENERAL THEORETICAL CONSIDERATIONS

A. Theory of Photoelectron Emission

The work reported in this thesis concerns the interpretation of photo emission spectra resulting from X-ray adsorption by core levels. Several detailed reviews of theoretical aspects of electron spectroscopy are given in the literature^{1,2,4,8}. The recent treatment by Fadley¹² is the most rigorous one. The energy conservation equation for a free atom or molecule is

$$h\nu + E^i = E_{\text{KIN}} + E^f(k)' , \quad (1)$$

where

$h\nu \equiv$ photon energy

$E_i \equiv$ total initial energy of the adsorber

$E_{\text{KIN}} \equiv$ Kinetic energy of the photo-electron

$E^f(k)' \equiv$ total final energy of the adsorber after the ejection of an electron from the K^{th} orbital as a photo-electron

For atomic states, the index k stands for the quantum numbers n_l or $n_l j$. For molecules, k is determined by the overall symmetry of the adsorbing molecular orbital. E^i and $E^f(k)'$ may include contributions from electronic, vibrational, rotational and translational energies.

The energy perturbation caused by factors other than X-ray adsorption (thermal excitation, secondary electron collision) are small compared to the resolving power of the instrument, which is 0.55 eV. Thus E^i is assumed to be unique or single-valued.

12. Fadley, C.S., Theoretical Aspects of Electron Spectroscopy, NATO Conference on Electron Emission, Ghent, 1973.

Relaxation processes can lead to uncertainty in the final energy of the state ($E^f(k)$). The photoelectron velocities arising from irradiation by soft X-rays are approximately non-relativistic. Considering momentum conservation $E^f(k)'$ can be written as the sum of a recoil energy E_r plus a term containing the energies corresponding to all other modes of motion $E^f(k)$

$$E^f(k)' = E_r + E^f(k). \quad (2)$$

For a given $h\nu$ and E_{KIN} , E_r increases with decreasing atomic or molecular mass¹. The recoil energies for different atoms calculated by Siegbahn are: H - 0.9 eV, Li - 0.1 eV, Na - 0.04 eV, K - 0.02 eV, Rb - 0.01 eV (AlK α , $E_{KIN} = 1486$ eV). E_r can be neglected with respect to instrumental resolution, and equation (1) reduces to

$$h\nu + E^i = E_{KIN} + E^f(k). \quad (3)$$

The binding energy of an electron is defined as the positive energy required to remove it to infinity with zero kinetic energy. Representing the binding energy of the k^{th} electron by $E_b(k)$, this relationship is

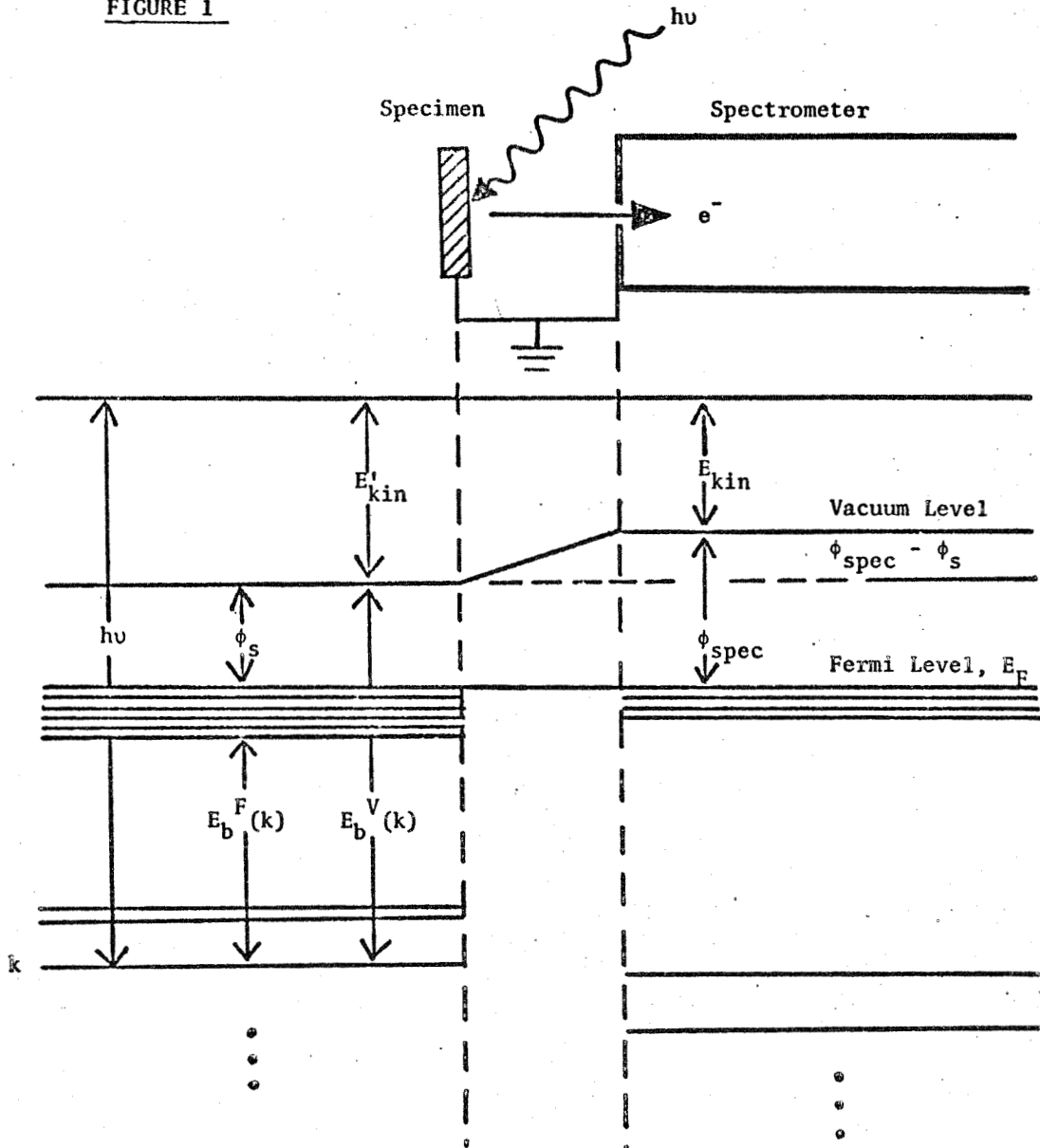
$$E_b(k) \equiv E^f(k) - E^i \quad (4)$$

and equation 3 can be rewritten as

$$h\nu = E_{KIN} + E_b(k). \quad (5)$$

Since equation (5) refers to an atom or molecule in free space, this binding energy is referenced to the vacuum level, and applies only to gases. As shown in Figure 1, solid specimens are electrically connected to the spectrometer and rest at a fixed potential.

FIGURE 1



Energy-level diagram for a metallic specimen electrically connected to an electron spectrometer. The closely spaced levels near the Fermi level E_F represent the filled portion of the valence bands. The deeper levels are core levels. An analogous diagram also applies in principle to semi-conducting or insulating specimens, with the only difference that E_F lies somewhere between the filled valence bands and the empty conduction bands above.

At absolute zero, the Fermi level, E_F , for a metal is the highest occupied level. This interpretation of E_F is approximately correct at room temperatures. The work function, ϕ , for a solid is defined as the energy separation between the vacuum and the Fermi levels. When the specimen and spectrometer are in thermodynamic equilibrium, the two Fermi levels will rest at the same potential. The respective vacuum levels need not be equivalent; see Figure 1. When the photo electron passes from the sample to the analyzer, it will experience a potential equal to $\phi_s - \phi_{\text{spectrometer}}$ where ϕ_s is the work function of the sample. The kinetic energy, E_{KIN} , of the electron inside the analyzer is related to the escaping kinetic energy, E'_{KIN} , at the sample surface by

$$E_{\text{KIN}} = E'_{\text{KIN}} + \phi_s - \phi_{\text{spectrometer}} \quad (6)$$

Binding energies in a metallic solid can be measured easily relative to the Fermi levels of sample and spectrometer. For solids, equation (5) becomes

$$h\nu = E_{\text{KIN}} + E^{\text{F}}(\text{K}) + \phi_{\text{spectrometer}} \quad (7)$$

where the superscript F refers to referencing at the Fermi level.

In semiconductors and insulators, the Fermi level is not easily defined, since it lies somewhere between the valence bands (predominately filled) and the conduction bands (predominately unoccupied)¹³. Thermodynamic equilibrium does not occur when the specimen impedes replenishing of the ejected electrons.

13. Kittel, C.K., Solid State Physics, Wiley, (1968) 2nd Edition, 1973.

Charging effects result in a net retardation of the photoelectrons before they enter the spectrometer. The magnitudes of these effects vary from 1 to 100 electron volts and are observed for both solids⁵ and gases³. The charging shift depends upon the photon flux, the secondary electron flux from spectrometer surfaces, the temperature, and the surface and bulk conductivities of solid samples.

If the charge is uniformly distributed over the surface of the sample (of magnitude, V_c) then, equation 7 becomes

$$h\nu = E_{\text{KIN}} + E^{\text{F}}(k) + V_c + \phi_{\text{spectrometer}} \quad (8)$$

If V_c is presumed to be zero, the binding energies would appear to be higher than they actually are. A non-uniform charging potential would result in a broadening and distortion of the photoelectron peaks.

B. Shifts in Binding Energy of Core Electrons

Molecular formation and reaction causes redistributions of valence electrons compared to the free atom. These redistributions affect the potential of the inner electrons and result in changes in their binding energies.

In Siegbahn's model¹ for predicting chemical shifts, the valence electrons are represented by a spherical shell of negative charge. The potential exerted by this shell on the core electrons within it is given by

$$V = \delta e^2/r, \quad (9)$$

where δ is the number of valence shell electrons and r is the radius of the shell. If one electron is lost, the screening potential seen by the core electrons is reduced by

$$\Delta E = e^2/r, \quad (10)$$

which is equivalent to the chemical shift. This model correctly predicts the order of magnitude of the chemical shift but overestimates the extent of charge transfer.

The chemical shifts of all core levels should be the same by this free atom model. Fadley, et al.¹⁴, in an investigation of iodine compounds, found that the shifts in the $2s_{1/2}$, $2p_{1/2}$, $2p_{3/2}$, $3d_{3/2}$, $3d_{5/2}$, $4s_{1/2}$, and $4p_{3/2}$ levels of iodine were equal within experimental error. Oxidation number was the first empirical quantity used to predict the chemical shift. This parameter, however, gives a poor illustration of the actual charge distribution in molecules. Here, the distribution is better approximated by a number of other models. The most important of these are:

1. The Pauling Valence Bond (PVB) model
2. The extended Huckel Molecular Orbital model
3. The CNDO molecular orbital method.

The PVB method empirically correlates bond lengths and electronegativities to estimate the distribution of atomic charge¹⁵. The atom charge is the sum of the formal charge on atom A and the charge transferred from bonds of partial ionic character. Expressing this algebraically,

$$q_A = Q_A \pm \sum_{B \neq A} nI \quad , \quad (11)$$

where

-
14. Fadley, C.S., Hagstrom, S.M.M., Klein, M.P., and Shirley, D.A., J. Chem. Phys., 48, 3779 (1968).
 15. Pauling, L., The Nature of Chemical Bond, Ithaca, New York, Cornell Univ. Press, 3rd edition, 1960.

$Q_A \equiv$ formal charge on covalently bonded atom A

$\Sigma \equiv$ summation over all bonds to atom A

$n \equiv$ average bond number

$I \equiv$ partial ionic character of bond

$$I \equiv 1 - e^{-0.25 (\chi_A - \chi_B)^2}$$

and $\chi_A - \chi_B \equiv$ electronegativity difference between A and B.

The predictability of these models was evaluated by Hollander and Shirley². The CNDO method gave the best correlations with experiment, while the empirical PVB model gave better results than the extended Huckel treatment.

C. Second Order Effects

If the initial state has a non-zero angular momentum J , then the hole created by the ejection of a core electron can couple to J to form two or more final states. This effect has been termed multiplet splitting⁵. Unrestricted Hartree-Fock calculations¹⁶ predict splittings of up to 12 eV. The free-atom model predicts that the relative intensities of the multiplet peaks are given by the statistical weight of the two final states.

For example, in the spectrum from the Mn^{2+} ion, (d^5 high spin) the final state spin (J) can be $5/2 \pm 1/2$ and the multiplet intensities would be in the ratio of $2J + 1$ or 7:5. The splitting observed for a series of iron compounds⁵ was 6 eV or about half the splitting predicted.

16. Bagus, P.S. and Liw, B., Phys Rev., 148, 79 (1966)

Processes involving more than one electron were first studied in detail by Kraus, Carlson and co-workers^{17,18,19}. These studies of neon and argon used photon energies of 270 eV to 1.5 keV. Two and three-electron transitions were predicted in photon adsorption with probabilities as high as 20% for each adsorbed photon.

Two types of two-electron transitions can be distinguished depending on whether the second electron is excited to a higher energy bound state (shake-up) or to an unbound continuum state (shake-off). These transitions can be written

Shake-up: (12)

$$(nl)_{L,S} (n'l')^P \xrightarrow{h\nu} (nl)^{q-1} (n'l')^{P-1} (n''l'')' + \text{Photoelectron}$$

Shake-off: (13)

$$(nl) (n'l')^P \xrightarrow{h\nu} (nl)^{q-1} (n'l')^{P-1} (E_{KIN}''l'')' + \text{Photoelectron,}$$

where $(n'l')^P$ represents some outer subshell from which the second electron is excited.

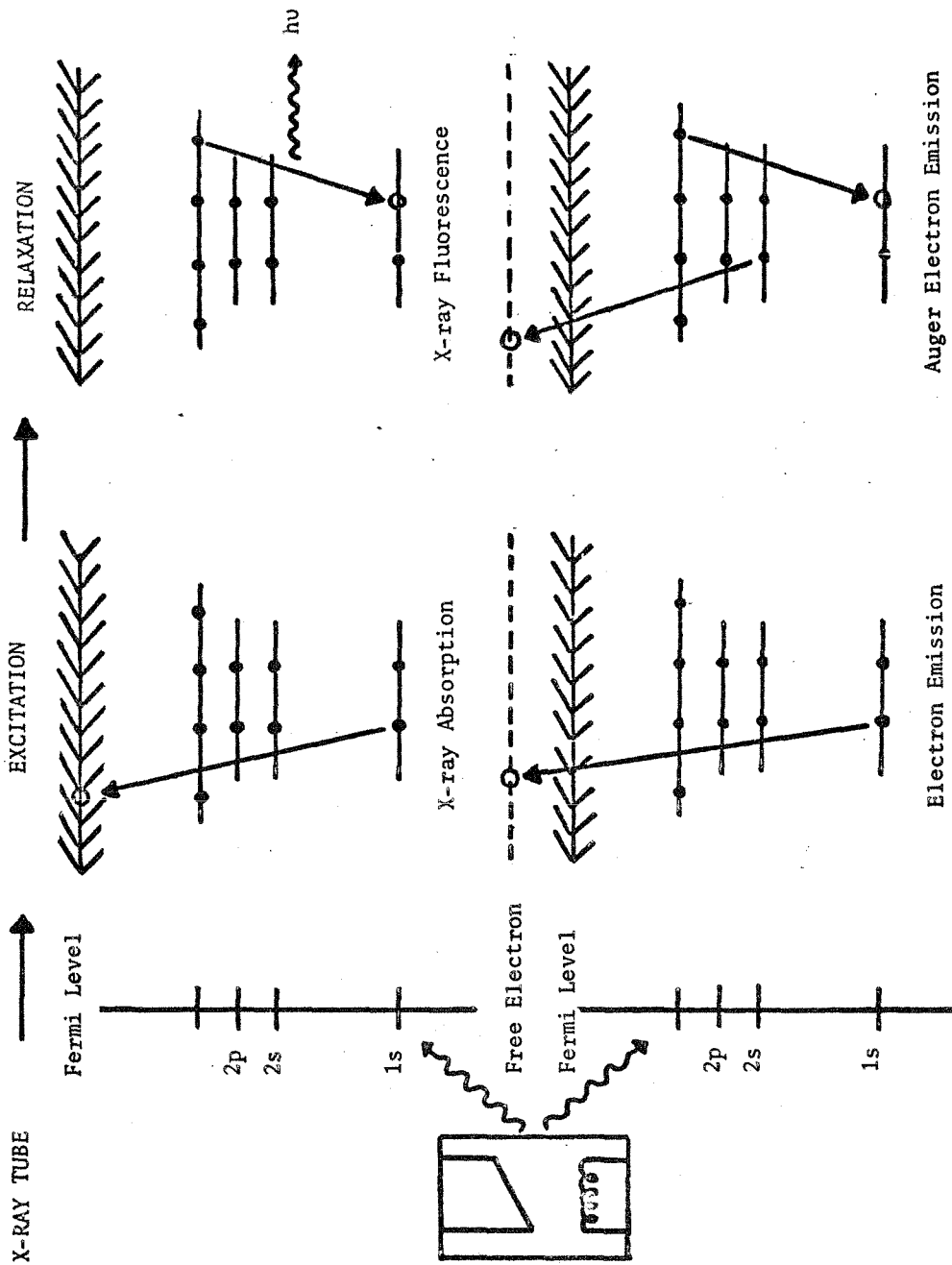
Both processes lower the kinetic energy of the primary photoelectron, which leads to satellite structure on the low-kinetic energy (high binding energy) side of the peak.

17. Kraus, M.O.; Vestal, M.L.; Johnston, W.H.; and Carlson, T.A.; Phys Rev, 133, A385 (1964)

18. Carlson, T.A., and Kraus, M.O., Phys Rev, 137, A1655 (1965)

19. Kraus, M.O., Carlson, T.A., and Desmukes, R.D., Phys Rev, 170, 37 (1968)

FIGURE 2 ELECTRON EVENTS STIMULATED BY X RAY PHOTON ADSORPTION



Initial work also demonstrated that for $AlK\alpha$ photons shake-off structure should be seen for binding energies less than 500 eV.

Multiple-electron transitions have been predicted for metals^{20,21}.

These processes are complicated by plasmon excitation.

D. Spectral Lines and Intensity Distributions

X-ray photon adsorption can result in the stimulation of four different processes as detailed in Fig. 2⁸.

The initial X-ray capture results in promotion of an electron to either a bound state (X-ray adsorption) or to the vacuum continuum (X-ray photoelectron emission). In either case, a K state vacancy is created.

Part of the energy of the photon stored in the system is dissipated by electron relaxation which can result in either X-ray fluorescence or Auger-electron emission. The potential emission of Auger electrons complicates the interpretation of the observed kinetic energy distribution, $N(E)$, because the apparent binding energies corresponding to the peaks are independent of the energy of the incident X-ray photons.

In general, photoelectron and Auger-electron lines can be separated if appropriate target materials are used (thus selecting the most suitable characteristic radiation). In most cases it requires substantial effort to change the target.

20. Hedin, L., and Lundqvist, S., Solid State Physics, 23, 1 (1969)

21. Doniach, S., Phys Rev, B2, 3898 (1970)

TABLE 1

PHOTOELECTRON AND AUGER LINES

(Al Xrays)

(A = Auger line; 1 = sub 1/2; 3 = sub 3/2; 5 = sub 5/2; 7 = sub 7/2)

18	*	Hf4f	63	*	Na2s	110		Te4p	180	*	Tm4d	271		Gd4p3
26	*	Ta4f	65		Hf5s	111	*	Be1s	181		Ge4s	273	*	Os4d5
29	*	Ge3d	66		Pt5p1	111	*	Rb3d	182	*	Br3p3	274		Re4d3
31		Hf5p3	66		V3s	111	*	Ce4d	182		Th5p3	279	*	Ru3d5
32	*	Sb4d	67		Cd4p	112		Ni3s	183		Zr3d3	280		Sr3p1
34		K3s	68	*	Ni3p	114	*	Pr4d	184	*	Yb4d5	284		Ru3d3
34	*	W4f7	70	*	Br3d	118	*	Al2s	186		I4s	284		Eu4p1
35		W5p3	71	*	Pt4f7	118	*	Nd4d	118	*	B1s	284	*	C1s
37		W4f5	71		Ta5s	118		Bi5p1	189	*	P2s	289		Gd4p1
37		Ta5p3	72		Au5p1	118	*	Tl4f7	189		Br3p1	290		Ce4s
38		Hf5p1	73	*	Al2p	120		Cu3s	192		Ba4p1	290		Os4d3
38	*	V3p	74		Pt4f5	120		Hg5s	193		La4p3	290		Th5s
38		Sr4s	74		Cr3s	122		In4s	195	*	Lu4d5	294	*	K2p3
40	*	Te4d	74	*	Cu3p	122	*	Ge3p3	197		Yb4d3	295	*	Ir4d5
41	*	As3d	75		Ru4s	122		Tl4f5	200	*	Cl2p	297		K2p1
43	*	Cr3p	76		Tl5p3	123		I4p	204		As3s	301	*	T3p3
43		Ru4p	77		W5s	129		Ge3p1	205		Lu4d3	305		Pr4s
44		Ca3s	77		In4p	130	*	Sm4d	205	*	Nb3d5	306		Ho4p3
45		Ta5p1	78	*	Cs4d	134	*	Sr3d	206		La4p1	307	*	Rh3d5
46	*	Re4f	81		Rh4s	134	*	Eu4d	208		Nb3d3	311		Tb4p1
46		Y4s	81		Hg5p1	135	*	P2p	208		Ce4p3	312		Rh3d3
46		W5p1	83		Re5s	137		Zn3s	214	*	Hf4d5	312		Ir4d3
46		Re5p3	84		Os5s	137		Sn4s	218		Pr4p3	313		Y3p1
48		Rh4p	84	*	Au4f7	137		Tl5s	224		Ce4p1	314	*	Pt4d5
49	*	Mn3p	84		Mn3s	138	*	Pb4f7	224		Hf4d3	316		Nd4s
50	*	I4d	86		Pd4s	141	*	Gd4d	225		Nd4p3	320		Er4p3
51	*	Os4f	86		Pb5p3	141	*	As3p3	227	*	Mo3d5	322		Rb3s
51		Os5p3	87		Au4f5	143		Pb4f5	229	*	S2s	322		GeA
51		Pt5p3	87	*	Zn3p	147		As3p1	229		Th5p1	324		U5s
51		Pd4p	89	*	Mg2s	148	*	Tb4d	230		Mo3d3	331	*	Zr3p3
52	*	Mg2p	89		Sn4p	148		Pb5s	230	*	Ta4d5	331		Pt4d3
52		Zr4s	90	*	Ba4d5	149	*	Si2s	231		Cs4s	332		Dy4p1
52		Ir5p3	93		Ba4d3	152		Sb4s	232		Se3s	334	*	Au4d5
54		Sc3s	93		Bi5p1	154	*	Dy4d	237		Pr4p1	335	*	Th4f7
54		Au5p3	95		Fe3s	158		Ga3s	239	*	Rb3p3	335	*	Pd3d5
55	*	Li1s	95		Ag4s	158	*	Bi4f7	242		Ta4d3	337		Tm4p3
56	*	Fe3p	96		Ir5s	159	*	Y3d	224		Nd4p1	340		Pd3d3
56		Ag4p3	99		Sb4p	160		Bi5s	246	*	W4d5	343		Ho4p1
57	*	Se3d	99	*	La4d	161	*	Ho4d	248		Rb3p1	343		Yb4p3
58		Nb4s	99	*	Hg4f7	162	*	Se3p3	249		Sm4p3	344		Th4f5
58		Re5p1	100	*	Si2p	162		Cs4p3	253		Ba4s	345		Zr3p1
58		Hg5p3	100		Tl5p1	163		Bi4f5	257		Br3s	347		Sm4s
59		Ti3s	101		Co3s	165	*	S2p	257		Eu4p3	347	*	Ca2p3
60	*	Co3p	102		Pt5s	168		Se3p1	259		W4d3	350		Ca2p1
60	*	Ir4f7	103	*	Ga3p3	168		Te4s	260		U5p1	352		Au4d3
62		Mo4s	103		Hg4f5	168	*	Er4d5	260	*	Re4d5	354	*	GeA
62		Ag4p1	105		Pb5p1	172		Cs4p1	267		Sm4p1	358		Sr3s
63		Ir4f5	107		Ga3p1	177		Er4d3	269	*	Sr3p3	359		Lu4p3
63		Os5p1	108		Cd4s	180	*	Zr3d5	270	*	Cl2s	360		Eu4s
63		Ir5p1	108		Au5s	180		Ba4p3	271		La4s	360	*	Hg4d5

TABLE 1

PHOTOELECTRON AND AUGER LINES (CONTINUED)

363 *	Nb3p3	469	Os4p3	608	Pt4p1	779 *	CO2p3	978 *	Nd3d5
366	Er4p1	472	Tm4s	609	Tl4p3	780	U4d3	981 *	CA
367 *	Ag3d5	479	Cua	617 *	Cd3p3	781 *	Ba3d5	984 *	IA
374	Ag3d3	480	ZnA	620 *	I3d5	782	CoA	998	Cs3p3
376	Gd4s	483	Ru3p1	625	Re4s	784	FeA	1000	Nd3d3
377 *	K2s	485 *	Sn3d5	627	Rh3s	794	Co2p1	1001	OA
379	Nb3p1	487	Yb4s	628	V2s	796	Ba3d3	1005 *	TeA
379	Hg4d3	492	W4p1	629	CuA	797 *	PrA	1006	Te3s
380	Hf4p3	493	GaA	631	I3d3	800	Hg4s	1007	CrA
381 *	U4f7	494	Sn3d3	632	La4d	806	Bi4p1	1007	Ni2s
386	Tm4p1	495	Ir4p3	640	Cua	812	Sb3p1	1015 *	TeA
386 *	Tl4d5	496 *	Rh3p3	640 *	NiA	819	Te3p3	1020	Va
392	V4f5	500 *	Sc2s	641 *	Mn2p3	826	In3s	1021 *	Zn2p3
393 *	Mo3p3	500 *	NaA	644	Au4p1	827 *	CeA	1032	Sba
395	Y3s	503 *	ZnA	645	Pb4p3	832 *	La3d5	1040 *	Sba
396	Yb4p1	505	Mo3s	648	CuA	835 *	FA	1044	Zn2p1
398	Tb4s	506	Lu4s	651	Cd3p1	838	CoA	1045	U4p3
399 *	N1s	511	GaA	652	Mn2p1	843	CoA	1055	SnA
400	GaA	513 *	V2p3	655	Os4s	845	Tl4s	1060 *	VA
402 *	Sc2p3	518	Re4p1	664 *	In3p3	845 *	FeA	1063 *	SnA
404 *	Cd3d5	519	Pt4p3	670	Pd3s	846	Fe2s	1063	Ba3p3
405	Ta4p3	520	V2p1	675 *	SmA	848	La3d3	1065	Cs2p1
407	Sc2p1	521	Rh3p1	677	Hg4p1	855 *	Ni2p3	1072	I3s
407	Tl4d3	522	GaA	677 *	Th4d5	861	FA	1072 *	Nals
410	Mo3p1	528 *	Sb3d5	679	Bi4p3	865 *	LaA	1077	TiA
410	Lu4p1	531 *	Pd3p3	686 *	Fls	870	Te3p1	1080	InA
411	Cd3d3	532 *	OlS	690	Ir4s	873	Ni2p1	1081 *	Sm3d5
413 *	Pb4d5	537	Sb3d3	695	Cr2s	875	I3p3	1087 *	InA
416	Dy4s	538	Hf4s	702	In3p1	884	Sn3s	1096	Cu2s
423	GeA	540	NaA	710 *	Fe2p3	884 *	Ce3d5	1107	Sm3d3
426	W4p3	546	Au4p3	712	CuA	890	BaA	1107 *	Na
427 *	GaA	547	Os4p1	712	NiA	894	Pb4s	1109	CdA
431	Zr3s	547	CuA	714	Th4d3	896	FeA	1113 *	TiA
435	Pb4d3	559	Pd3p1	715 *	Sn3p3	902	Ce3d3	1116 *	CdA
436	Ho4s	564 *	Ti2s	715	CoA	903 *	BaA	1116 *	Ga2p3
437	Hf4p1	566	Ta4s	717	Ag3s	908 *	MnA	1124	La3p3
438 *	Ca2s	567	ZnA	722	Tl4p1	915	CsA	1131	AgA
440 *	Bi4d5	568 *	CuA	723	Fe2p1	926	Co2s	1131 *	Eu3d5
443 *	In3d5	571	Hg4p3	724	Pt4s	927 *	CsA	1136 *	AgA
444	GeA	571 *	Ag3p3	726 *	Cs3d5	931	I3p1	1137	Ba3p1
445	Re4p3	572 *	Te3d5	738 *	U4d5	931 *	Pr3d5	1143	Ga2p1
449	Er4s	575 *	Cr2p3	740	Cs3d3	931 *	Cu2p3	1157 *	ScA*
451	In3d3	577	Ir4p1	755 *	NdA	939	Bi4s	1158 *	PdA
454	GeA	581	ZnA	757	Sn3p1	944	Sb3s	1190 *	RhA
455 *	Ti2p3	582	Te3d3	759	Au4s	951	Cu2p1	1198 *	CaA
461	Ti2p1	584	Cr2p1	764	Pb4p1	951	Pr3d3	1215 *	RuA
461 *	Ru3p3	585	Ru3s	766	Sb3p3	952	MnA	1230 *	CA
464	Bi4d3	590	ZnA	769	Mn2s	967 *	CrA	1239 *	KA
465	Ta4p1	595	W4s	770	Cd3s	968	Th4p3	1307 *	C1A
469	Nb3s	602	Ag3p1	778	NiA	972	IA	1315 *	BA
								1333 *	SA

* Strongest Auger Line or one of the two strongest photoelectron lines in the element spectrum, not including minor lines of spin doublets.

Figure 2a PRINCIPAL PHOTO ELECTRON ENERGIES

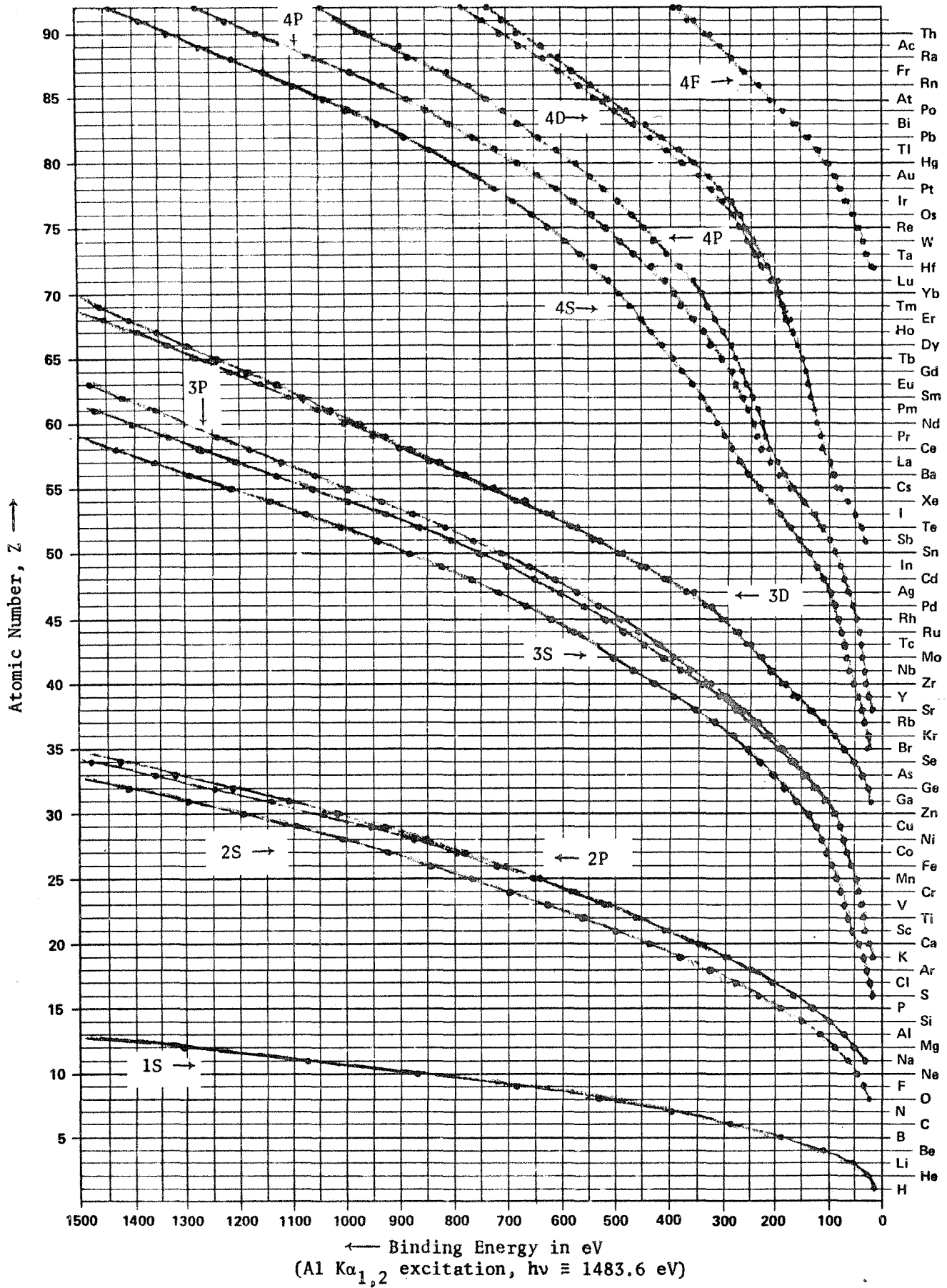
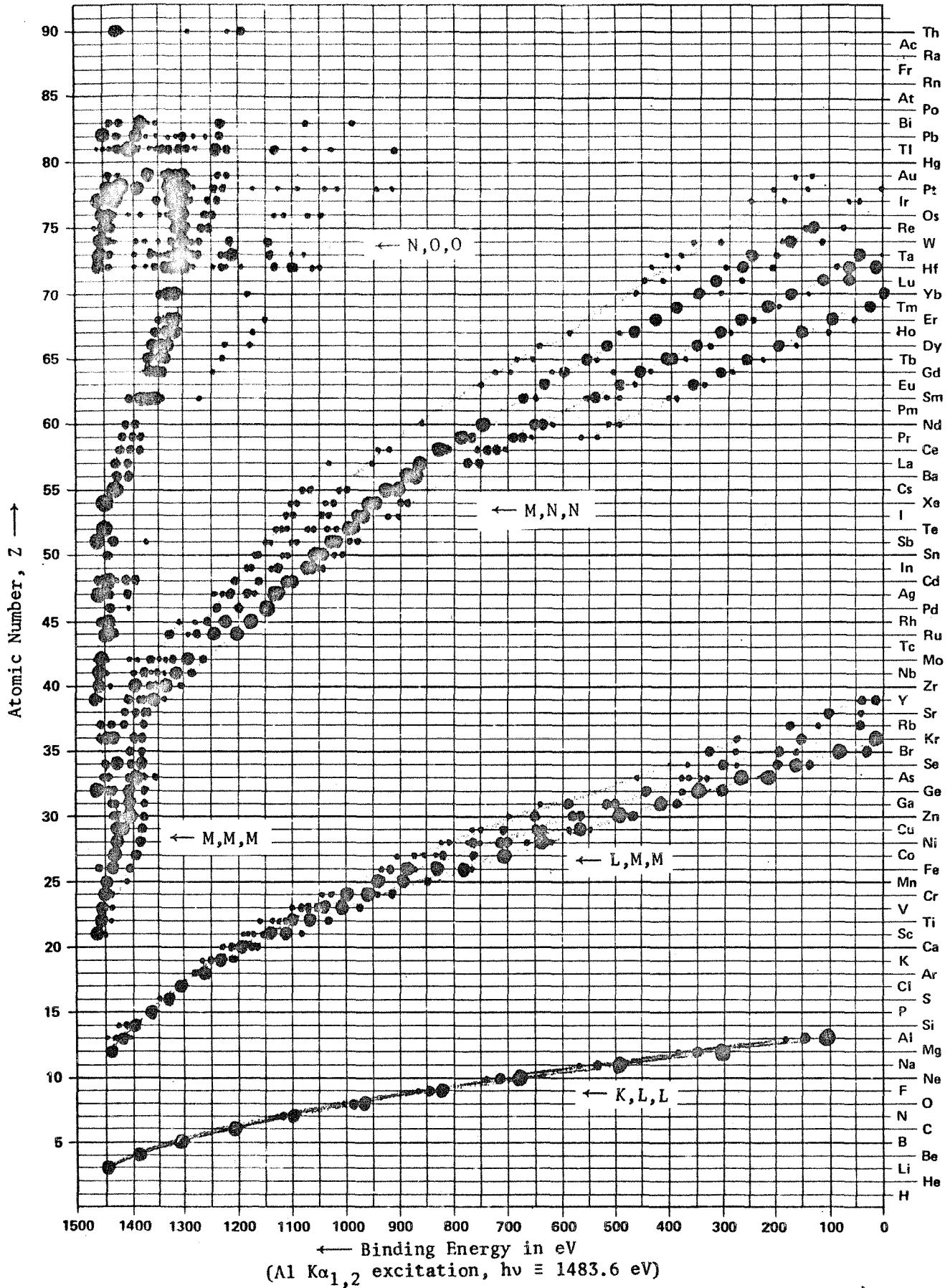


Figure 2b PRINCIPAL AUGER ELECTRON ENERGIES



The Hewlett-Packard 5950A spectrometer has no provision for changing the target. As most photoelectron spectra presented in this thesis were taken with this spectrometer, observed x-ray photoelectron lines and major Auger-electron lines have been catalogued for analysis of this data (Table 1). The strongest photoelectron and Auger lines are marked by an asterisk (*). The energies given in that table are compiled from observations by Siegbahn¹, and Wagner²².

The intensity of the photoelectron line is proportional to the concentration of the element to be studied in the region of observation. Henke²³ has given a phenomenological model for the intensity of a photoelectron line originating from a homogeneous sample with a smooth surface. For very thick samples, his equation reduces to

$$\Phi_i = Q A \frac{\omega}{4\pi} \tau_i N_i \lambda_i, \quad (14)$$

where

- $\Phi_i \equiv$ intensity of the photoelectron line
- $Q \equiv$ photon flux
- $A \equiv$ effective sample area
- $\omega \equiv$ solid angle of acceptance for the spectrometer
- $\tau_i \equiv$ photoelectric cross section
- $N_i \equiv$ number density of emitting atoms
- $\lambda_i \equiv$ mean free path for i photoelectrons in the sample.

When a parameter for the electron emission of surface contaminants is included, the intensity becomes

$$\Phi_i = Q A \sin \frac{\omega}{4\pi} \tau_i N_i \lambda_i T_i, \quad (15)$$

22. Wagner, C.D., Anal Chem, 44, 967 (1972)

23. Henke, B.L., X-ray Optics and X-ray Microanalysis, Academic Press, New York, N.Y., 1963, pp. 157-72.

after simplifying for the uniform intensity of the exciting photons over the illuminated region.

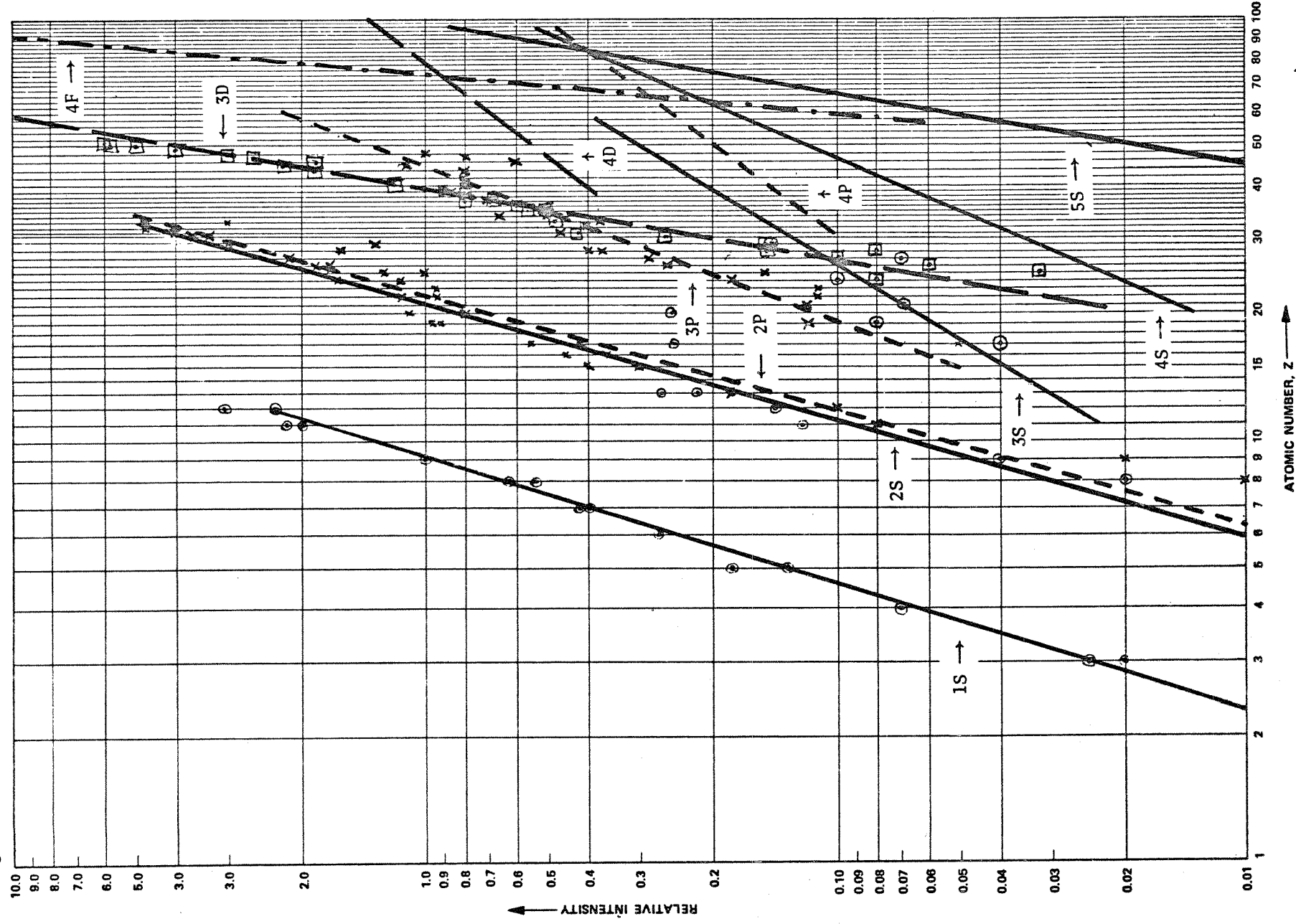
Regrettably, experimental values for λ_i and τ_i are lacking, and only relative correlations can be made within the same sample. An extensive series of photoemission sensitivities have been given by Wagner²⁴. These are referenced to the Fluorine 1s line (AlK_{α} excitation). Additional data have appeared recently^{24a,24b}. These provide relative estimates of photoelectric cross-sections, scattering coefficients and mean-free photoelectron paths for a series of elements and their major photoelectron lines. Plotting the data on Log Log scale has permitted enhanced estimation of true sensitivities by linear regression. This empirical correlation of elemental sensitivities is displayed in Figure 3 to facilitate reduction of data given in this thesis.

24. Wagner, C.D., Anal Chem, 44, 1050 (1972)

24a. Jorgensen, C.K., and Berthou, H., Farad. Disc. Chem. Soc., 54, 269 (1972).

24b. Nefedov, V.I., Sergushin, N.P., Bond, I.M., and Trzhaskovskaya, M.B., J. Elec Spec, 2, 383 (1973).

Figure 3 Relative Intensities of the Photoelectron Lines



III. EXPERIMENTAL METHODS

A. General Experimental Description

The experiments described in this thesis are based on an analysis of the kinetic energy distribution of electrons photo emitted from solid specimens upon irradiation with X-rays. The basic experimental arrangement consists of a sample chamber, a mechanism for sample introduction, x-ray photon source, electron kinetic energy monochromator, electron pulse detector, magnetic-field compensator, and supporting vacuum system.

Low pressures, $<10^{-5}$ torr, are required to avoid line broadening otherwise caused by collisions with gas molecules. In commercial electron spectrometers, the vacuum is produced by diffusion pumps, turbo-molecular pumps or ion pumps. Each of these gives rise to specific problems.

The diffusion and turbomolecular pumps produce cracking products of pump oils that may deposit on the sample surface. The composition of these products are ill-defined, although they appear to be oxidation products²⁵

The ion pump/vac sorb method results not only in lower pressures but also in a hydrocarbon-free environment, containing essentially CO, CO₂ and H₂O (at 10^{-8} torr). With these lowered pressures, the signal strength is increased significantly.

Virtually each modern electron spectrometer has an electrostatic energy analyzer²⁶, of the kind first described by Purcell²⁷ in 1938. This analyzer consists of concentric spherical segments with the outermost

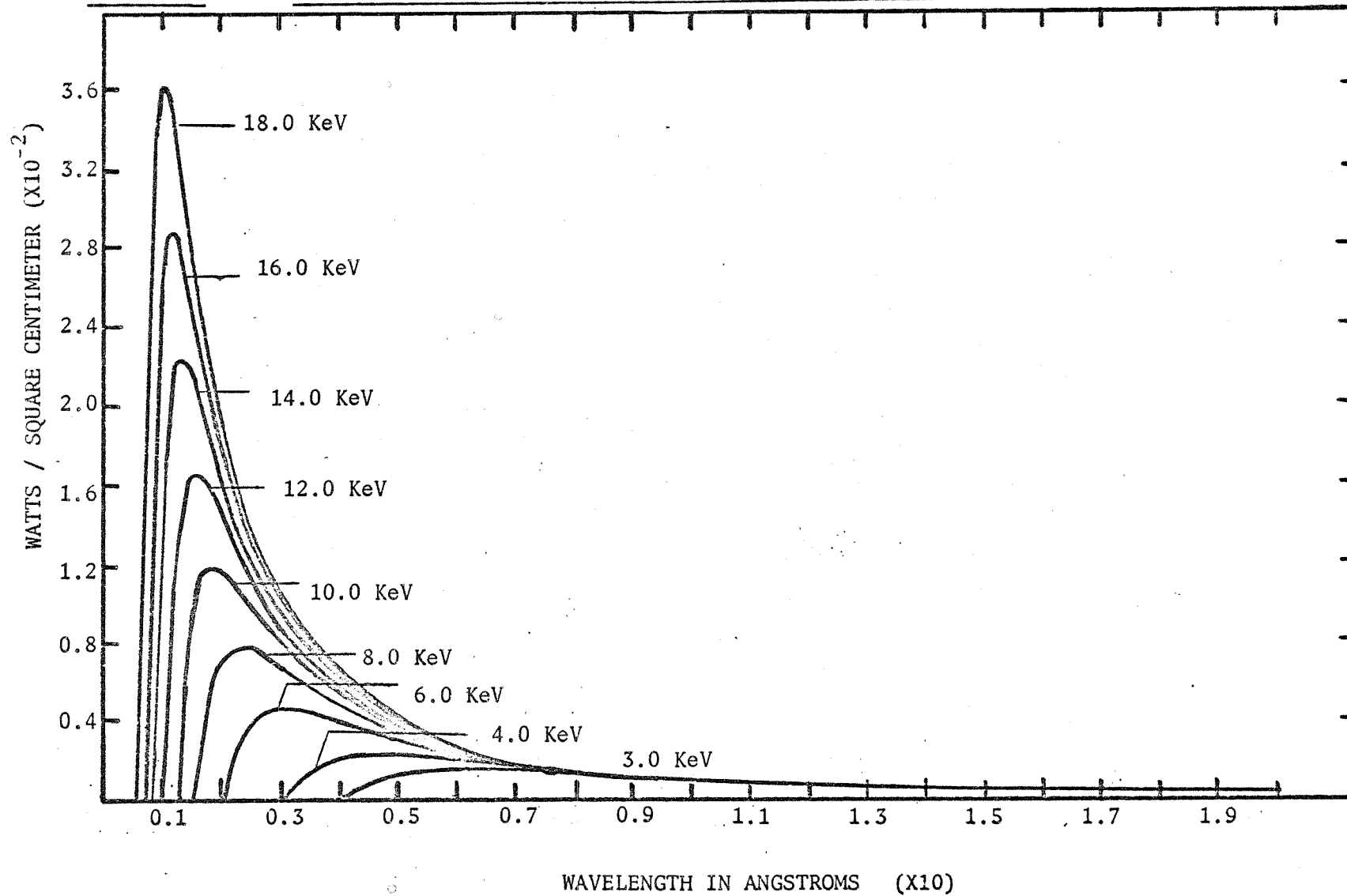
25. Riggs, Wm. M., Private Communication

25a. Brundle, C.R., and Roberts, M.W., Proc R Soc Lond, A 331, 383 (1972)

26. Luccesi, C.A., and Lester, J.E., J. Chem Ed, 50, A205 (1973)

27. Purcell, E.M., Phys Rev, 54, 818 (1938)

FIGURE 4 BREMSTRAHLUNG FROM MAGNESIUM TARGET WITH ELECTRON EXCITATION ENERGIES OF 3 - 18 KeV



sphere negatively charged. Potentials are adjusted to give a $V = 0$ plane along the central radial dimension. The use of inlet and exit slits, placed at 180° separation, to govern electron pathways through the monochromator results in maximum transmission through the analyzer. The analyzer resolution is determined by the radius of the spheres and relative slit widths. Commercial spectrometers employ central radii ranging from 15.5 cm. to 36.0 cm.

The several commercial and experimental approaches vary considerably in the choice of a source of X-ray photons. Siegbahn's initial work described a demountable X-ray tube which used an aluminum or magnesium target. These sources emit considerable energy in the $K\alpha_{1,2}$ doublet. Additional X-ray energy is emitted as Bremstrahlung, which is plotted in Figure 4, as a function of accelerating voltage. In addition to the characteristic emission ($K\alpha$), a series of satellites are generated. The strongest of these is the $K\alpha_{3,4}$ line, which gives two peaks in the photoelectron spectrum at lower binding energy. Magnesium radiation gives separations of 8.412 eV at 9.48% primary peak intensity for the α_3 line and 10.142 eV at 4.54% relative intensity⁵ for the α_4 transition⁵. The linewidth of the $K\alpha_{1,2}$ doublet is 0.8 eV for magnesium and 1.0 eV for Aluminum.

An x-ray monochromator offers an alternative to the "raw" x-ray source. It reduces the net linewidth to 0.1 eV and eliminates the complications of peaks due to satellite transitions. Bent crystal x-ray monochromators have been described in the monograph of the Uppsala group¹. This approach results in reduced x-ray flux and electron counting rates.

The electron detectors are usually discrete electron multipliers. Spectrometers using monochromated sources employ multi-channel detectors to recover lost intensity. The combination of electron multiplier arrays with a phosphor videocon can provide 128 element detectors (MCA).

The line width in an electron spectrum is generally represented as the full width of the observed peak at half the maximum intensity (FWHM).

The contributions to the line width can be summarized as

$$\Delta^2 = \Delta_B^2 + \Delta_X^2 + \Delta_K^2 + \Delta_W^2, \quad (16)$$

where

- $\Delta_B \equiv$ the natural line width
- $\Delta_X \equiv$ width of the exciting x-ray line
- $\Delta_K \equiv$ broadening by the analyzer
- $\Delta_W \equiv$ broadening due to solid state effects in the sample.

With a non-monochromatized x-ray source, Δ_X predominates, whereas Δ_B and Δ_W are dominant when monochromated x-rays are used.

B. Instrumental Characteristics

Several spectrometers were employed in this work:

1. The Jet Propulsion Laboratory-Utah State University spectrometer
2. The McPherson ESCA 36 spectrometer
3. The Hewlett-Packard 5950A spectrometer
4. The DuPont 650 electron spectrometer.

The JPL-USU spectrometer and the McPherson ESCA 36 are based on the electrostatic instrument described by the Uppsala group^{1,3}. These employ 36 cm. mean radius spheres machined to an accuracy of 0.5 parts per 10,000. Both use turbo-molecular pumps but the McPherson

unit²⁸ also uses a supplementary cryopump for still lower chamber pressures.

During the development of the JPL-USU spectrometer, we experienced that a very high degree of accuracy and superb workmanship is required for the construction of the electron analyzer. Misalignment of the analyzer spheres by parts per thousand gave multiple images and broadenings of gold $4f_{7/2}$ spectra to 2.2 eV from 1.6 eV FWHM²⁹.

The JPL-USU spectrometer is shielded against the earth's and other magnetic fields by means of Helmholtz coils. In addition, the analyzer section is surrounded by a paramagnetic shield. The McPherson ESCA 36 spectrometer employs a series of three concentric paramagnetic shields to prevent inhomogeneities in the residual field.

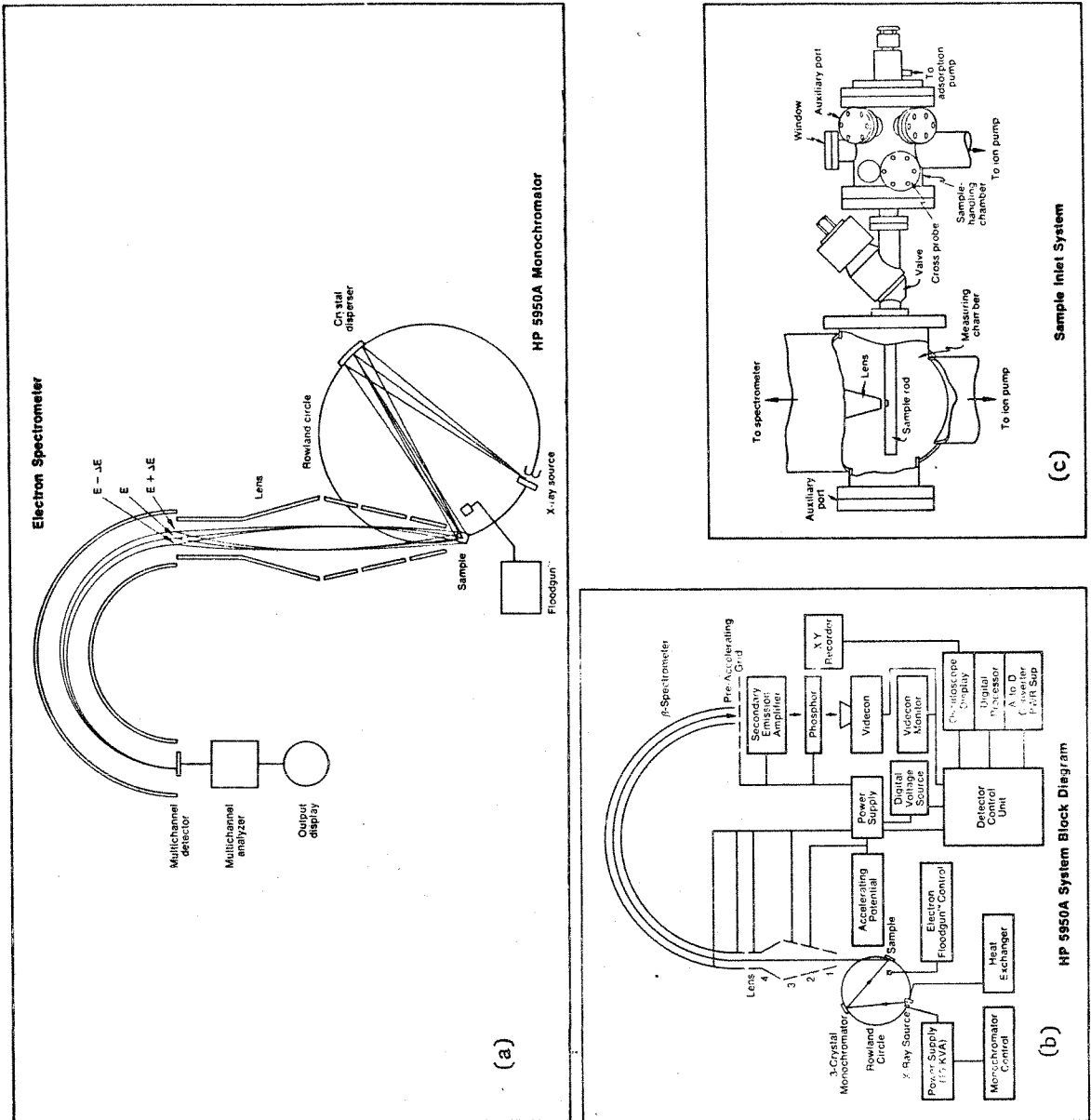
The JPL-USU spectrometer was operated at 10^{-6} to 10^{-7} torr and gave about 2×10^3 counts per second (cps) for a freshly cleaned gold sample (Au $4f_{7/2}$ line, FWHM ranging from 2.0 to 1.6 eV). The McPherson ESCA 36, operated at a gauge reading of less than or equal to 10^{-8} torr, gave about 2×10^4 cps with the same sample in place (FWHM 1.0 to 1.5 eV). In both cases, a single-channel detector and Mg $K\alpha_{1,2}$ radiation was used.

Most of the quantitative work reported in this thesis was performed with the Hewlett-Packard 5950A spectrometer. This instrument employs a bent quartz-crystal x-ray monochromator, an electrostatic electron-beam monochromator, dispersion compensation electron optics, retarding potential

28. Rendina, J., American Laboratory, 6, 27 (1972)

29. Wood, J.K., and Grunthaner, F.J., unpublished results

FIGURE 5



electron lens, a multichannel detector and a multi-channel analyzer³⁰ (see Fig. 5).

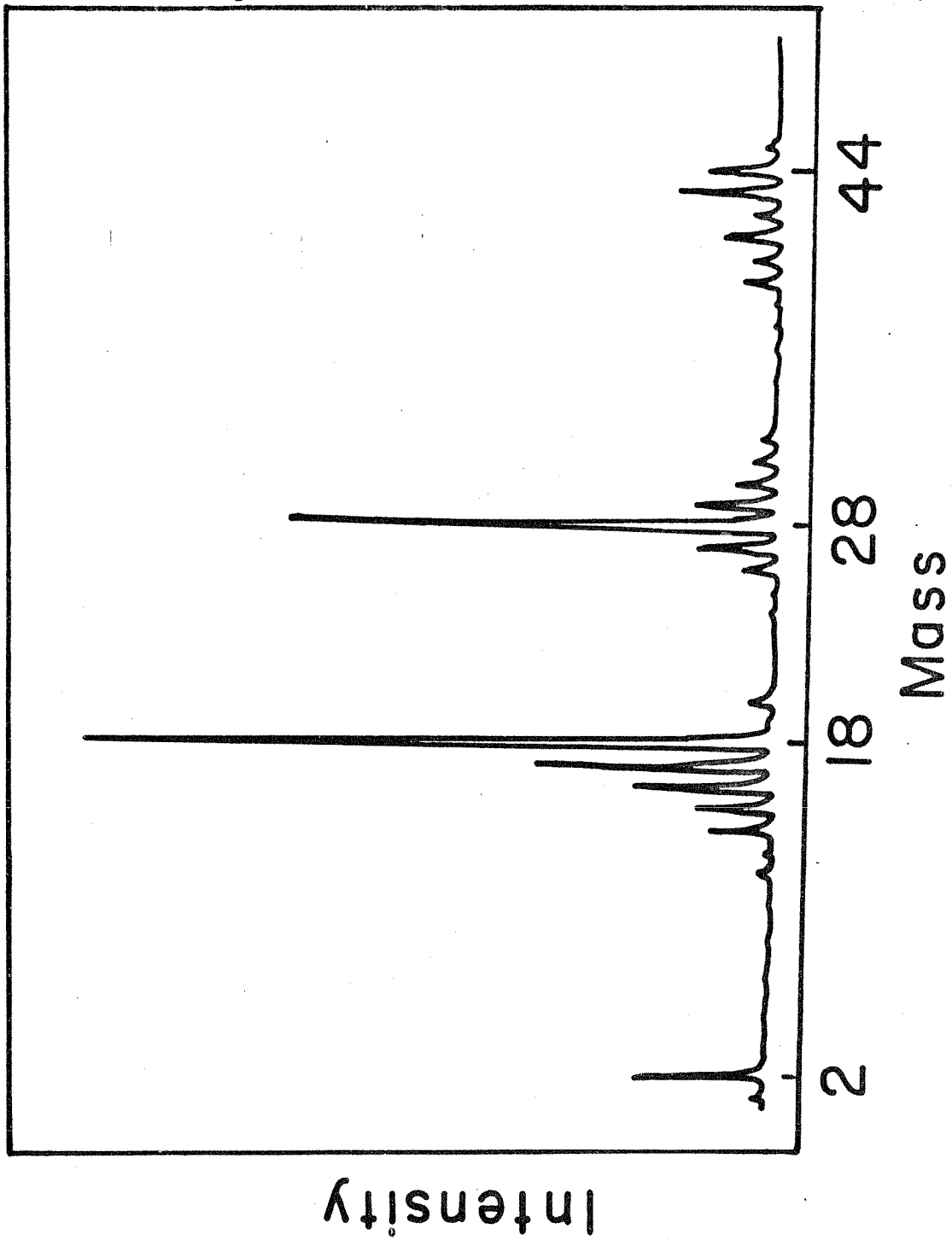
The dispersion monochromators pass an energy packet $E - \Delta E$ to $E + \Delta E$ (ΔE is the dispersion of the analyzer). In this design, the electron analyzer is arranged so that its energy dispersion is antiparallel to that of the photon monochromator. If the dispersion ΔE_1 of the electron analyzer is set equal to the dispersion ΔE_2 of the x-ray monochromator the transmitted line widths nearly cancel each other.

In theory, natural linewidths could be observed in this dispersion compensation system, but second and third order aberrations limit the minimum widths to 0.5 eV.

The monochromator illuminates a well-defined region of the sample (1 x 5 mm) but reduces the total x-ray flux by about two orders of magnitude. The sample chamber and x-ray source are isolated from each other by an aluminum window and care is being taken to avoid irradiating the chamber walls. Thus, the number of secondary stray electrons impinging on the sample is very low and an auxiliary electron gun (flood gun) has to be used to neutralize the charge that builds up on the sample.

The vacuum is produced by noble ion pumps giving an operating pressure of 3×10^{-9} in the main analyzer chamber. During normal operation of the unbaked spectrometer, the residual gas in the main chamber consists primarily of water, CO and H₂, and small quantities of hydrocarbons and

30. Siegbahn, K., Hammond, D., Fellner-Feldigg, H., Barnett, E.F., Science, 176, 245 (1972).

Figure 6. Mass Spectrum of Residual Gas in HP 5950A at $\sim 10^{-9}$ torr.

rare gases. A typical mass spectrum⁶ taken with the EAI Quad 250 quadrupole residual-gas analyzer attached to the main chamber is shown in Fig. 6.

The potential of the retarding lens is swept to trace the spectrum (Fig. 5) and the analyzer is operated at constant energy (110 eV). The analyzer transmits a 10 eV band which is detected by a 128 element multichannel array. A phosphor/vidiocon system is used to detect the electron count rate. The information is stored in the multichannel detector (MCD). The spectrum is scanned over a selected voltage range so that each element in the array "sees" each energy twice during a single scan. Data are recorded by a paper tape punch and x-y plotter.

Signal-to-background ratios observed in this work varied from 82 to 163:1 and signal-to-noise ratios from 12 to 1700:1. The background is defined as the signal measured at a point 7 eV lower in binding energy than the peak of interest. The noise is approximated by the standard deviation of each measurement which is given by the square root of the number of counts per channel in the background. Observed FWHM of Au $4f_{7/2}$ was 0.72 eV with count rates of about 8.5 to 9.7×10^4 counts per second.

Dispersion compensation changes the inherent line shape of the photoelectron peaks from an asymmetric to a symmetrically broadened (by 0.55 eV) Lorentzian form⁵. This symmetry simplifies deconvolution as is discussed in Chapter IV.

This system requires smooth sample surfaces³⁰ since uncertainties in the sample height affect the scaling of the record, which introduces an error of 0.1 eV/0.3 mm in the measurement. Errors of this kind are greatly reduced by using a sample on which a thin gold film is later deposited for

use as a reference.

C. Voltaic Potential Effects

The referencing of binding energies for metals is straightforward, but presents some difficulties for insulators. In this case, the definition of a Fermi Level is questionable and charging effects can displace the photoelectron lines.

If the charging domains are inhomogeneous, a distortion of the peak shape is observed. Changes in the flux are also observed apparently due to retardation caused by the surface potential.

In most experimental systems, the flux levels of the secondary electrons cannot be controlled. The magnitude of the V_C is often irreproducible because of the variation x-ray flux density and surface contamination³¹. The voltaic potential introduces considerable uncertainty as regards the position of the photoelectron lines in non-metallic samples.

Siegbahn-type electron spectrometers show charging effects of up to 3 eV, while monochromatic systems can show shifts of up to 130 eV because of the lack of stray electrons. Measurement of absolute binding energies requires a calibrant or a device controlling the irradiation of the by low-energy electrons or both.

Calibrant standards are usually deposited externally on the sample, The Uppsala group used the carbon line from adsorbed pump oil. This line was assigned a binding energy of 285.0 eV. Since many species have been

31. Bremser, W., Lennemann, F., Chemiker-Ztg, 95, 1011 (1972).

observed in this surface contaminant³², this reference is unsatisfactory. Seven carbon components have been found in experiments on Ag_2HgI_4 crystals in this present work.

Other reference standards are obtained by deposition of graphite from a sooty flame³³, by utilizing the carbon from double-stick adhesive tape³⁴ or by evaporation of gold or lead onto the sample. The last procedure is accepted as the most reliable one³⁵.

A difficulty which may arise from the disposition of too thin a gold layer is formation of islands of only a few hundred angstroms in diameter. The voltage difference between gold and the sample material arising from the difference in the photo yield is given by

$$V = \frac{2kTr_0l}{eL^2} \frac{n_0-n_1}{n_s}, \quad (17)$$

where

- L ≡ electron diffusion length
- r_0 ≡ radius of calibrant islands
- n_0-n_1 ≡ difference in photo yield
- n_s ≡ yield of low energy electrons inside the sample
- l ≡ penetration depth of x-rays.

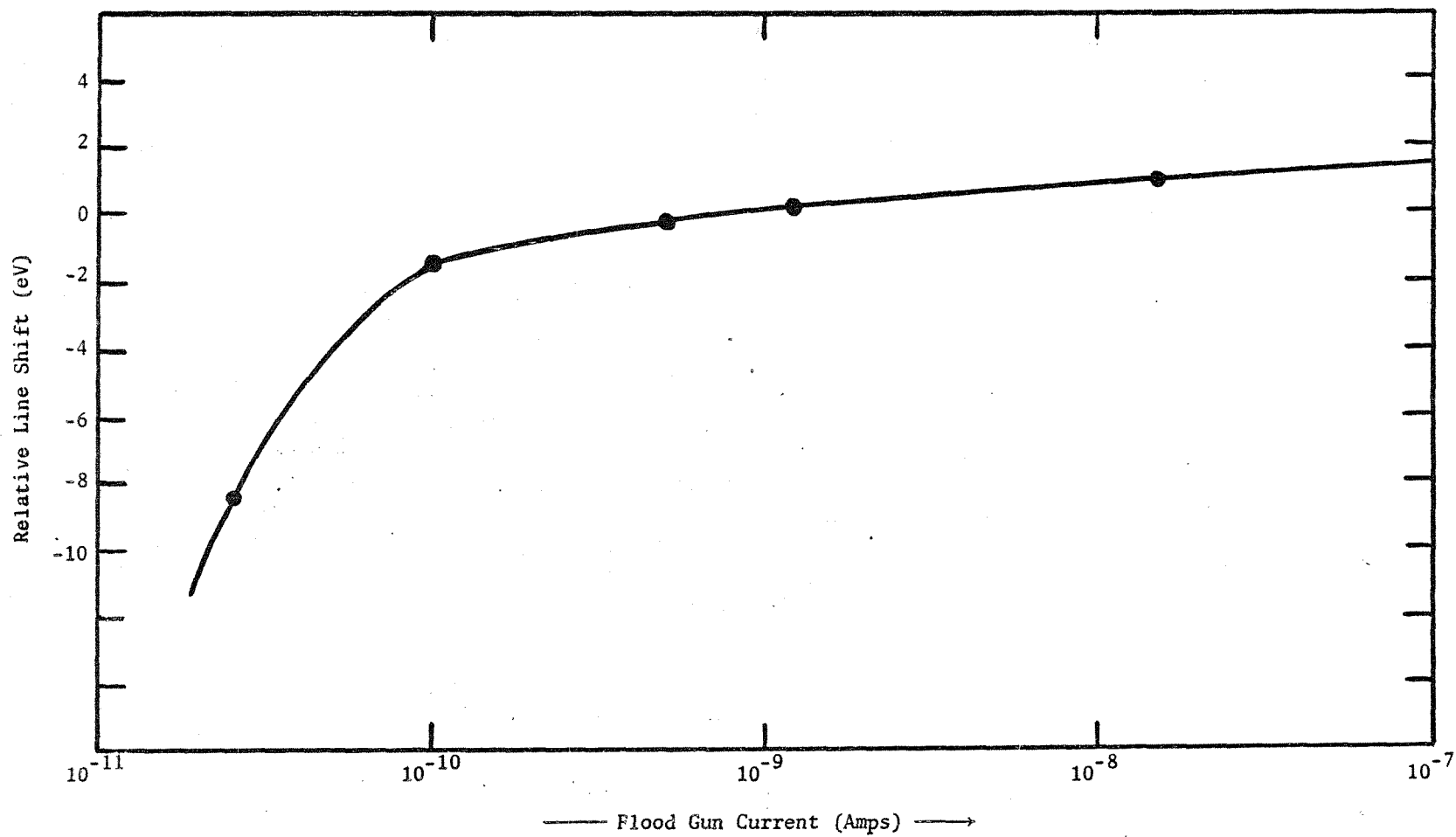
If the electron diffusion length is assigned the typical value of $\sim 500\text{\AA}$, r_0 is given the same value, and the x-ray penetration depth is a few microns, then eq. 17 reduces to

$$V = 3 \frac{n_0-n_1}{n_s} \text{ eV.} \quad (18)$$

-
- 32. Olgilvie, J.L., and Wolberg, A., Applied Spectroscopy, 26, 401 (1972)
 - 33. Brundle, C.R., Appl Spectroscopy, 25, 8 (1971)
 - 34. Jorgensen, C.K., Chimia, 25, 213 (1971)
 - 35. Hnatowich, P.J., Hudis, J., Perlman, M.L., Ragaini, R.C., J. Appl. Phys., 42, 4883 (1971)

FIGURE 7 ESCA Line Shift versus Flood Gun Current

F (1s) Teflon Sample



Since $n_s < 1$, detectable shifts should result for $\Delta n > 0.01$. Similar photovoltaic shifts should occur in other metal insulator systems, and ΔV could be several volts³⁶.

For internal calibrations several schemes have been developed such as mixing the sample with graphite³¹, and impregnating the sample with a common element³². In cases, where methyl or aliphatic carbons are present in the sample these can be used as a reference representing energies of 285.0 and 285.4 eV respectively^{37,38}. These standards offer corrections for Mandelung Potentials³⁹ and variations in the work function. This method was used throughout in this thesis work.

The method of illuminating the sample with electrons of zero kinetic energy to neutralize the charge can also be used to obtain a reference. This technique was first described by Huchital⁴⁰ and is routinely utilized in the HP5950A spectrometer, supplied with a flood gun of variable flux (from 0 to 40 eV).

The observed shift of the Fls peak in experiments with Teflon⁴¹ has been plotted versus the flux from the electron gun; see Fig. 7. Peak positions can be shifted positive or negative with appropriate flood gun currents. Replenishment currents below 10^{-10} amps are insufficient to avoid charging shifts. The linear (linear ΔeV , log current) relationship between current and peak shift greatly facilitates the application of correction factors.

In the experiments reported in Chapter V, the photoelectron spectrum of

36. Uebbing, J.J., Private Communication

37. Lindberg, B.J., Hamrin, K., Johansson, G., Gelius, U., Fahlman, A., Nordling, C., Siegbahn, K., Physica Scripta, 1, 286 (1970)

38. Gelius, U., Hedin, P.F., Hedman, J., Lindberg, B.J., Manne, R., Nordberg, R., Nordling, C., Siegbahn, K., Physica Scripta, 2, 70 (1970).

fresh vanadium diboride showed major variations in detail as a function of the flood gun current. This seemed surprising at first since the sample is a metallic conductor and apparently was in electrical contact with the spectrometer. Subsequent examination of the sample revealed that it was covered by an oxide layer of low conductivity. Fig. 8 shows the spectra obtained by applying four different flood gun currents.

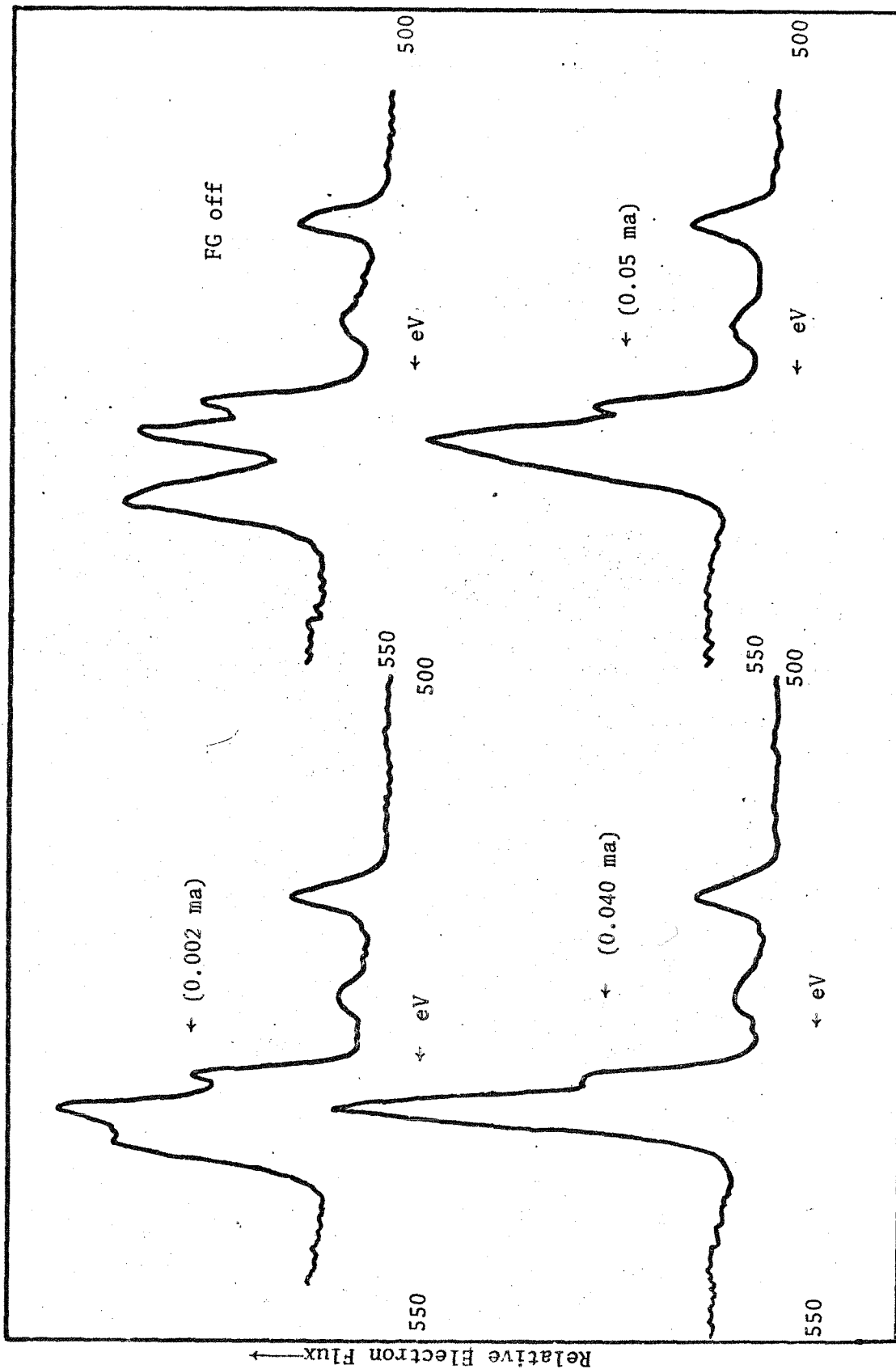
The vanadium $2p_{3/2}$ lines do not change position as the flood gun current is varied. Two peaks in the O1s part of the spectrum also remain stationary. These invariant peaks serve as internal reference standard. Other lines that are not stationary are completely eliminated by air oxidation or other treatment of the sample (see Chapt. V) apparently decreasing the impedance of the surface layer. Thus, this experiment provided valuable information as regards the problem of eliminating the charging peaks. The same results were obtained with the McPherson ESCA 36 spectrometer by inserting a DC power supply between the sample and holder. The spectra recorded in this configuration are depicted in Fig. 9. (The binding energies indicated have been corrected for the applied bias.) In Fig. 10, the bias potential is plotted against the shift (curve A) and the width (curve B) of the charging peak. A bias potential of -6 volts gives spectra which are similar to those recorded on the HP5950A when the flood gun is off. A continued increase in the negative bias permitted further separation of the insulating oxides peak from the other oxygen lines.

39. Mandelung, E., *Z. Physik*, 19, 528 (1918)

40. Huchital, D.A., and McKeon, R.T., *Appl Phys Lett*, 20, 158 (1972)

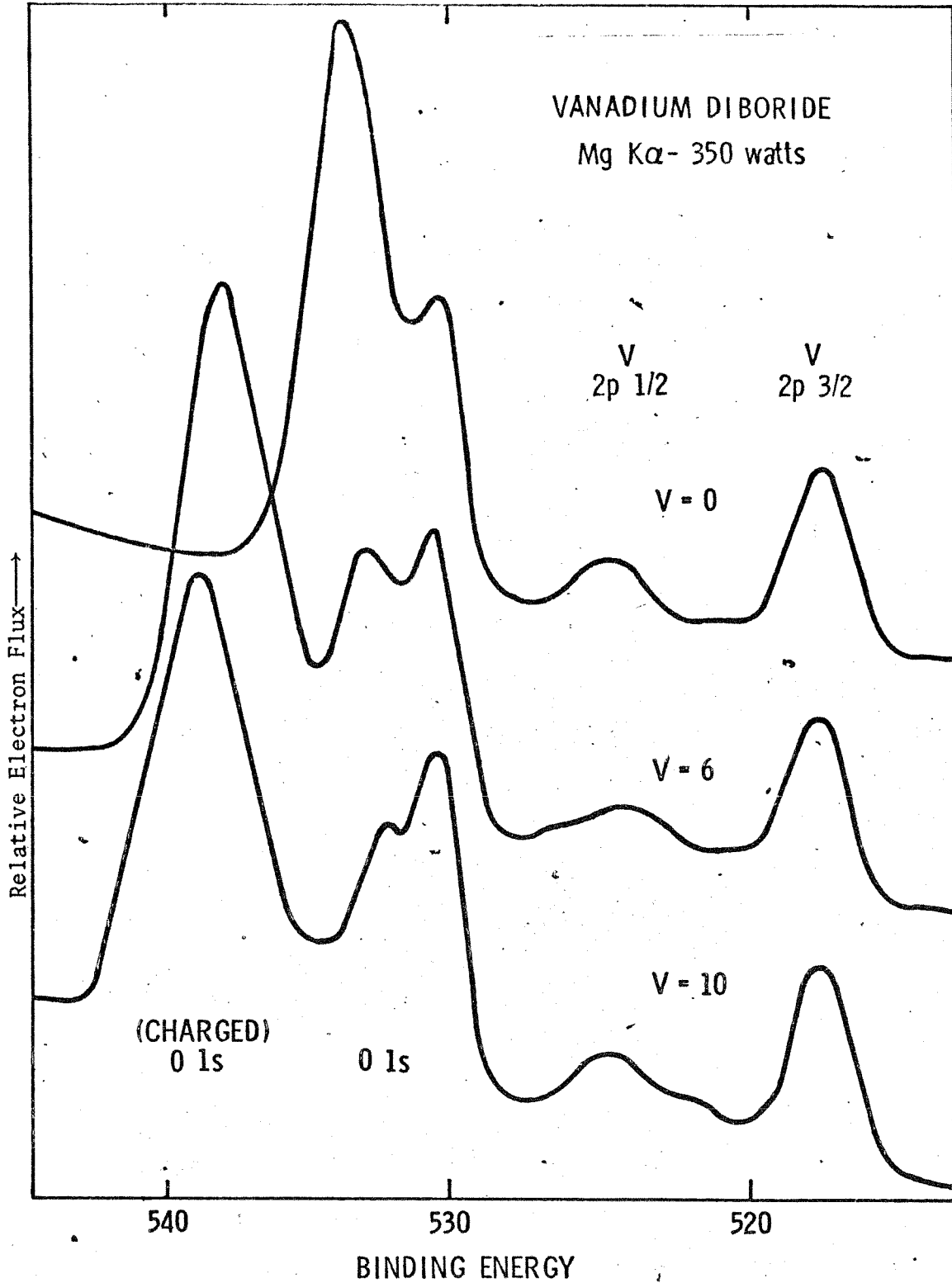
41. Melera, A., and Kelly, M., Private Communication.

Figure 8. O_{1s} , V_{2p} Photoelectron Spectra of VB_2 (Fresh) with various Flood Gun Settings.



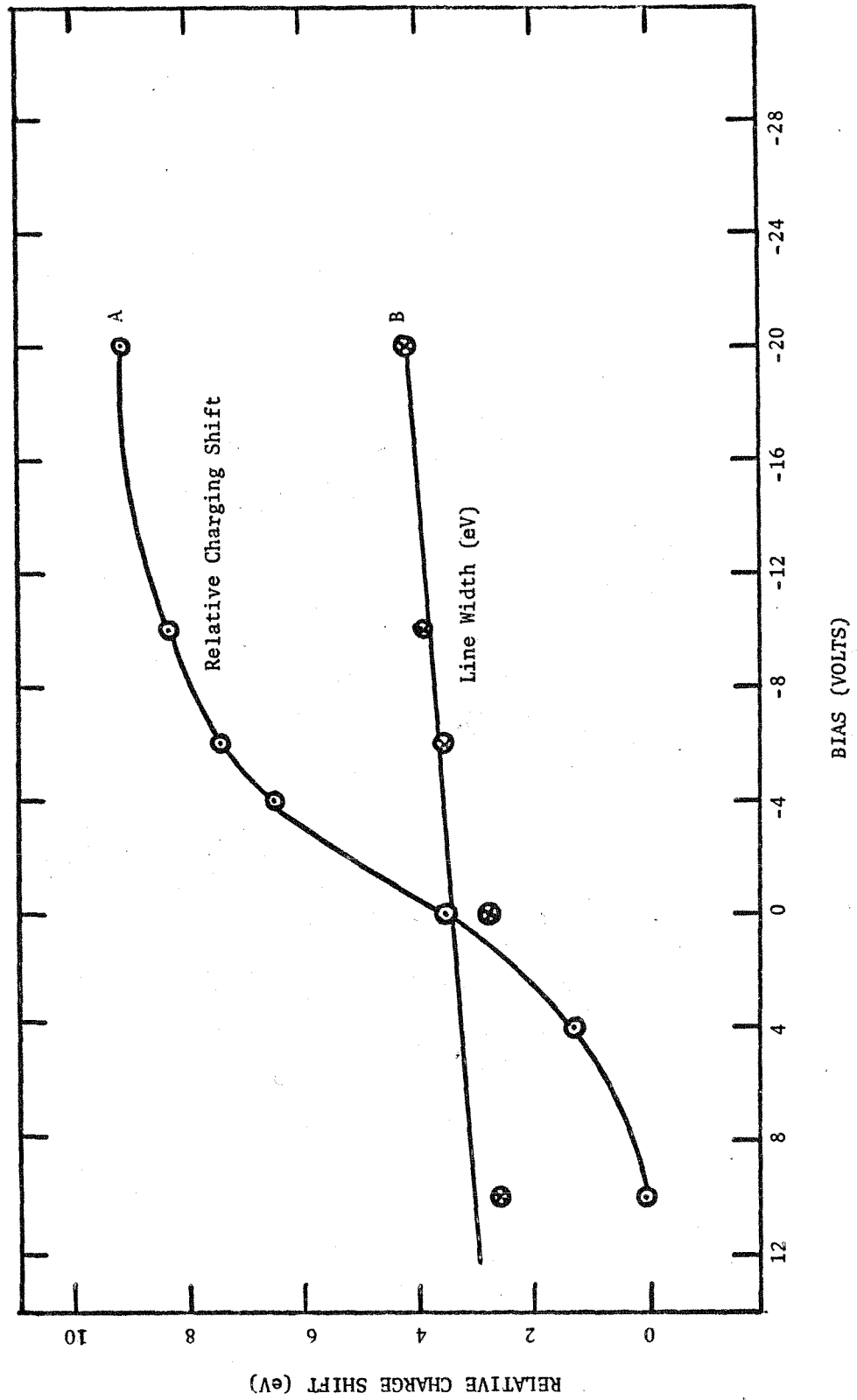
The filament current settings for the Flood Gun are listed in the parenthesis. All spectra were reproducible at a given filament current with sampling time of 20 minutes per curve.

Figure 9. Bias-Potential Experiment



Spectra are recorded with a bias of V volts applied between sample and spectrometer. Charging the surface negatively repels the incident low energy electrons.

FIGURE 10 CHARGING EXPERIMENTS BY BIAS POTENTIAL METHOD



The McPherson experiments used a magnesium-target x-ray tube with an aluminum window between the source and sample chambers. This spectrometer has a restricted geometry of the sample-chamber as shown in Fig. 11. The sample subtends a large solid angle of the secondary-electrons emitted from the aluminum window. This geometry provides large currents of these electrons to the sample surface and therefore reduces charging shifts to <5 eV.

The surface potential of a sample undergoing photoemission (Fig. 11) is given by

$$V_C = V_A + V_E - V_S - V_B - V_K - V_R \quad (19)$$

where

- V_A \equiv charge caused by photoemitted electrons which are captured by the analyzer
- V_E \equiv photoemission current other than V_A
- V_S \equiv charge due to secondary electrons from the x-ray window and sample-chamber walls
- V_B \equiv charge dissipated by bulk currents in the sample
- V_K \equiv charge neutralized through surface conductivity
- V_R \equiv charge eliminated by electrical contact of sample with the holder.

The replenishment currents will discharge the surface potential in metallic conductors. For insulators and semiconductors, however V_C can be represented by a steady state approximation.

The foregoing experiments indicate that the important contributions to V_S are electrons with energies less than 6 eV. Although the secondary electrons could have energies up to the exciting photon energy, only slow electrons can be captured by the surface.

High resolution spectra of metals demonstrate that there are approximately 3×10^5 times as many electrons emitted with kinetic energy less than 5 eV than there are core electrons emitted. This emission of low energy electrons can be explained by their larger escape depth and by secondary processes caused by the core level photoelectrons. Thus, the flood gun is really required. The electrical aspects of the charging effect experiments (Fig. 11) require that charged domains of the sample must have a high impedance ($R \gg 10^9$ ohms). Each domain is then isolated, and V_C is given by

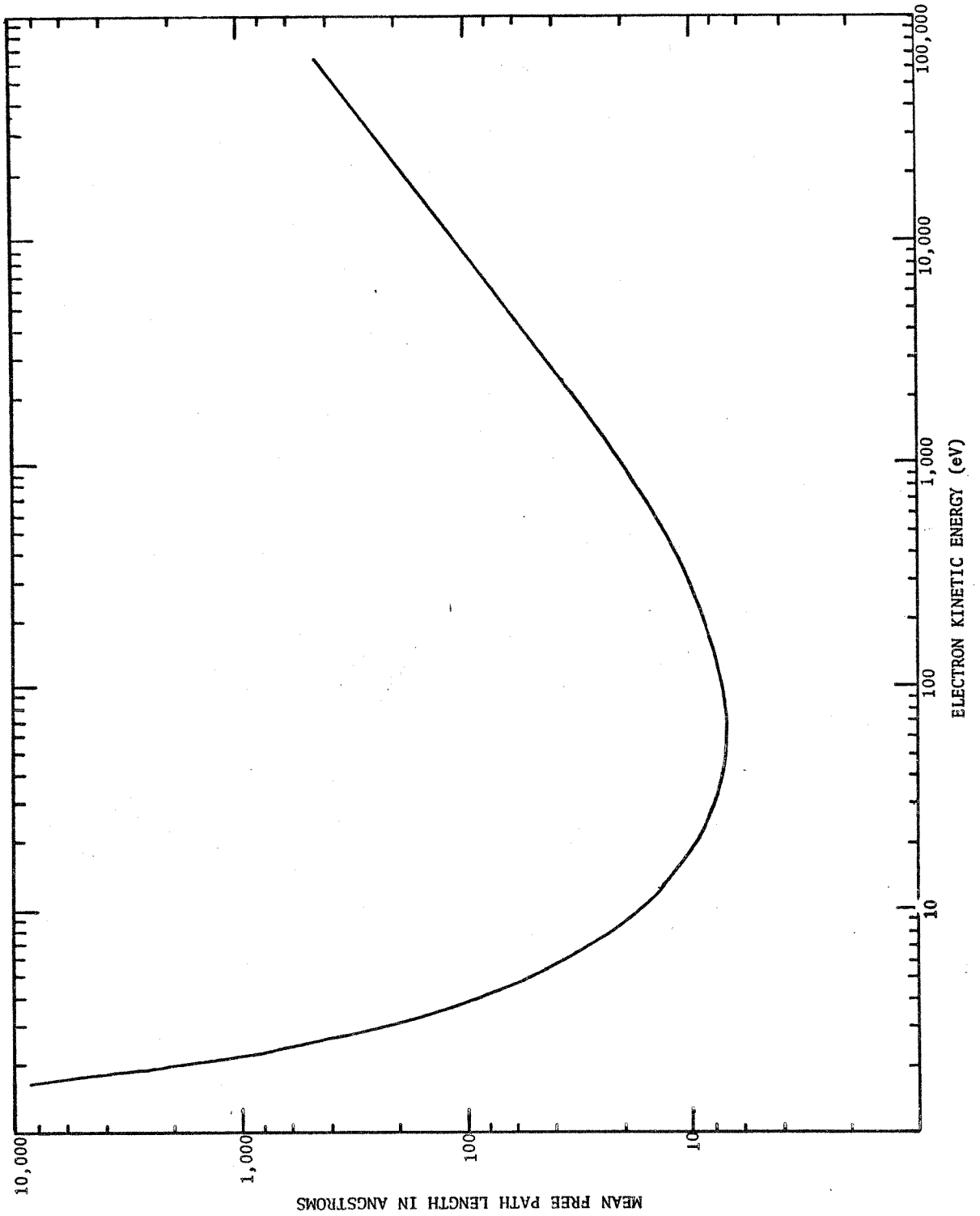
$$V_C = V_A + V_E - V_S - V_K \quad (20)$$

D. Sample Preparation

As mentioned in the Introduction, much of the initial enthusiasm in ESCA vanished because of a succession of disappointing results. Spectral features, which were anticipated, were not observed, and attempts to establish oxidation states in mixed valence compounds gave ambiguous results. Many of the disappointing results must be attributed to poor sample preparation and poor experimental techniques. Though x-rays penetrate to considerable depths, the photoelectrons must come from the solid without scattering. The escape depth of unscattered photoelectrons is a function of the mean-free path, which, in turn, is determined by their kinetic energy and by the material. Riggs and Wendt^{41a} suggested

41a. Riggs, Wm., and Wendt, R., Private Communication

FIGURE 11a MEAN FREE PATH LENGTH FOR INELASTIC SCATTERING



that the scattering of photoelectrons in solids also depends on the average binding energy of the valence electrons. Shorter mean-free paths are predicted for electrons scattered in materials exhibiting valence electrons of lower binding energies. For metals, the average binding energy of the valence electrons is about 3 to 5 eV, and for insulators, 10 to 14 eV.

When this work was started, only two sets of data on escape depths were available: 3-5Å for Auger electrons in metals, and 100Å observed in ESCA experiments on iodosterates.

Figure 11a shows a relationship between the mean-free path and the kinetic energy of the electron which is consistent with recent data tabulated in the review article by Brundle^{41b}. Electron ranging from spectra of the valence region (0 to 40 eV) correspond to depths of 0 to 100Å depending on the density and atomic number of the material. Cls and S2p peaks profile material at shorter depths while iron and copper 2p spectra (binding energies of 710 to 930 eV respectively) come from 15 to 50Å.

As noted before, misleading experimental results can be obtained if surface effects are not properly taken into account. Small amounts of impurities may accumulate at the surface and their spectra be erroneously interpreted as those originating from the bulk material. This problem is aggravated if samples are deposited from solution.

Samples that oxidize in solutions probably have an extensively reacted surfaces. Standard anaerobic methods can only suppress the extent of

41b. Brundle, C.R., J. Vac. Sci. Technol. 11, 212 (1974)

surface oxidation but not eliminate it. Hydrocarbons surrounding the human body provide a major source of contamination of reactive surfaces. Experimental reproducibility requires extremely clean handling techniques, freshly prepared samples, and control of sample exposure to the laboratory and personnel.

A number of sample mounting procedures exist to solve the difficulties of positioning a sample in vacuum. Metals present the least physical and electrical problem. Cleaving of single crystals in vacuo gives reproducible surfaces, and mechanical attachment is adequate.

Polycrystalline and amorphous materials must be protected against the burst of high velocity air passing over the sample during evacuation, and good electrical contact must be achieved.

The various methods which have been developed over the years to solve these problems are summarized briefly as follows:

1. Double-sided adhesive tape³⁴ -- the specimen is dusted on the tape and the Cls line arising from the tape is used as a reference standard. The method is convenient but the non-uniformity of composition and the poorly defined conductivity of the tape are serious disadvantages. Sample contamination can occur from the outgassing of the hydrocarbon vehicles present in the adhesive mixture. As these hydrocarbons "back off" the tape during evacuation they form an atmosphere which envelops the sample.
2. Pellets⁴¹ analogous to the preparation of KBr pellets used in IR Spectroscopy. The pellet represents a sandwich consisting of one layer of sample and one layer of graphite. Electrical contact between the graphite and sample holder is easily established and some of the graphite serves as an external energy calibrant. Reproducible results are obtained with cohesive powders but for extremely fine samples, this method is ineffective.

3. Gallium substrate⁴³ -- a metal substrate is freshly wetted with Gallium metal. The sample is dusted over the tacky surface, which introduces less contamination than Item 1.
4. Aluminum matrix -- powders are simply pressed into an aluminum sheet which has been treated chemically so as to produce a porous and rough surface.
5. Gold, platinum or copper matrices^{32,42} -- sample powders are pressed into fine grid mesh of the metal. This method has no advantage over the pellet system (Item 2) except where required by the geometry of the spectrometer.
6. Deposition from solution -- developed in the course of this work, solutions formed with inert solvents of high vapor pressure are evaporated to give thin films and thin single crystals by techniques similar to those described by C. Cowman⁴⁴. The substrates consisted of 304 stainless steel sheets in which a 0.2 mm deep and circular relief was cut. Uniform films which were thin enough to be transparent gave the narrowest peaks and the best signal-to-background ratios. Dichloromethane, acetone and water were used as solvents for most work.
7. Deposition from slurry -- insoluble samples were prepared (this work) from a solid slurry which was poured onto the relieved sample platens of Item 6. The samples were sufficiently adhesive to maintain contact with the sample platen during the experiment.

In this work, methods 2, 3 and 7 were used for insoluble samples and method 6 was used whenever possible. The other methods were rejected because of contamination, interference in the spectrum or problems in achieving good electrical contact.

42. Swartz, W.E., Watts, P.H., Watts, J.C., Brasch, J.W., Lippincott, E.R., Analyt. Chem., 44, 2001 (1972).

43. Diamis, W.P., Lester, J.E., Analyt Chem., 45, 1416 (1973).

44. Cowman, C., Thesis, California Institute of Technology (1974).

Investigation of liquid samples presents a very difficult problem because of the high vacuum required. Recently, Siegbahn⁴⁵ described an experimental approach which uses a liquid beam as the sample, and which requires very efficient differential pumping of the chamber. This technique is presently prohibitive for most laboratories outside the Uppsala group, because of the severe instrumental requirements. Techniques employing frozen solutions (glasses at low temperatures) have been well documented^{46,47}. The chemical shifts for the dissolved compounds have been compared with those found for the pure solids. Differences in these shifts have been observed and these have been attributed to solution effects, but might be explained in terms of the variation of the work function of solids with temperature⁴⁸.

In this work two methods were applied to the investigation of protein samples; (1) A protein solution frozen under nitrogen at 200°K and (2) A protein deposited by evaporation of the solvent (water). On each case gold was used as a substrate. The spectra were identical when taken at the same temperature.

-
45. Siegbahn, H., Physica Scripta, 4, 164 (1973)
 46. Kramer, L., Klein, M., J. Chem. Phys., 57, 3620 (1969)
 47. Liebfritz, D., Angew Chem, 84, 156 (1972)
 48. Butler, M.A., Wertheim, G.K., Rousseau, D.L., and Hufner, S., Chem. Phys. Lett., 13, 374 (1972)

IV. DATA ANALYSIS

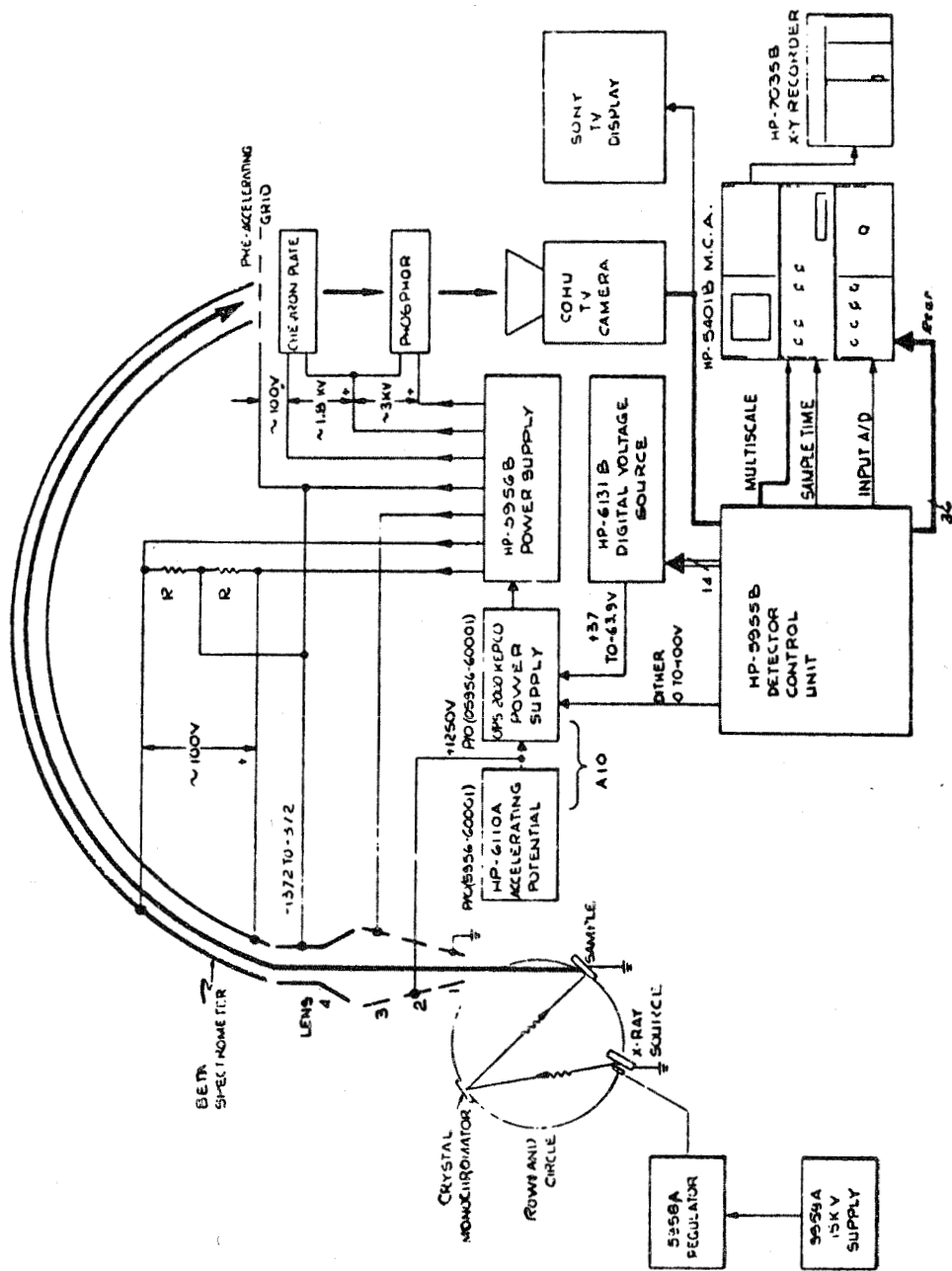
A. Description of Data Characteristics

The experimental data represent measurements of the flux as well as the kinetic energies of the electrons emitted from the sample as it is irradiated with x-rays of 8.46\AA ($\text{AlK}\alpha$, 1.486K eV). The number of electrons within small energy intervals are recorded, thus forming an image of the density of electronic states that are related to the binding energies. The electrons enter a detector (Chapter 3) and are processed electronically to give a count rate as a function of kinetic energy.

The noise in the recorded spectrum arises from a variety of effects such as, Johnson noise, dark current, Shott noise, Auger electron and Compton scattering noise, occurring in the channel-plate electron multiplier, the vidiocon detector, the pulse height converter, the filament circuitry and the x-ray power supply. A schematic of the HP 5950A is given in Fig. 13⁴⁹. Additional potential noise sources are stray-fields in the electron spectrometer and stray electrons. The standard deviation is given as \sqrt{N} where N represents the total number of counts at any point. Excellent counting statistics are required for correct assignment of fine structure and detection of elements in low concentrations. The count rate capability of virtually any electron spectrometer exceeds by far the photon flux presently available. To obtain reasonable standard deviation, long counting times are necessary, sometimes even resulting in radiation damage of the sample.

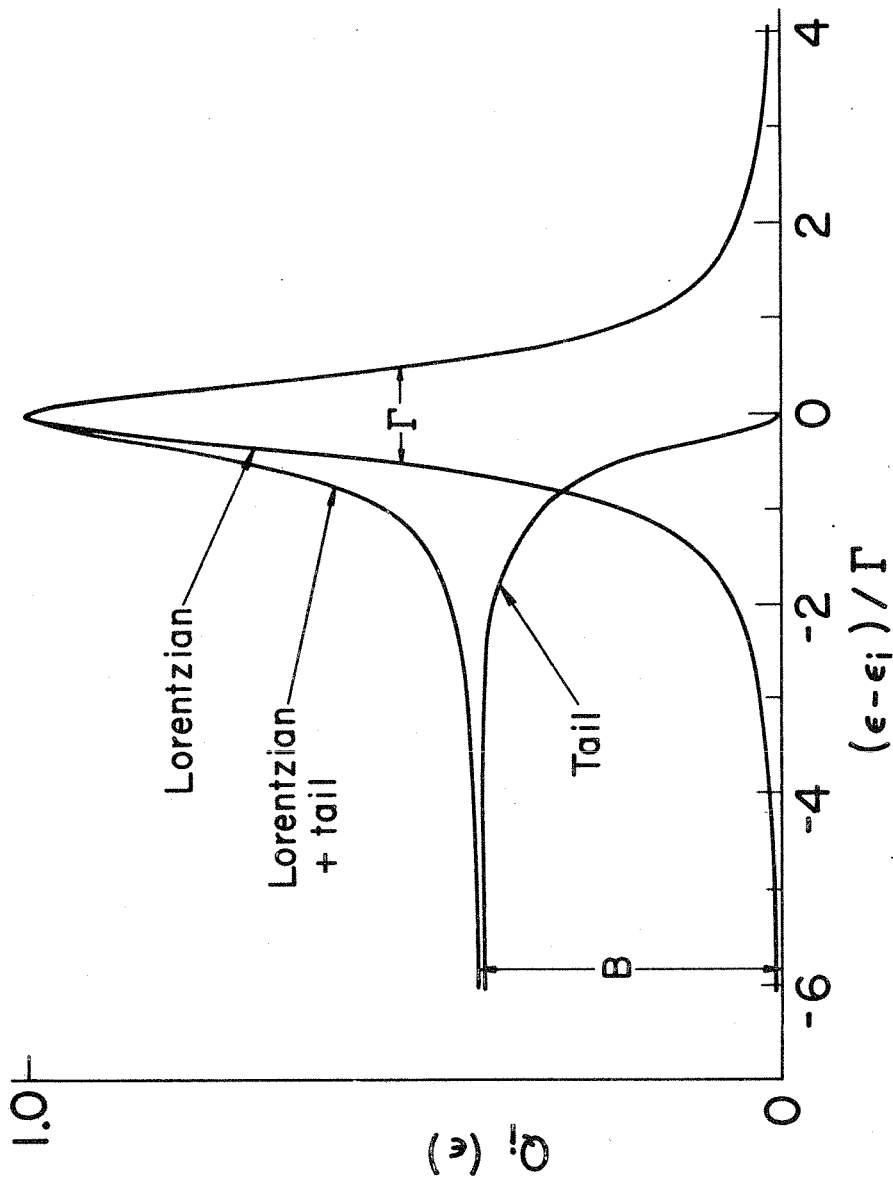
49. Figure from HP 5950A manual.

FIGURE 13



Schematic of HP 5950A monochromator, electron optics, and data system.

FIGURE 14



Extensive studies by Fadley⁵ indicated that the best description of a photoelectron peak was a Lorentzian distribution with an additive Lorentzian tail

$$Q_i(\epsilon) = \begin{cases} A(B/(\Gamma/2)^2 + (1-B)/((\epsilon-\epsilon_i)^2 + (\Gamma/2)^2)) & \epsilon < \epsilon_i \\ A/((\epsilon-\epsilon_i)^2 + (\Gamma/2)^2) & \text{for } \epsilon > \epsilon_i \end{cases} \quad (21)$$

This intensity distribution is described by four independent parameters: the width (Γ), the position (ϵ_i), the tail height to peak height ratio (B), and an intensity factor (A). The distribution is given as a function of the electron kinetic energy; see Fig. 14.

Analysis of spectral data obtained from the HP 5950A indicate⁶ that the instrumental impulse function corresponds to about 0.5 to 0.6 eV (gaussian distribution). Symmetries introduced by the combination of monochromatization and dispersion compensation make the Lorentzian line shape a reasonable fit to the data in this thesis.

B. Standard Smoothing Methods

Smoothing of experimental pulse data by analogue and digital methods is described in several extensive reviews^{50,51,52,53}. Digital methods are more versatile than analogue methods and are developed in this section.

The simplest methods of smoothing are based on convolution of the data with various weighting functions. The moving-average procedure is a typical example. Here the ordinates of a set number of points, spaced at a constant interval are totaled and normalized, thereby obtaining the average ordinate at the central abscissa of the group. The group is then incremented by one point and the process repeated over the range of the data. The concept of convolution can be generalized by defining a set of convolution integers, and an appropriate normalization factor. Convolution reduces to multiplication of the ordinates point by point by the appropriate coefficients. For generation of the most representative ordinate at x_0 , the products $C_i Y_i$ would be formed and normalized, that

is

$$Y_j = \frac{\sum_{i=-m}^{+m} C_i Y_i}{N} \quad (22)$$

where j is the running index of the ordinate data in the original data file.

-
50. Ernst, R.C., Sensitivity Enhancement in Magnetic Resonance in Advances in Magnetic Resonance, J. Waugh, Ed., Vol. 2 (1966)
 51. Moore, L., Brit J Appl Phys (J Phys D) 1 (2), 237 (1968)
 52. Morrison, J.D., J Chem Phys, 39, 200 (1963)
 53. Petersson, G.A., Thesis, California Institute of Technology (1970).

The moving-average routine would correspond to $C_i=1$. In general, this method is not very useful. For this reason, a number of integer tables have been devised. These are based on symmetric triangular functions, exponential functions, stepwise box car representations and others.

The most sophisticated of these methods is given by Savitsky⁵⁴. His algorithm generated a set of convolution integers which estimated the ordinate of the central abscissa in the convolution interval by fitting a least-square curve through the data points. The functional basis of this curve could be linear or polynomial. Savitsky's method gave the most representative results as regards line shape and noise rejection.

C. Filtration of Noise by Fourier Methods

Virtually all published XPS data has been smoothed by digital convolution methods in real space. In each case, the signal-to-noise ratios have been enhanced thus considerably reducing the scanning times. The effect of this procedure on the line shape has not been investigated.

This author has assumed that the basic line shape contains much of the information available in this spectroscopy. The photoelectron peaks of single species are usually symmetrical. Asymmetrical lines are attributed to the existence of subtly different chemical or physical species in the same sample.

The data manipulation employed in this thesis has been aimed at achieving the best representation of the line shapes. Enhancement of the

54. Savitsky, A., and Golay, M.J.E., Anal Chem, 36, 1627 (1964).

signal-to-noise ratio by a factor of 10 was needed because of the extremely low concentration of metal in proteins. Here, the metal content is 3 to 7 times lower than in any previously reported work. Experimental time had to be reduced because of radiation damage in the sample. The convolution techniques described above were inadequate to solve the problem.

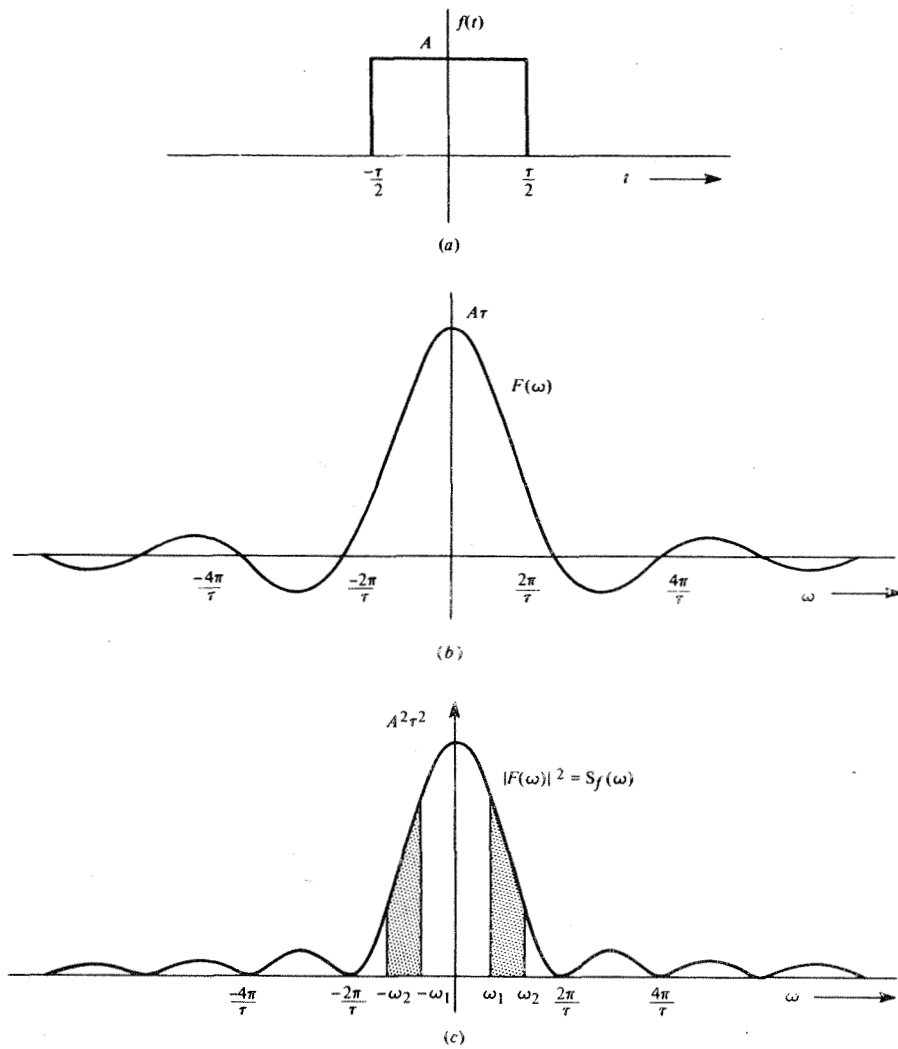
The application of Fourier methods to signal analysis has been particularly fruitful in other fields^{53,55}. The Fourier transform of physical data can be described as fitting the observed spectrum to a sine, cosine series. This is equivalent to reducing the real space spectrum to its frequency components. Analysis of the amplitudes of the series as a function of the frequency, enables separation of signal from noise.

The signal power (amplitude) in Fourier space of an ESCA spectrum is concentrated in the first few terms of the series, whereas the noise is represented by high-frequency terms, which are rejected.

The most common method of filtration (smoothing) using the Fourier transform involves truncation of all the terms of frequency greater than a chosen cut-off point. This is equivalent to convolving in frequency space with a step function which is unity for all x less than x_t and zero for all x greater than x_t , where x represents the frequency of a given term. This corresponds to convolving in the real or time domain with the function $\sin(x)/x$ as illustrated in Fig. 15.

55. Castleman, K.R., and Welch, A.J., "Feature Extraction in Visual Evoked Potential Analysis" TR 72, Biomedical Research Laboratory, University of Texas, Austin (1969).

FIGURE 15



(a) (b) The spectral density function. (c) The energy density function.

This procedure, although reducing high-frequency noise in the real spectrum (time domain) generates a new low-frequency component, referred to as ringing, which is determined by the sharpness of the roll-off of the filter function in Fourier space (frequency domain).

The convolution theorem states that if $f(t)$ and $g(t)$ are functions with Fourier transforms $F(\omega)$ and $G(\omega)$ respectively, then the convolution of $f(t)$ and $g(t)$, given in the time domain by

$$h(t) = f(t) * g(t) = \lim_{T \rightarrow \infty} \frac{1}{2T} \int_{-T}^T f(t)g(\tau-t)dt \quad , \quad (23)$$

is expressed in the frequency domain by

$$H(\omega) = F(\omega) \cdot G(\omega) \quad (24)$$

Thus, convolution in the time domain and pointwise multiplication in the frequency domain are equivalent. If $x(t)$ is an input signal to a filter with impulse response $h(t)$, the resultant output $y(t)$ is given by

$$y(t) = F^{-1} \{F\{x(t)\}F\{h(t)\}\} \quad , \quad (25)$$

where $F\{ \}$ indicates the Fourier-transform operation.

The physical interpretation of this is as follows: At each frequency ω the magnitude of $H(\omega)$ gives the attenuation factor for the component of $x(t)$ at frequency ω . Low pass filters start with the attenuation factor $H(\omega)$ equal to unity which then decreases with higher ω . Signal terms are strongly enhanced at the expense of noise terms. The inverse transform synthesizes a new version of the signal with reduced high frequency content (frequency refers to spatial frequency of oscillations in the plane of the spectrum as plotted).

In electron spectroscopy, the signal shape is reasonably well defined^{1,5,6}. There is a very clear distinction between the frequency of the signal

and that of the noise. The problem of generating filter functions ($H(\omega)$) for data manipulation has been treated at length in information theory^{56,57,58}.

From the quoted work, a number of filters were selected that appeared to be well suited for the specific problems treated here.

The author applied a filter designed for optimum resolution in a linear system. The algorithm of this filter function (Weiner Estimator) is directed to obtain the best estimate of the signal before it is mixed with the noise. Derived from the Weiner-Hopf condition, this filter generates a spectrum which is the minimum mean-square-error estimate of the natural spectrum.

To obtain optimal resolution, the cross correlation of the input signal and the desired output signal should be equal to that of the input signal and the actual output signal as regards each point in the sample. This requires that the error caused by filtration be uncorrelated with the data. With minimum mean-square-error criteria, $\epsilon(t)$ is zero, which requires orthogonality between $x(t)$ and $\epsilon(t)$.

-
56. Bracewell, R., The Fourier Transform and its Applications, McGraw-Hill, New York (1965)
 57. Papoulis, A., The Fourier Integral and its Applications, McGraw-Hill, New York (1962)
 58. Weiner, N., The Fourier Integral and Certain of its Applications, Dover, New York (1960).

For signals $x(t)$ and $y(t)$ with Fourier transforms of $X(\omega)$ and $Y(\omega)$ respectively, the cross-correlation function $R_{xy}(\tau)$ is defined as

$$R_{xy}(\tau) = \lim_{T \rightarrow \infty} \int_{-T}^T x(t)y(t+\tau)dt, \quad (26)$$

which is expressed in the frequency domain by

$$S_{xy}(\omega) = X(\omega)Y^*(\omega), \quad (27)$$

where Y^* denotes the complex conjugate.

Defining the problem as one of filtering a signal mixed with noise to obtain the best minimum mean-square-error estimate of the natural signal, we proceed to derive the filter function as follows:

Let $s(t)$ represent the signal and $n(t)$, the noise. The received signal is then given by

$$x(t) = s(t) + n(t). \quad (28)$$

We wish to separate the signal from the noise. The desired output is then given by

$$y(t) = s(t). \quad (29)$$

If the arithmetic means of $s(t)$ and $n(t)$ are assumed to be zero, then

$$\begin{aligned} R_x(\tau) &= \overline{(s(t) + n(t))(s(t+\tau) + n(t+\tau))} \\ &= R_s(\tau) + R_n(\tau) + R_{sn}(\tau) + R_{ns}(\tau) \end{aligned} \quad (30)$$

Since $s(t)$ and $n(t)$ are presumed to be non-correlated, and $(\bar{s} = \bar{n} = 0)$ then,

$$R_{sn}(\tau) = R_{ns}(\tau) = 0$$

and

$$R_x(\tau) = R_s(\tau) + R_n(\tau) \quad (31)$$

In frequency space, 31 becomes

$$S_x(\omega) = S_s(\omega) + S_n(\omega). \quad (32)$$

Similarly, for the cross-correlation function of x and y ,

$$\begin{aligned} R_{xy}(\tau) &= ((t) + n(t))(s(t+\tau)) \\ R_{xy}(\tau) &= R_s(\tau) + R_{ns}(\tau) \\ &= R_s(\tau) \end{aligned} \quad (33)$$

and therefore,

$$S_{xy}(\omega) = S_s(\omega). \quad (34)$$

By the objectives of the problem, we are given

$$S_y(\omega) = S_s(\omega). \quad (35)$$

According to Wiener⁵⁸, the optimal linear filter is given by

$$H(\omega) = \frac{S_{xy}(\omega)}{S_x(\omega)}. \quad (36)$$

Therefore,

$$H(\omega) = \frac{S_s(\omega)}{S_s(\omega) + S_n(\omega)}. \quad (37)$$

The optimal filter increases the amplitude of the frequency components in the signal range, while suppressing those in the range where the desired signal is weak and the noise strong.

The mean-square estimated error is given by

$$\begin{aligned} \bar{\epsilon}^2 &= \frac{1}{2} \int_{-\infty}^{\infty} S_s(\omega) - \frac{S_s^2(\omega)}{S_s(\omega) + S_n(\omega)} d\omega \\ &= \frac{1}{2\pi} \int_{-\infty}^{\infty} \frac{S_s(\omega) S_n(\omega)}{S_s(\omega) + S_n(\omega)} d\omega \end{aligned} \quad (38)$$

If the frequency spectra of $S(t)$ and $n(E)$ do not overlap, then

$$S_s(\omega) S_n(\omega) = 0 \quad (39)$$

and the error of estimation must be zero.

Given the functional form of the Wiener filter just derived, application to electron spectroscopy requires knowledge of the true signal spectrum and an estimate or sample of noise.

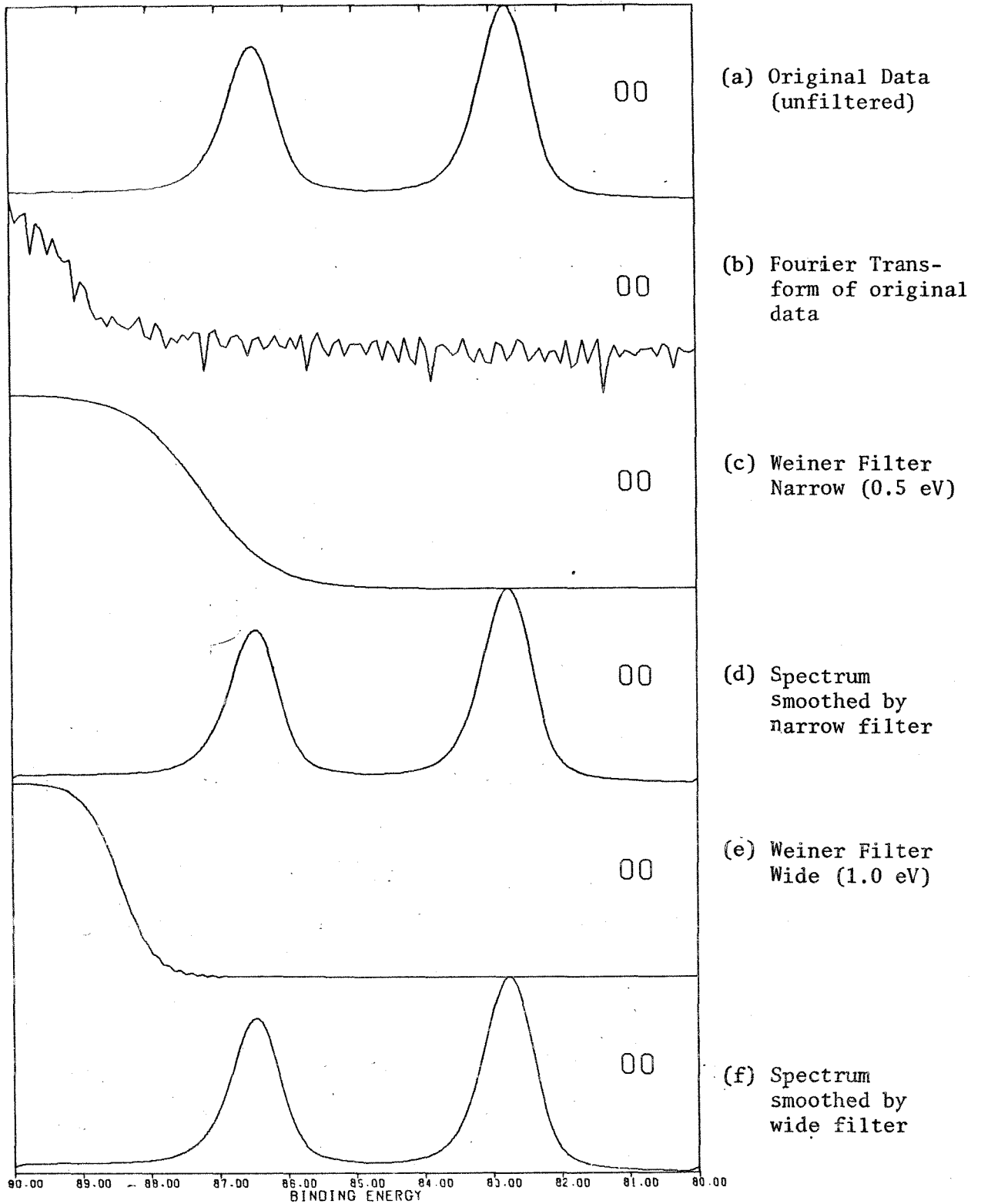


Fig. 16 Au 4f region of gold reference standard. Spectra (a), (d), and (f) plot relative electron flux (y) vs. binding energy. Section (b) plots magnitude ($\log y$) vs. frequency and sections (c) and (e) plot relative magnitude (linear y) vs. Fourier frequency.

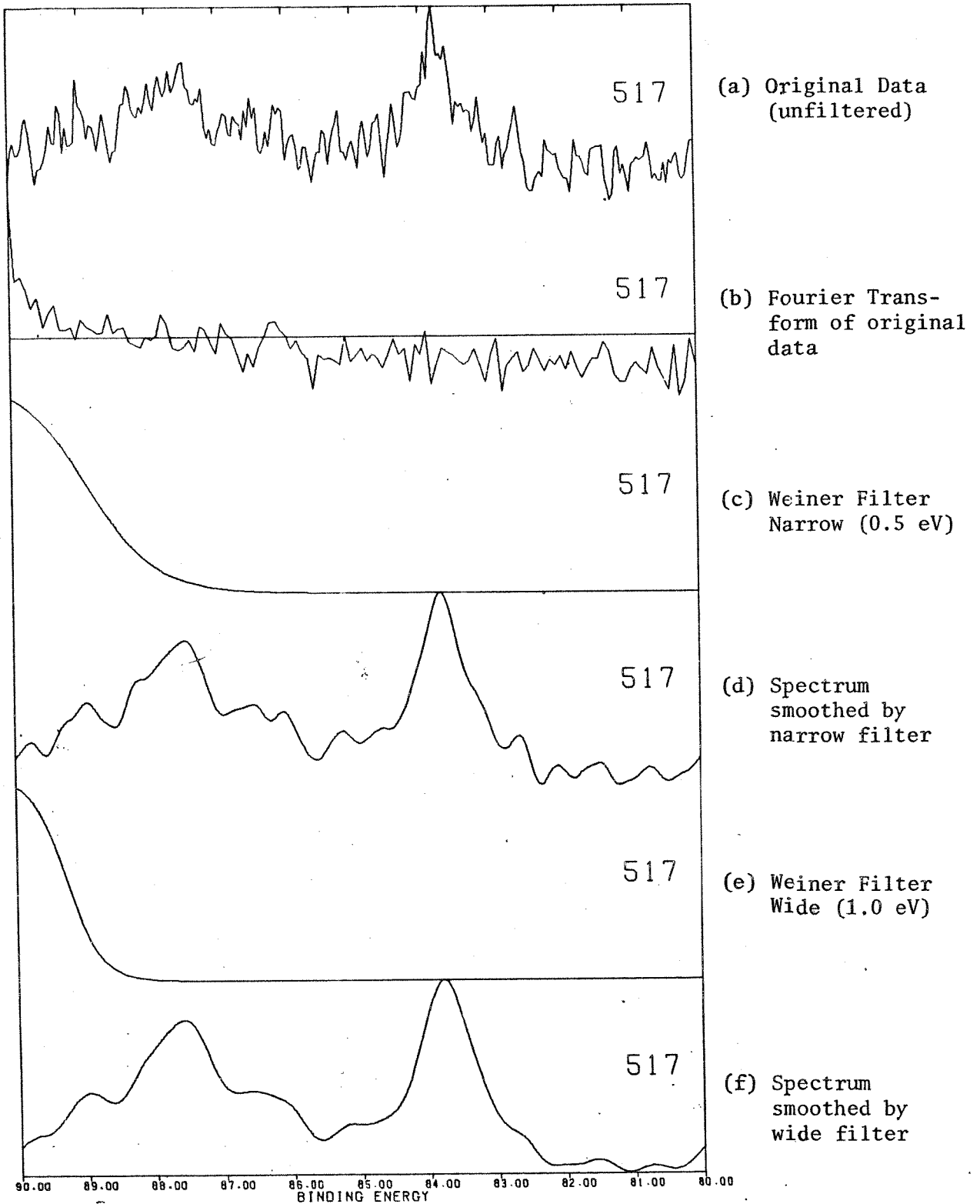


Fig. 17 Au 4f region of gold substrate under thin layer of sample. Spectra a, d, and f plot relative electron flux (y) vs binding energy. Section b plots magnitude ($\log y$) vs frequency and sections c and e plot relative magnitude (linear y) vs Fourier frequency.

A number of experimental signal shapes were generated by convolving the instrumental function (gaussian distribution of 0.55 eV FWHM) with a number of Lorentzian distributions of different line widths. No detectable difference in resulting filtered spectra was observed between this approach and that of line shape estimation by Lorentzian distributions of different half-widths.

The total energy of a function $f(t)$ of duration T is given by⁵⁵

$$E = \frac{1}{T} \int_0^T f^2(t) dt \quad (40)$$

and by Rayleigh's theorem⁵⁹

$$\int_{-\infty}^{\infty} |f(t)|^2 dt = \int_{-\infty}^{\infty} |F(\omega)|^2 d\omega. \quad (41)$$

The total energy of a time-domain function is given by integration of the square of the amplitudes in frequency space. This relationship has been cited to develop the power spectral density of time functions given as

$$W_T(\omega) \equiv E_T(\omega) / 4\pi \quad (42)$$

Random functions in the time domain are characterized by power spectral densities which are independent of frequency in Fourier transform space. The power spectral density of white noise would be frequency independent.

Fig. 16 illustrates Weiner's treatment of a $\text{Au}4f_{7/2}$ reference signal. This sample was used for energy calibration purposes. The spectrum from the instrument is plotted point by point as 16a. The Fourier transform of the original data is plotted with logarithmic ordinate as 16b. The original spectra from the gold substrate beneath a thin film of sample compound is given in Fig. 17a. The corresponding Fourier transform is plotted in Fig. 17b.

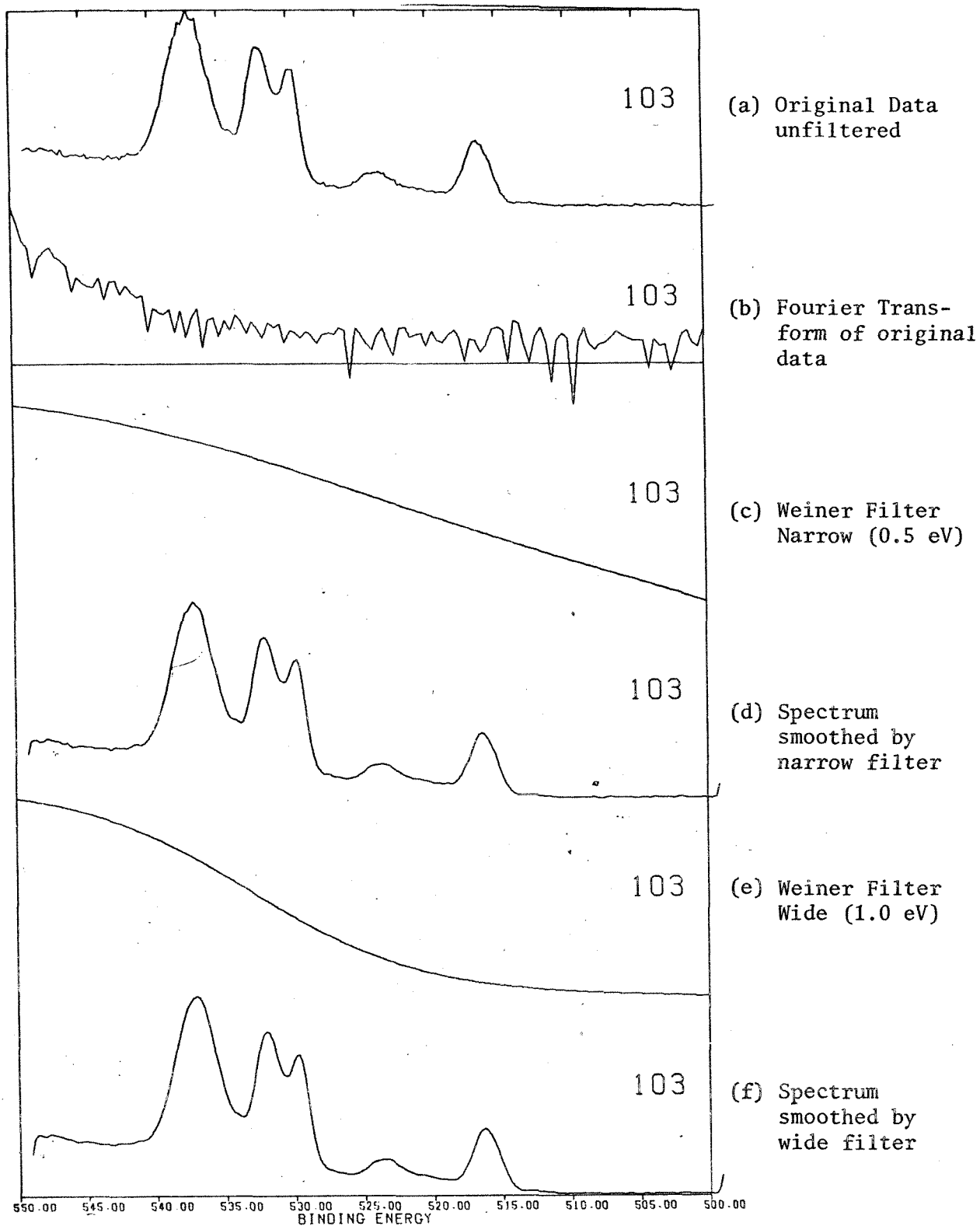


Fig. 18 V-O region of fresh Vanadium Diboride (Flood Gun Off). Spectra a,d, and f plot relative electron flux (y) vs binding energy. Section b plots magnitude ($\log y$) vs frequency and sections c and e plot relative magnitude (linear y) vs Fourier frequency.

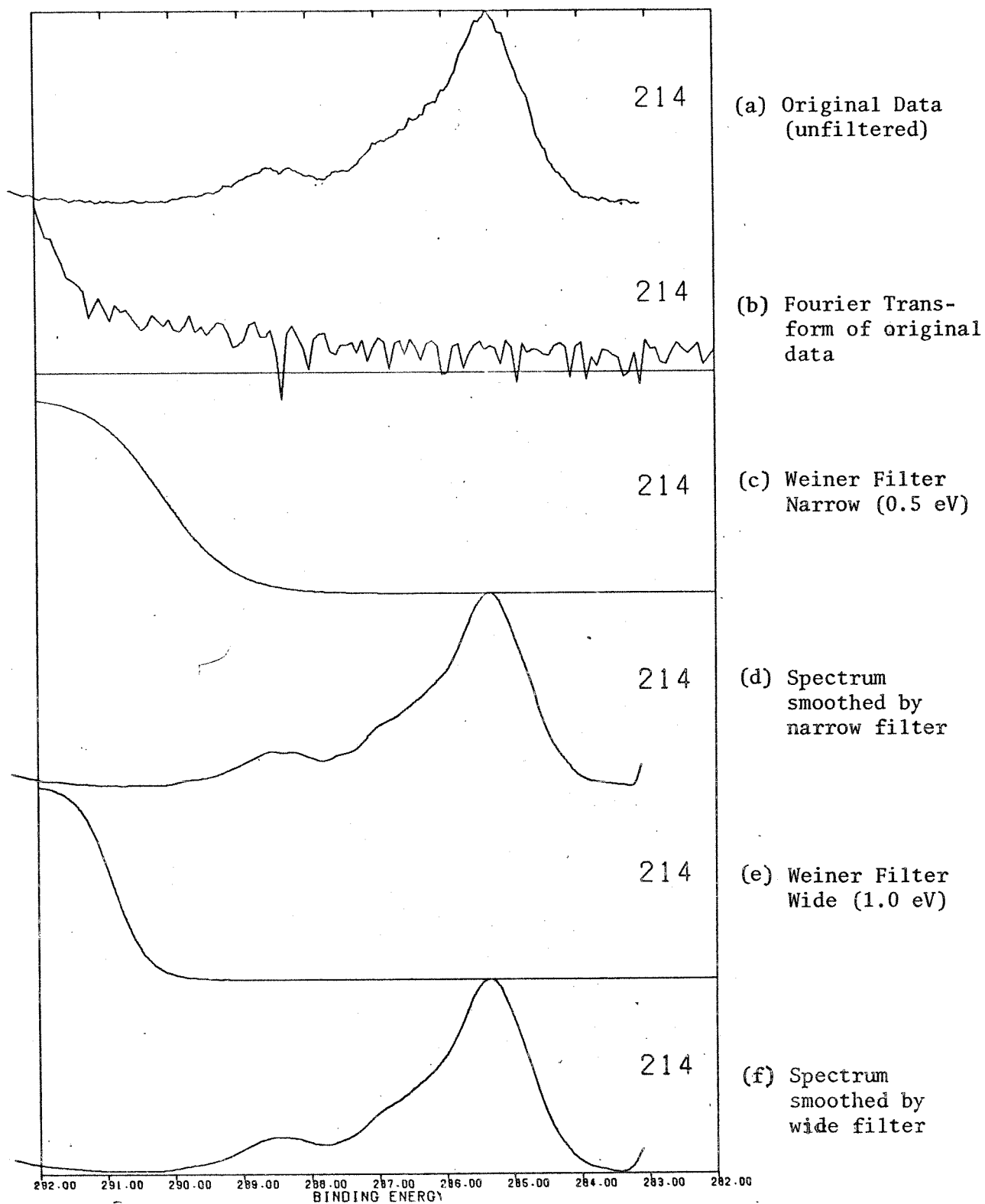


Fig. 19 Carbon 1s spectrum of Stellacyanin. Spectra a, d, and f plot relative electron flux (y) vs binding energy. Section b plots magnitude ($\log y$) vs frequency and sections c and e plot relative magnitude (linear y) vs Fourier frequency.

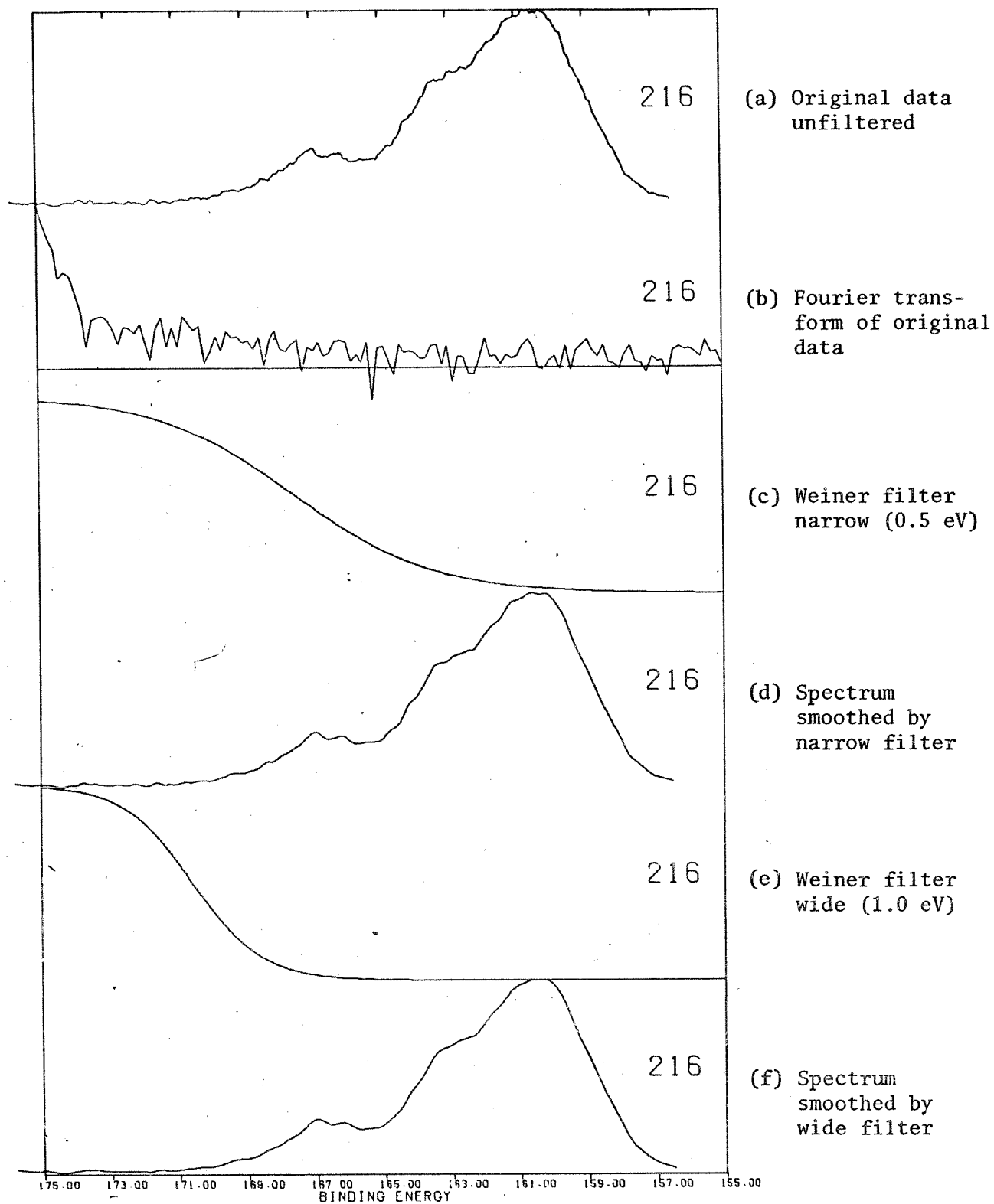


Fig. 20 Sulfur 2p region of Laccase. Spectra a, d, and f plot relative electron flux (\bar{y}) vs binding energy. Section b plots magnitude ($\log y$) vs frequency and section c and e plot relative magnitude (linear y) vs Fourier frequency.

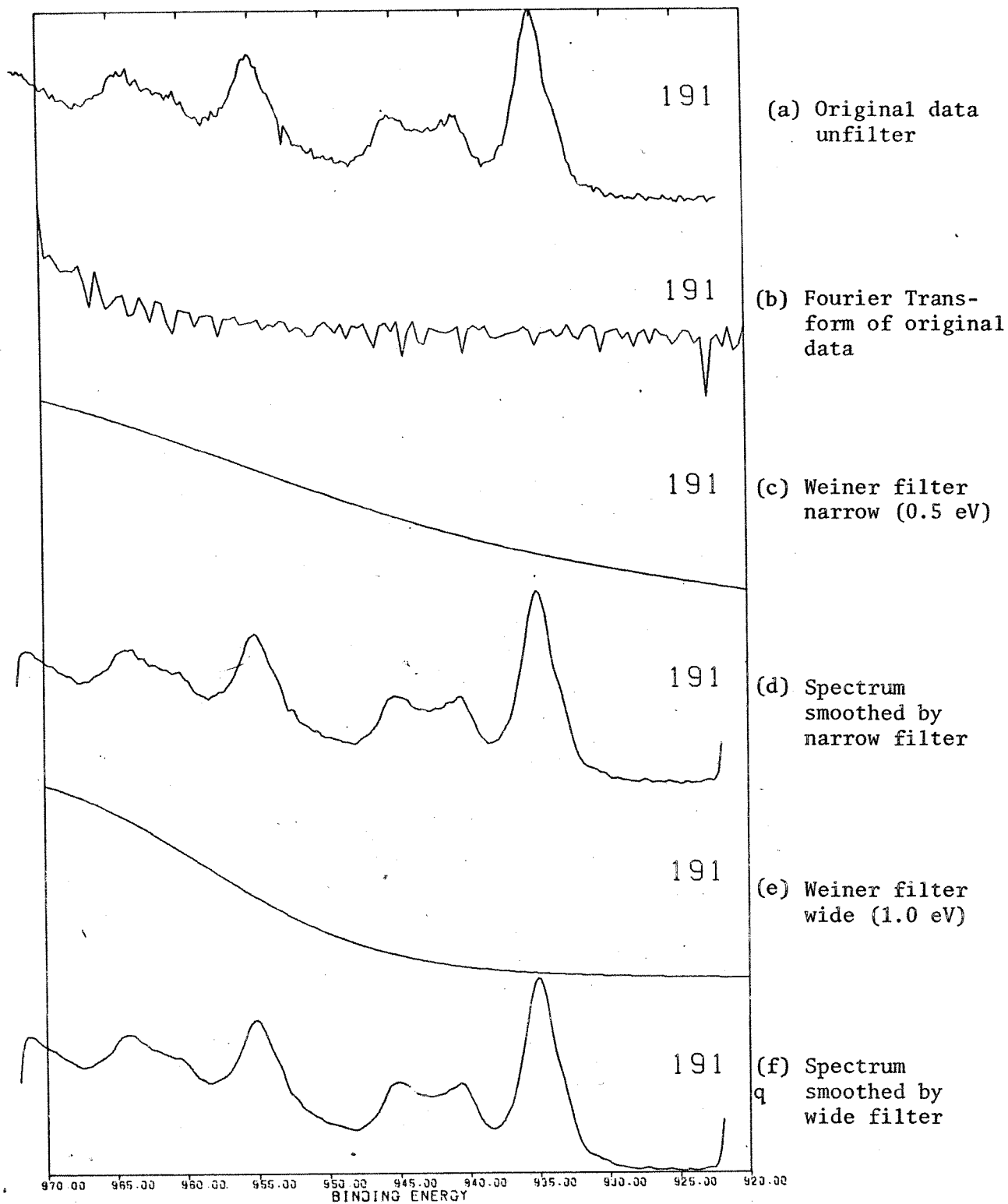


Fig. 21 Cu 2p region of copper penicillamine complex. Spectra a, d, and f plot relative electron flux (y) vs binding energy. Section b plots magnitude ($\log y$) vs frequency and sections c and e plot relative magnitude (linear y) vs Fourier frequency.

Each sample spectrum was taken for an accumulation of 10 scans over a 10 electron volt window from 90 to 80 eV with a scan rate of 1 eV/sec and with data stored in 256 channels. In each of the figures 16b and 17b, the last 80% of the frequency components have equivalent amplitudes.

A spectrum of vanadium diboride in the vanadium 2p, 01s region, is given in Fig. 18; the original is 18a and the Fourier transform 18b.

Here, a 50 volt energy sweep was displayed in 1024 channels at a scanning rate of 1 eV/sec. The sampling frequency (number of points per eV) in Fig. 18 is different from that in Figures 16 and 17.

The carbon 1s core-level spectrum of Stellacyanin given in Fig. 19 was obtained with 10 volt window, 256 channels, and 1 eV/sec scan rate. Here as before, 19a gives the original spectrum and 19b the Fourier transform. The sulfur 2p core-level spectrum for laccase given in Fig. 20 represents 30 accumulated scans taken with a 20 volt window, 256 channels, 1 eV/sec scanning rate.

Figure 21 displays a copper 2p spectrum (copper penicillamine complex) taken with a 50 volt window, 256 channels and 1 eV/sec scan rate. The copper 2p region of the metalloprotein laccase is given in Fig. 22. (50 volt window, 256 channels and approximately 200 scans at 1 eV/sec.) The iron 2p spectra from an iron sulfur cluster complex is given in Fig. 23 (50 volt window, 256 channels and 1 eV/sec scan rate). Figure 24 shows the iron 2p level in the 2 iron Ferredoxin protein with identical sampling parameters as Fig. 23 but with 10 times more scans.

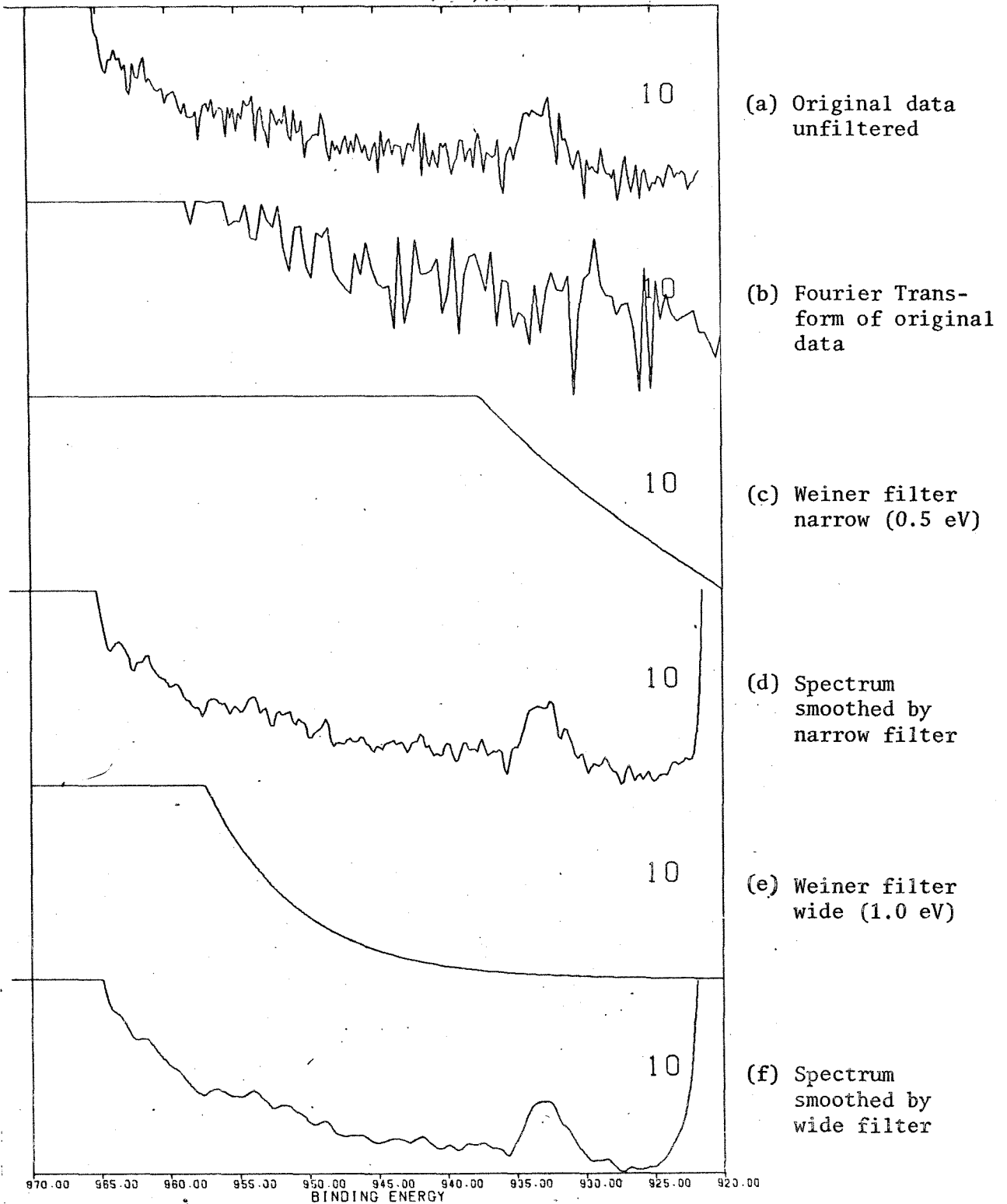


Fig. 22. Cu 2p region (ordinate X100) of Laccase. Spectra a, d, and f plot relative electron flux (y) vs binding energy. Section b plots magnitude ($\log y$) vs frequency and section c and e plot relative magnitude (linear y) vs Fourier frequency.

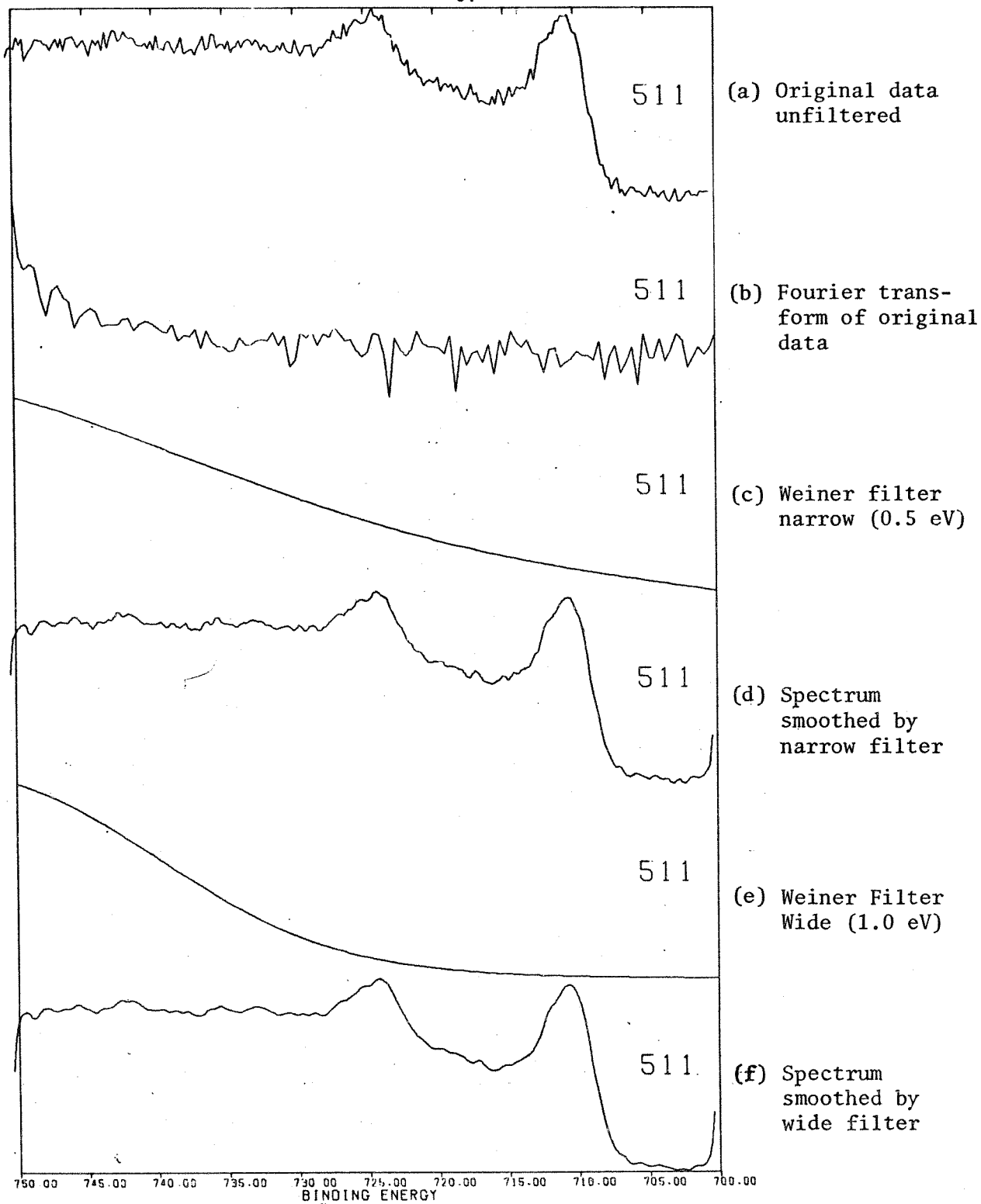


Fig 23. Fe 2p region of Holm's cluster complex. Spectra a, d, and f plot relative electron flux (y) vs binding energy. Section b plots magnitude ($\log y$) vs frequency and sections c and e plot relative magnitude (linear y) vs Fourier frequency.

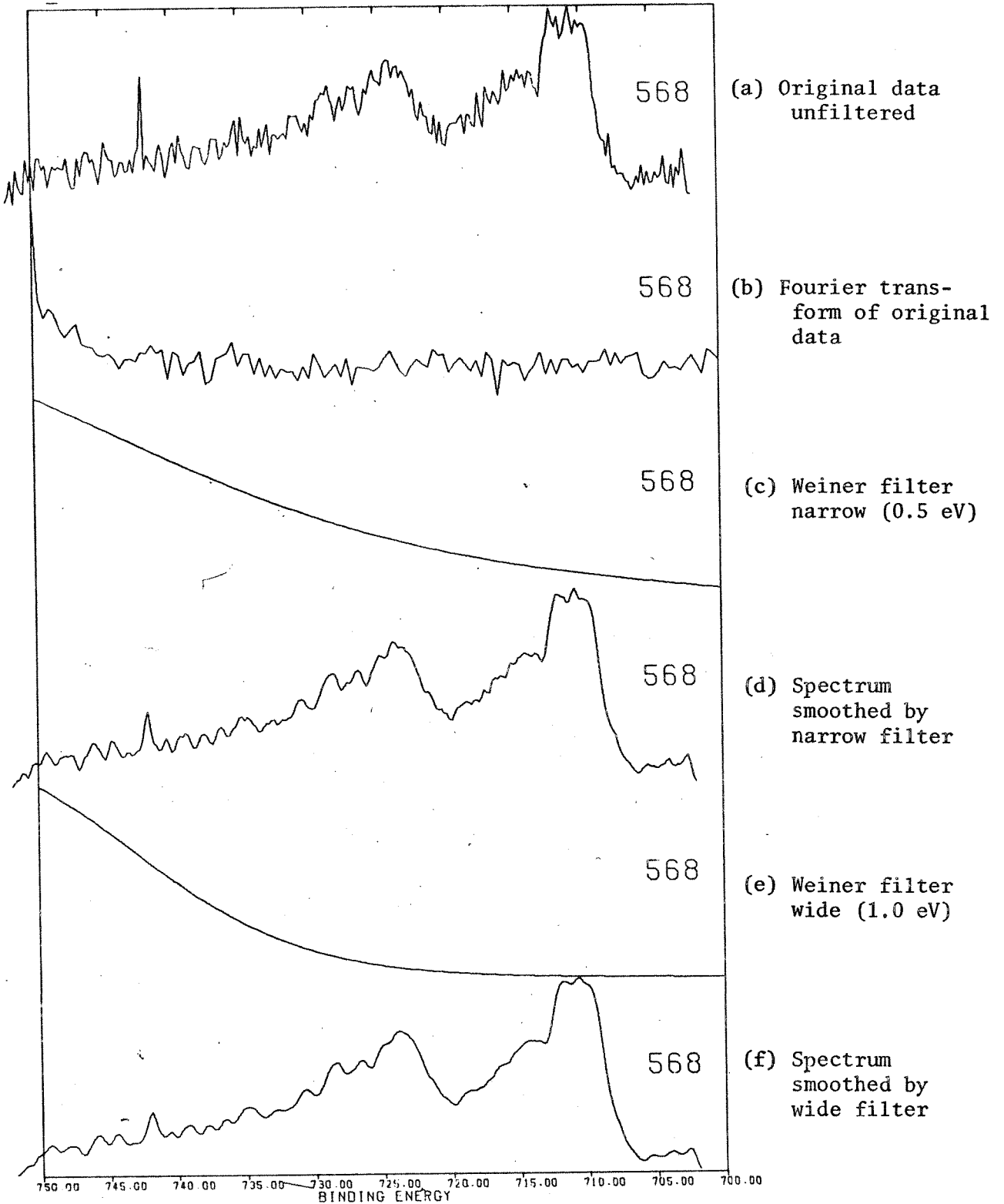


Fig. 24. Fe 2p region of spinach Ferredoxin. Spectra a, d, and f plot relative electron flux (y) vs binding energy. Section b plots magnitude ($\log y$) vs frequency and sections c and e. plot relative magnitude (linear y) vs Fourier frequency.

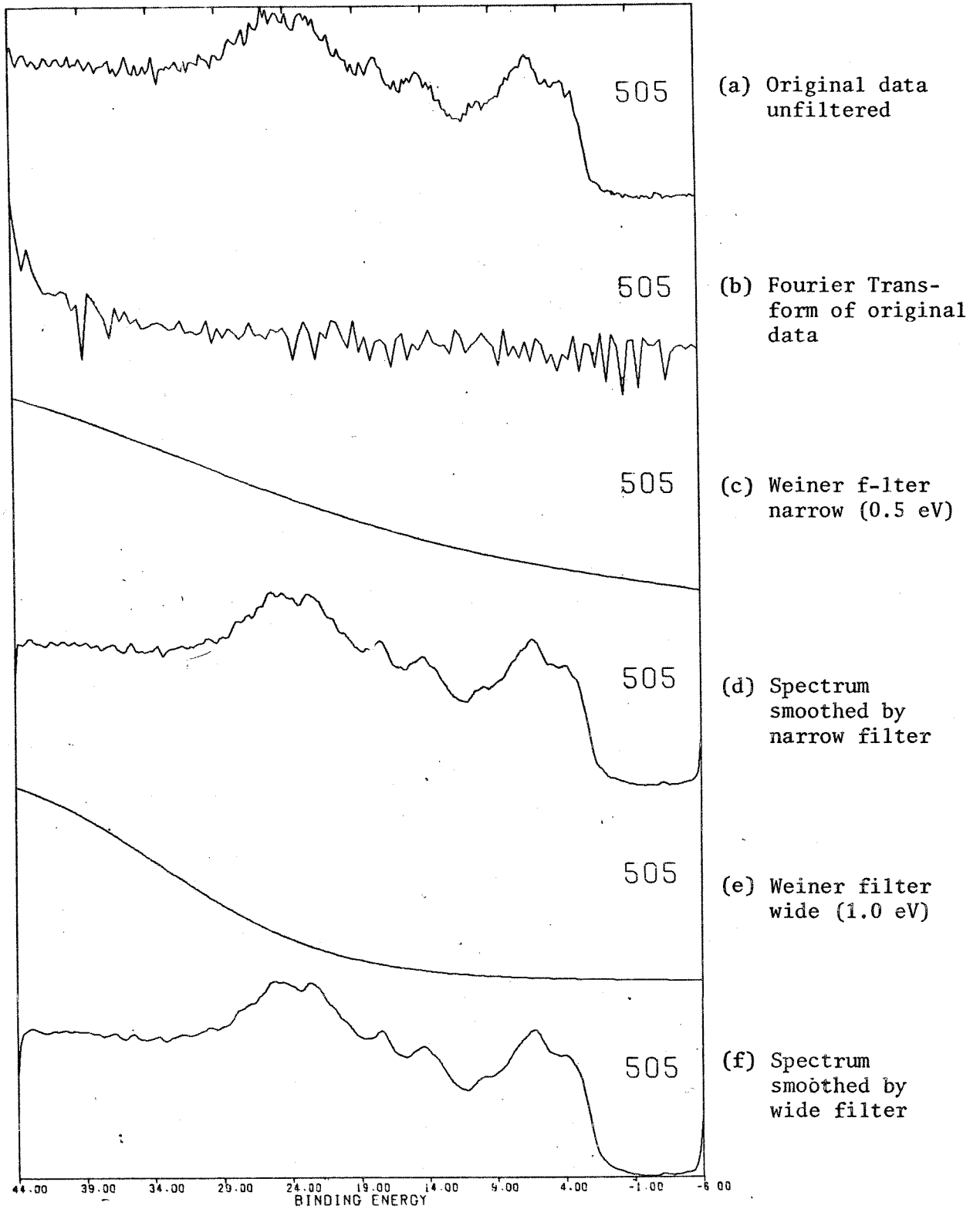


Fig. 25 Valence band region of Holm's cluster complex. Spectra a, d, and f plot relative electron flux (y) vs binding energy. Section b plots magnitude ($\log y$) vs frequency and sections c and e plot relative magnitude (linear y) vs Fourier frequency.

Finally, the valence-band spectra from the cluster complex of Fig. 22 is given in Fig. 25 (50 volt window, 256 channels, 1 eV/sec scans).

Note that Fig. 17 is a poor signal-to-noise (S/N) case of Fig. 16; similarly, Figures 21 and 22, and Figures 23 and 24 are related, (same region for the same elements, same sampling frequencies but different signal/noise ratios). Figures 16, 17, and 19 correspond to 10 volt windows, (the total spectrum encompassing 10 electron volts was displayed in 256 channels). Figures 18, 21, 22, 23, 24, and 25 were obtained with 50 volt windows. In each case, 256 channels were used, except for Fig. 18, which corresponds to 1024 channels. Figure 19 is the only one displaying a 20 volt spectrum.

These different sampling frequencies, regions, spectral band shapes, and concentrations have been reproduced in order to demonstrate the similarity of the Fourier transforms despite the different experimental parameters. In each case, the amplitude of the Fourier curves falls off with increasing frequency until a minimum is reached after which the spectral power density remains relatively constant although random.

In this work, the right half of each Fourier transform displayed in the figures has been chosen to represent the noise. The filtering function used corresponds to equation 37 employing the Fourier transform of a Lorentzian of width W as the signal spectrum. The width W is defined as the minimum observable line width in the spectrum given in electron volts. The c segment of Figures 16 through 25 displays the filter function which results from a minimum intelligence width of 0.5 eV. The d segment gives the resultant filtered or Weinered spectrum. Filters based on 1.0 eV FWHM definitions of minimum line width are displayed as the e group of

the cited figures, while the filtered spectra are shown in the f section. In each case, the plot of the c series of the Weiner filter at 0.5 eV FWHM demonstrates that more high frequency terms are transmitted than at 1.0 eV FWHM as in the e plots. The low-pass filter function rolls off smoothly, eliminating ringing in the resultant spectrum. The shape of the filter is unique to each combination of the spectral noise/sampling frequency. This is demonstrated by the shape of the function corresponding to 50 volt/256 channels (Figs.21-25) in contrast to that corresponding to 10 volt/256 channels (Figs. 16, 17, 19). The filter for 50 volt/1024 channels (Fig. 18) is similar to that for 50 volt/256 channels (Figs.21-25).

The shape of the filter is more drastically affected by the amount of noise, cf., Fig. 16 vs. 17, and Fig. 21 vs. 22, than by the difference between observed spectral band shapes, cf., Fig. 18, 21, and 23. Analysis of spikes in the Fourier transforms permits the assignment of power-line noise terms and is the object of continued work.

A number of other filtration forms were attempted based on criteria such as optimal linear and non-linear resolution, but these gave no improvements. The matched filter^{53,55} and Weiner estimator functions were programmed into the ESCA Data-Handling Program listed in Appendix C⁶⁰.

Data from the HP 5950A, the ESCA 36 or the JPL-USU spectrometers stored on paper tape were compiled by computer and analyzed with the filter criteria described here using $W = 1.0$ eV.

60. This program was developed and implemented by L.K. Scheffer. The functional filter relationships were provided by K. Castleman and F. Grunthaner.

D. Deconvolution

In Chapter III, it was noted that the $\text{Au}4f_{7/2}$ photoelectron peak was not narrower than 0.72 eV, although the instrumental function ($b(t)$) for the HP 5950A spectrometer was 0.55 eV FWHM. The function ($b(t)$) can be removed in Fourier space, through deconvolution. If $y(t)$ is the observed signal and $x(t)$ the input signal, then,

$$y(t) = F^{-1}\{F\{b(t)\}F\{x(t)\}\} \quad (43)$$

and, accordingly,

$$x(t) = F^{-1}\left\{\frac{F\{y(t)\}}{F\{b(t)\}}\right\} \quad (44)$$

The natural signal $x(t)$ can be recovered by means of equation 44 if $b(t)$ is known. Unfortunately, this requires pointwise multiplication of the spectrum transform with a positive exponential function. This amplifies the high-frequency components of the spectrum by factors of 10^{25} and higher which obliterates the signal. The deconvolution function must be truncated smoothly in transform space at some frequency where the S/N ratio of the deconvoluted spectrum is of the order of 1.

Since the deconvolution function is a multiplier which restores the intensity of the proper frequency components, truncation is equivalent to multiplication by unity in transform space and to convolution with a delta function in real space.

Preliminary results indicate that the true $\text{Au}4f_{7/2, 5/2}$ spectrum should consist of a Lorentzian doublet with the peaks 3.67 eV apart, having an intensity ratio of 4:3. Each of the two peaks has a FWHM of 0.42 eV. Present efforts to remove this broadening have been plagued by low-fre-

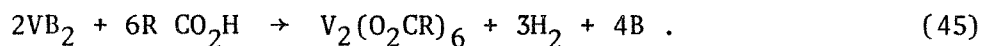
quency ringing in the deconvolved spectrum. Recently, a new approach has been employed which promises to solve this problem. Several papers have appeared in the literature^{60a, 60b} which describe a superresolution algorithm developed by Jansson. In this algorithm, the function resulting from the deconvolution is constrained to be non-negative and single-valued. This boundary condition appears to help arriving at unique solutions. Au4f_{7/2} spectra with FWHM of 0.53 eV FWHM and with signal/noise ratio of 70:1 have been constructed from S/N = 500:1 spectra. This work is continuing.

60a. Jansson, Peter A., J Opt Soc Am, 60, 184 (1970)

60b. Jansson, Peter A., and Hunt, R.H., Optical Spectra, Sept., 1972, p. 36.

V. SURFACE STUDIES OF VANADIUM DIBORIDEA. Introduction

The refractory vanadium diboride undergoes attack by a number of different carboxylic acids resulting in vanadium (III) carboxylate dimers. Greenwood et.al.⁶¹ found that hydrogen evolves during the reaction and proposed the formula:



He suggested that the boron liberated in the reaction formed a passivating layer over the surface of VB_2 . The reaction of carboxylic acids with a number of other vanadium compounds was investigated at Caltech in an unsuccessful effort to increase the yield (~15%) reported for the synthesis when VB_2 was used as a starting material⁶². Vanadium diboride exhibited exceptional reactivity with anhydrous carboxylic acids, whereas VB_2 separated from the reaction vessel and added to a fresh reaction mixture underwent no reaction.

The importance of vanadium oxides in catalysis is well known^{63,64,65,66}.

-
61. Greenwood, N.N., Parish, R.V., and Thornton, P., J. Chem Soc (A), 320 (1966).
 62. Clendening, P., and Powers, D.P., unpublished results.
 63. Larrson, R. and Nunziata, G., Acta Chem Scand, 24, 1 (1970)
 64. Lavison, R., Acta Chem Scand, 26, 549 (1972).
 65. Goodenough, J.B., in Progress in Solid State Chem, ed., H. Reiss, Pergamon, Oxford, Vol. 5, 155 (1971).
 66. Hamrin, K., Nordling, C., and Kihlberg, L., Ann Acad Reg Sci Upsaliensis, 14, 1 (1970).

Since the application of X-ray photoelectron spectroscopy to the study of vanadium surfaces^{67,68,69,70,71} has yielded conflicting information as regards surface chemistry, it seemed that VB_2 presented a more favorable material for this study. The ESCA experiments were, therefore, initiated. Thus, the charging experiments detailed in Chapter III were observed for the first time in the course of this work, and it soon became obvious that a re-examination of the previous work on the oxides was necessary.

B. Experimental

In Greenwood's procedure used for the preparation of vanadium carboxylate dimers, finely-powdered vanadium diboride is added to a deoxygenated solution of a carboxylic acid and its acid anhydride. This slurry is refluxed at 110°C for 2 weeks during which time the system is purged with nitrogen. The slurry is then filtered (again under nitrogen) and the dark green liquid phase is processed further to recover the dimeric compounds.

The surface reactions of VB_2 with carboxylic acids were studied in this work by examining the solid phase which was separated during this final step. Additional samples were taken by stopping the reaction after 10 minutes, 1 hour, 6 hours, and 36 hours. After separation from the liquid phase, the treated VB_2 powder was washed with glacial acetic acid, acetone and ethyl ether to remove traces of soluble reaction products.

-
67. Honig, J.M., Van Zandt, L.L., Board, R.D., and Weaver, H.E., Phys Rev. B, **6**, 1323 (1972).
 68. Fiermans, L., and Vennik, J., Surface Science, **35**, 42 (1973).
 69. Calpaert, M.N., Clauws, P., Fiermans, L., Vennik, J., Surface Science, **36**, 513 (1973).
 70. Wertheim, G.K., Rosencwaig, A., Gallagher, P.K., and Buchanan, D.N.E., Bull Am Phys Soc, **16**, 322 (1971).
 71. Larsson, R., Falkesson, B., and Schon, G., Chemica Scripta, **3**, 88 (1973).

In order to investigate the possible effects of oxygen and water on the VB_2 surface, three different sets of samples were prepared from fresh and acid-exposed VB_2 . One set was processed under nitrogen with anhydrous solvents, while another was exposed to oxygen for 36 hours before introducing it into the ESCA spectrometer. The final set was prepared by following the organic solvent treatment of the solid residue (described above) with a series of rinses with deoxygenated water.

Control samples of elemental boron were treated in an identical manner. These samples and those of the treated vanadium diboride were supplied by P. Clendening and D. Powers. Their starting materials and the other vanadium compounds examined in this work were obtained commercially as analytical reagent grade.

The preparation of V_2O_5 single crystals is described in Ref. 68. Clean (010) surfaces were obtained by cleaving inside the spectrometer. Reduced V_2O_5 was prepared by heating a freshly cleaved single crystal in butene at 1 atmosphere pressure and 550°C for 24 hours. Vacuum reduced V_2O_5 was prepared by heating V_2O_5 in ultra high vacuum (10^{-10} torr) at 550°C for 24 hours.

All photoelectron spectra were taken with the use of powders except for V_2O_5 of which single crystals were also studied. The powder specimens were pellets of the "graphite sandwich" type described in Chapter III. These were mounted on gold-coated platens covered with a gold-plated window.

The electron spectra were taken with the HP 5950A spectrometer operated at an X-ray power of 800 watts with an indicated pressure in the sample

chamber of less than 3×10^{-9} torr. Temperatures were controlled with the H.P. "variable-temperature sample probe" and kept at 300°K .

The electron spectra for vanadium diboride samples were recorded in the oxygen 1s, vanadium 2p (550-500 eV), and the boron 1s region (205-185). All scans of 50 volt width were taken with 1024 data channels. For 20 volt widths, 512 channels were used and for 10 volt widths, 256 channels. All $N(E)$ maxima were reproducible to ± 2 channels with an average variation of ± 1 channel. The above parameters result in 20 to 26 points per volt and deviations of less than ± 0.1 eV in the assignment of peak positions. All spectra shown in the figures have been filtered in "transform space" (See Chapter IV) with a definition of minimum signal width of 1.0 eV FWHM. All the figures are plotted in the same format with corrected binding energy along the abscissa and relative electron flux along the ordinates. The data were taken on the HP 5950A spectrometer of the Application's Laboratory of the Scientific Instruments Division of Hewlett-Packard and were recorded on paper tape. The tape was edited on the CIT PDP 10 system and transferred to cards on the CIT 370/158 computer. The card decks were then processed by the JPL 1108/9300 system with the ESCA Data Handling Program listed in Appendix C.

Table 2 lists all the statistically relevant inflections observed in the spectra of the vanadium-oxygen region. The spectra are listed in columns with decreasing energy from top to bottom. All data corresponding to peaks are underlined and those corresponding to secondary peaks or shoulders are indicated by broken lines. The B1s spectra are displayed in a similar way in Table 3.

TABLE 2

Major Inflections Recorded for the Vanadium 2p / Oxygen 1s Regions

Spectrum Identification Number →

	101	103	105	107	109	111	113	116	117	121	128	129	131	132	133	134	136	138
		538.5			538.5			538.3					538.2			538.4		
		<u>537.8</u>				538.1	538.1		537.9								538.1	
				538.1		537.4	537.4	537.3	<u>537.2</u>	537.6			<u>537.6</u>				537.4	
		<u>537.1</u>							537.1	536.8				536.9	537.0	536.8		
		<u>536.7</u>		<u>536.4</u>	536.5		<u>536.6</u>	536.4			<u>536.4</u>	536.5	536.4			536.3		
		535.8			535.8		<u>536.0</u>	536.0	535.9		535.8			535.8			535.8	
						535.5	<u>535.2</u>					535.7	535.2		535.5	535.3		535.2
		535.1		534.9	534.8	534.7		535.1				535.2		535.1			534.8	
									<u>534.4</u>	<u>534.7</u>	534.4			534.3				
		534.2		533.7	<u>534.1</u>			<u>534.0</u>					<u>533.8</u>		534.0		<u>534.1</u>	<u>534.1</u>
						<u>533.3</u>			<u>533.4</u>		533.2			<u>533.2</u>		533.2	<u>533.4</u>	<u>533.3</u>
	533.0				<u>532.7</u>					<u>532.7</u>				<u>532.0</u>				<u>532.7</u>
	532.4					<u>532.5</u>	<u>532.3</u>				532.3							<u>532.2</u>
	<u>532.1</u>	<u>532.1</u>		531.8	531.8	<u>532.0</u>	<u>532.0</u>	532.0	531.8			532.0						
			<u>531.5</u>		<u>531.2</u>		<u>531.3</u>						<u>531.6</u>	<u>531.5</u>		<u>531.3</u>		
	530.8			<u>531.1</u>				<u>531.0</u>	<u>530.9</u>							<u>531.0</u>		
				<u>530.5</u>				530.3										530.6
	<u>530.1</u>	<u>529.7</u>				<u>529.7</u>					<u>529.8</u>	<u>529.9</u>	<u>529.8</u>	<u>529.8</u>	<u>529.8</u>	<u>530.0</u>	<u>530.0</u>	<u>530.0</u>
	<u>529.8</u>				<u>529.3</u>		<u>529.7</u>											
									529.1	528.7								
				<u>528.3</u>			528.5						<u>528.3</u>	<u>528.3</u>	528.4		<u>528.7</u>	528.7
	527.7				528.1			528.0		527.7	527.8		527.7					527.8
		<u>527.4</u>			<u>527.4</u>	<u>527.4</u>	527.6		527.6				527.6	527.2		<u>527.4</u>	<u>527.3</u>	
	527.1									526.9	527.0							
		526.7		526.3	526.5			526.4				526.3		526.5		526.6		
						526.0	525.8		<u>525.7</u>	<u>526.2</u>	525.5	525.9					<u>526.2</u>	<u>525.6</u>
	525.6			<u>525.3</u>	<u>525.5</u>			525.2		<u>525.6</u>	525.5	<u>525.2</u>			<u>525.2</u>	525.4		
	524.9	525.2				<u>524.9</u>				<u>524.7</u>	<u>524.8</u>		525.0	<u>525.1</u>			525.0	
	<u>524.2</u>	<u>524.3</u>	<u>524.5</u>	<u>524.4</u>	<u>524.6</u>		<u>524.4</u>	<u>524.6</u>	<u>524.6</u>	<u>524.7</u>	<u>524.8</u>		<u>524.2</u>	<u>524.6</u>	<u>524.3</u>	<u>524.2</u>	<u>524.4</u>	
	<u>523.9</u>			523.8	<u>524.0</u>	<u>524.1</u>	<u>523.9</u>	<u>523.9</u>	<u>523.7</u>	<u>523.7</u>		<u>523.7</u>	<u>524.0</u>			<u>523.7</u>	<u>523.9</u>	<u>524.0</u>
		<u>523.6</u>			<u>523.5</u>	<u>523.3</u>	<u>523.2</u>	523.2				523.3	<u>523.4</u>	<u>523.5</u>	<u>523.3</u>			<u>523.3</u>
	<u>523.1</u>	523.1		523.1	522.9			522.7	<u>522.9</u>		522.7						<u>523.2</u>	<u>522.9</u>
	522.7	<u>522.4</u>			522.3	<u>522.6</u>	<u>522.6</u>		522.3	522.6	522.6	522.6	<u>522.3</u>		522.6			
	522.1	521.8		521.8			<u>521.2</u>			521.7	522.1	521.9				<u>522.2</u>	<u>521.9</u>	<u>521.9</u>
	521.7				521.5	521.6		521.5	521.4			521.3		<u>521.5</u>	<u>521.5</u>			
	521.0	521.0		520.8			520.8	520.9			520.9		<u>520.8</u>				<u>520.8</u>	<u>520.6</u>
	520.6	520.3			520.6	520.2	520.3	520.2	520.4	520.6		520.6		520.5		520.6		
	520.1								519.7	519.7	519.8					<u>520.0</u>		
	519.6	519.6		519.4	519.6		519.6	519.3				519.7		519.3		519.3	519.3	519.6

TABLE 2, CONTINUED

Spectrum Identification Number \longleftrightarrow

	101	103	105	107	109	111	113	116	117	121	128	129	131	132	133	134	136	138
518.8	519.0								519.0			518.7						
		518.6	518.6	518.2	518.2	518.2	518.2	518.0	518.4	518.2	518.6	518.6	518.6		518.4		518.1	517.7
517.2		517.8	517.7				518.0	517.8	517.8	517.8								
	517.7	517.2	517.2				517.2											
517.1								517.1	517.1		517.0	516.2	516.2	516.2	516.2	517.1		516.4
516.4	516.4			516.4	516.1	516.4	516.5	516.6	516.7	516.6								
515.8		516.0	516.0		516.1	515.8	515.8	515.2	515.9		515.6	515.4	515.2	515.2	515.2	515.2	515.6	515.6
	515.2				515.2	515.7					515.0	515.0						
		514.8				514.7	514.2						514.2					
514.6	514.4							514.2	514.2	514.2								
513.9					512.2			512.2	513.4	513.7			513.8	513.7				
	513.3				512.2			513.4	513.4	513.2			513.5	513.2	513.2	513.6		
513.1						512.0	512.7	512.2	512.2									
512.2	512.6				512.2	512.2		512.2	512.2	512.6	512.5	512.6						
											511.8							
	511.4				511.5	511.6	511.5	511.4	511.5	511.7								
									510.9	511.0	510.8			510.8	510.8	510.8		
	510.3				510.4		510.6						510.5					
							509.8	510.1	509.9	510.1								
							509.3	509.4						509.2				509.3

Binding Energy (eV) \uparrow

TABLE 3 Major Inflections Recorded for the Boron Is Region

Spectrum Identification Number		102	104	106	108	112	114	119	120	153	155	160	162	267
	204.8								204.9	204.7				
								204.5	204.1					
								203.6		204.0				
	203.4	203.3	203.3						203.3	203.2				
	203.0	202.7	202.7					202.9	202.9	202.7				
	202.2	202.1	202.1		202.4			202.3	202.5					
						202.2	201.5	201.5	201.2	201.9				
	201.5	201.2			202.2		200.6	200.8	201.3	201.4				
	200.9	200.5	200.9		200.4		200.6	200.8	200.9					
	200.1						200.1	200.8	200.4	200.4				
	199.6						199.9	200.1	200.2	199.7				
							199.4	199.1	199.3					
	198.7	198.6	199.3		198.9	198.7	198.4	198.5	199.5	198.9				
					198.3	198.3	198.4	198.5	198.3	198.2				
	197.7	197.6	197.5	197.6	197.6	197.6	197.6	197.7	197.7	197.8				
									197.2					
	196.9	196.8			196.6	196.8	196.8		196.8	196.7				
	196.2	196.8			196.0	196.2		196.2	196.4					
							195.6	195.7	195.9	195.9				
	195.5	195.2	195.1	195.0	195.1		195.6	195.0	195.0	195.4		195.2		
	194.8	194.8					194.8	195.0	195.0			(218.7)		
							194.2	194.2	194.4	194.3	194.4	194.2	(208.0)	
	194.0				194.2				194.4					193.0
	193.2	193.5	193.2		194.0		193.1	193.4	193.2	193.2	193.4	193.4		
							192.8	192.4	193.2	193.2	193.4	193.4	(216.5)	192.7
	192.3	192.5	192.3	192.3	192.3	192.8	192.2	192.3	192.2	192.3	192.3	192.3	192.3	192.2
	191.5	191.8	191.8	191.8	191.6	191.6	191.4	191.7	191.4	191.4	191.2	191.8	(216.0)	191.3
							191.1	191.1	191.4	191.4	191.3	191.8		
	190.6	190.7			190.9	190.9	190.9	190.9	190.9	190.8	190.7	190.8	(214.8)	190.5
							190.1	190.0	190.0	190.4	190.0	189.6		189.8
	190.0								190.0	190.4	190.0	189.6		189.8
	189.4	189.2	189.1				189.5		190.0	189.5	189.6	189.6	(213.2)	189.8
	189.0	188.6	188.7	188.8			188.6	188.6	189.2	189.5				188.8
	188.4				188.5				188.4	188.0		188.3	(212.0)	188.0
	187.8	187.7	187.8	187.6	187.6	187.6	187.8	187.9	188.4	187.7	188.3	188.3	187.6	187.6
							187.3	187.3	187.1	187.1	187.0	187.0	(211.1)	187.6
	186.7		186.7	186.8			186.9	186.9	186.7					(210.3)

Additional experiments were conducted with the McPherson 36 ESCA spectrometer (Chapter III C, Voltaic effects). In this case, samples of VB_2 were pressed into coarse aluminum plates, and the spectra were recorded using Magnesium $\text{K}\alpha$ radiation. Data were taken with a 40 eV window and displayed in 211 channels. Charging effects were studied by biasing the sample from +10V to -20V with respect to the spectrometer as shown in Fig. 11.

Results and Discussion

Variation of flood-gun⁷² currents resulted in different spectra for the vanadium-oxygen and Bls region when fresh VB_2 was used. As mentioned, VB_2 is an excellent conductor, and charging effects were not anticipated. Figure 26 shows the electron spectra obtained from several of these experiments in the region of 550 eV to 500 eV binding energy. Spectrum 101 is that of fresh VB_2 , where the flood gun had been adjusted to provide currents which neutralize the charging shift of teflon. The spectrum shows the vanadium $2p_{3/2}$ line at 520-515 eV binding energy with the vanadium $2p_{1/2}$ peak at 528 to 522 eV, and the oxygen 1s line at 535 eV to 529 eV. The intensity of the oxygen peak indicates that the surface of the sample is extensively oxidized. The effect of turning off the flood gun in this experiment is given in spectrum 103. Although the region of the vanadium 2p doublet seems unchanged, the oxygen 1s region differs drastically and a new line appears at higher binding energy and the original peak-with-shoulder system of 101 has become at least two well-resolved

72. The term flood gun refers to the irradiating device for low-energy electrons described in Chapter III. The reproducibility of the flood gun or voltaic-potential experiments is described in Chapter III - Section C.

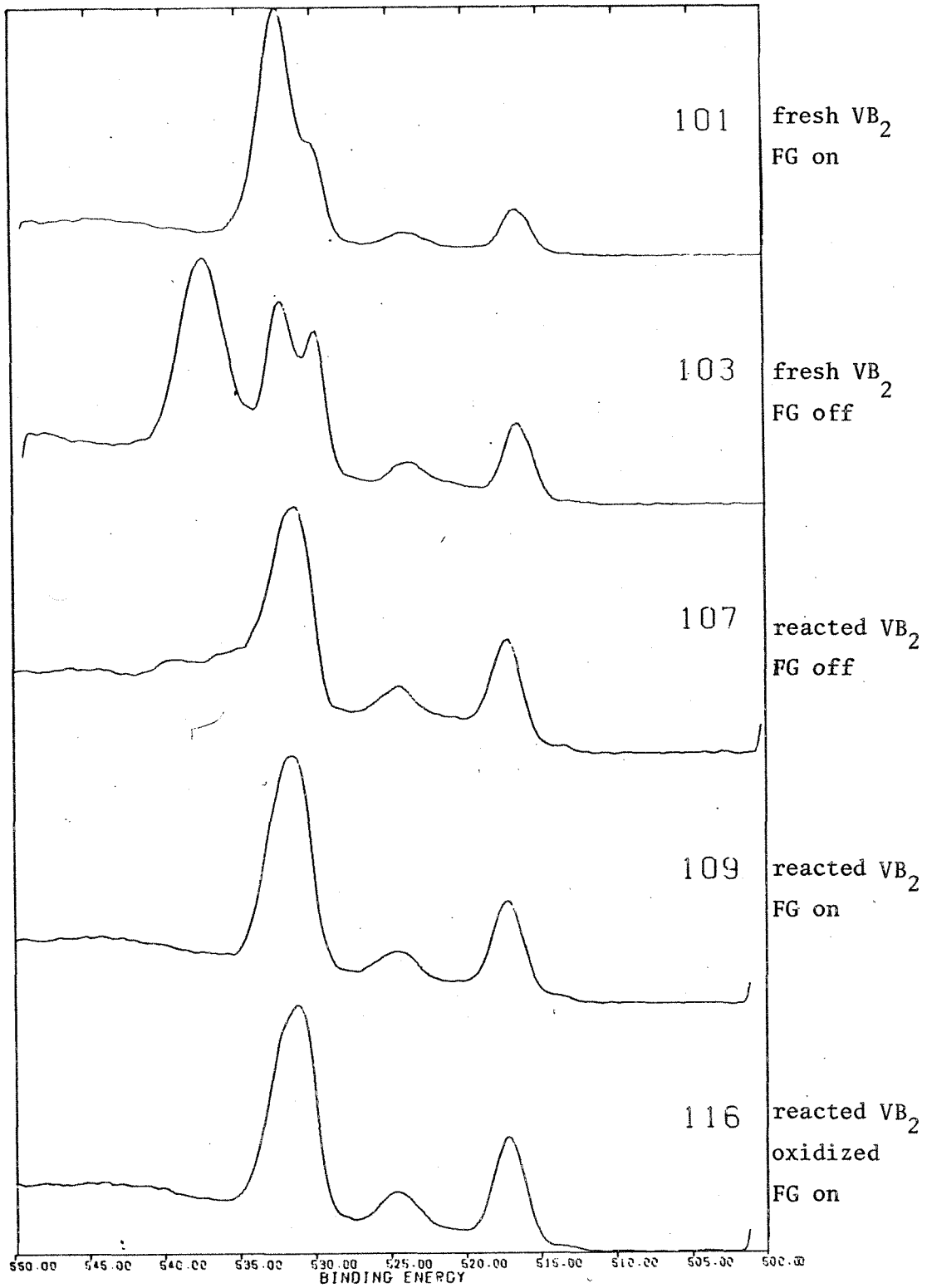


Fig. 26 Vanadium oxygen region of vanadium diboride compounds

peaks. These spectra are reversible within the time frame of data acquisition (minutes).

The spectra due to reacted VB_2 is given in 107. Here, the Flood Gun was off (FG off) and in 109 the Flood Gun was on. The shape of the oxygen 1s peak has changed, and the charging effect has been considerably reduced.

The Boron 1s spectra of these compounds are displayed in Figure 27.

Spectrum 102 arises from uncharged fresh VB_2 (FG on) while 104 is from charged VB_2 (FG off). The symmetric peak of 102 assumes the two-peak structure of 104 when charging is introduced. Spectra 106 (FG on) and 108 (FG off) are due to passivated VB_2 and show peaks in the same energy position as in 102 and 104 but an additional peak occurs at lower binding energy.

As developed in Chapter III, specimens having an impedance of much less than 10^9 ohms do not exhibit charging while samples having impedences greater than 10^9 ohms will rest at some potential determined by the steady state of the electron currents. In Figs. 26 and 27, some peaks of the spectrum exhibit charging while others correspond to domains that remained in good electrical contact with the spectrometer. This implies that the $V_C=0$ (FG on) case permits the identification of species by means of chemical-shift correlations. The $V_C=n$ case (FG off) permits exploratory investigation of the variation in conductivity across the sample. Subtraction of the FG on spectra from the FG on spectra should give the contribution from the insulating species.

In Fig. 28, the results of such an experiment are displayed. Spectrum 101 is shown at the top of the figure and spectrum 103 at the center.

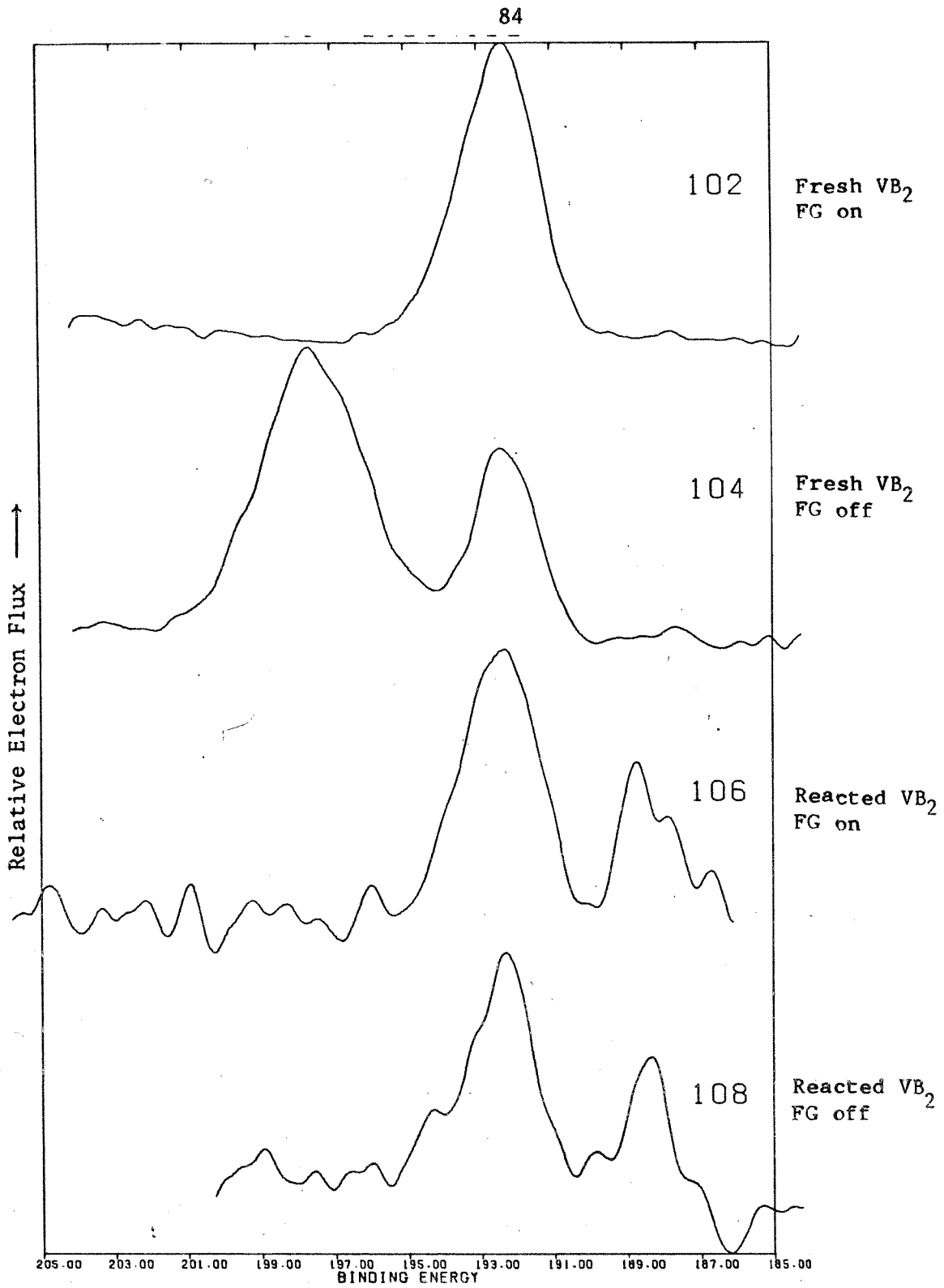


Fig. 27 Boron 1s spectra of vanadium diboride compounds

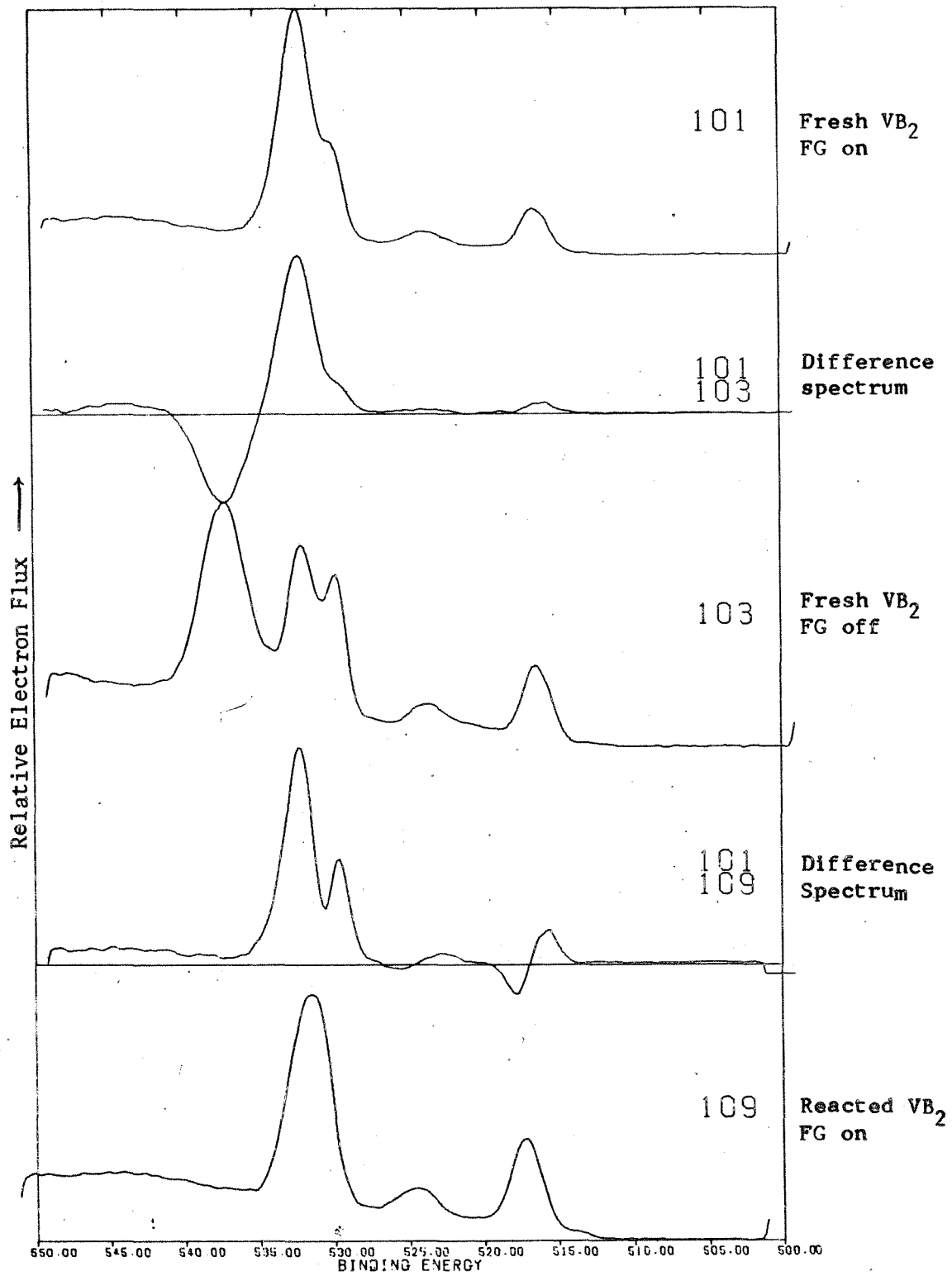


Fig. 28 Difference analysis of Vanadium Diboride spectra in V-O region

Between the two is the difference spectrum 101 minus 103 marked $\begin{cases} 101 \\ 103 \end{cases}$.

This notation will be used throughout the thesis. A line is drawn through the difference spectrum at the zero point. Peaks below the line correspond to species giving the spectrum that was subtracted while features above the line belong to the initial spectrum. In this representation, charging species are emphasized and the voltaic potential can be directly assigned. In 101-103, a broad oxygen peak at 532.1 eV shifts to 537.1 eV for a 5.0 volt difference in charging potential. Fig. 28 also shows the difference spectrum between fresh and passivated VB_2 . It indicates that considerably more oxygen is present in the fresh sample than in the reacted one and that at least two different vanadium species are present. The intensity in the O1s spectrum of 101 has been significantly reduced in the region of 531 eV binding energy.

Figure 29 shows the boron 1s curves obtained from a similar treatment. The difference spectra 102-104 show that the charged peak has been broadened. A shift of 197.7-192.5 or 5.2 eV is indicated, compared to 5.0 eV for the O1s region. Also, the difference spectrum, 102-106, is displayed in the same figure, where 106 is the boron 1s spectrum of the reacted VB_2 . This spectrum, which does not go through zero, shows the negligible amount of boron present on the surface. To forestall confusion, it should be noted that the spectra in these figures are plotted from maximum to minimum while the difference spectra are point-wise subtraction of filtered spectra.

When the fresh VB_2 samples were removed from the spectrometer, they were stored on a clean bench under dust covers. After 16 hours, they were

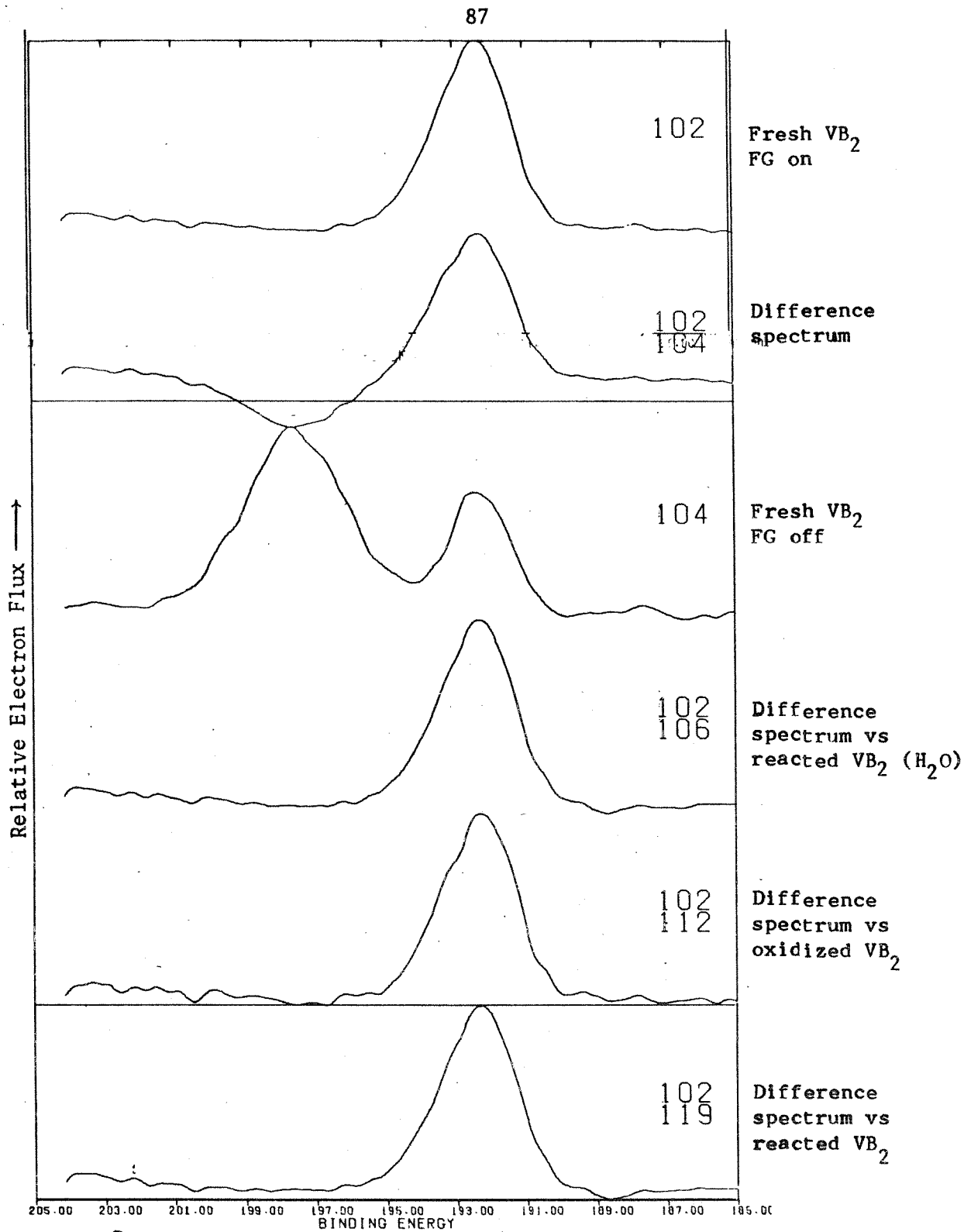


Fig. 29 Difference analysis of vanadium diboride spectra in Boron 1s region

re-examined in the spectrometer (spectra 111 and 113 vanadium-oxygen region). These are given in Figure 30, where 111 corresponds to flood gun on and 113 to flood gun off. A considerable change in the chargeable component of the spectrum and an enhancement of the peak at 529.7 eV is noticeable. Spectra 117 and 121 of Figure 30 represent the V-O region of a passivated sample of VB_2 , where all procedures (reaction, separation and filtration) were carried out under anhydrous conditions. (121 is the FG-off case.)

The boron 1s region of the oxidized specimen is given in Figure 31 as 112 (FG on) and 114 (FG off). The boron 1s spectra from a sample of VB_2 passivated and not exposed to water are given in Fig. 31 as 119 (FG on) and 120 (FG off). The narrow profile of the peak at lower binding energy in 119/120 should be noted as well as the considerable structure on both peaks.

The difference spectrum 111-113 is given in Figure 32, along with 111 and 113 for comparison. Here the charging shift has decreased (536.0-532.0 4.0 eV) with respect to that of fresh VB_2 and the peak attributed to the insulating domains is reduced.

Difference spectra for the corresponding boron 1s regions are given in Fig. 33. The charging shift of about 2 volts in the peak at lower binding energy in 119/120 should be noted since it is considerably less than that occurring in the oxidized boron as seen in 114.

Very little quantitative information exists concerning vanadium XPS spectra. Peak shapes are complicated and often show multiplet splittings as well as shake-up satellites as discussed in Chapter 2^{68,71}.

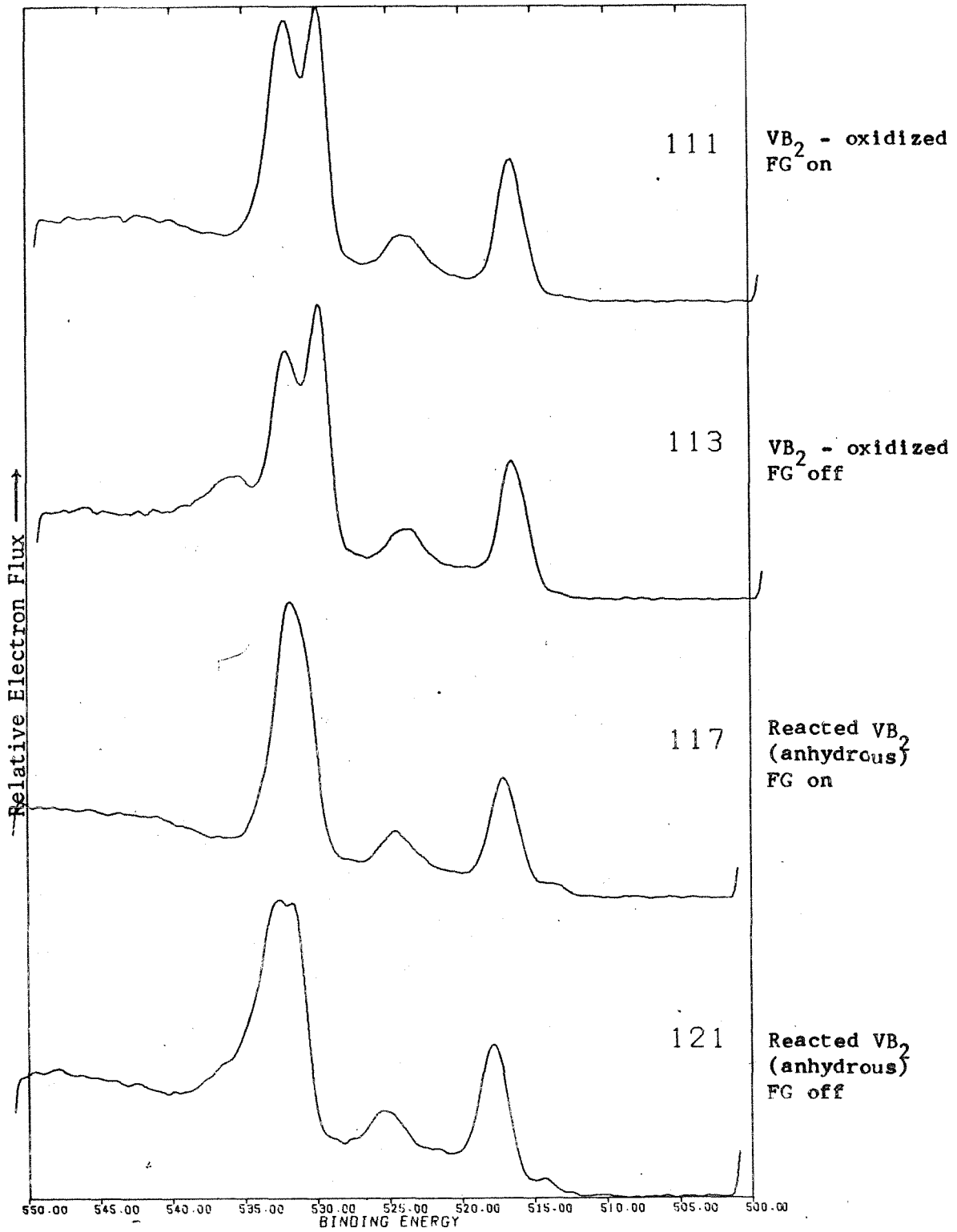


Fig. 30 Vanadium oxygen region of vanadium diboride spectra (charging comparison)

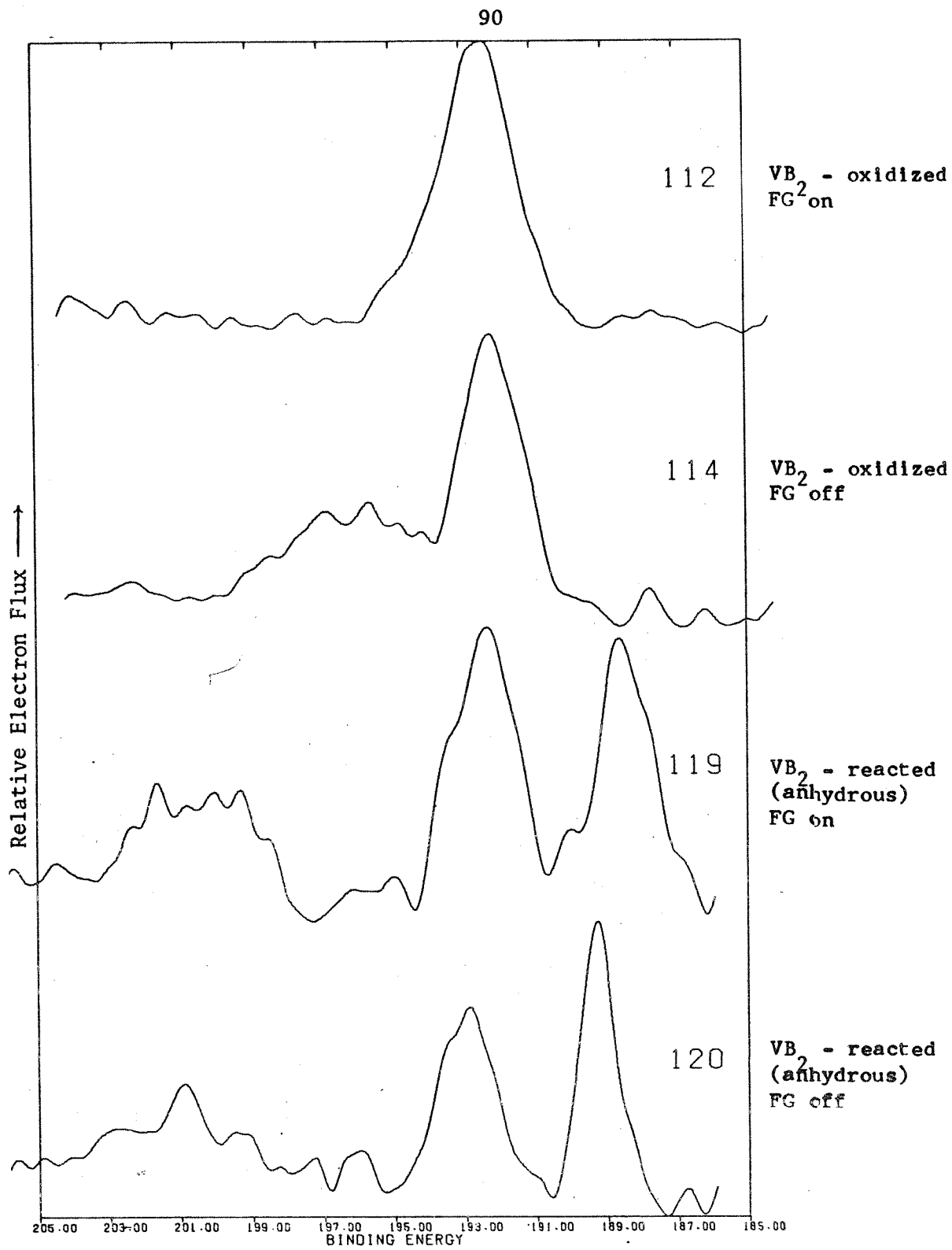


Fig. 31 Boron 1s spectra of VB_2 compounds (charging comparison)

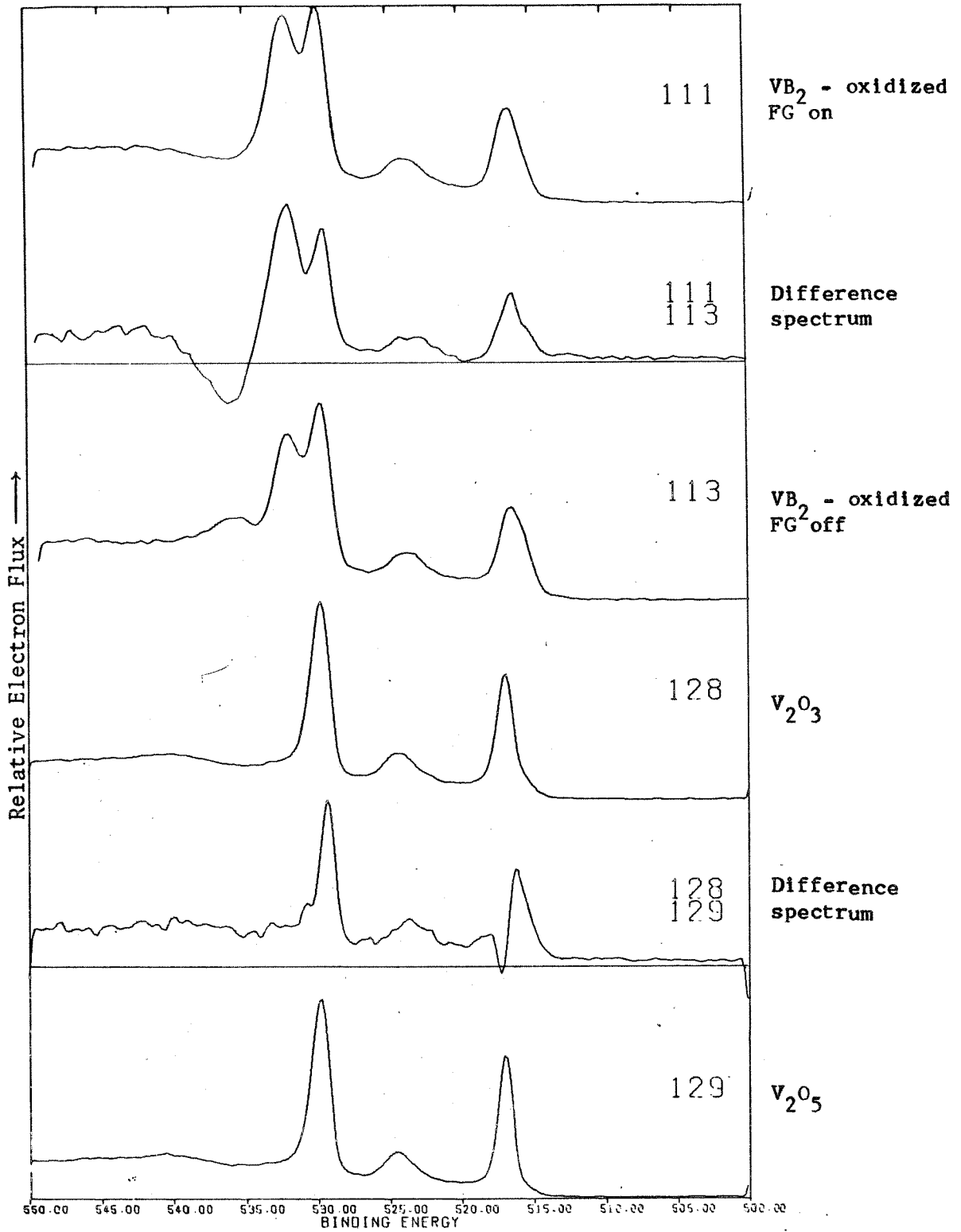


Fig. 32 Difference analysis of spectra in vanadium - oxygen region.

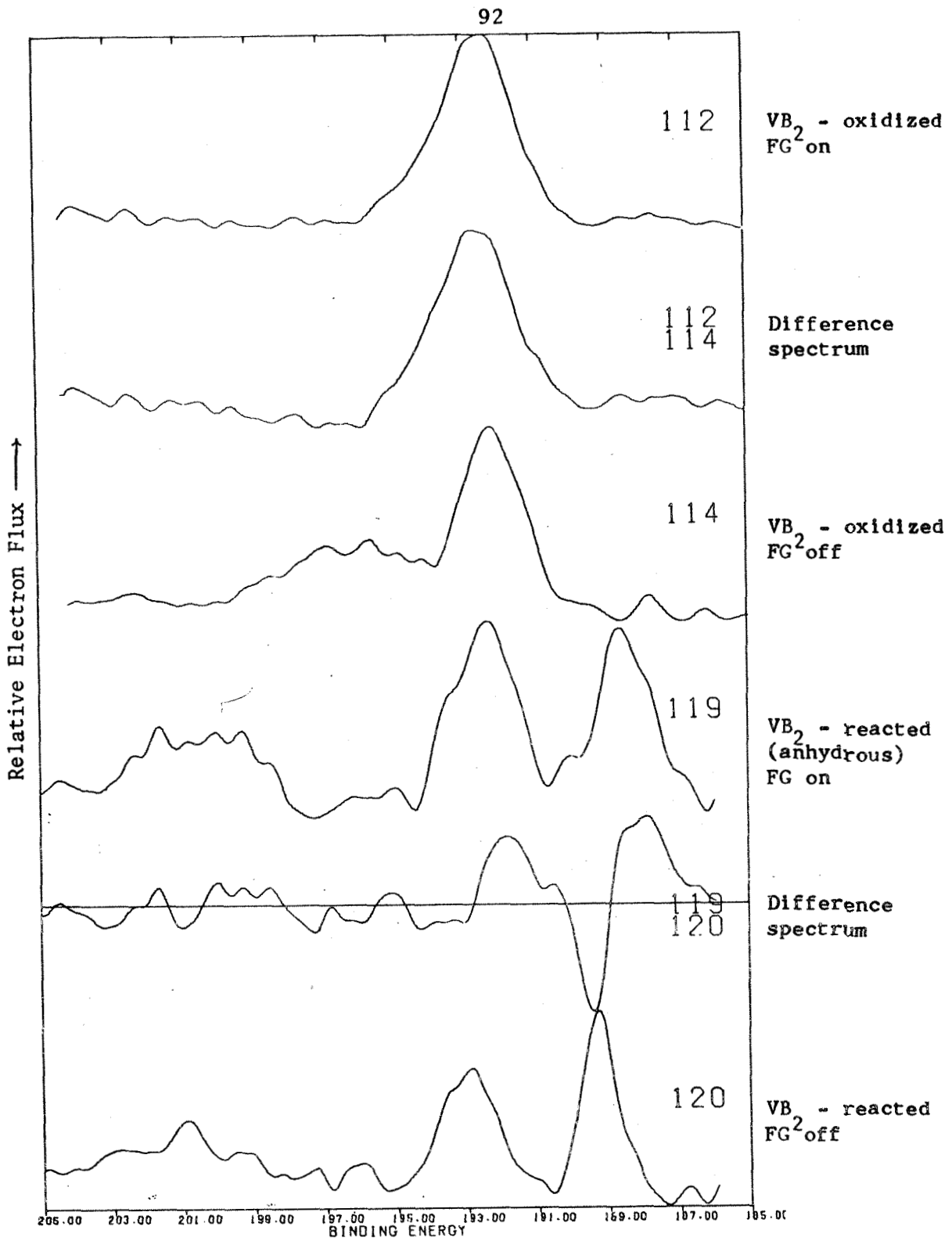


Fig. 33 Difference analysis of vanadium diboride compounds for the boron 1s region.

The spectra of the model compounds taken in the course of this study are illustrated in Figure 34. Spectrum 128 represents V_2O_3 , 129 V_2O_5 powder, 132 VN, 133 granular vanadium metal, 134 $VOSO_4$, 135 Na_3VO_4 , and 157 the oxygen region of $Na_2B_4O_7$. It becomes immediately clear that all of the vanadium samples have significantly oxidized surfaces. Further, the differences in energy between the oxygen 1s peak and the vanadium 2p peak are not uniform, ranging from 12.8 eV (V_2O_3) to 16.3 eV (V metal). Identical vanadium oxygen species should exhibit constant differences. Thus, a wide range of different V-O species are believed to be present in any system.

The vanadium $2p_{3/2}$ line in spectrum 129 (V_2O_5) is about 0.92 eV FWHM, that is, significantly narrower than any other vanadium line observed in this work. It is suggested in Chapter II that a photoelectron peak would be symmetrical in the absence of multiplet and satellite effects and that the observed linewidth would be governed by the lifetime of the hole state and other solid-state factors.

The spectrum of VN in 132 Figure 34, shows the nitride peak at the low binding-energy region and is superimposed on the vanadium peak arising from vanadium oxide. Even in vanadium metal (133-Fig. 34) several peaks in the V 2p region are seen (133, Fig. 34) which are attributable to oxides. Magnification by a factor of 5 is required to make the vanadium-metal peak at 513.5 eV visible. The high intensity of the oxygen 1s line relative to that of the vanadium peak in 134-Fig. 34 is not explained by the stoichiometry of $VOSO_4$. The structure of the Na_3VO_4 spectrum in 136-Figure 34 is due in part to a sodium Auger line near the oxygen 1s peak, while the line at 534.1 can be attributed to water.

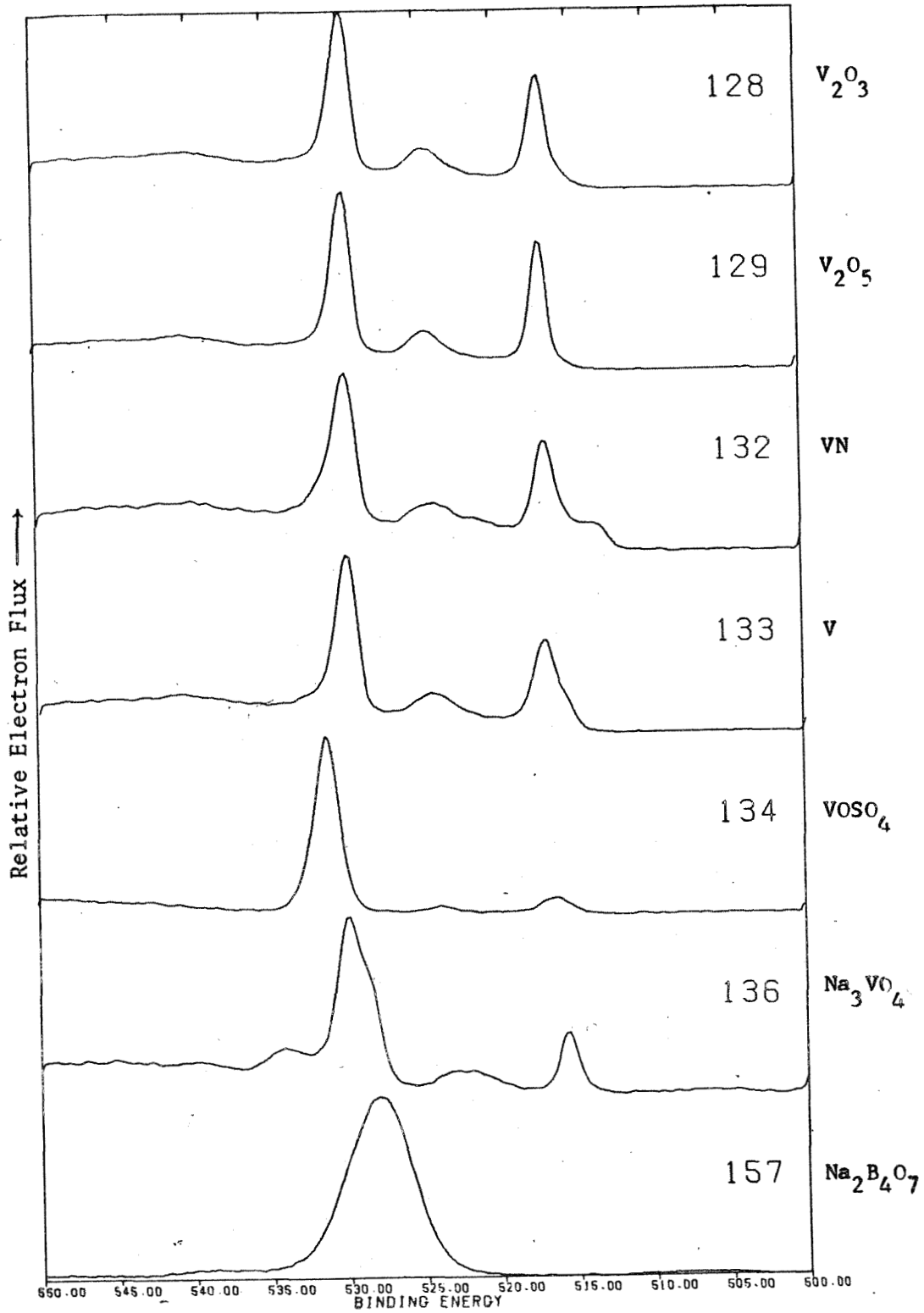


Fig. 34 Vanadium oxygen reference spectra of model compounds

The spectra of the model compounds shown in Fig. 34 show the existence of a variety of surface oxides. Because of the complexity of vanadium oxide spectra, and the possibility of the existence of a number of similar oxides on the VB_2 surface, the model-compound spectra were used as line shape models. These are used to correct for contributions from similar species in the VB_2 spectra.

Since the oxygen and vanadium peaks observed in Fig. 34 are considerably stronger than those of vanadium diboride, it was necessary to normalize the model spectra prior to subtraction. Algebraically, this can be represented as

$$h_i(e) = x_i(e) - c y_i(e) , \quad (46)$$

where,

- $h_i(e) \equiv$ particular points of the difference spectra
- $x_i(e) \equiv$ points of the initial spectra
- $y_i(e) \equiv$ points of the subtracted spectra
- $c \equiv$ normalization coefficient which is constant for a given difference spectrum.

First, the maximum negative value is determined which results when subtracting the raw spectrum. The normalization coefficient is then calculated which would make that term zero.

In Figure 35, this data is displayed for fresh vanadium diboride. The first difference spectra compares 101 with the oxidized sample of unreacted VB_2 . Note that the peak at 532.1 eV is enhanced in fresh material, but more vanadium oxide is present in 111. Curve 117 displays the spectrum of anhydrous reaction product (anhydrous passivation) while 116 is the spectrum of anhydrous reaction product exposed to air for 16 hours. In

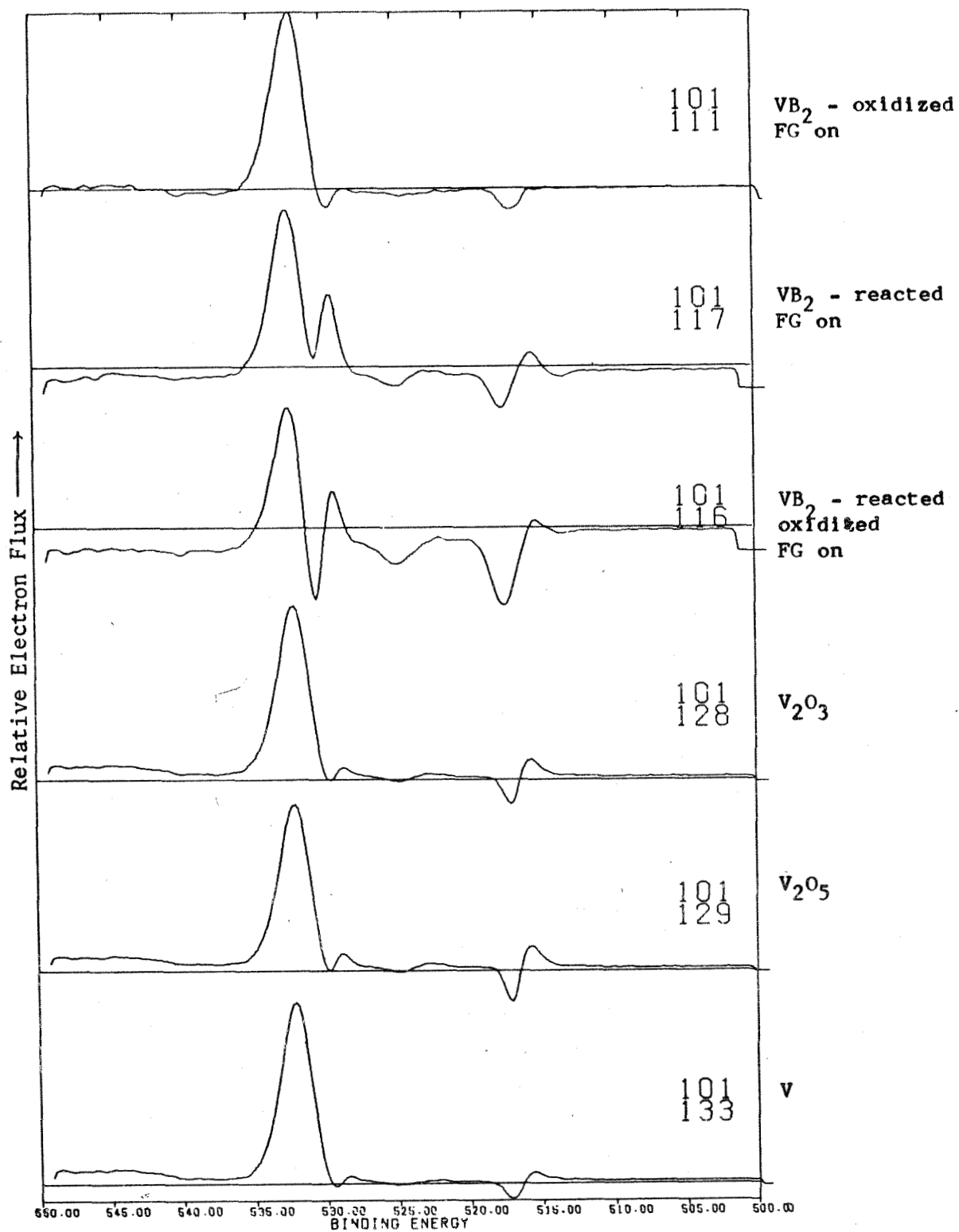


Fig. 35 Difference analysis of VO region of fresh VB₂ (FG on) by comparison with spectra identified along ordinate

both 116 and 117 (FG on), the major contribution of a new peak corresponding to higher binding energy is indicated. The oxygen peak is located at 530.7 eV.

Difference spectrum 101-128 (Fig. 35) compares V_2O_3 with VB_2 . In this case, subtraction of V_2O_3 spectrum would remove too much vanadium signal. Similar conclusions can be drawn from the difference spectra 101-129 (V_2O_5) and 101-133 (V metal). It appears, however, that the peak at lower binding energy in the O1s portion of the spectrum appears in the right region for a vanadium oxide assignment.

Figure 36 shows similar comparisons but with the Flood-Gun off experiments. Spectrum 103 provides greater detail in the oxygen 1s spectrum of fresh vanadium diboride than that of 101 and affords a more fruitful comparison with model spectra.

Figure 36 first displays a difference spectrum between 107 (reacted VB_2 FG-off) and 103. The differences between reacted and unreacted VB_2 are strongly accentuated. The different oxide peaks apparently correspond to the specific vanadium peaks at 531.3/518.1 and 529.8/515.8 eV. The presence of an additional O1s peak at higher binding energy as well as the O1s peak corresponding to the charged domain is emphasized in the difference spectrum 103-107.

The latter half of Fig. 36 is devoted to the Flood Gun on/off experiments with the reacted species. The apparent splitting of the charging oxygen species is a detail also seen in the vanadium 2p region.

Comparative analysis of 103 is continued in Fig. 37. Comparison of 103 with the air-oxidized experiment (113) indicates the build-up of a

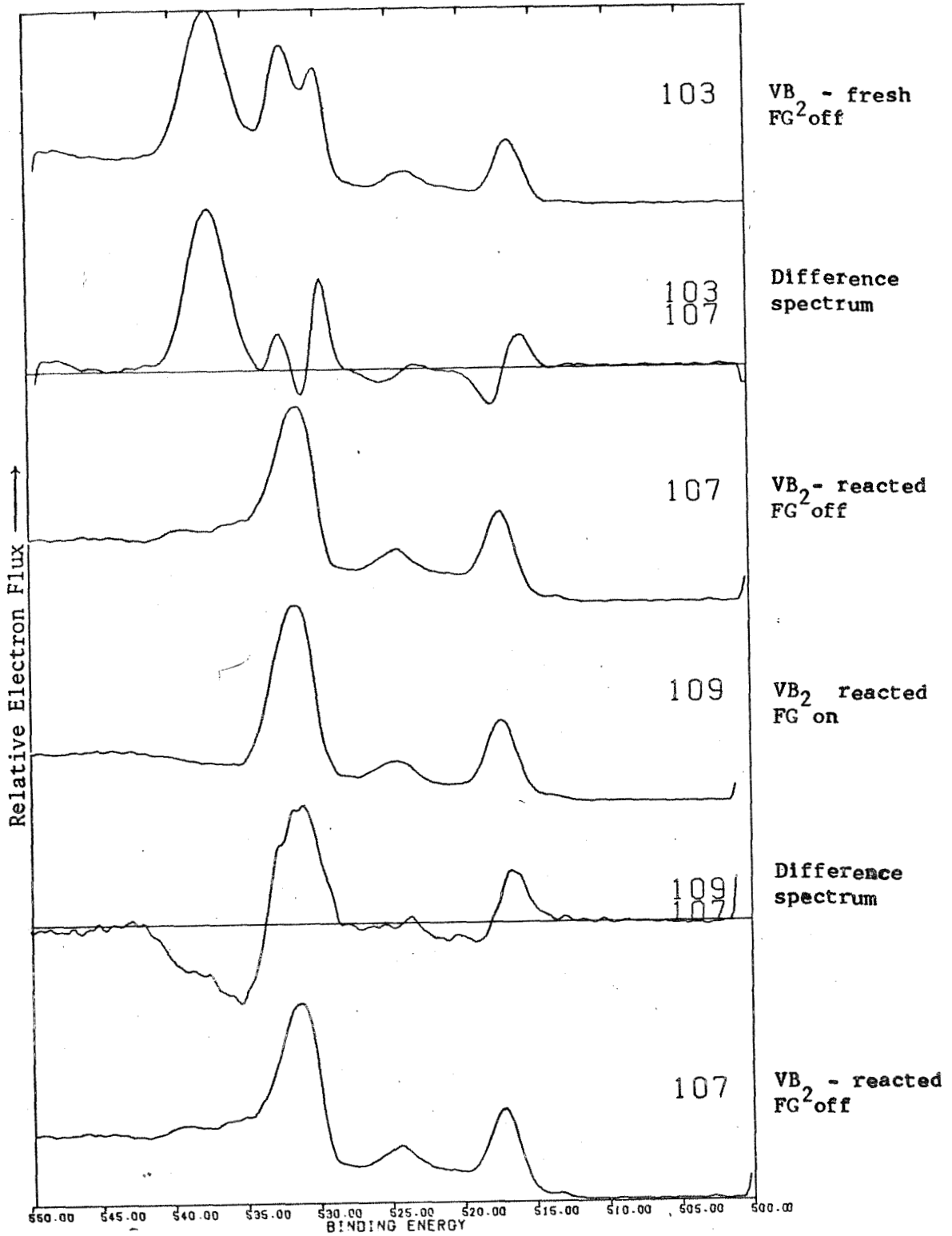


Fig. 36 Difference analysis, V-O region of vanadium diboride compounds

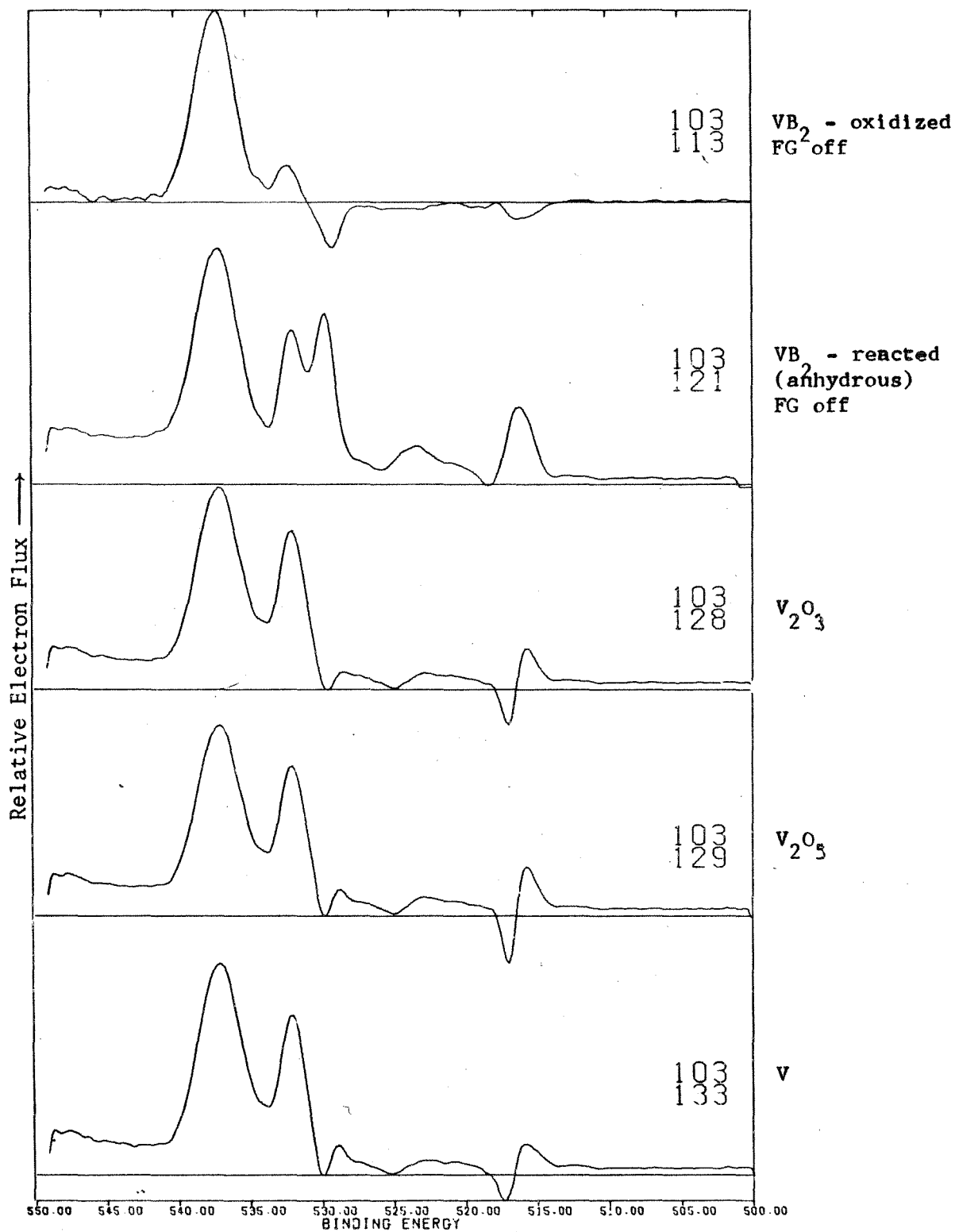


Fig. 37 Difference analysis of V-O region of fresh VB₂ (FG off) by comparison with spectra identified along ordinate

vanadium oxide upon oxidation. The difference spectrum of anhydrous reaction product, 103-121, shows increased deepening of the valley between the two oxygen peaks of 103 along with implied multiplet detail in the range between the vanadium $2p_{1/2}$ and the vanadium $2p_{3/2}$ lines. Comparison with V_2O_3 (128), V_2O_5 (129) and V metal (133) demonstrates over subtraction of the vanadium 2p line from these oxides. It seems appropriate to attribute the line occurring at lower binding energy (in the oxygen group) to these species. In Fig. 38, the spectrum (109) of reacted VB_2 is compared with that of the oxidized VB_2 (111), FG on. More intense signals representing low-binding energies of oxygen and vanadium are given by the oxidized unreacted sample. A vanadium oxide species representing higher binding energy is shown in 109. The difference spectrum 109-116 indicates a large amount of vanadium oxide at low binding energy and a small amount of oxide at high binding energy. The sample corresponding to 109 was passivated material which had been exposed to water and 116 was reacted and air-exposed VB_2 . Figure 38 shows that the differences in the spectra are minor.

The sample representing 117 in the difference spectrum 109-117 (Fig. 38) was processed in an anhydrous manner. The oxygen species at 531 eV binding energy is more pronounced in 117 while those corresponding to binding energies above and below that value are more pronounced in 109.

Comparison of 109 with V_2O_3 (128), V_2O_5 (129) and V metal (133) leads to the conclusion that the vanadium oxide in the reacted material is similar to that observed in the model compounds.

Figure 39 affords comparison of the boron 1s regions. Serious difficulties

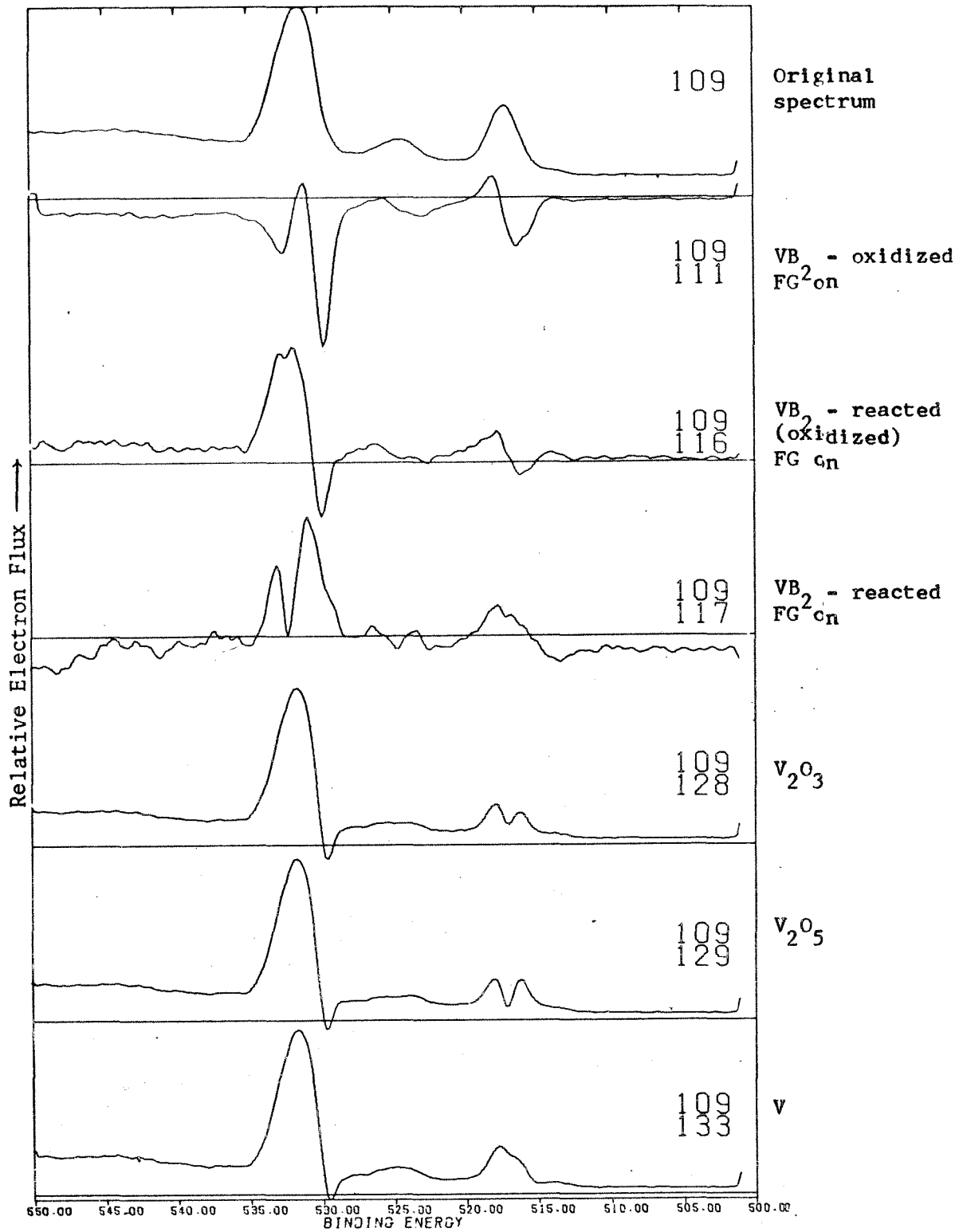


Fig. 38 Difference analysis of V-O region of reacted VB₂ exposed to water (FG on) by comparison with spectra identified along ordinate.

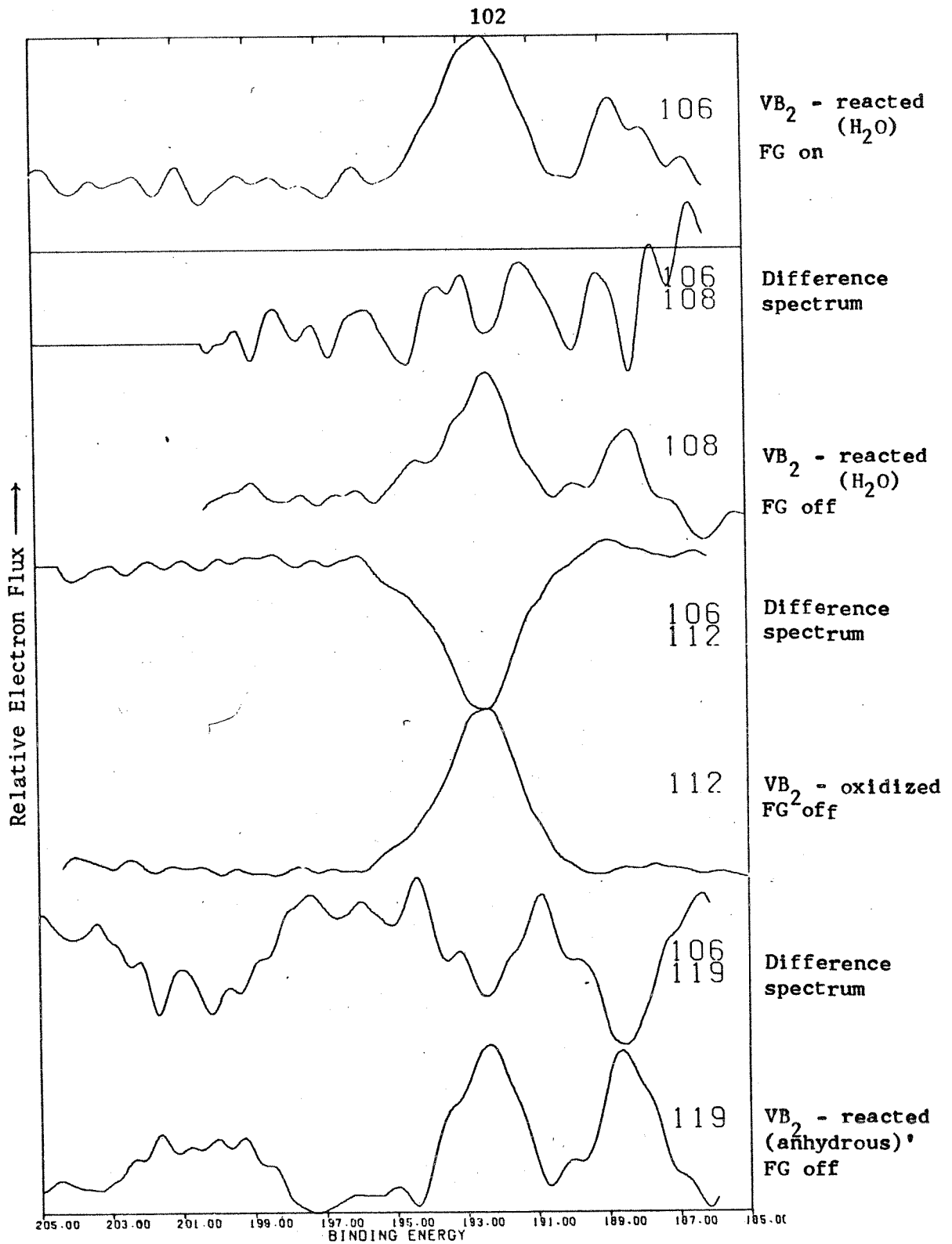


Fig. 39 Difference analysis of Boron 1s region of vanadium diboride compounds

arise because of the poor capture cross-section of boron for the $AlK\alpha$ radiation. Since the signal is weak, the noise terms become accentuated by the difference approach. In 106-108, noise predominates whereas in 106-112, a relatively high concentration of boron (VB_2 sample) in oxidized form exists. Passivated VB_2 exposed to water (106) and anhydrous passivated VB_2 (119) give rise to relatively strong boron peaks at lowered binding energy as is evident in the curve (119).

The VO spectrum 107 of reacted VB_2 (FG off) is given in Fig. 40. Comparison with 121 (VB_2 - anhy.-react) shows that oxide of lowered binding energy predominates in the spectrum of the water exposed sample, while the boron oxide peak is more intense in the anhydrous case.

Comparison of 107 with the spectra of the oxides V_2O_3 (128), V_2O_5 (129) and V metal (133) indicates, again, that vanadium oxides of the kind present in the model samples are registered.

The spectrum and difference spectra obtained by using oxidized unreacted VB_2 (111) is shown in Figure 41. The spectrum at the top of the figure serves as a reference. Comparison with 116 (air-exposed, reacted VB_2) shows predominant intensity in the oxygen peak at lower binding energy. The 531 eV oxygen peak of primary intensity corresponds to a kind of oxide not present in 111. Comparisons with V_2O_3 (128), V_2O_5 (129) and V metal (133) again show the inappropriateness of using the model compounds as a basis for analysis. The same conclusion applies to the Flood Gun off experiments shown in Fig. 42.

Differential charging experiments with anhydrous passivated VB_2 are shown in Fig. 43. The uncharged case is shown as 117. The difference spectrum

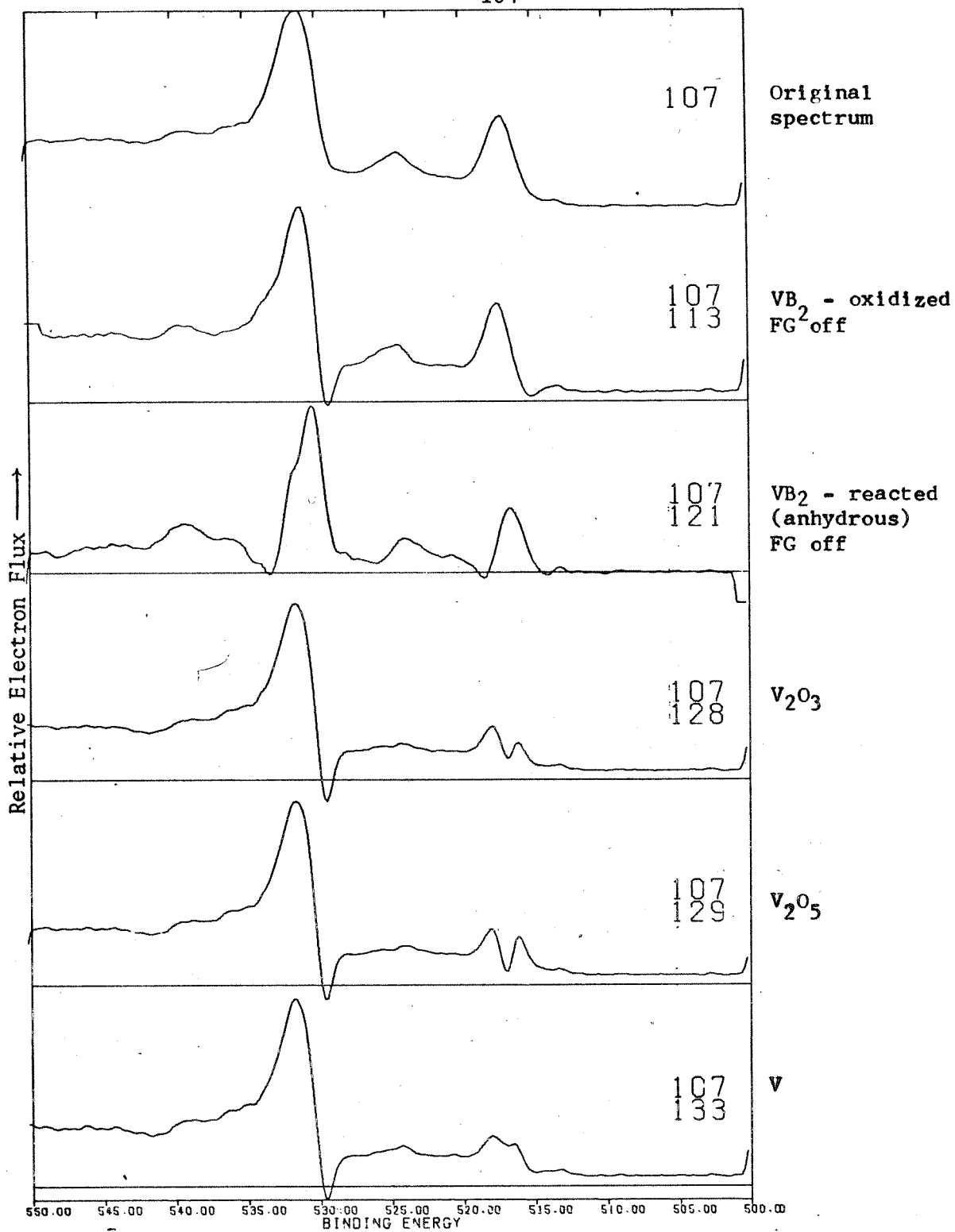


Fig. 40 Difference analysis of V-O region of reacted VB_2 (FG off) exposed to H_2O by comparison with spectra identified along ordinate

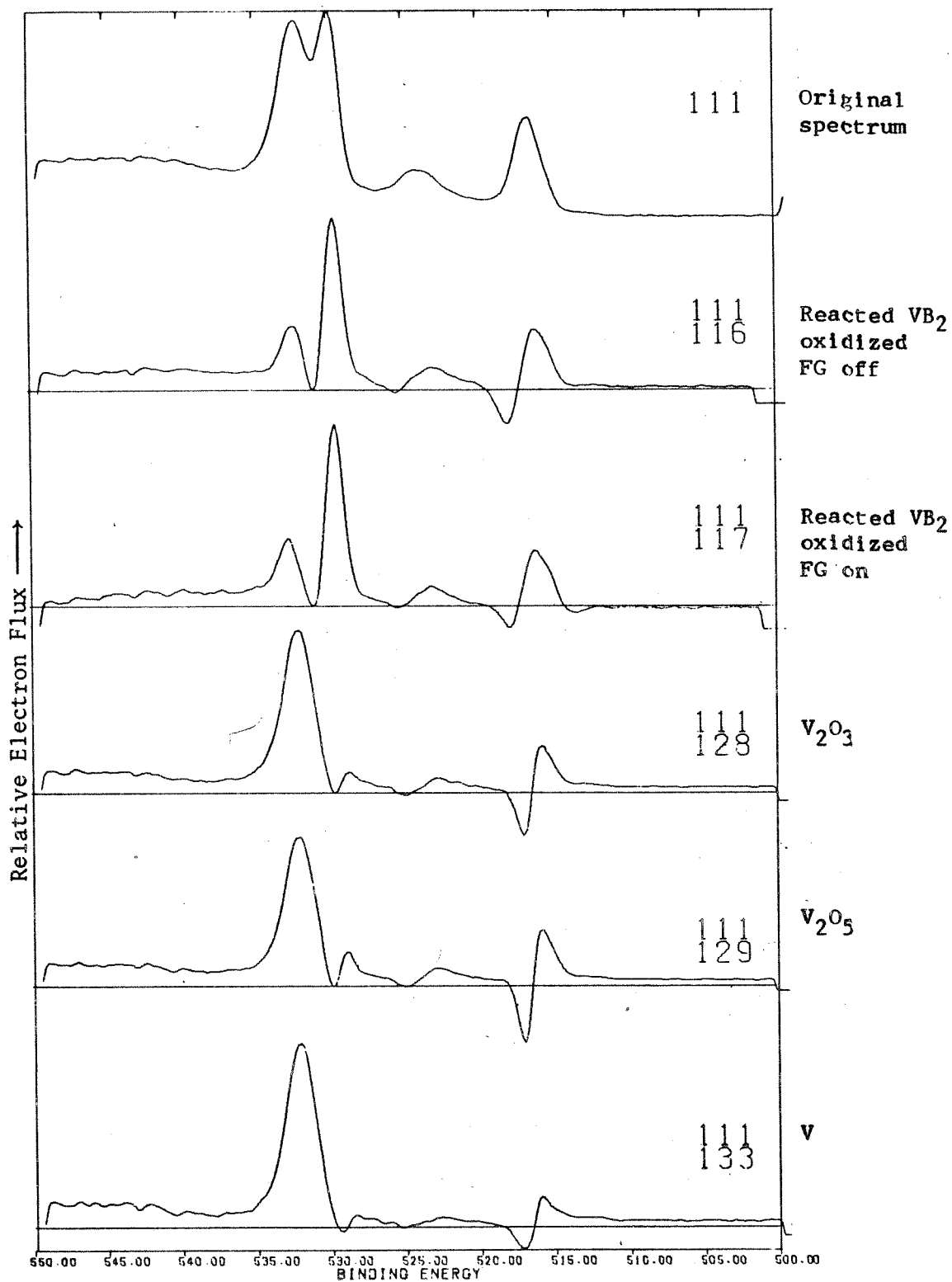


Fig. 41 Difference analysis of V-O region of air-oxidized VB_2 (FG on) by comparison with spectra identified along ordinate.

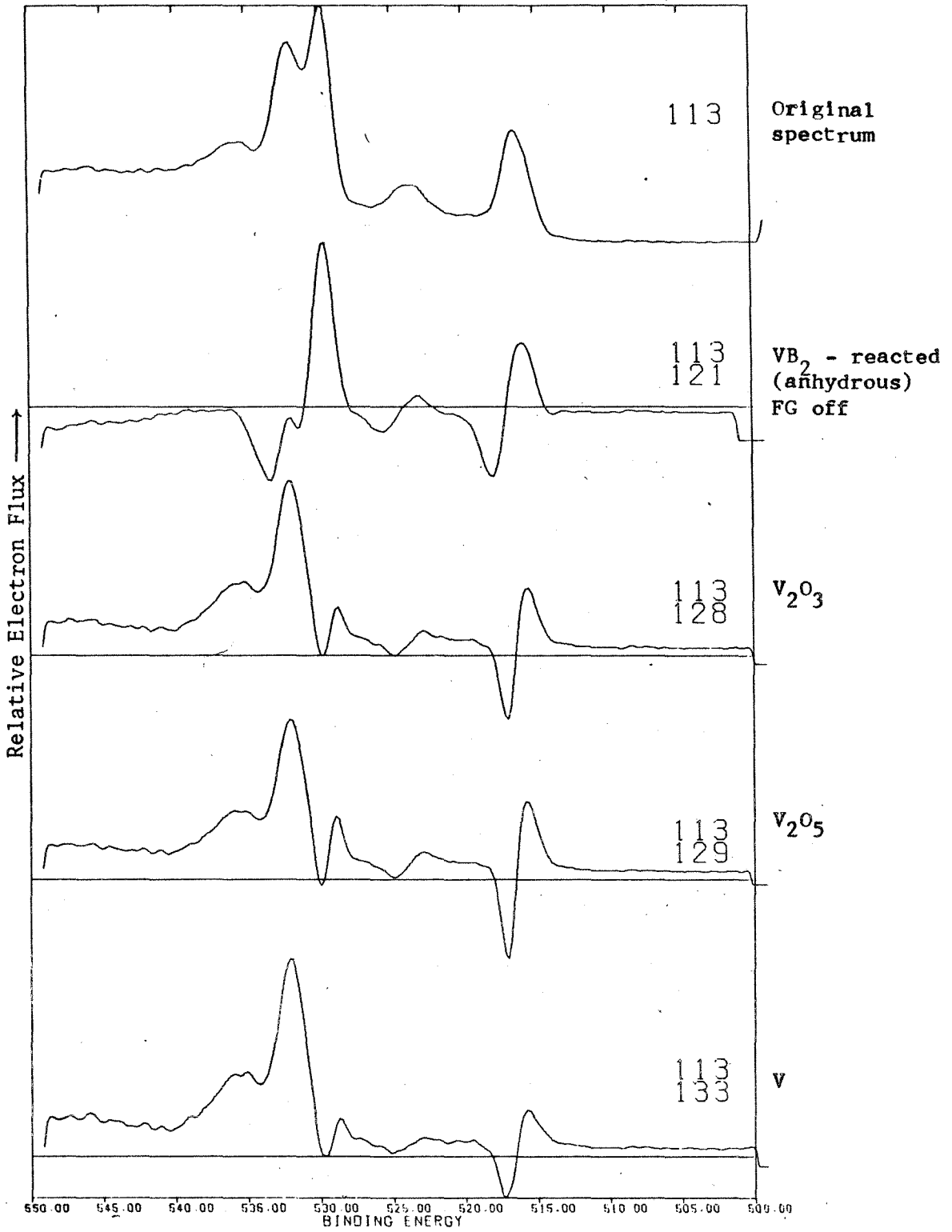


Fig. 42 Difference analysis of V-O region of air oxidized VB₂ (FG off) by comparison with spectra identified along ordinate.

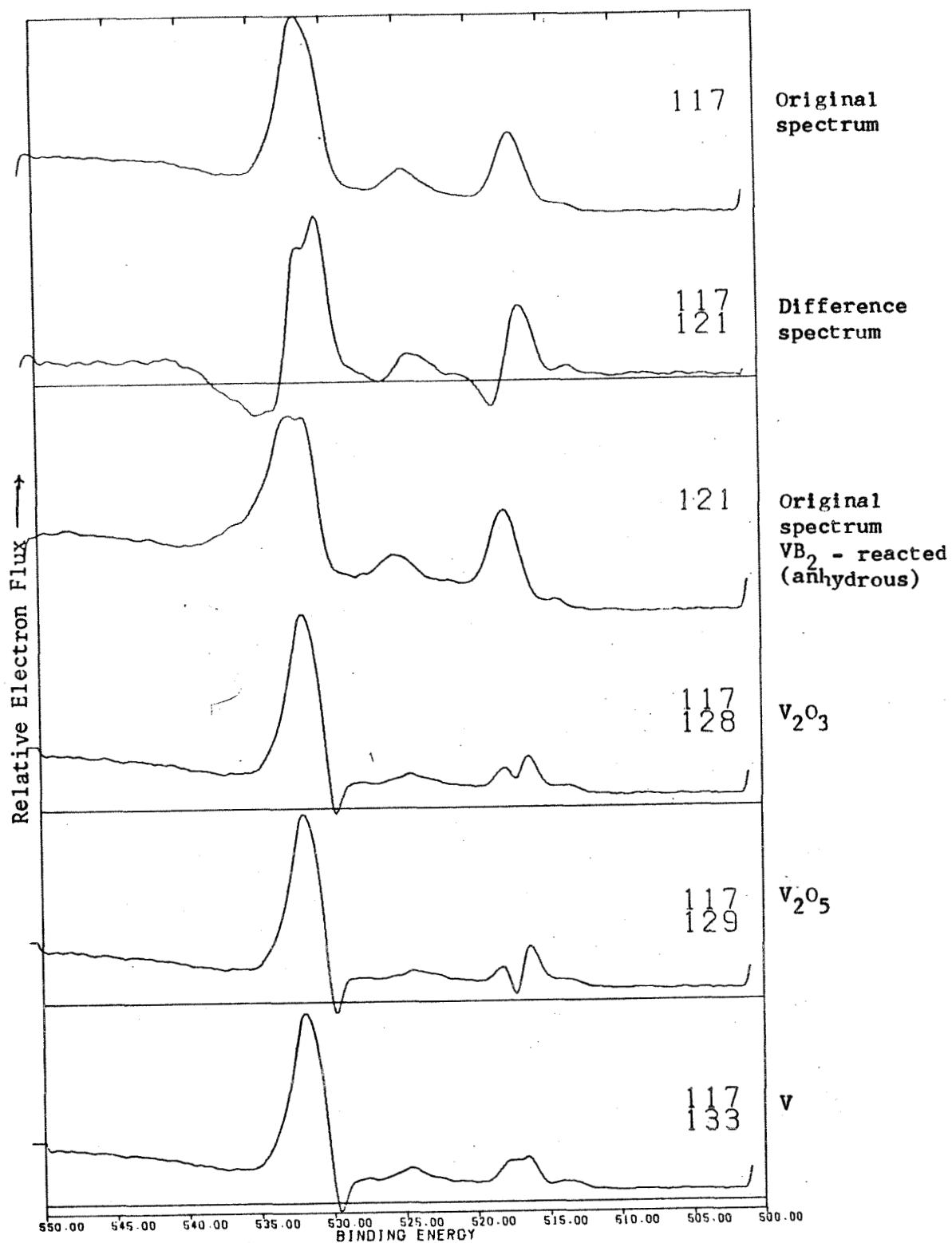


Fig. 43 Difference analysis of V-O region of reacted VB_2 (FG on) which has been air-oxidized by comparison with spectra identified along the ordinate.

117-121, implies voltaic shifts in the vanadium species. Integration of the areas under the curves indicates that fewer electrons are being emitted in the FG off case as well, although the magnitude of the noise indicates that the actual amplitude of 117-121 is small. Enhancement of the vanadium peak at 513.3 assignable to VB_2 indicates that the VB_2 is immersed in or otherwise in contact with the vanadium domains which are electrically isolated from the bulk specimen.

Comparison of 117 with the model compounds indicates that the surface of reacted VB_2 predominately consists of stoichiometric oxides whereas freshly prepared material does not.

Figure 44 shows that no significant charging effect occurs in vanadium nitride on its surface oxide.

Enhancement of the spectra made possible by using the model compounds as references for the line shape of surface oxides is sharply demonstrated in the 132 series of difference spectra. The reduction of the oxide peak (in the V 2p region) is evident as is the enhancement of the nitride peak. The remaining oxide peak (O1s region) can be ascribed to a nitrogen-bound oxide which is indicated in the nitrogen spectrum in which two distinct peaks are observed at 401.2 eV and 396.8 eV. It appears from Fig. 44 that the oxide occurring on the surface of VN is similar in composition to that occurring on the surface of vanadium metal.

The surface oxide of vanadium metal is compared to V_2O_3 (128) and V_2O_5 (129) in Fig. 45. Both of these oxides give similar results suggesting that the surface of vanadium metal consists of a complex mixture of a large variety of oxides.

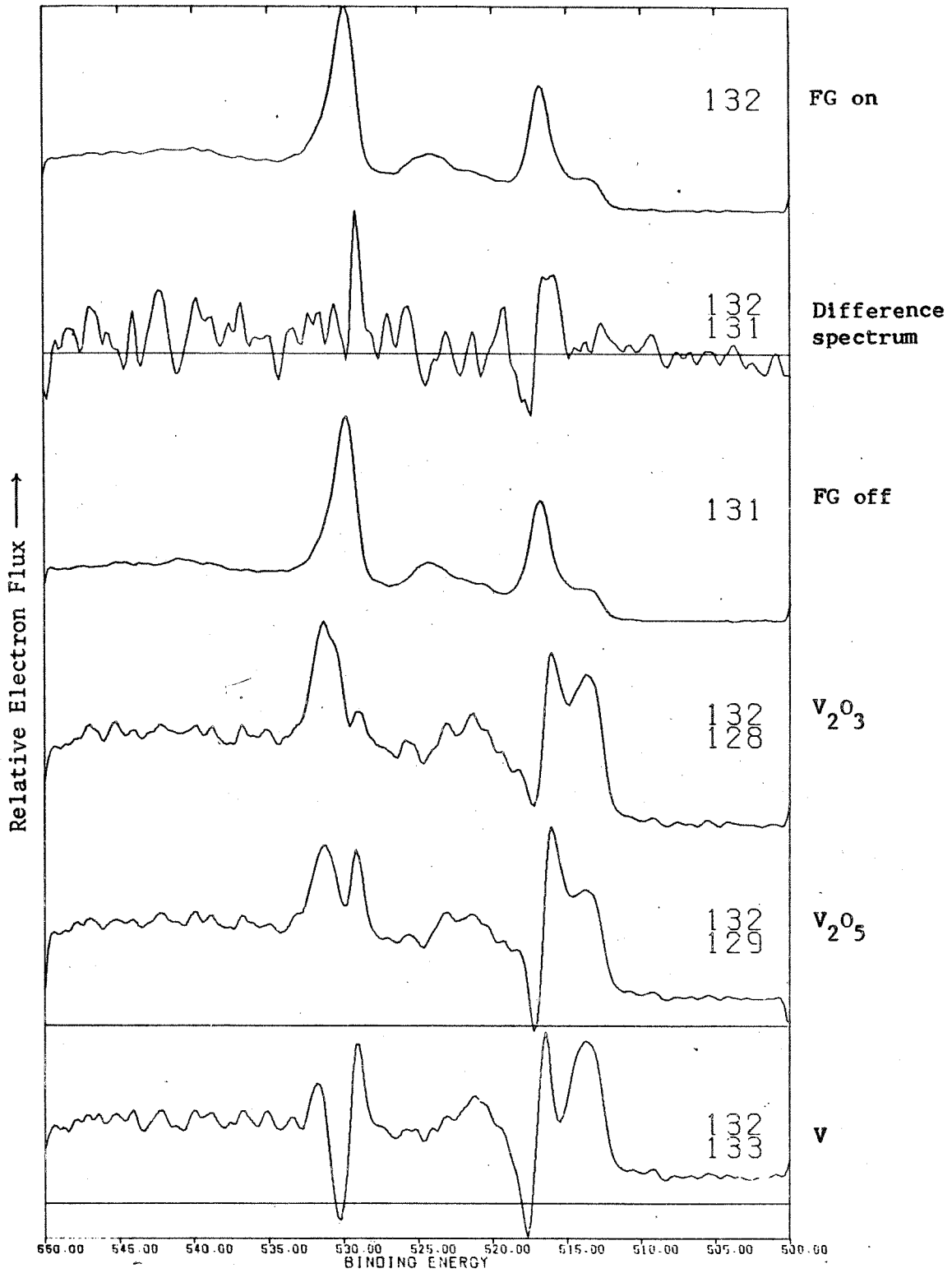


Fig. 44. Difference analysis of V-O region of vanadium nitride by comparison with spectra identified along ordinate.

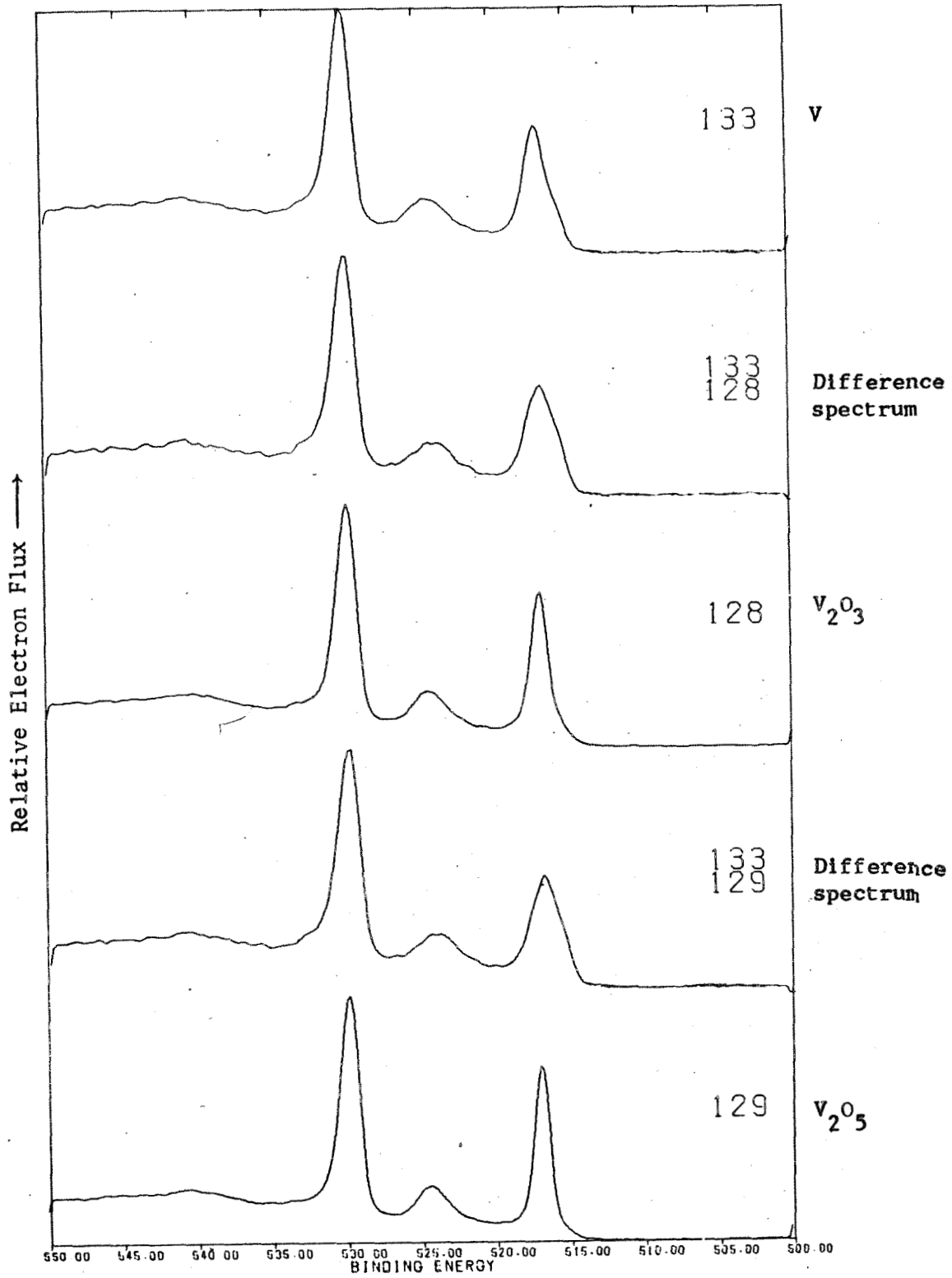


Fig. 45 Difference analysis of V-0 region of various vanadium surface oxides

Figure 46 shows difference spectra obtained by using the salt Na_3VO_4 (136). The sodium auger line is enhanced. The separation in core level binding energies between the $01s$ peak and the $V2p$ line in V_2O_3 (128) and V_2O_5 (129) differs from that of the vanadate. A similar line separation is observed on vanadyl sulfate (134).

In the study of a number of other boron compounds, a peak was consistently observed in the region of 192.2 eV. Boron metal gives rise to a line at 188.0 eV. Similar peaks were observed in the spectra of different VB_2 samples. Other investigators^{73,74,75} have assigned the boron $1s$ peak at 192.2 ± 0.1 eV to boron oxide species. All of the boron oxides studied in this work have shown an oxygen $1s$ peak at 531.6 ± 0.1 eV above the boron $1s$ line assigned to oxidized boron. Thus, it seems reasonable to assume that the line at 531.6 eV originates from boron oxide.

Similarly, the $01s$ peak at 529.8 ± 0.2 eV in the vanadium diboride spectra can be assumed to arise from vanadium oxide. This assumption is consistent with previous work^{67,68,69,70,71,74,76}.

The observation of the charging shift in VB_2 and its disappearance upon oxidation is suggestive as regards previous work on systems relevant to

-
73. Hendrickson, D.N., Hollander, J.M., and Jolly, W.L., Inorg Chem, **9**, 612 (1969).
 74. Mavel, G., Escard, J., Costa, P., and Costaing, J., Surface Science, **35**, 109 (1973).
 75. Allison, D.A., Johansson, G., Allan, C.J., Gelius, U., Siegbahn, H., Allison, J., and Siegbahn, K., Journal of Elect Spectroscopy and Related Phenomenon, **1**, 269, (1973).
 76. Hamrin, K., Johansson, G., Gelius, U., and Nordling, C., J. Chem Phys Solids, **32**, 2669 (1970).

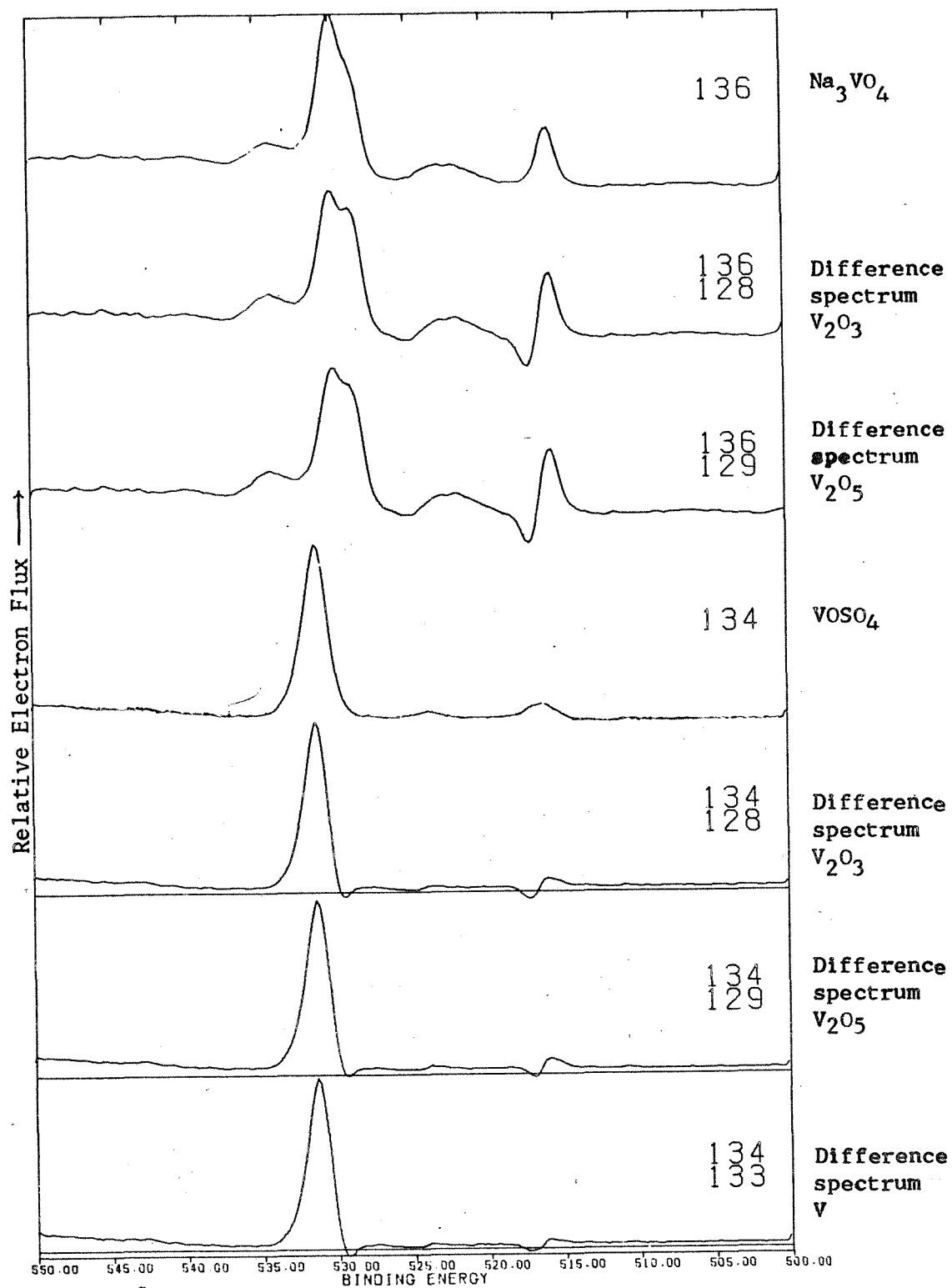


Fig. 46 Difference analysis of V-O region for various vanadium oxide spectra

vanadium oxide catalysts⁷⁷. The spectra of powder samples of V_2O_3 and V_2O_5 (both semiconductors) taken in the course of this thesis showed no charging shift.

Close inspection of Fiermans' published data⁶⁸ on V_2O_5 indicated a shoulder at higher binding energy on reduced V_2O_5 samples. Conversations with H. Weaver (co-author with Honig) at Hewlett-Packard brought to light that some of Honig's results⁶⁷ on V_2O_3 had been irreproducible.

At this point, several samples of V_2O_3 were prepared by vigorous grinding in an agate mortar. The preparation was immediately pelletized and introduced into the spectrometer. Charging shifts of O1s peaks were now observed, although of lower magnitude than those observed in VB_2 .

Samples of V_2O_5 were then reduced as described in Ref. 68, then re-examined and again the charging shift was encountered. Freshly ground V_2O_5 samples gave similar results.

The quantitative aspects of electron spectroscopy were developed at some length in Chapter II. To summarize, the area under a photoelectron peak and above the baseline is proportional to the concentration of the emitter. The efficiency of capture of x-ray photons (photoelectric cross-section) is a function of the atomic number and the angular momentum of the electron. The functional dependence of photoemission sensitivity on Z renders estimation of relative intensities of photoelectron lines most difficult.

77. The flood gun accessory is a relatively new development in the field of electron spectroscopy having only been available since Dec., 1972 on the HP SID spectrometer. Previous work on this instrument would give results reported in this thesis as FG off data. Discrepancies between this and data from other spectrometers were often relegated as spurious.

Wagner²⁴ catalogued the sensitivities of the elements for photoemission relative to a Fluorine 1s standard. The data were shown to be amenable to linear regression analysis for each angular momentum. Least-squares lines for each group were plotted as shown in Figure 3. To a first approximation, the regression lines appeared to override the variations in the data anticipated from the widely varying samples used in Wagner's study.

For oxygen, vanadium, and boron, relative sensitivities of 0.65, 1.5, and 0.135 can be estimated from Fig. 3. Thus, the area of a photoelectron line from oxygen 1s, vanadium 2p or boron 1s has to be scaled by $\frac{1}{0.65}$, $\frac{1}{1.5}$, $\frac{1}{0.135}$ before it can be used for quantitative comparison of line intensities.

The area under each photoelectron peak was determined in a number of these spectra by means of a K & E planimeter. The measurements were reproducible to $\pm 2\%$. The different parameters used in the accumulation of the data were normalized to 256 channels with 10 scans at 1 eV/sec. Graphical data was normalized for interpretation to 1K counts per electron volt. These data were then multiplied by the sensitivity ratios cited above and are listed in Table 5. The observed ratios are given based on a relative intensity for the vanadium $2p_{3/2}$ line of 10 units.

These intensities are then listed for O1s, $V2p_{3/2}$, and B1s lines together with each compound. Ratios are calculated for O/V, O/B and V/B.

We see that the O/B ratios for the boron model compounds average 2.5 ± 0.1 . Consequently, a column has been added to the VB_2 group in which the signal intensity of the boron 1s line (multiplied by 2.5) is subtracted

TABLE 4
OBSERVED BINDING ENERGIES USED FOR THE VB_2 INVESTIGATION

Compound	Spectra #	O1s BE(eV)	Comment	Spectra #	$\text{V2p}_{3/2}$ BE(eV)	Comment	Spectra #	Bi s BE(eV)	Comment
V_2O_5	(129)	529.9	538.8(sh)	(129)	516.9				
V_2O_5 (Red)	(351)	530.0	531.2(sh)	(351)	516.8	515.8(sh)			
$\text{VO}(\text{OH})$ (oxinate) $_2$	(312)	531.1		(312)	517.0				
Na_3VO_4	(136)	530.0		(136)	515.6				
VO Cl_2	(317)	531.5	532.3(sh)	(317)	516.8				
$\text{VO}(\text{pc})$	(316)	532.1		(316)	516.6				
VO SO_4	(134)	531.3	530.0(sh)	(134)	516.3				
$\text{VO}(\text{oxinate})_2$	(313)	530.2		(313)	515.9				
$\text{VO}(\text{AcAc})_3$	(315)	529.8		(315)	515.4				
$\text{V}(\text{AcAc})_3$	(318)	530.0		(312)	514.4				
V_2O_3	(128)	529.8		(128)	517.0				
VB_2 -Fresh	(103)	532.1	529.7	(103)	516.4		(104)	192.5	187.7(ch5)
VB_2 -Reacted (H_2O)	(107)	531.8	531.2(sh)	(107)	517.3		(108)	192.3	188.8(sh)
VB_2 -Oxidized	(113)	532.0	529.7	(113)	516.5	518.2(sh)	(114)	192.2	

TABLE 4 (Continued)

Compound	O1s		Comment	Spectra #	V2p3/2 BE(eV)	Comment	Spectra #	B1s	
	Spectra #	BE(eV)						BE(eV)	Comment
VB ₂ -Reacted (Anh)	(121)	531.6	532.7(sh)	(121)	517.8		(120)	192.9	
VB ₂ -Reacted (ox)	(116)	532.0	531.0(sh)	(116)	517.2				
VN	(132)	529.8	531.5(sh)	(132)	516.9(ox)	513.5(N)			
VC	(331)	529.9		(331)	515.2				
V _{metal}	(133)	529.8		(133)	513.5				
B ₂ O ₃	(158)	531.6					(160)	192.3	
H ₃ BO ₃	(350)	531.7					(349)	192.2	
Na ₂ B ₄ O ₇	(157)	531.5					(153)	192.3	
B _{Amor}	(265)	531.0	531.3(sh)				(267)	188.0	192.2 (small)
B _{Amor} + Glacial Acetic Acid	(349)	532.1					(346)	192.6	
BN	(360)	529.8					(362)	190.2	
BC	(369)	526.4					(367)	186.7	

TABLE 5 PEAK AREAS NORMALIZED FOR PHOTOELECTRON SENSITIVITY USED FOR THE VB_2 PROBLEM

Compound	O1s	V2p	B1s	O/V	O/B	$\frac{0-2.5B}{V}$	$\frac{0-3.5V}{B}$	$\frac{V}{B}$	$\frac{0-2.5B-3.5V}{V}$
VB_2 Fresh-On	176.6	10.0	14.4	17.7	12.4	14.1	9.8	0.69	10.5
VB_2 Fresh-Off	179.8	10.0	14.1	18.0	12.8	14.6	10.3	0.71	11.0
	95.1	10.0	9.8	9.5	9.7	7.6	6.1	1.0	3.6
	49.4	10.0	4.3	5.0	11.4	3.9	3.3	2.3	0.4
	35.2	10.0		3.5		3.5			
VB_2 React-On	69.5	10.0	4.4	3.0	15.8	5.8	7.8	2.3	2.4
VB_2 React-Off	77.4	10.0	3.2	7.7	24.2	6.9	13.3	3.1	3.4
VB_2 Ox-On	77.7	10.0	8.3	7.8	9.4	5.7	5.2	1.2	2.2
VB_2 Ox-Off	90.0	10.0	4.6	9.0	19.6	7.9	11.9	2.2	4.4
$Na_2B_4O_7$	24.5		10.0		2.5		2.5		
B_2O_3	24.1		10.0		2.4		2.4		
B_{Amor}	26.0		10.0		2.6		2.6		
V_2O_3	36.0	10.0		3.6		3.6			
VN	25.1	10.0		2.5		2.5			
Vmetal	36.5	10.0		3.7		3.7			

TABLE 5 (Continued)

Compound	O1s	V _{2p}	B _{1s}	O/V	O/B	$\frac{0-2.5B}{V}$	$\frac{0-3.5V}{B}$	$\frac{V}{B}$	$\frac{0-2.5B-3.5V}{V}$
V ₂ O ₅	34.2	10.0		3.4		3.4			
V ₂ O ₅ (Butene red)	64.2	10.0		6.4		6.4			
V ₂ O ₅ (UHV red)	74.6	10.0		7.5		7.5			

from the oxygen intensity and then divided by the vanadium signal. This is consistent with the assignment of the B1s peak at 192.2 eV to a boron oxide.

The model spectra for vanadium can be considered in two major groups. The first of these includes V_2O_3 , V_2O_5 , VN and V_{metal} where average V/O ratio of 3.6 is observed. The value of 2.5 for VN can be rejected because vanadium nitride and vanadium oxide could not be separated completely in the observed spectrum (Fig. 34, spectrum 132). The spectra from reduced V_2O_5 form the second group.

Note that reduction of V_2O_5 increases the O/V ratio to exceed that of the fully oxidized parent compound. UHV reduction, which basically involves loss of oxygen from the surface, results in still higher O/V ratios.

Clearly, one of the two following explanations may apply to this observation: (1) With reduction, the electron transmission of the oxide changes and more electrons from deeper levels are seen at the analyzer. This implies considerable interaction of photoelectrons with the electrons bound in the lattice. In view of the similarities of the kinetic energies of the vanadium 2p and the oxygen 1s photoelectrons, such transmission enhancements should effect both oxygen and vanadium lines equally, yet the O/V ratio has been observed to change.

(2) The observed increase in oxygen intensity is due to the chemisorption of CO and/or H_2O from the spectrometer atmosphere onto the vanadium oxide surfaces. Fig. 6 gives a mass spectrum of the atmosphere within this electron spectrometer. It is seen that H_2O and CO are major atmospheric constituents, with their partial pressures in the range of 10^{-9} torr.

It is known that catalysts must provide bound sites on the surface for heterogeneous activity. Chemisorbed species are bound on metal oxides by covalent, ionic, or Van der Waals forces. The author suggests that a figure of merit for a catalytic surface is the existence of a structure whose atoms can donate or accept charge from physically adsorbed species. This electron donation can result in bond formation with the adatom reducing its activation energy for chemical attack by other adatoms on the same surface.

The degree to which this electron transfer is accomplished is of crucial importance for catalysis. The surface layer must have the properties of a semiconductor.

When such surfaces are formed on a compound exposed to the atmosphere inside the spectrometer, chemisorption occurs and reaches rapidly a certain limiting value. The observed binding energy of the adsorbed species is higher than the binding energy of the oxide of the surface. This may indicate that the charge distribution of the oxygen atom of the adcompound within its electronic core is very similar to that of the surface oxide. Bound and activated CO or H₂O is then electronically intermediate between the adatom and the host lattice. This model contends that catalysis and reactivity is imaged by this rapid oxygen uptake and change in the O/V ratios observed in the electron spectrum.

The observed charging effect is a property of the reactive reduced oxide which is a semiconductor having an impedance greater than 10⁹ ohms.

Turning back to the VB₂ section of Table 5, it can be seen that fresh VB₂ has higher O/V ratio than the model oxides. Note that the O1s peak at low

binding energy observed in VB_2 with Flood Gun off can be assigned to a stoichiometric vanadium oxide. Note further that the passivated VB_2 shows lower O/V ratios than the fresh material and that oxidation of fresh VB_2 increases the amount of vanadium (reduces the amount of oxygen) in the observable region.

The passivation of VB_2 can now be discussed in terms of the observed data. The most striking aspect of the difference between reactive and passivated VB_2 is to be found in the charging effect experiments. Reactive VB_2 shows a significant charging effect in which a material with peaks in the O1s, B1s, and C1s regions of the photoelectron spectrum are displaced toward a higher binding energy by identical amounts. Little charging is observed in the V2p region of the spectrum. The oxygen/vanadium ratios in the spectrum of the reactive material are quite different from those observed for model vanadium oxides. The spectrum of the unreactive material shows no charging shift and the O/V ratios are much smaller. A new vanadium species at higher binding energy is observed in the passivated material when compared to the fresh VB_2 compound. The reacted material also shows evidence of the presence of elemental boron on the surface of the particles. Both the reactive and the passive VB_2 compounds are totally oxidized on their surfaces (probably to a depth greater than 70\AA). This surface is predominantly a boron oxide phase mixed with a complicated series of vanadium oxides.

Passivation of VB_2 can then be ascribed to the depletion of the reactive (charging) vanadium oxide which was present in fresh VB_2 . These spectra indicate that exposure of fresh VB_2 to oxygen will result in passivation of the material. They further suggest that the active reagent in the

synthesis of carboxylate dimers may actually be the insulating vanadium oxide. It is suggested that freshly ground V_2O_3 , V_2O_5 or vanadium oxides prepared in a reducing atmosphere would serve as good starting materials for this synthesis.

Finally a statement about the complexity of this problem. As was mentioned, all samples studied here were heavily oxidized. Back-sputtering methods (argon ion bombardment) could have been used to scrub the surfaces and thereby simplify the VB_2 problem. However, the author has observed reduction of iron oxides by sputtering (selective ejection of lighter elements). Oxidation by Ar^+ has been observed by other workers. Either of these processes would have added additional complication. Back-sputtering was not feasible in this experiment because of the use of pelletized powder samples.

The overwhelming majority of the spectroscopic work in the field of catalysis is based on Auger-Electron Spectroscopy. Here, the surface is irradiated by a high-energy electron beam and the kinetic energy distribution of the resulting Auger electrons is determined.

This technique imparts considerable energy to the surface of the sample and could raise the temperature or internal energy of the surface to a point where the chemisorbed species could be desorbed from the lattice. These electron currents can also reduce or oxidize the surface oxides thereby changing the electronic structure of the compound. Since the Auger work reported to date has seen much different oxygen and vanadium ratios than those reported by XPS, one can conclude that the electron excited experiment is perturbing the surface. Thus, a different structure

exists when the compound is observed by Auger electron spectroscopy and the adsorbed species is not found. The inappropriateness of Auger spectroscopy in this work is suggested.

VI. COPPER METALLOPROTEINSA. Introduction

Considerable insight into the biochemical behavior of metalloproteins has been gained by studying the structure and function of the active sites containing transition metals. It has been especially fruitful to compare the magnetic, electronic and kinetic properties of these with those of model complexes.

Because of the complexity and size of the metalloproteins and their susceptibility to denaturation, it has been difficult for crystallographers to get a firm handle on the functional details of the active sites.

In some cases, the valency of the metal ion can be estimated by means of optical, paramagnetic and electrochemical measurements. So far, these have mostly provided ambiguous results. It seems that ESCA is a superior tool to study the effect of the environment on the valence state of the transition metal.

This chapter details the application of ESCA in particular to the study of Laccase and Hemocyanin, both containing copper at the active site.

The electronic structure of copper-containing proteins has been treated in a number of recent reviews^{9,11,78,79}. Three chemically different types of copper have been found⁷⁸: (1) An EPR detectable cupric ion which is responsible for the intense blue color (Type 1); (2) an EPR detectable

78. Malkin, R., and Malmstrom, B.G., Adv in Enzymology, 33, 177 (1970).

79. Vallee, B.L., and Wacker, W.E.C., "The Proteins", H. Neurath, ed. Vol. V., Metalloproteins, 2nd ed., Academic, N.Y., (1970).

cupric ion with a low extinction coefficient compared to blue Cu^{2+} which is referred to as "non blue" (Type 2); and (3) a form not detectable with EPR (Type 3).

Type 3 is present in the oxidases and in Hemocyanin, an oxygen transport protein. This 2-electron transfer site containing two copper atoms does not contribute to the magnetic susceptibility of the protein, but manifests itself by an absorption of 330 nm radiation. In Laccase it has been described as a dimeric Cu(I) or spin paired 2Cu(II) center^{78,79,80} and is subject to much controversy.

The electron spectra of the "blue" copper proteins, Stellacyanin and Plastocyanin, have been studied to find more detailed information as to the nature of the diamagnetic site. The "Rhus Blue Protein", Stellacyanin, isolated from the Japanese lacquer tree⁸¹, is a copper protein of 16,800 gm molecular weight with one Type 1 copper per molecule. The optical and magnetic properties as well as the circular dichroism of this electron-carrier protein are consistent with a highly-asymmetric binding site of copper.

Plastocyanin, likewise, is a copper protein. It is present in the chloroplasts of plants and algae and is not auto-oxidizable. This protein contains 2 Type 1 copper atoms per 21,000 gm molecular unit, and has been

80. Byers, W., Curzon, G., Garbett, K., Speyer, B.E., Young, S.N., and Williams, R.J.P., Biochem and Biophys Acta., 210, 38 (1973).

81. Omura, T., J. Biochem (Tokyo), 50, 264, and 389 (1961).

proposed to serve as an intermediary in the electron transfer of chloroplasts^{82,83,84}.

The "Blue oxidase", Laccase, contains 4 copper atoms per 120,000 molecular weight. This enzyme is present in several plants and fungi; the samples used in this work were taken from *Rhus vernicifera*^{85,86}. Of the 4 copper atoms per molecule, one is of Type 1, one of Type 2, and two of Type 3, forming the diamagnetic center.

The study of the copper $2p_{3/2}$ electron spectrum of the cupric Type 1 atom in Stellacyanin and Plastocyanin is used in this report to establish the part of the spectrum of Laccase that corresponds to the Type 1 site.

The author presumed that the spectra of Type 1 and Type 2 copper are very similar. Thus, subtraction of a cupric Type 1 spectrum from the spectrum of Laccase should give a representation of the Type 3 copper site.

As was mentioned previously, the Type 3 copper site is also present in the oxygen transport protein, Hemocyanin. This blue protein is found in the hemolymph of several mollusks and has a molecular weight of 3,750,000.

82. Katoh, S., Nature, 186, 533 (1960).

83. Katoh, S., Shiratori, I., and Takamiya, A., J. Biochem (Tokyo), 51, 32 (1962).

84. Blumberg, W.E., and Peisach, J., Biochem Biophysics Acts, 126, 269 (1966).

85. Mosbach, R., Biochem Biophys Acts, 73, 204 (1963).

86. Reinhammer, B., Biochem Biophys Acta, 205, 35 (1970).

87. Hemmerich, P., in Oxidases and Related Redox Systems, King, T.E., Mason, H.S., and Morrison, M., eds., p. 216, Wiley, N.Y. (1964).

The molecule can be broken into a number of sub-units of molecular weight of 25,000 to 75,000 with 2 copper atoms per molecule^{88,89}.

Oxyhemocyanin has been described in terms of both Cu^{II} and Cu^I models⁹⁰. Its photoelectron spectrum has been examined in this work and was compared to that of the blue copper proteins.

Recently, extensive work on the photoelectron spectroscopy of a number of copper complexes has appeared⁹¹. This work and concurrent work by the author indicated that cupric and cuprous ions have overlapping ranges of binding energies which make the assignment of oxidation state by the ESCA method very difficult. However, the d⁹ Cu(II) ion gives high-intensity satellite structure in the electron spectrum between the copper 2p_{3/2} and the copper 2p_{1/2} line while no such transitions occur in cuprous complexes. This makes possible a clear distinction between oxidation states. It was also observed that cupric systems underwent x-ray photo reduction to cuprous states.

This observation helps to explain the anomalously low binding energies observed in the only reported x-ray photoelectron spectrum of metallo-proteins^{92,93,94}. Here the copper-containing protein erythrocyprin (2 Type 2 copper per 32,600 gm. molecular weight) was found to have a broad featureless Cu 2p_{3/2} line at 931.9 eV. This work assigns this spectrum to a photo-reduced protein, resulting from radiation damage.

-
88. Boas, J.F., Pilbrow, J.R., Troup, G.J., Moore, C., and Smith, T.D., *J. Chem Soc A* 1969, 965 (1969).
89. Ghiretti, F., ed., *Physiology and Biochemistry of Hemocyanin*, Academic, N.Y., (1968).
90. Van Holde, K.E., *Biochemistry*, **6**, 93, (1967).
91. Frost, D.C., Ishitani, A., and McDowell, C.A., *Molecular Phys.*, **24**, 77 (1973).

In addition to this photoreduction, other radiation damage was observed during room-temperature experiments. In this work, the effect was minimized by operating at lowered temperatures.

A series of copper model complexes with sulfur ligands was investigated for the first time by XPS to establish the details of the satellite structure and to determine the magnitude of the chemical shift for copper.

Finally, the sulfur spectrum of the proteins and various model complexes were studied in an effort to assign the nature of possible sulfur-copper centers. The sulfur spectra are correlated with data presented more extensively in Chapter VII.

B. Experimental

In the course of these studies, four different electron spectrometers were used, the HP 5950A, the JPL-USU spectrometer, the McPherson ESCA 36, and the DuPont 650 electron spectrometer. Most of the quantitative data reported were taken with the HP 5950A described in Chapter III.

The proteins Stellacyanin, Plastocyanin, and Laccase were supplied as buffered (potassium hydrogen phosphate) solutions by R. Holwerda. The basic preparative method for isolating these proteins in high purity from the commercially available extract is described by Reinhammer⁸⁶.

-
92. Jung, G., Ottnad, M., Bohnenkamp, W., Bremser, W., and Weser, U., Biochem Biophys Acta, 295, 77 (1973).
 93. Jung, G., Ottnad, M., Bohnenkamp, W., and Weser, U., FEBS Lett, 25, 346 (1972).
 94. Jung, G., Voelter, W., and Weser, U., Z Physiol Chem, 353, 720 (1972).

R. Holwerda has made extensive modifications of this procedure and his work has recently been described in detail^{94a}. Solutions of Hemocyanin in phosphate buffer were provided by Dr. D. Guttermann. Cu^{I} -n-propylthiouracil, Cu^{II} bis-n-butylthioacetate, 1, 2 di-butylthioethane $\text{Cu}^{\text{II}}\text{Cl}_2$, Cu^{II} di(acetothio)ethane, and $(\text{Cu}^{\text{I}})_2 \text{Cu}^{\text{II}}(\text{penicillamine})_2$ complexes were provided by Dr. H.J. Schugar. Copper acetylacetonate complexes and their derivatives were supplied by J. Swanson. Other copper and sulfur compounds were obtained commercially as analytical reagent grades.

ESCA spectra were taken using two different types of protein samples. One set of experiments used protein which has been "freeze-dried" (water removed by pumping at low temperature). These powdered samples were processed by the techniques referred to earlier as "graphite sandwich" and "gallium-wetted substrate" (see Chapter III). An alternate set of samples were prepared from buffered solutions, which were quickly frozen on gold templates in a nitrogen atmosphere and immediately introduced into the spectrometer, or were evaporated at room temperature onto the gold platens in a nitrogen stream to form thin transparent films.

The spectra taken with the use of the various types of samples differed insignificantly from each other. The most reproducible data and the highest S/N and S/B ratios were obtained with the thin films. All protein spectra shown in the figures were obtained by this method.

94a. Holwerda, R., Ph.D. Thesis, California Institute of Technology, 1974.

The soluble copper model complexes were prepared in the same manner, whereas insoluble samples were used in the form of pellets.

Charging shifts of 2 to 7 eV were observed on protein samples and were compensated by use of the flood gun (0.40 ma, 0.0 eV). All spectra were taken at reduced temperatures (220^oK to 240^oK) to minimize photoreduction of cupric sites. The onset of radiation damage was followed by scanning the Cls spectral region (280-290 eV, 1 eV/sec, 256 channels, 10 scans) repeatedly over a period of several hours. These spectra obtained at 10.5 minute intervals were sequentially dumped on paper-tape and then analyzed using the differential methods described in Chapter V. At room temperature, differences in the carbon spectra were discernible after approximately 21 minutes irradiation with the monochromatized source. Radiation damage decreased as the temperature was lowered to about 240^oK, at which no changes in the spectrum could be observed after 6 hours of irradiation. As the temperature was reduced still further, radiation damage could be observed once again. At 100^oK significant and irreproducible spectral changes occurred after about 21 minutes irradiation. The extent of cupric photoreduction was inversely proportional to temperature down to 190-200^oK, where cuprous species were being rapidly generated. At 150^oK, sharp splittings of Cu 2p_{3/2} lines occurred along with an increased background in the region of high binding energy. This is attributable to greater Auger intensities of oxygen in H₂O, CO, or CO₂ condensed on the sample surface.

The optimum temperature range at which the effect of all these competing factors is reduced is 220^o to 240^oK.

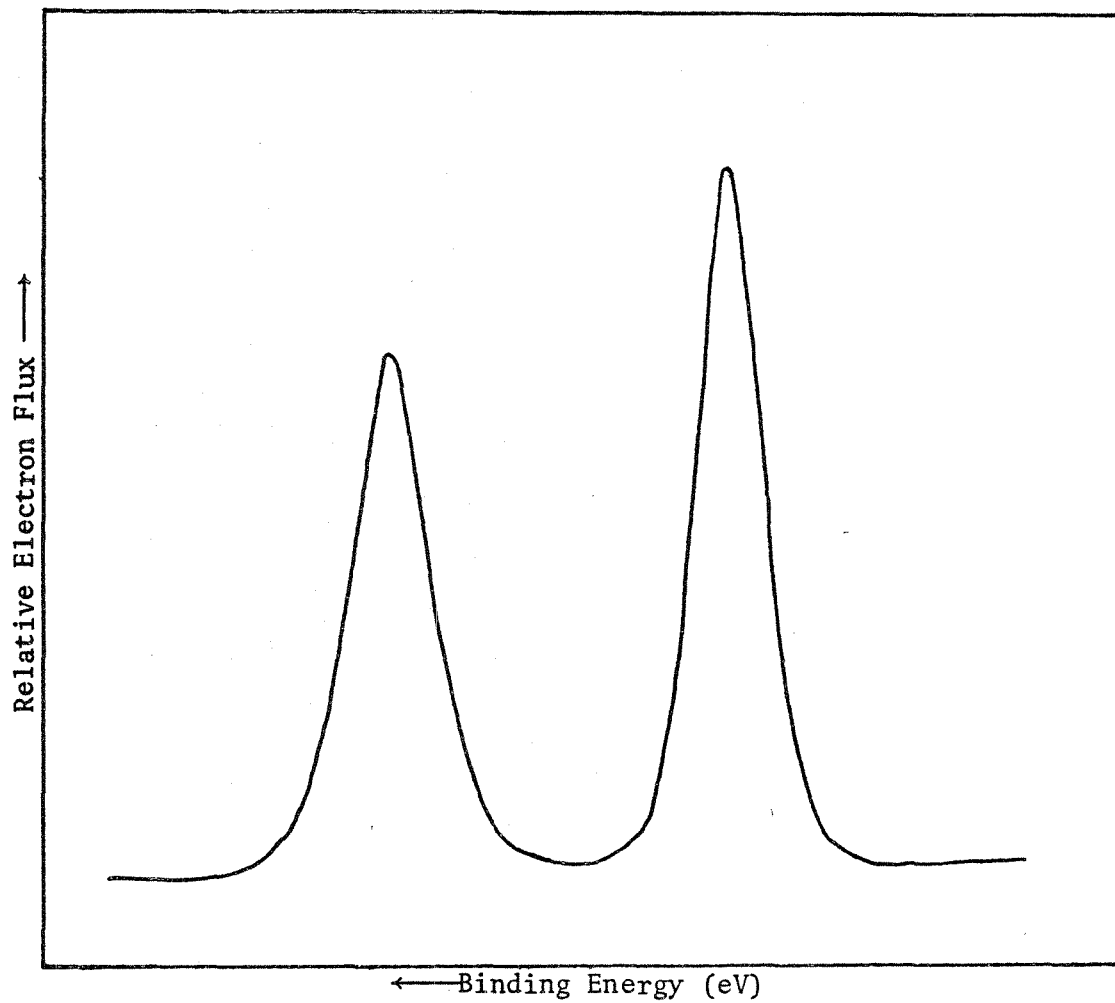


Figure 47. Reference spectrum of gold 4f region recorded on the HP 5950A (50 scans, 10 eV window, 1024 channels, 1 eV/sec).

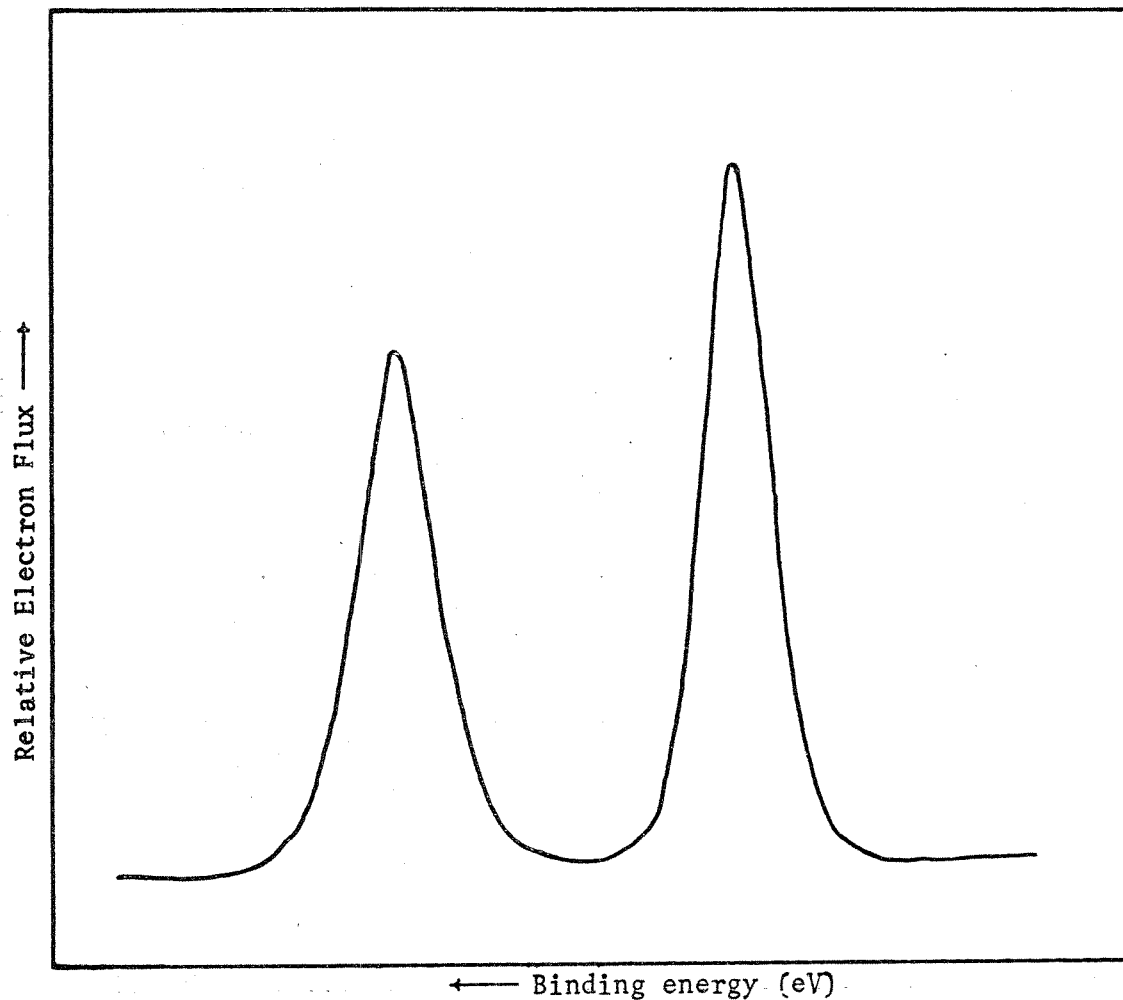


Figure 48. Reference Gold 4f spectrum as recorded by Dupont 310 curve resolver. The line shape is indistinguishable from the original spectrum; see Fig. 47.

All reported binding energies are referenced to the standard gold sample (Au $4f_{7/2}$ @ 84.0 eV, Fermi level @ 0.0 eV). This is internally augmented by the choice of methyl carbon at 285.0 eV and aliphatic carbon at 285.4 eV binding energy, in order to correct for variations in the work function of each sample.

All spectra displayed in this chapter were taken at 1 eV/sec with 256 channels per 10, 20 or 50 eV windows. The plotted data were smoothed through Weiner analysis of the raw curves (1.0 eV FWHM as minimum width). Peak positions and inflection points were determined (using filtered data) by differential convolution described by Savitsky⁵⁴.

A DuPont 310 curve analyzer was used to deconvolve the spectral detail observed in the Cu $2p_{3/2}$ and the S $2p_{3/2}$ regions. The actual line shape observed in monochromated x-ray photoelectron spectroscopy is Lorentzian convolved with a Gaussian function of fixed width (See Chapter II). The most symmetrical line shapes encountered in the course of this work were (1) Au $4f_{7/2}$ line of the gold reference standard; (2) Cls line from ultra-high purity graphite; (3) Silicon 2p doublet from freshly cleaned silicon wafers, and (4) the Cu $2p_{3/2}$ line from Cu(I) n-propyl-thiouracil complex. The gold reference $4f_{7/2}$ line was used as a representative shape in order to calibrate the breakpoints, positional amplifiers and scew parameters for 9 channels on the DuPont 310 Curve Resolver. Figure 47 shows the reference gold spectrum while Fig. 48 shows the resulting line shape programmed into the curve resolver.

TABLE 6 Major Inflections Recorded for the Copper 2p Region

Spectrum Identification Number	187	173	177	191	199	212	213	217	219	220	222	223	229	230	231	232	233	234	552	559	560	566	
	966.0	965.7	965.8																				
		964.6																					
		964.5		964.1	964.0																		
		963.5	963.2	962.9	962.8																		
		962.7	962.6	962.5	962.4	962.3	962.2																
		962.1	962.0	961.7																			
	961.0	960.3	960.4	960.3	960.0																		
	960.0	959.7	959.3	959.1	959.0	959.0																	
	959.0	958.6	958.4																				
	957.6	957.1	957.0	957.5	957.1	957.1																	
	956.6	955.8	955.8	955.9	955.9	955.9																	
	955.1	954.3	954.4	954.1	954.1	954.1	954.1	954.1	954.1	954.1	954.1	954.1	954.1	954.1	954.1	954.1	954.1	954.1	954.1	954.1	954.1	954.1	954.1
	953.0	953.0	952.9	952.9	952.9	952.9	952.9	952.9	952.9	952.9	952.9	952.9	952.9	952.9	952.9	952.9	952.9	952.9	952.9	952.9	952.9	952.9	952.9
	950.8	950.9	950.8	950.5	950.5	950.5	950.5	950.5	950.5	950.5	950.5	950.5	950.5	950.5	950.5	950.5	950.5	950.5	950.5	950.5	950.5	950.5	950.5
	950.0	950.0	949.6	949.4	949.4	949.5	949.5	949.5	949.5	949.5	949.5	949.5	949.5	949.5	949.5	949.5	949.5	949.5	949.5	949.5	949.5	949.5	949.5
	948.8	948.7	948.8	948.4	948.4	948.4	948.4	948.4	948.4	948.4	948.4	948.4	948.4	948.4	948.4	948.4	948.4	948.4	948.4	948.4	948.4	948.4	948.4
	947.7	948.0	947.9	948.0	947.9	948.1	948.1	948.1	948.1	948.1	948.1	948.1	948.1	948.1	948.1	948.1	948.1	948.1	948.1	948.1	948.1	948.1	948.1
	947.4	947.4	947.2	947.2	947.2	947.2	947.2	947.2	947.2	947.2	947.2	947.2	947.2	947.2	947.2	947.2	947.2	947.2	947.2	947.2	947.2	947.2	947.2

Binding Energy (eV) ↑

TABLE 6. CONTINUED

Spectrum Identification Number		167	173	177	191	199	212	213	217	218	219	220	222	223	229	230	231	232	233	234	252	259	260	266	
946.5	947.0	947.0	947.0	947.7	947.0	946.8	946.5	946.2	946.5	946.5	946.6	946.6	946.6	946.9	946.7	946.9	946.7	946.9	946.7	946.7	946.7	946.7	946.7	946.7	946.7
945.5	945.7	945.7	946.0	945.9	945.7	946.2	945.7	945.3	945.7	945.9	945.9	945.9	945.9	945.9	945.9	945.9	945.9	945.9	945.9	945.9	945.9	945.9	945.9	945.9	945.9
944.6	944.1	944.1	944.4	944.2	944.4	944.3	944.2	944.4	944.3	944.3	944.3	944.3	944.3	944.3	944.3	944.3	944.3	944.3	944.3	944.3	944.3	944.3	944.3	944.3	944.3
943.5	943.2	943.2	943.6	943.2	943.2	943.8	943.5	943.5	943.5	943.4	943.8	943.5	943.5	943.5	943.5	943.5	943.5	943.5	943.5	943.5	943.5	943.5	943.5	943.5	943.5
942.6	942.1	942.1	942.6	942.5	942.2	942.2	942.6	942.6	942.5	942.2	942.2	942.2	942.2	942.2	942.2	942.2	942.2	942.2	942.2	942.2	942.2	942.2	942.2	942.2	942.2
940.5	940.1	940.1	940.6	940.2	940.0	940.0	940.2	940.2	940.2	940.2	940.2	940.2	940.2	940.2	940.2	940.2	940.2	940.2	940.2	940.2	940.2	940.2	940.2	940.2	940.2
939.3	939.3	939.3	939.5	939.2	939.5	939.1	939.2	939.2	939.2	939.2	939.2	939.2	939.2	939.2	939.2	939.2	939.2	939.2	939.2	939.2	939.2	939.2	939.2	939.2	939.2
938.5	938.0	938.0	938.0	938.2	938.6	938.6	938.2	938.2	938.2	938.2	938.6	938.6	938.6	938.6	938.6	938.6	938.6	938.6	938.6	938.6	938.6	938.6	938.6	938.6	938.6
935.6	934.9	934.9	935.0	935.1	935.4	935.4	935.1	935.1	935.1	935.1	935.4	935.4	935.4	935.4	935.4	935.4	935.4	935.4	935.4	935.4	935.4	935.4	935.4	935.4	935.4
933.2	933.1	933.1	933.2	933.2	933.2	933.2	933.2	933.2	933.2	933.2	933.2	933.2	933.2	933.2	933.2	933.2	933.2	933.2	933.2	933.2	933.2	933.2	933.2	933.2	933.2
931.2	931.1	931.1	931.1	931.2	931.2	931.2	931.2	931.2	931.2	931.2	931.2	931.2	931.2	931.2	931.2	931.2	931.2	931.2	931.2	931.2	931.2	931.2	931.2	931.2	931.2
930.2	930.3	930.2	930.2	930.2	930.2	930.2	930.2	930.2	930.2	930.2	930.2	930.2	930.2	930.2	930.2	930.2	930.2	930.2	930.2	930.2	930.2	930.2	930.2	930.2	930.2
929.4	929.5	929.5	929.2	929.2	929.2	929.2	929.2	929.2	929.2	929.2	929.2	929.2	929.2	929.2	929.2	929.2	929.2	929.2	929.2	929.2	929.2	929.2	929.2	929.2	929.2

↑ Binding Energy (eV)

TABLE 7, CONTINUED

Spectrum Identification Number		174	188	193	216	503	515	516	519	525	534	538	546	558	564	572	577
164.5	164.4	164.5	164.6	164.6	164.3	164.1	164.4	164.4	164.4	164.4	164.4	164.5	164.4	164.4	164.2	164.2	164.4
163.9	163.7	163.8	163.8	163.8	163.6	163.8	163.8	163.8	163.8	163.8	164.0	163.8	163.8	163.8	163.8	163.8	163.8
163.7	163.3	163.7	163.7	163.6	163.6	163.6	163.6	163.6	163.6	163.7	163.4	163.5	163.1	163.2	163.2	163.2	163.2
162.8	162.4	162.5	162.5	162.6	162.6	162.7	162.7	162.7	162.7	162.8	162.8	162.8	162.8	162.8	162.8	162.8	162.8
162.5	162.4	162.7	162.7	162.6	162.6	162.7	162.7	162.7	162.7	162.8	162.4	162.4	162.1	162.0	162.3	162.0	162.0
162.0	161.9	162.1	162.1	162.1	162.1	162.0	162.0	162.0	162.0	162.0	161.8	161.4	161.6	161.6	161.6	161.6	161.5
161.5	161.7	161.8	161.8	161.6	161.6	161.5	161.5	161.5	161.5	161.5	161.3	161.4	161.1	161.1	161.0	161.2	161.1
161.1	161.1	161.1	161.1	160.9	160.9	160.9	160.9	160.9	160.9	160.8	160.7	160.5	160.8	160.8	160.8	160.8	160.3

↑ Binding Energy (eV)

TABLE 8 Major Inflections for the Oxygen 1s Region

Spectrum Identification Number		157	158	172	190	220	226	265	522	523	535	542	544	551	557	563	570	575
534.7				534.9		534.7			534.4	534.7	534.8			534.9		534.8		534.8
	534.6			534.6	534.5	534.4	534.4		534.4	534.2	534.5		534.3	534.4	534.5		534.6	534.6
		534.4		534.3		534.1			534.0	534.2		534.5	534.0			534.3	534.1	534.1
533.9		534.0		533.9	533.9	533.6	533.6		533.5	533.2	533.5	533.8		533.7	534.0	533.8		533.7
	533.6			533.6		533.2			533.1	533.2		533.2		533.5	533.5	533.3		533.6
533.3		533.1		533.1	533.1	533.2		533.2	533.1	532.9	533.1	533.1		533.2	533.2	533.3		533.1
	532.8	532.7		532.7	532.7	532.6	532.8	532.9	532.5	532.6	532.9	532.1	532.8	532.7	532.9	532.7	532.2	532.2
				532.2	532.4	532.2			532.5	532.5	532.5		532.8	532.7	532.2	532.7	532.6	532.6
532.0	532.1	532.1		531.8	532.1	532.0	532.0	532.2	532.1	532.0	531.8	531.9		532.1	532.2		532.1	532.2
		531.6		531.8	531.7	531.7			532.1	532.0	531.8	531.9	531.6	531.7	531.7	531.8	531.8	531.8
531.2				531.4	531.4	531.5		531.2	531.0	531.4	531.2	531.2	531.2	531.3	531.3	531.4	531.2	531.4
				531.1	531.1	531.1	531.1	531.0	531.0	531.4	531.2	531.2	531.2	531.0	531.2	531.1	531.2	531.1
				530.7	530.8	530.6	530.7	530.8	530.8	531.0	530.8	530.8	530.6	530.6	530.8	530.9	530.9	530.7
530.4		530.4		530.4	530.4	530.2	530.2	530.2	530.2	530.5	530.4	530.2	530.2	530.2	530.2	530.2	530.4	530.4
	530.0	530.1		530.0	530.0	530.1	530.1	530.0	530.0	530.2	530.0	530.2	530.1	530.1	530.0	530.1	530.0	530.0
				529.9		529.8				530.0	530.0	530.2	530.1	529.8	530.0	529.9	530.0	530.0

TABLE 9, CONTINUED

Spectrum Identification Numbers →

	124	125	126	127	140	164	171	176	189	194	214	215	219	227	230	502	508
288.03		288.16							288.17	288.15		288.05					
			287.97				287.98			287.80			287.85	287.92	287.90		287.85
287.68	287.76	287.79	287.62	287.67	287.77		287.68				287.52	287.58	287.50		287.42	287.48	287.51
	287.48						287.44										
		287.35							287.27	287.28			287.17	287.13			287.08
	287.11		287.25	287.17	287.20												286.99
286.88			286.83				286.98	286.97		286.85	286.90			286.88	286.78		286.80
	286.66	286.58				286.73						286.68				286.62	286.52
286.53			286.47				286.48	286.42					286.47		286.45		140
	286.33		286.33	286.37					286.25	286.33				286.32			286.62
286.20		286.17					286.13										286.13
	286.03							286.00			286.07	286.07	286.02	286.03	286.03		186.18
			285.80			285.95				285.82	285.83				285.82		
285.71			285.75				285.70					285.75	285.70				285.71
						285.62					285.65				285.60		
	285.50						285.55										
		285.47					285.43	284.42					285.43		285.47	285.43	
			285.35				285.39		285.37	285.35				285.36			285.37
285.23		285.29	285.27									285.27	285.20		285.25		
	285.11													285.15			
						285.02						285.00			285.00		
							284.95	284.93	284.95					284.90		284.94	284.91

↑ Binding Energy (eV)

TABLE 9, CONTINUED

Binding Energy (eV) ↑	Spectrum Identification Number →																
	124	125	126	127	140	164	171	176	189	194	214	215	219	227	230	502	508
284.88							284.82				284.83						
	284.75		284.77	284.75	284.75								284.73		284.73		
		284.65						284.60						284.63			
284.58									284.57								
	284.40		284.44		284.42										284.42		284.45
284.31							284.38			284.35							
							284.22	284.27					284.20			284.23	
	284.11	284.19							284.15					284.18			284.14
								284.03									
283.98		283.90		283.95				283.90							283.90		
	283.71		283.87		283.88		283.78		283.75								
		283.54		283.55	283.53		283.50	283.57			283.65			283.67			283.62
			283.45														
283.31	283.35														283.32		
							283.27			283.23							
				283.15	283.10	283.12		283.10									
283.01									283.00					283.00			
		282.99															
	282.86																
			282.75														
				282.65	282.63	282.62	282.65										
282.53									282.58								
	282.30			282.30													
		282.22															
282.15								282.18	282.10								
	282.01		282.02														
				281.98													
281.81								281.73									
	281.68																
		281.40															
	281.35			281.30													
	281.25																
	280.90			280.99													
			280.74														
			280.30														

TABLE 9, CONTINUED

Spectrum Identification Numbers →														
510	513	518	526	529	531	539	543	549	555	562	565	567	571	573
						292.09							291.37	
						291.69								
						291.28								
						290.95	290.95						290.94	290.89
							290.85							
			290.77		290.70	290.71					290.62			290.51 290.50
				290.48	290.33	290.36								
			290.23											290.15 290.11
				289.94		289.96		290.05				289.96		
			289.81								289.87			
			289.65			289.66					289.62		289.76	289.68
						289.53								
				289.40	289.43									
			289.25					289.32						289.31 289.36
				289.11										289.10
289.17	289.01				288.93				289.06			289.05		
			288.92							288.90				
						288.81	288.89			288.82				
		288.67						288.52	288.50			288.64		288.60
			288.48			288.47						288.40		
288.28	288.38							288.21						288.29

↑ Binding Energy (eV)

TABLE 9, CONTINUED

		Spectrum Identification Number →															
		510	513	518	526	529	531	539	543	549	555	562	565	567	571	573	
↑ Binding Energy (eV) ↓			284.58		284.52							284.52			284.56		
						284.42	284.48	284.42						284.45			
									284.34							284.21	284.20
						284.16					284.16	284.17	284.18				
		284.07															
		283.96					283.90	283.94	283.92	283.99							
											283.81			283.83			
															283.76	283.78	
				283.50				283.50	283.56	283.51		283.57					
				283.42							283.46		283.44				
							283.37							283.34		283.32	
								283.25									
				283.04				283.07		283.02			283.12			283.14	
														282.96			282.95
											282.88					282.80	
				282.67		282.75	282.77	282.79				282.74		282.76			
											282.53						
														282.47			
										282.38							
						282.29	282.29				282.21						
											282.07				282.04		
						281.95			281.93		281.90						
							281.69		281.64	281.68							
										281.18							
											280.75						

The other reference spectra could be fit consistently by merely varying the height, width, and position for each channel. In addition to curve resolution, the normalized area of each channel was determined reproducibly within $\pm 1\%$. At least three deconvolutions were made for each of the spectra and those displayed in this thesis are composites.

The inflection points observed in the spectra (passed by the 1.0 eV filter) of several copper complexes and metalloproteins are given in Table 6. The major lines are marked with a solid underline and shoulders with broken underlines as in Tables 2 and 3 of Chapter V.

The sulfur $2p_{3/2}$ data are given in Table 7 and Table 8 lists the oxygen 1s data. The spectral region of Carbon 1s is given in Table 9. All binding energies reported in the thesis are referenced to this table.

Additional tables of Cls binding energies and peak assignments are given by Gelius et.al.³⁸. Summaries by Lindberg report extensive work on sulfur compounds and give a number of assignment tables³⁷. Because of the greater resolution of the Hewlett-Packard instrument as compared to the magnetic instrument of the Swedish group, there is a difference in the reported sulfur values. The Lindberg results are based on the weighted average of the unresolved Sulfur 2p doublet whereas the HP 5950A has resolved the doublet. The author, therefore, reports the sulfur $2p_{3/2}$ line. Thus, 0.4 eV should be subtracted from all Lindberg values if these are to be compared with those given in this work.

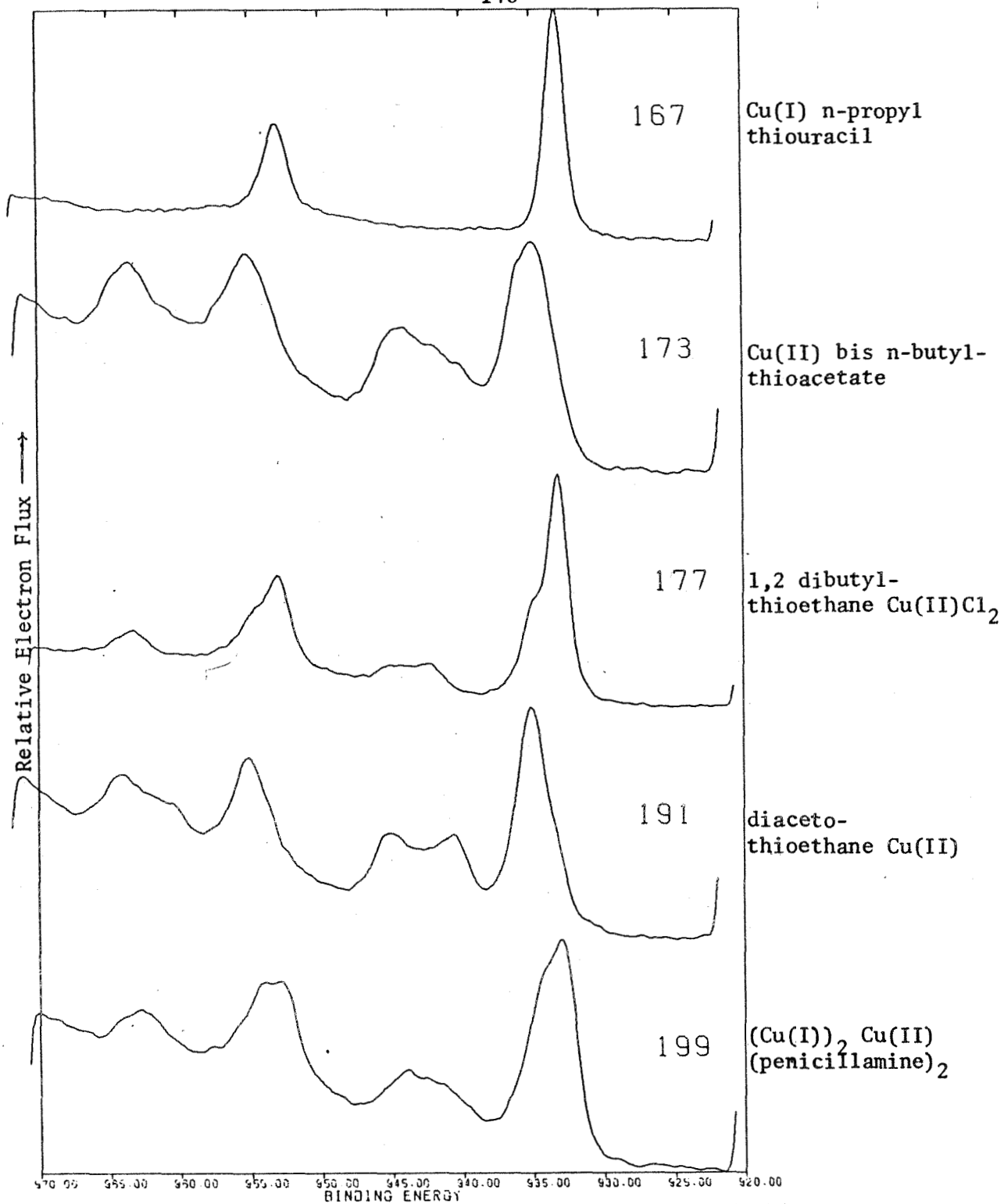


Figure 49. Copper 2p spectra of various copper-sulfur model complexes.

C. Results and Discussion

As noted in the introduction to this chapter, the electron spectrum of copper compounds has been the object of considerable recent work which was stimulated by Novakov's observation⁹⁵ of satellite structure in cupric salts^{91,96,97,98,99,100}. He interpreted his data in terms of a band-structure model which is similar to the shake-up model discussed in Chapter II. He also observed satellites in cuprous compounds and suggested that the observed satellites actually arose from matter adsorbed on the sample surface⁹⁶. Subsequent work^{91,97,98,99,100} and experiments conducted by the author indicate that the d^9 Copper (II) exhibits satellite and multiplet structure whose intensity and magnitude is determined by the coordination of the metal ion. Diamagnetic d^{10} Cu(I) compounds do not give rise to such satellites.

This is shown in Fig. 49 displaying spectra of copper-sulfur complexes. These spectra all represent the composite of 3 or more spectra in the binding energy interval 970 to 920 eV. This region shows the copper $2p_{3/2}$ - $2p_{1/2}$ doublet with the $2p_{3/2}$ line at 938.0 to 930.0 eV. The peak structure in the region of 947.0 to 938.0 eV represents the satellite

-
95. Novakov, T., Phys Rev, **B3**, 2693 (1971).
 96. Novakov, T., and Prins, R., Solid State Comm, **9**, 1975 (1971).
 97. Robert, T., Bartel, M., and Offergeld, G., Surface Sci, **33**, 123 (1972).
 98. Castle, J.E., Nature Physical Science, **234**, 93 (1971).
 99. Schon, G., Surface Science, **35**, 96 (1973).
 100. Rosenzwaig, A., and Wertheim, G.K., J. Electron Spec & Related Phen, **1**, 493, (1973).

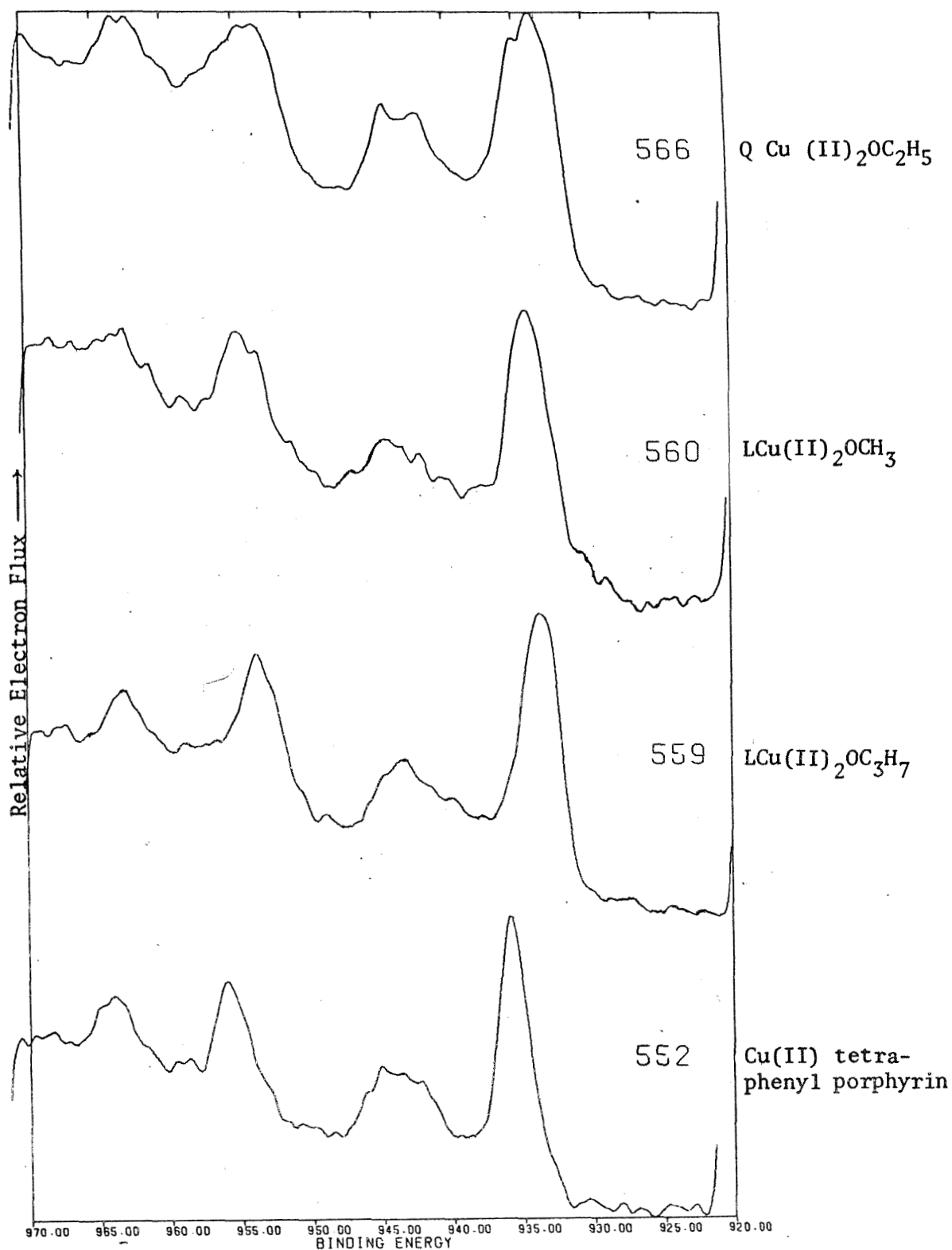


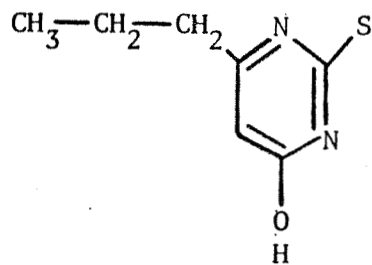
Figure 50. Copper 2p electron spectra of model copper complexes with nitrogen-containing ligands.

which has split from the $2p_{3/2}$ line, while the structure in the region of 967.0 to 960.0 eV arises from satellites of the $2p_{1/2}$ line.

Spectrum 167 represents Cu(I) n-propyl thiouracil and clearly shows the diamagnetic satellite-free Cu(I). The Cu^{II} bis n-butylthioacetate complex is given in spectrum 173. Here, copper (II) is in a 2 sulfur-2 oxygen coordination. Spectrum 177 is that of 1, 2-di-butylthioethane $\text{Cu}^{\text{II}}\text{Cl}_2$ with a ligand environment of 2 thioether sulfurs and 2 chloride ions. Spectrum 191 is another 2 sulfur-2 oxygen ligand system (di (aceto thio) ethane Cu^{II}) but now showing an altered geometry of the coordination as compared to the complex of spectrum 173. Spectrum 199 is that of the $(\text{CuI})_2 \text{Cu}^{\text{II}}$ (penicillamine)₂ complex.

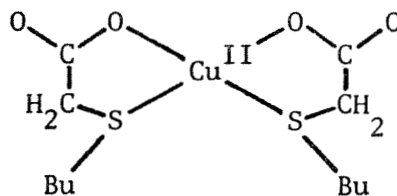
Each of the cupric complexes has different ligands and a corresponding different satellite structure. In addition to the major differences in satellites between different ligand systems, significantly different satellite intensity distributions for different geometries are observed with the same ligand, e.g., 173 vs. 191. At about 933.0 eV for each complex, a sharp line is evident in the structure of the $2p_{3/2}$ line (most obvious in 177 though observable in 173, 191 and 199). This line is imaged about 20 eV higher at 935.0 eV in the $2p_{1/2}$ region and increases in intensity with irradiation time. It is assigned to the photoreduced state (originally cupric ion).

Several additional spectra of copper model complexes are given in Fig. 50. 552 is the spectrum of Cu(II) tetraphenylporphyrin while 559, 560, and 556 are clathrate complexes having 2 Copper (II) atoms per molecule. The metals have identical sulfur and nitrogen coordination but share a

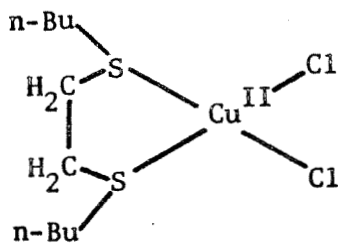


Cu^I

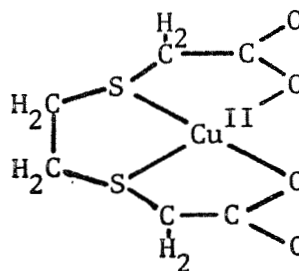
Cu^I n-propylthiouracil



Cu^{II} bis-n-butylthioacetate

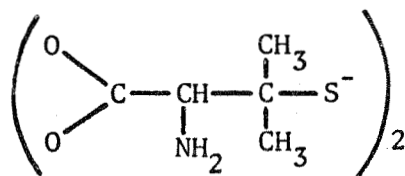


1,2-dibutylthioethane Cu^{II}Cl₂



Cu^{II} di(acetothio)ethane

(Cu^I)₂(Cu^{II})



(Cu^I)₂Cu^{II} (penicillamine)₂

TABLE 10

BINDING ENERGIES AND SATELLITE SPLITTINGS FOR COPPER SYSTEMS

SPECTRUM #	Cu ^I (3/2)	Cu ^{II} (3/2)	SATELLITES	Cu ^I (1/2)	Cu ^{II} (1/2)
167	933.1	934.8		953.1	955.1
173	933.1	934.6	5.3, 7.1, 9.3	953.0	954.4
177	933.3	935.0	7.7, 9.4, 10.4	953.6	955.1
191	932.9	934.2	5.6, 7.8, 10.1	952.7	954.0
199	932.7	935.8	7.1, 9.4, 9.7	953.1	955.9
552	Copper TPP		6.4, 7.7, 9.2	952.4	954.1
05,06	Stellaecyanin		4.0, 6.0, 8.7, 10.3	953.2	954.2
19,20	Plastocyanin		3.3, 5.5, 6.7, 8.2, 11.2	951.9	
08,09,20,11	Laccase		3.4, 5.4, 6.6, 7.9, 9.5, 10.7	953.3	
24,25,26	Hemocyanin			953.3	
806	Cu(EtAc) ₂	933.9	3.6, 4.9, 6.1, 8.0, 9.9, 11.9		
809	Cu(AcAcNO ₂) ₂	934.5	6.3, 9.1		954.3
811	Cu(Soc) ₂	933.7	5.4, 10.0		953.7
812	CuF ₂	935.1	3.9, 7.0, 9.4		954.9
816	CuF ₂ ·2H ₂ O	938.8	6.7		958.7
817	Cu(OH) ₂	937.2	7.5		957.0
818	CuCO ₃	936.5	7.6		
821	Cu(OAc) ₂ ·H ₂ O	936.3	7.8		956.2
824	Cu(OAc) ₂ 2en H ₂ O	935.8	5.8, 9.0		955.7
825	CuO	935.3	8.8		955.1
828	K ₂ Cu(C ₂ O ₄) ₂	935.2	7.8, 9.4		955.3
829	Cu(NO ₃) ₂ ·3H ₂ O	934.9	6.2, 9.2		955.1
832	Cu(∅COO) ₂	935.0	6.2, 9.3		955.1
835	Cu(AcAc) ₂	934.8	5.9, 9.4		955.0
836	CuSO ₄	934.5	5.1, 9.5		954.6
839	CuSO ₄ ·H ₂ O	936.2	4.6, 8.4		956.3
845	CuSO ₄ ·3H ₂ O	935.6	5.0, 8.6		955.2
846	CuSO ₄ ·5H ₂ O	937.0	7.2		956.8
847	CuSO ₄ ·dip·2H ₂ O	936.9	8.0		957.0
850	CuSO ₄ ·3 dip·7H ₂ O	934.6	8.2		954.7
		934.2	9.8		954.1

TABLE 10 (CONTINUED)

BINDING ENERGIES AND SATELLITE SPLITTINGS FOR COPPER SYSTEMS

<u>SPECTRUM #</u>		<u>Cu^I (3/2)</u>	<u>Cu^{II} (3/2)</u>	<u>SATELLITES</u>	<u>Cu^I (1/2)</u>	<u>Cu^{II} (1/2)</u>
853	CuSO ₄ .en.H ₂ O		935.6	8.4		955.7
854	CuSO ₄ .2en.H ₂ O		935.2	8.4		955.4
858	CuCl ₂		935.5	8.5		955.2
862	CuCl ₂ .2H ₂ O		935.6	8.4		955.5
866	CuCl ₂ .dip		934.4	8.3		954.3
867	CuCl ₂ .2dip.3H ₂ O		934.5	8.5		954.0
869	CuCl ₂ .en.H ₂ O		935.6	8.4		955.4
870	CuCl ₂ .2en.H ₂ O		934.7	9.0		955.0
873	CuBr ₂		934.9	9.7		954.7
877	CuBr ₂ .dip		934.2	8.9		954.0
878	CuBr ₂ .2 dip.2H ₂ O		934.3	8.7		954.8
880	CuBr ₂ .en.H ₂ O		935.4	9.0		955.3
881	CuBr ₂ .2en.H ₂ O		935.0	8.7		954.8
885	CuBr ₂ .3en.5H ₂ O		935.1	8.4		954.9
890	CuCN	934.6			954.4	
893	CuI	934.7			954.4	
894	Cu ₂ O	934.1			954.1	
896	CuSCN	934.0			953.8	
898	Cu ₂ S	934.0			953.7	
899	Cu ₃ P	933.7			953.5	
903	CuBr	933.6			953.5	
906	CuCl	934.0			953.9	
907	CuCl. ϕ ₃ P	933.5			953.1	
911	CuCl.(O ₃ P) ₃	933.5			953.2	
919	CuCl.(O ₂ PH) ₃	933.4			953.2	
920	CuCl.(O ₃ P)(O phen)	932.5			952.3	

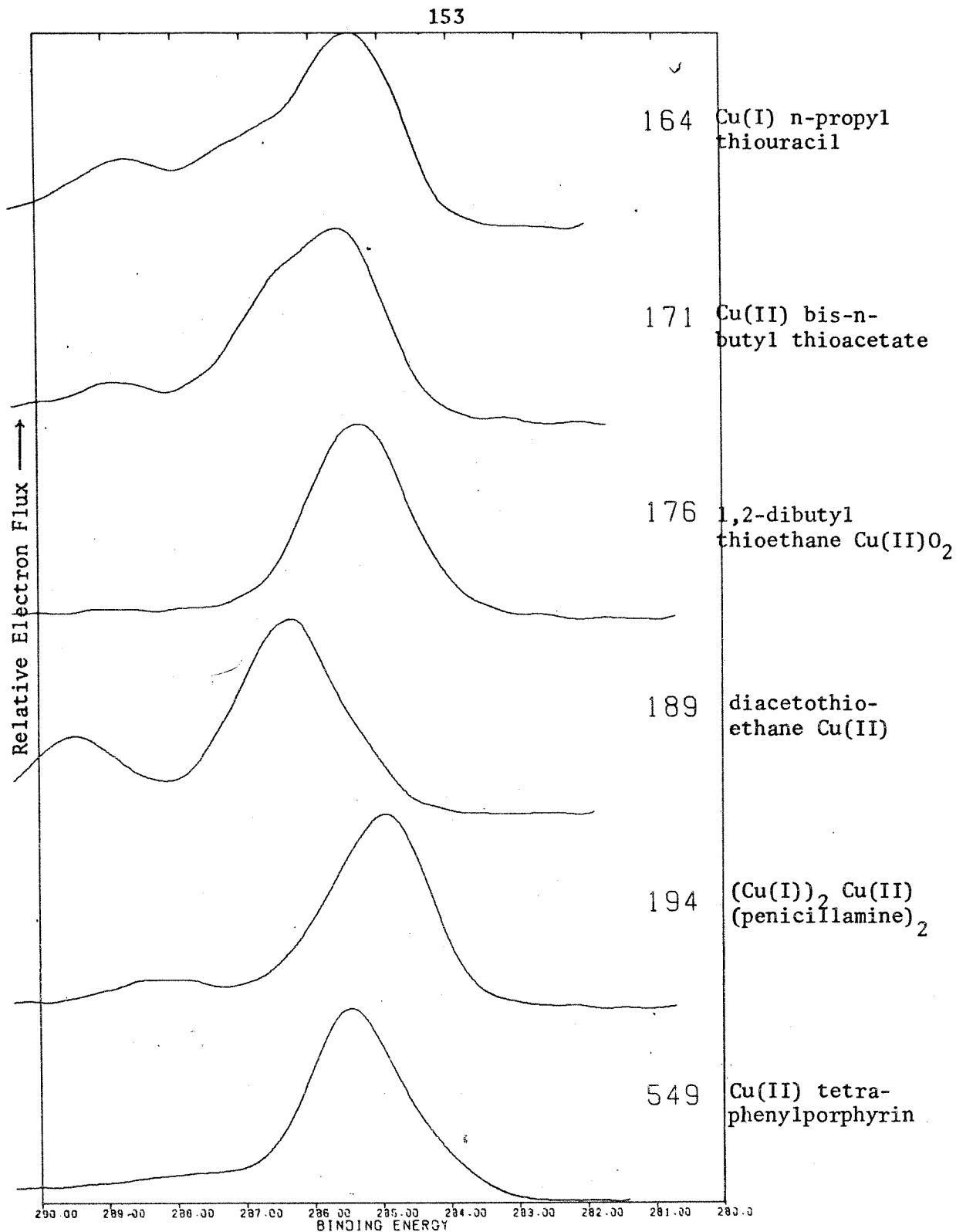


Figure 52. Carbon 1s spectra of the model copper complexes of Figures 49 and 50.

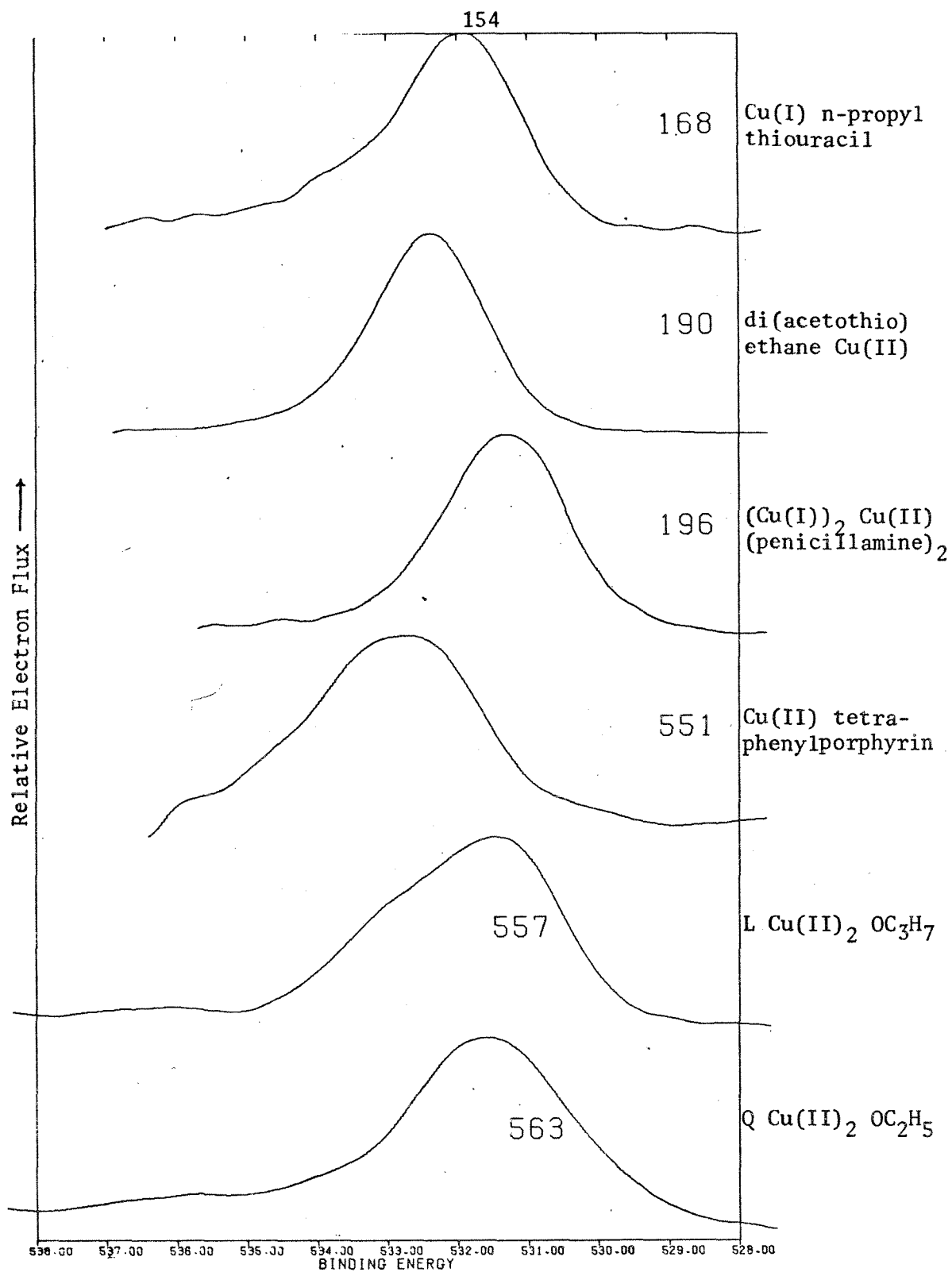


Figure 53. Oxygen 1s spectra of the copper model complexes.

bridging oxygen.

The structures of these model complexes are represented in Fig. 51. Table 10 lists by spectral number the major Copper 2p binding energies and the positions of a number of the satellites. Additional data are included for comparison. These were taken with the McPherson ESCA 36 and the JPL-USU spectrometers as well as from the extensive compilations of Frost et al⁹¹. The Frost data has been corrected where possible so as to be consistent with the present work.

As mentioned in the experimental section, all the spectra are referenced to a common aliphatic carbon binding energy. The spectra for the model complexes of Figures 49 and 50 in the Carbon 1s region are given in Fig. 52. Spectrum 549 is that of Cu TPP and the others follow the order given in Fig. 49.

The oxygen 1s region of the photoelectron spectrum of these complexes is given in Fig. 53. Spectrum 168 is that of the phenolic oxygen of the thiouracil complex. The carboxylate oxygens of the di(acetothio)ethane Cu^{II} complex are shown in spectrum 190, while 196 gives the carboxylate oxygens of the penicillamine complex. Spectrum 551 is that of Cu TPP, and spectra 557 and 563 are due to the 2 copper clathrate complex with bridging oxygen ligands.

The primary peak in spectrum 551 falls at significantly higher binding energy than would correspond to carboxylate oxygens (532.5 eV). In accordance with literature data^{97,99}, this oxygen is assigned to water bound by copper (II).

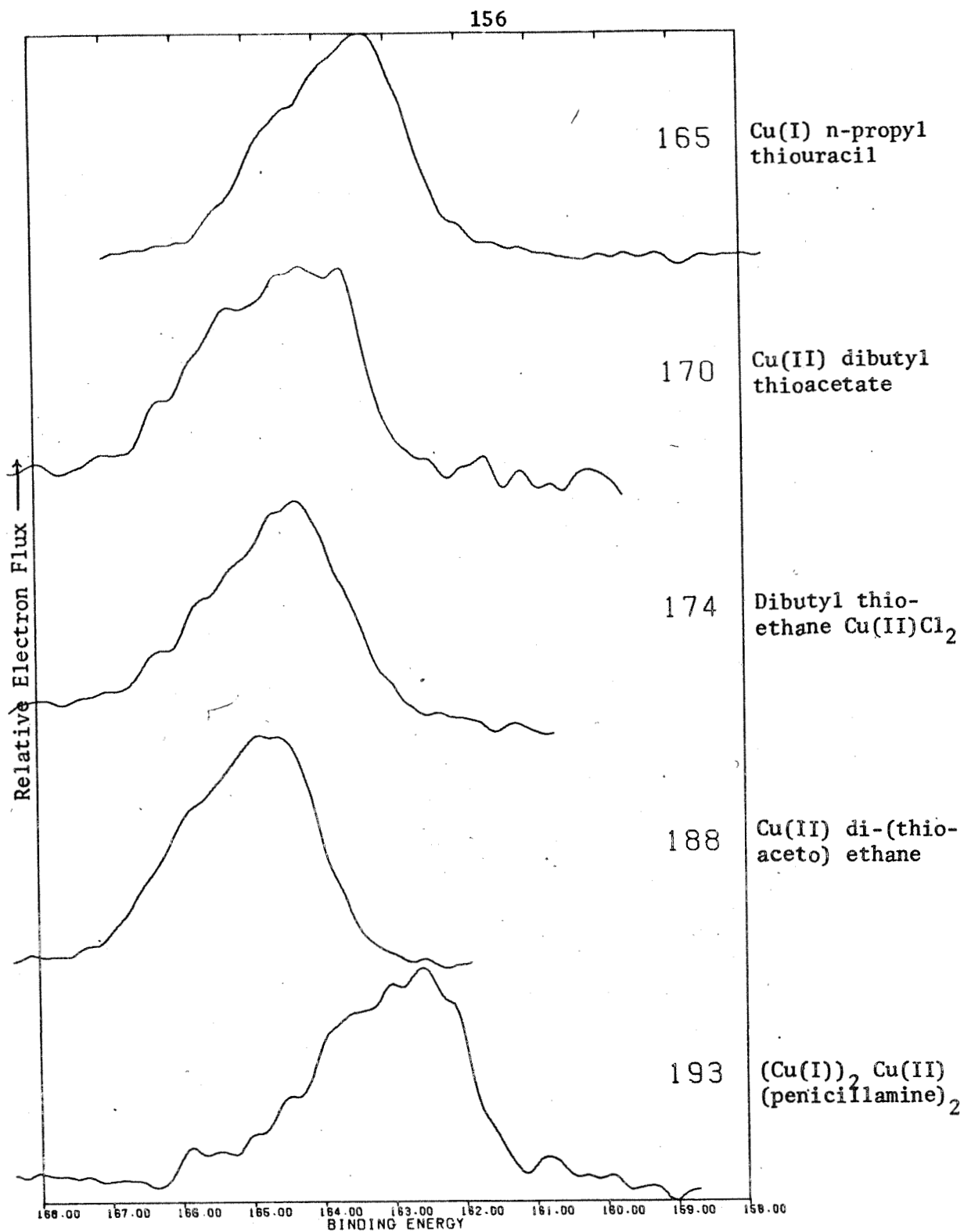


Figure 54. Sulfur 2p spectra of the copper model complexes.

Part of the spectrum 190 can be assigned to water and part to carboxylate oxygen bound to Cu^{II} . Thus, there is an ambiguity in the interpretation of the low binding energy peak of the penicillamine complex (196).

These oxygens can be assigned through comparison with the spectra of the other model complexes. For example, the bridging oxygens of the clathrate complexes L $\text{Cu}_2\text{OC}_3\text{H}_7$ (557) and Q $\text{Cu}_2\text{OC}_2\text{H}_5$ (563) consist of a phenolic oxygen bound to Cu^{I} , we would expect the analogous cupric-bound oxygen to occur at higher binding energy (less electron transfer from metal to oxygen). Thus, the 531.0 eV peak in spectrum 557 and the 531.5 eV peak of spectrum 563 can be assigned to the bridging alkoxide oxygen. The 533.0 eV peak then corresponds to the phenolic oxygen bound to Copper (II). In general, we have observed that the O1s binding energy for oxygen- Cu^{II} is about 1 eV higher than that for oxygen- Cu^{I} . From Table 9, the carboxylate oxygen (of spectrum 190) is found at 532.1 eV (O- Cu^{II}). Assigning the peak at 531.2 eV in 196 to carboxylate oxygen would correspond to a shift of about 1 eV toward lower binding energy. This suggests that the penicillamine carboxylate oxygens are primarily bound to Cu^{I} .

Figure 54 shows the sulfur $2p_{3/2}$ spectra of these model complexes. The sulfur of the thiouracil Cu^{I} complex (165) is intriguingly similar to that in (193) penicillamine. This suggests that the coordination of Cu^{I} in the $\text{Cu}^{\text{I}}_2\text{Cu}^{\text{II}}(\text{penicillamine})_2$ complex is $\text{S}\cdots\text{Cu}^{\text{I}}\cdots\text{O}$. Spectrum 170 represents the Cu^{II} butylthioacetate system and 174 the dibutylthioethane $\text{Cu}^{\text{II}}\text{Cl}_2$ complex. The sulfur spectrum of the dithioacetoethane complex is given in 188.

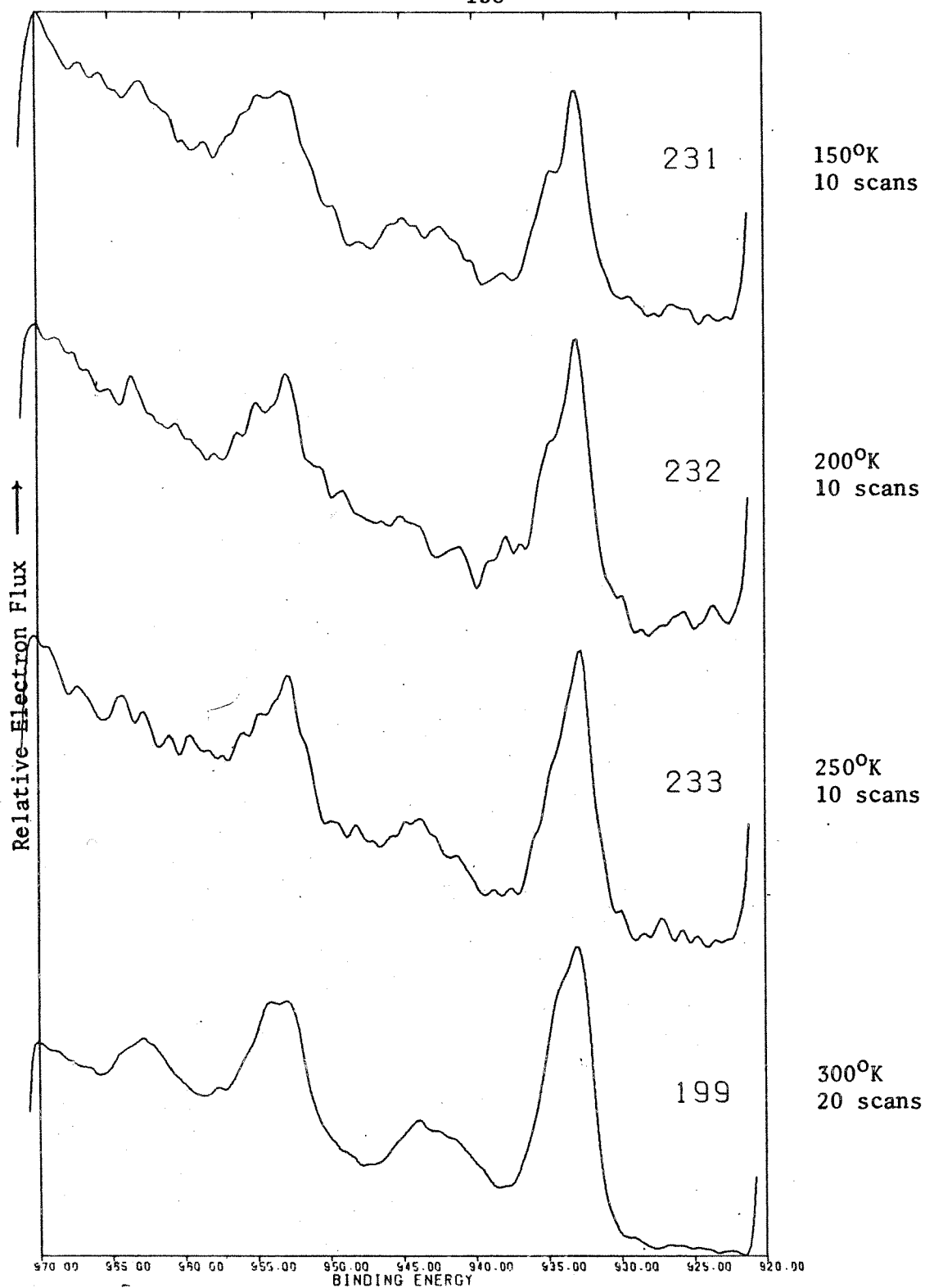


Figure 55. Copper 2p spectra of $(\text{Cu(I)})_2 \text{Cu(II)} (\text{penicillamine})_2$ taken as a function of temperature and time to illustrate photoreduction.

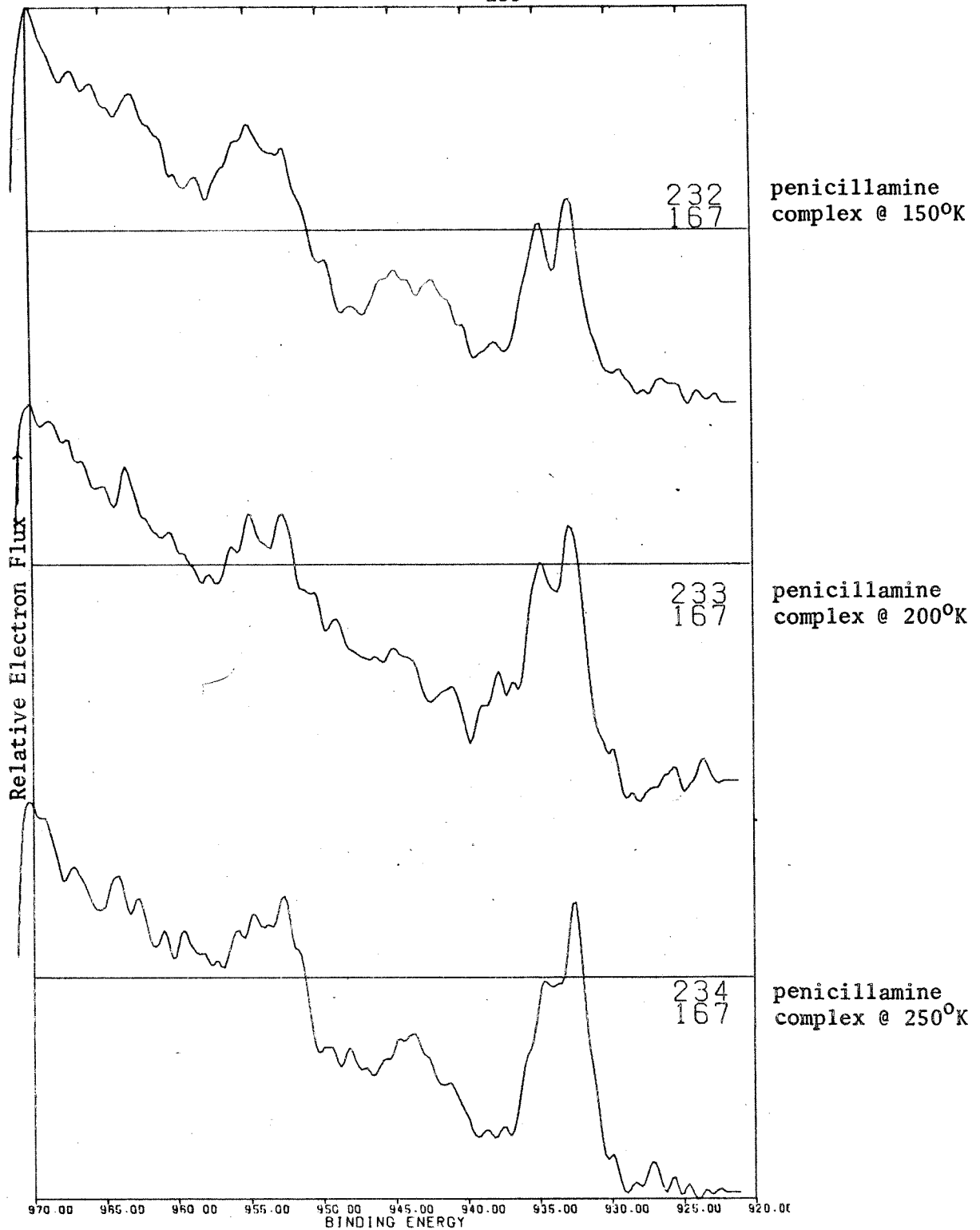


Figure 56. Difference spectra in which the Cu 2p curve due to the Cu(I) n-propyl thiouracil complex is subtracted from the spectra of Fig. 55 to decrease the Cu(I) component of the resulting trace.

The photoreduction of cupric systems was followed by the experiment illustrated in Fig. 55. Here, the $(\text{Cu}^{\text{I}})_2\text{Cu}^{\text{II}}(\text{penicillamine})_2$ complex was studied as a function of temperature and irradiation time. Thin films of three samples on gold coated substrates were placed in the spectrometer, simultaneously, and were kept at 150°K while the spectrum was taken (10 scans, 1 eV/sec., 256 channels, 970-920 eV). The result is given as spectrum 231. The temperature was then increased to 200°K keeping all other instrumental parameters the same (spectrum 232). In like manner, spectrum 233 was taken at 250°K , while spectrum 199 was taken at room temperature with 20 scans. The Cu^{I} peak at 933.0 ± 0.1 eV increases in intensity relative to the Cu^{II} peak at about 934.8 ± 0.2 eV. Each spectrum of Fig. 55 is normalized to the value of its maximum term on the plot. An increase in the intensity of the strongest, 933.0 eV, peak is seen as an effective decrease in the intensity of the 934.8 ± 0.2 eV peak.

Since the penicillamine complex is a mixed valence $(\text{Cu}^{\text{I}})_2\text{Cu}^{\text{II}}$ system¹⁰¹ there exists the possibility that the photoreduction product of $\text{Cu}^{2+} \rightarrow \text{Cu}^+$ does not have the same binding energy as the original Cu^{I} state. This is shown in Fig. 56 using the spectral difference techniques developed in Chapter V. 100,000 counts have been arbitrarily added to the spectrum in order to decrease the signal power of spectrum 167, (Cu^{I} thiouracil complex). This spectrum is then subtracted from the spectra of Fig. 55.

101. Schugar, H.J., Private Communication.

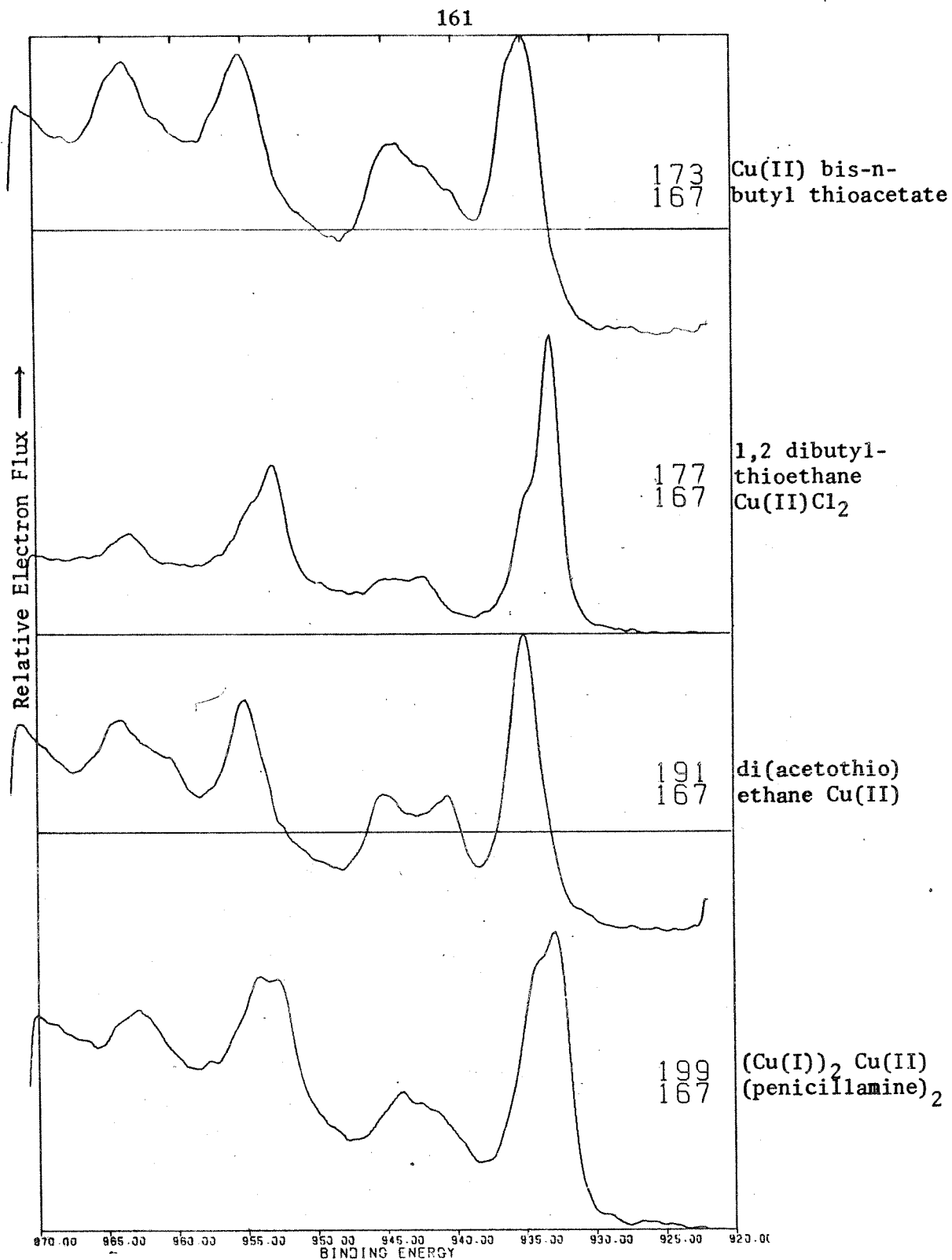


Figure 57. Difference spectra in the Cu2p region in which spectrum 167 arising from Cu(I) thiouracil is subtracted from spectra of the model complexes identified along the ordinate.

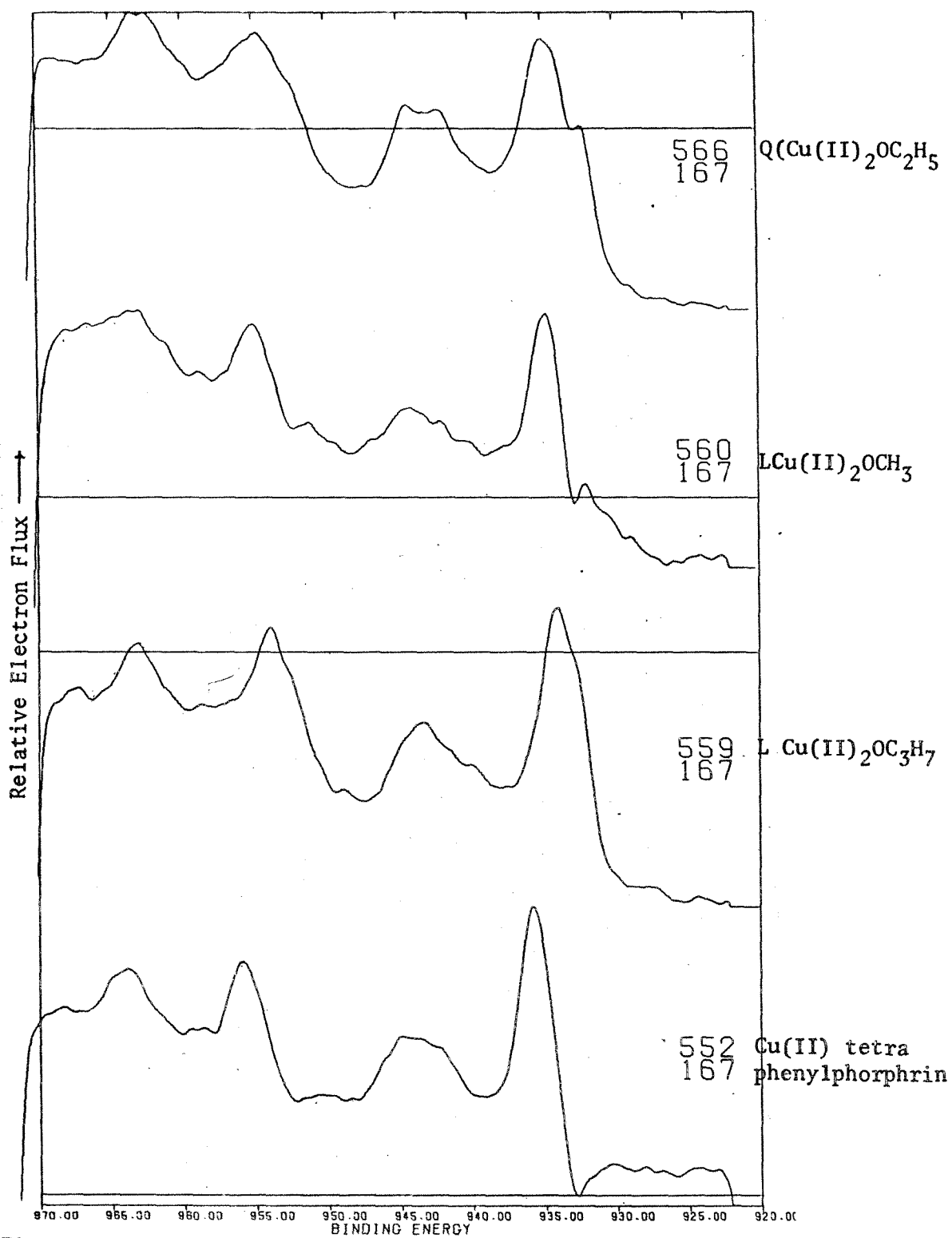


Figure 58. Difference spectra in the Cu 2p region in which spectrum 167 arising from Cu(I) thiouracil is subtracted from spectra of the model complexes identified along the ordinate.

The Cu^{II} part is enhanced in the difference spectra. A shift is observed of about 1.9 eV between the parent Cu^{II} line and that of the photoreduction product.

Figures 57 and 58 show the difference spectra obtained by subtracting the Cu^{I} -thiouracil spectrum from each one of the model complexes. The spectra detailed in Fig. 58 exhibit high signal-to-noise ratios and permit a clearer assignment of the $2p_{3/2}$ line and its multiplet components.

The spectra shown in Figs. 49, 50 and 55 were deconvolved in the $\text{Cu } 2p_{3/2}$ region by means of the DuPont 310 curve analyzer as described in the experimental section of this chapter. Either the low-binding side of the Cu^{I} peak or the high-binding side of the Cu^{II} peak was fitted with the analyzer depending upon which of these was the best resolved one. The overall peak shape was then generated with additional channels as needed. By applying at least 3 successive deconvolutions for each of the spectra described in this thesis, a difference of 1.92 ± 0.04 eV between Cu^{II} and the Cu^{I} decomposition product was established.

The susceptibility of alkyl-nitrogen compounds to radiation damage has been shown by the Swedish group¹. At Berkeley the extent of damage to the protein was studied by the use of nitrogen and sulfur spectra^{102,103}. These early experiments could not follow changes in the transition-metal spectra because of the weakness of the signal.

102. Klein, M., and Kramer, L., "Proceedings of the Symposium on Improving Plant Protein by Nuclear Techniques".

103. Wurzbach, J., Private Communication.

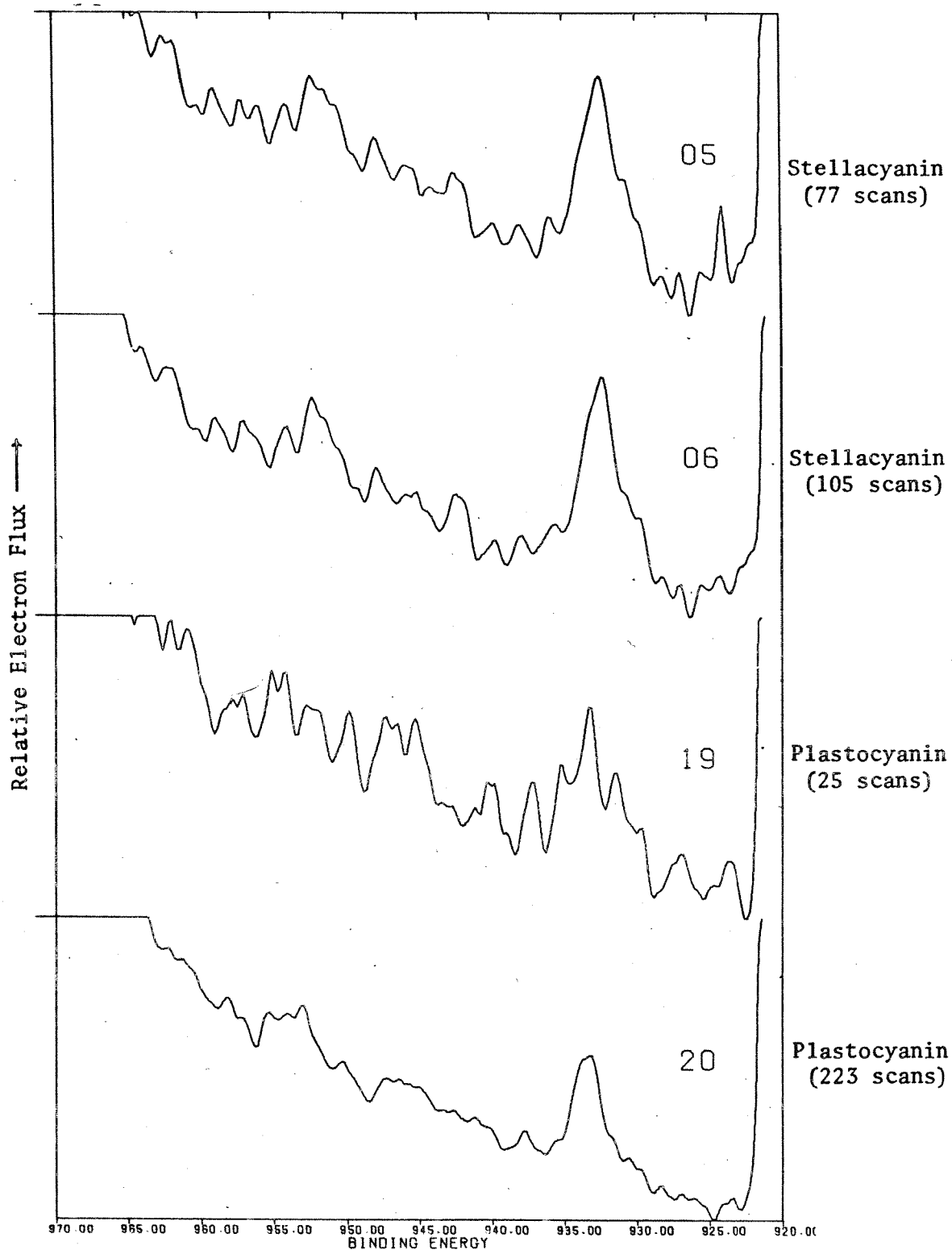


Figure 59. Copper 2p spectra of the metalloproteins Stellacyanin and Plastocyanin.

In this work, several spectrometers were employed, each having a different source. The McPherson ESCA 36 employs a high intensity Mg-target tube giving about one order of magnitude higher flux than the $MgK\alpha_{1,2}$ source used in the JPL-USU spectrometer. The monochromatized $AlK\alpha_{1,2}$ source of the HP 5950A spectrometer delivered two orders of magnitude lower x-ray flux than the JPL-USU unit.

The Cls, N1s, and S2p spectra of the same protein samples varied from one spectrometer to another. This can be explained in terms of radiation damage caused by the different flux levels.

Thus, it suggested itself to investigate the metal-ion spectra of the proteins as a function of irradiation time. Previous experimenters studying the electron spectra of metalloproteins have used long scanning times (as much as 4 days) and intensities considerably higher than those provided by the McPherson instrument in order to separate the signal from the background. The data-handling techniques discussed in Chapter IV and the recent instrumental improvements made it possible for the author to acquire data in intervals of one hour or less with better signal-to-noise ratios than those reported previously.

In experiments with the model copper proteins, Stellacyanin and Plastocyanin, data were dumped at fixed scan intervals from instrument memory onto paper tape for computer treatment. In spectrum 05, the copper 2p region of Stellacyanin is shown after accumulation of 77 scans which took 3 hours 15 minutes (256 channels and 1 eV/sec) and after 105 scans (4 hours 24 minutes, spectrum 06), see Fig. 59. The Cu2p spectrum of Plastocyanin is also given in Figure 59 at 25 scans (spectrum 19) and

after 223 scans or 9 hours 25 minutes (spectrum 20).

These spectra all show a major off-scale peak at high binding energy assignable to the KLL oxygen Auger line. Therefore, all of these spectra fall on a decreasing background (970 eV \rightarrow 920 eV).

Stellacyanin (Table 10) shows a strong line at 932.5 eV which increases and a shoulder at 933.9 eV which decreases in intensity with further irradiation. In Plastocyanin, a strong line is observed at 933.3 eV and a shoulder at 934.4 eV which decreases in intensity with time.

Spectrum 19 of Plastocyanin most closely approximates the spectrum of the unreduced Type 1 copper while comparison of 19 and 20 shows that significant signal-to-noise enhancement was attained by a 10-fold increase in number of scans. In addition to the reduction of the low-frequency noise, the satellite structure (peaks in the region 947-938 eV) has been significantly diluted. The copper $2p_{3/2}$ line has narrowed, and in spectrum 20 falls in the region of the anticipated Cu^{I} photo-reduction product.

In Table 6, the inflection points are listed by spectrum number. The recurrence of inflections between the $2p_{3/2}$ and the $2p_{1/2}$ peaks suggests that satellite structure may be observed in the metalloproteins (though the low frequency noise is quite significant). The peaks at 4.0, 6.0, 8.7, and 10.3 eV above the estimated Copper (II) peak (933.9 eV) in the Stellacyanin spectrum are presumably due to satellite transitions. Similar analysis of Plastocyanin spectra lead to assignments of satellite transitions at 3.3, 5.5, 6.7, 8.2, and 11.2 eV. The assumption that Cu^{II} corresponds to 933.9 eV and the radiation damage product to 932.5 eV for

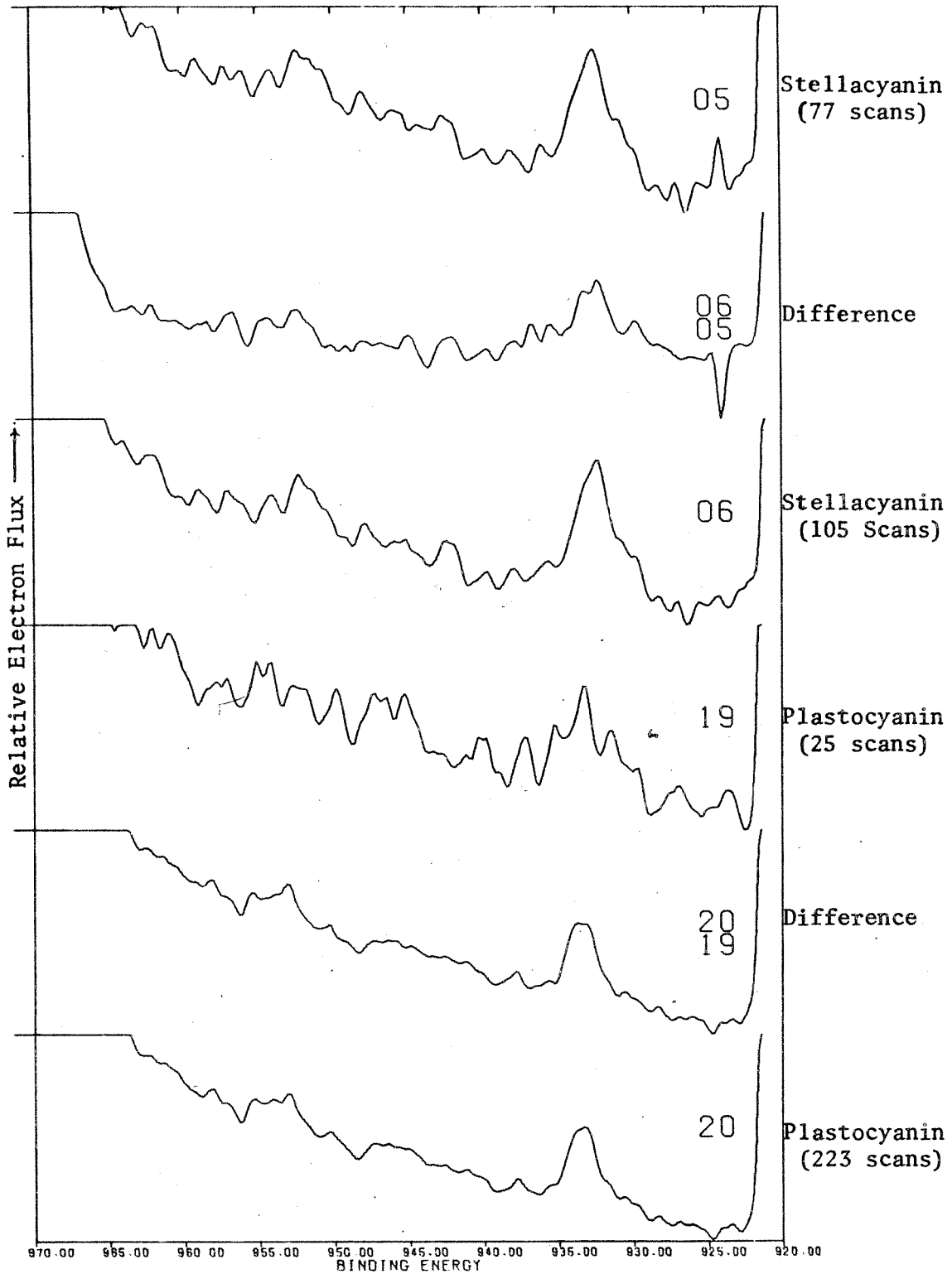


Figure 60. Difference spectra for the Cu 2p region of Stellacyanin (05, 05-06, 06) and Plastocyanin (19, 19-20, 20).

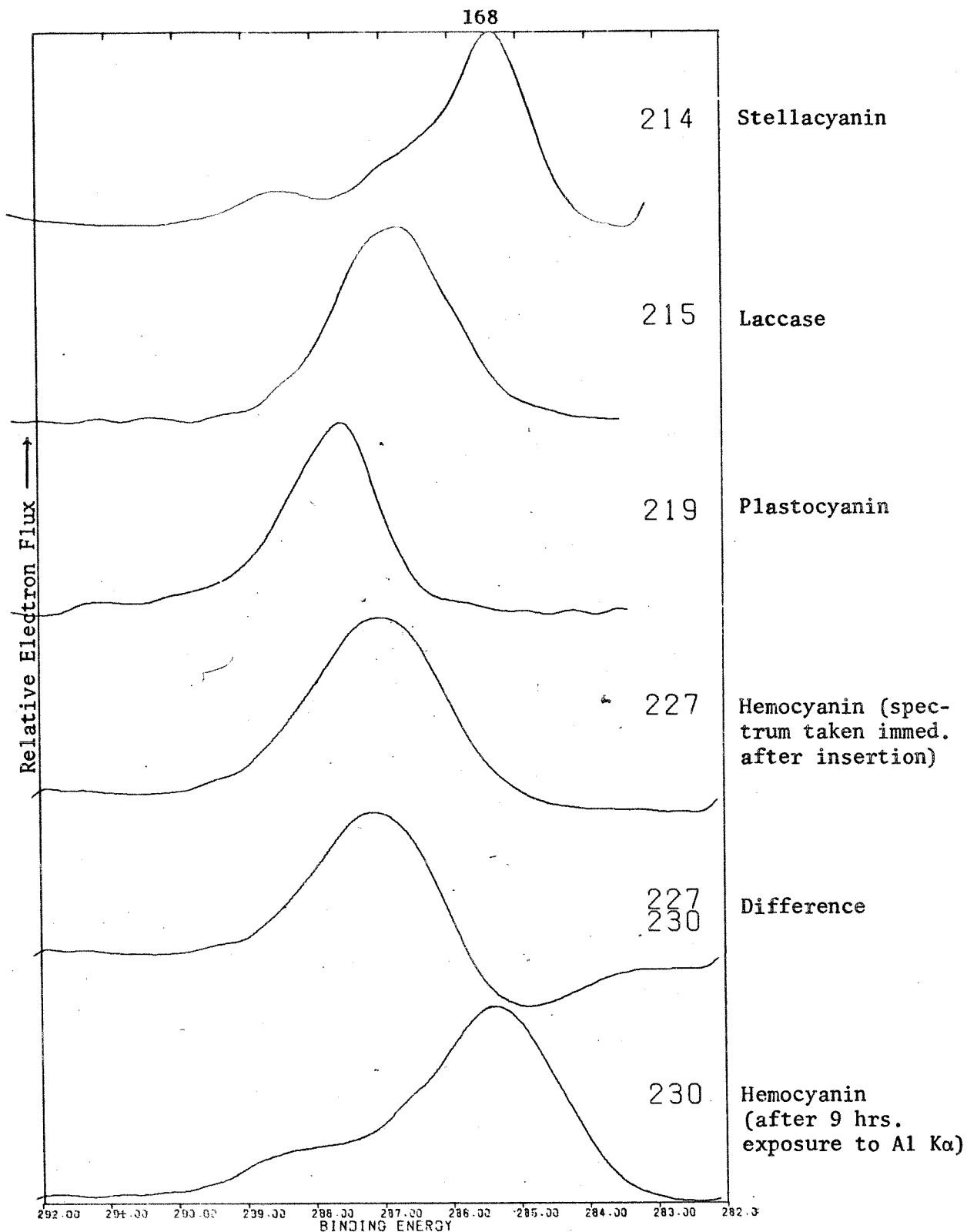


Figure 61. The Carbon 1s spectra of various metalloproteins. The original Binding Energy positions are shown before referencing the spectra to the C1s standard (aliphatic carbon @ 285.4 eV).

Stellacyanin (934.4 eV and 933.3 eV for Plastocyanin) is based on estimates of these peak positions from the composite curves. The difference of $\Delta E = 1.4$ eV in the binding energies is observed between parent species and photo-reduction product of Stellacyanin (1.1 eV for Plastocyanin).

The difference in binding energy between Cu^{II} and Cu^{I} in model complexes corresponds to an average ΔE of 1.6 eV, whereas the deconvolution of the spectra showed ΔE at 1.9 eV. If estimation errors of up to 0.3 eV are assumed, the $\text{Cu}^{\text{I}}-\text{Cu}^{\text{II}}$ peak separation for proteins seems less than that for the model systems. The shoulders on the lower binding energy side of the $\text{Cu } 2p_{3/2}$ line in both metalloproteins can be assigned to Cu^{0} resulting from reduction of Cu^{I} .

The difference spectra in Figure 60 are used to determine the spectrum of the metal-ion species which existed during the time intervals in which the spectra were recorded. The curve labeled 06-05 represents the photoelectron spectra of Stellacyanin which existed after 3 hours of irradiation. The $\text{Cu}^{\text{I}}-\text{Cu}^{\text{II}}$ decomposition couple is readily observed as is the satellite structure and the $2p_{1/2}$ spin-orbit doublet. The difference spectrum 20-19 is almost identical to curve 20 because the latter one represents 10 times as many scans as the former.

The Cls spectra of the various metalloproteins used as an internal reference standard are illustrated in Fig. 61. Spectrum 214 represents Stellacyanin, 215 represents Laccase, and 219 Plastocyanin. The Cls spectrum of Hemocyanin taken immediately after inserting the sample into the spectrometer is given as 227 and that taken after 9 hours of irradiation is 230. The difference spectrum between the latter two, labeled

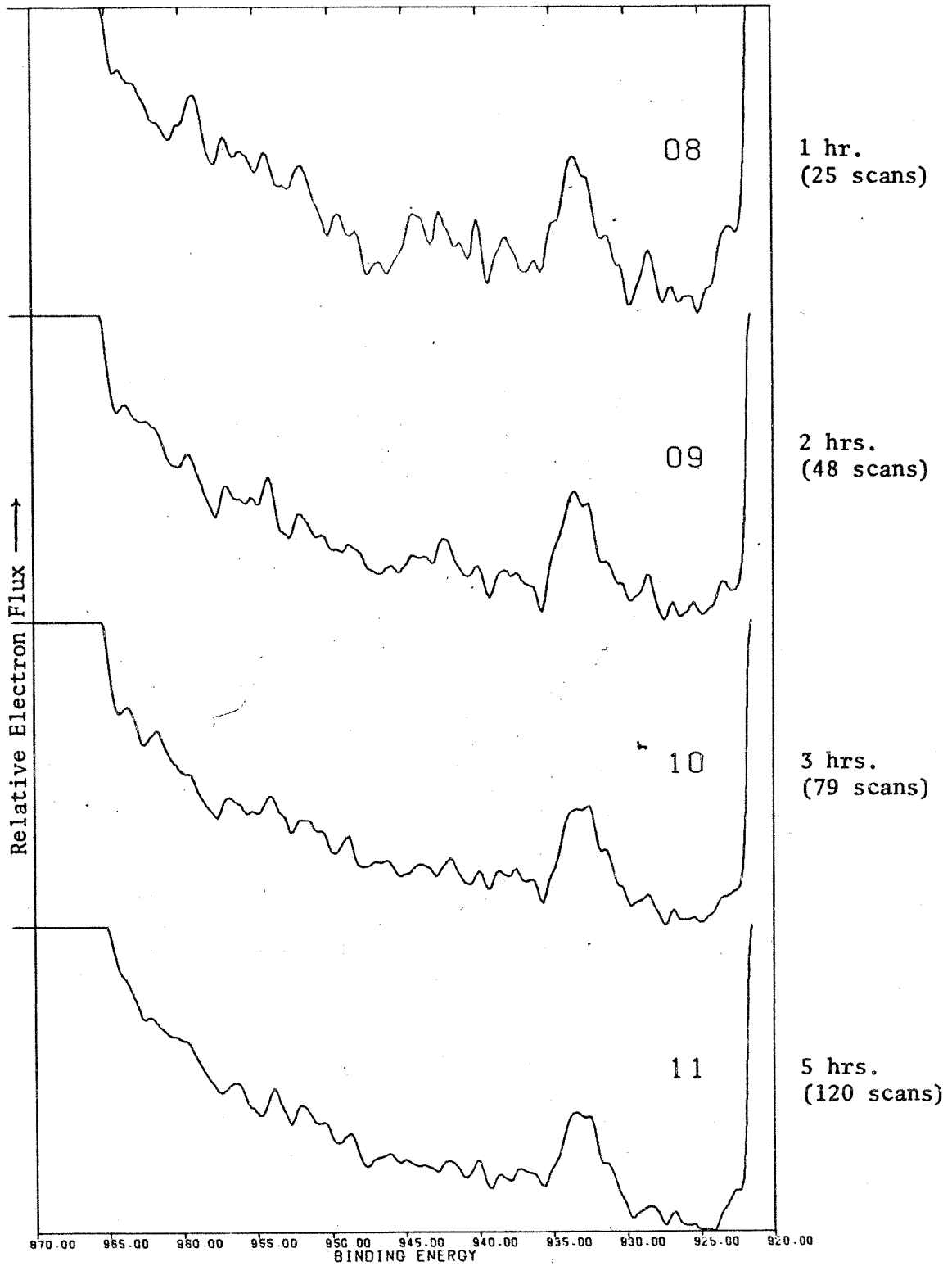


Figure 62. Copper 2p spectra of Laccase, dumped at time intervals given along ordinate.

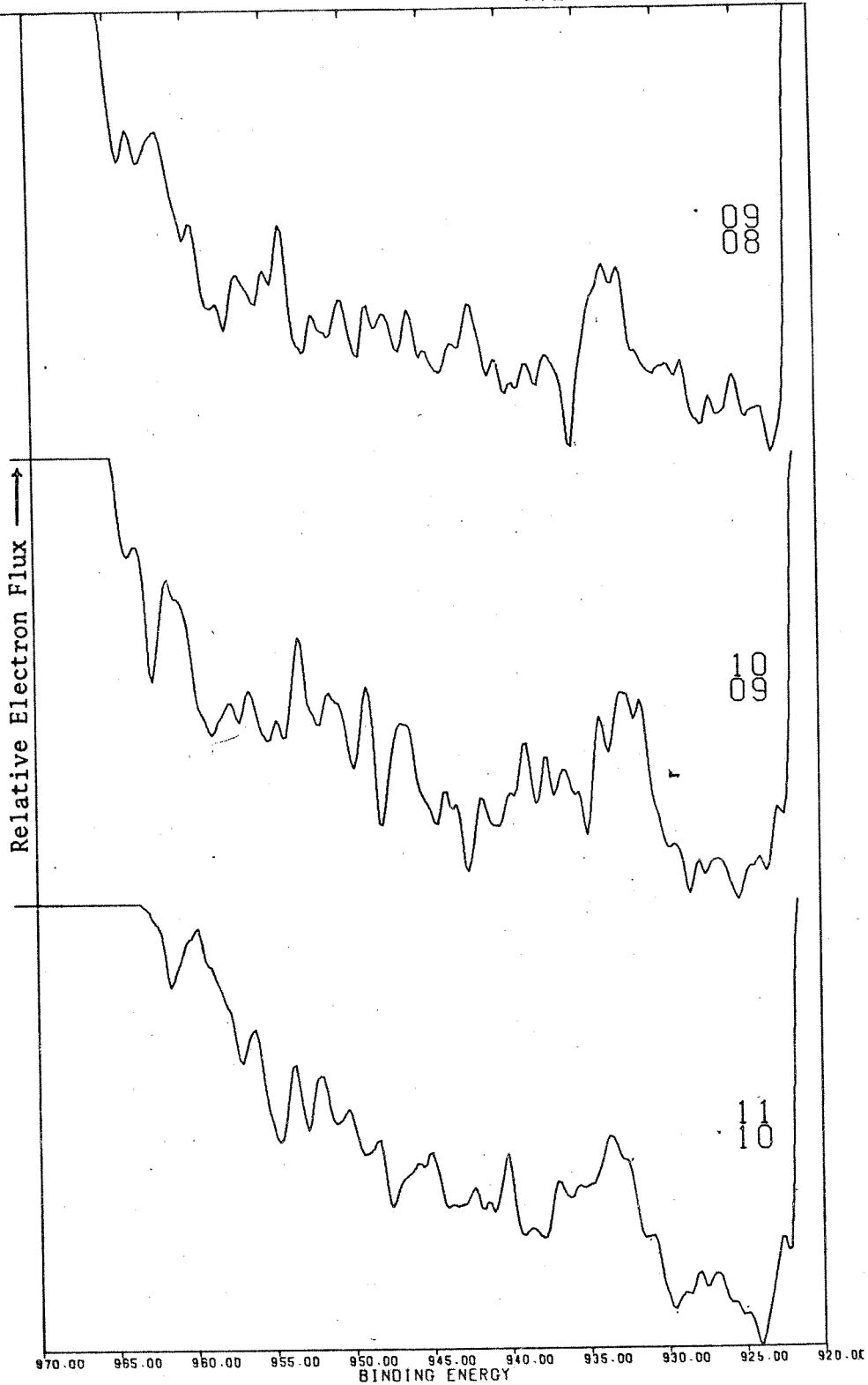


Figure 63. Difference spectra for Laccase, Cu 2p region. Sequential spectra have been subtracted from each other to show the curve due to the components that existed during the accumulation time.

227-230, shows the change due to photo decomposition.

In all of these spectra, the value of 285.4 eV has been assigned to the maximum in the C1s region which is representative for aliphatic and aromatic carbons according to Siegbahn's work³⁸. The correction required to convert from Au 4f reference to the C1s reference is 1.5 ± 0.5 eV.

In order to follow the change in the $\text{Cu}^{\text{I}}/\text{Cu}^{\text{II}}$ ratio of the diamagnetic copper site in Laccase, the data were dumped on tape at intervals of approximately one hour. The spectra thus obtained are shown in Fig. 62; spectrum 08 corresponds to 25 scans (1 hour); 09 to 48 scans (~ 2 hours); 10 to 79 scans (~ 3 hours); and 11 to 120 scans (~ 5 hours).

The satellite structure and the pronounced $2p_{3/2}$ line is evident in Figure 62. However, the satellite intensity in the region 948 eV to 937 eV decreases with time relative to the major peak at 933.5 eV which is strong and apparently invariant with time. The structure of this peak is similar to that observed for Stellacyanin and Plastocyanin. The shoulder at 932.7 eV increases while the shoulder at 934.6 eV decreases as a result of radiation damage. Also, the shoulders at 931.3 and 930.4 eV increase with time. These are presumed to be caused by Cu-metal reduction products similar to those observed for Stellacyanin and Plastocyanin.

The change in the spectra caused by a gradual increase in radiation-damage products can be seen in Fig. 63, which shows three difference spectra. As before, 09-08 corresponds to species which are present between 1 and 2 hours of irradiation while 10-09 gives the 2 to 3 hour interval and 11-10 is due to those species which are present after 3 hours but before

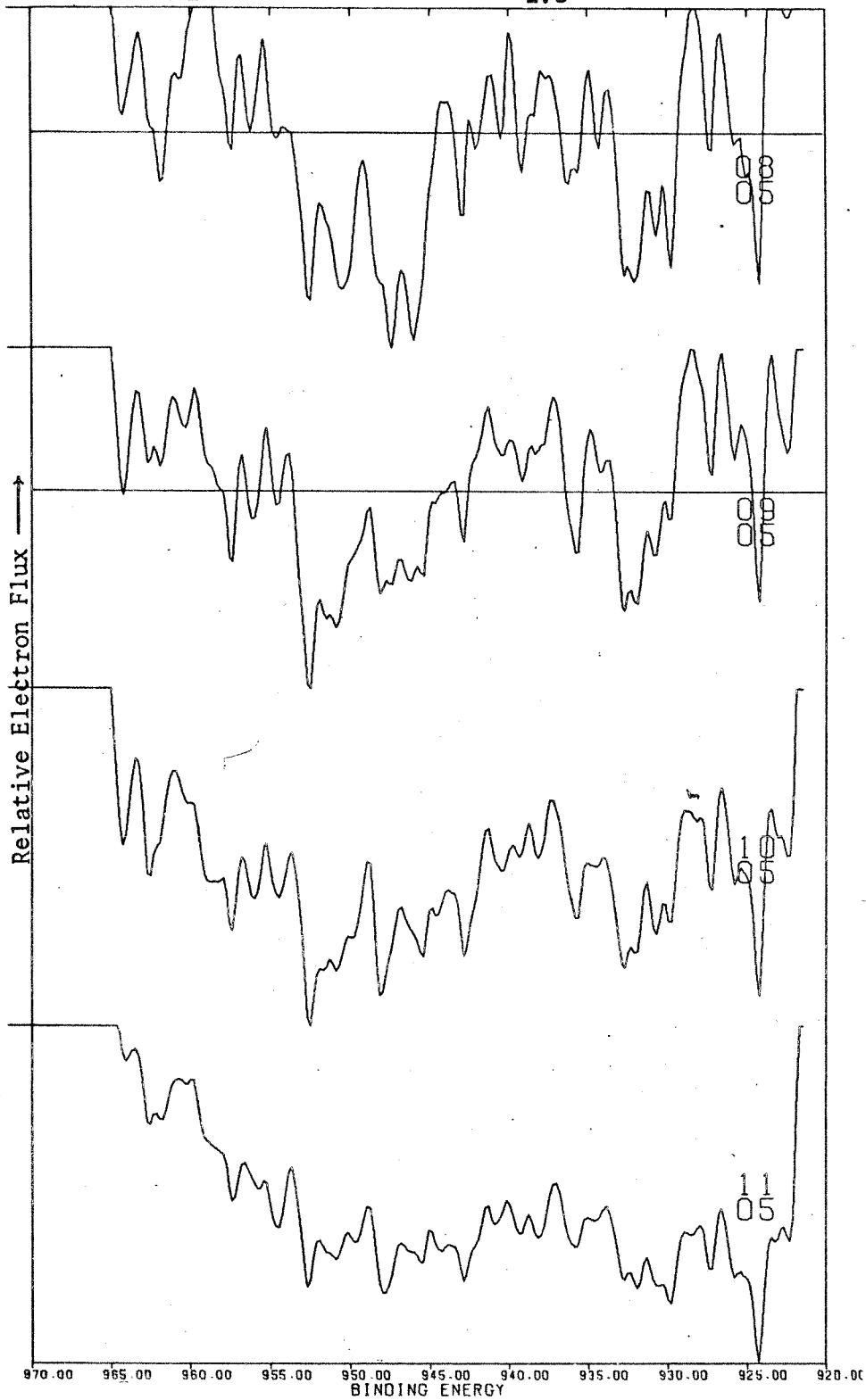


Figure 64. Difference spectra in which the Stellacyanin Cu 2p spectrum after 77 scans (05) is subtracted from the Laccase spectra of Fig. 62.

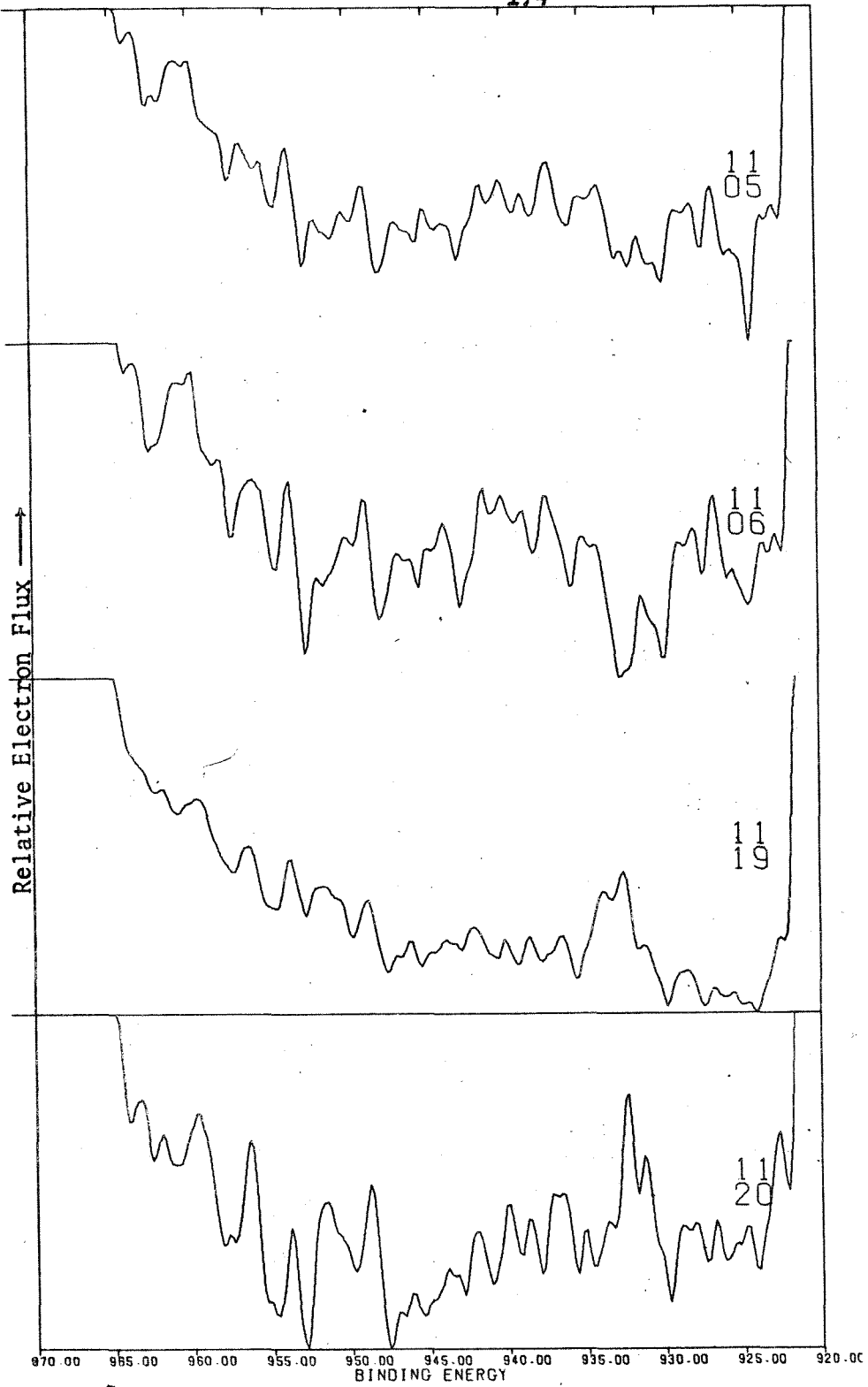


Figure 65. Difference spectra showing the result of subtracting the Stellacyanin spectra (05, 06) and the Plastocyanin spectra (19,20) from the Laccase spectrum (11) accumulated with 5 hrs. exposure.

5 hours. The method used has enhanced the noise component but also the shoulder at the low binding side, and yet the main peak at 933.5 eV is retained. On the high binding side of this peak, a negative trough occurs which the author assigns to the Type 1 Copper II site of Laccase (934.6 eV).

Fig. 64 shows Laccase spectra from which the Stellacyanin spectrum 05 has been subtracted. In each case, 08-05, 09-05, 10-05, and 11-05, the noise has been increased sharply, but the strength of the oxygen Auger line (981 eV as referenced to $AlK\alpha_{1,2}$) shows that the Laccase spectrum in each case has a higher count level per channel than the Stellacyanin spectrum. Further, in the $Cu2p$ region, the Stellacyanin spectrum overcompensates the Laccase 2p line, while in the satellite region 943.0 eV to 934.0 eV, more power is evidenced in the Laccase spectrum while the Stellacyanin spectrum shows more power in the satellite region from 948.0 eV to 943.0 eV. This suggests the possibility of different Cu^{II} environments in Laccase and Stellacyanin.

Continuing these comparisons by means of difference spectra, Fig. 65 contrasts Laccase directly with Stellacyanin and Plastocyanin at more equivalent exposure times. Spectrum 11-05 and 11-06 re-emphasize the observations developed in the discussion of Fig. 64 concerning the increased $Cu 2p_{3/2}$ signal in Stellacyanin as compared to that of Laccase. However, spectrum 11-19 and 11-20 reinforce the initial observations made in the review of the basic Laccase spectra (Fig. 62). Spectrum 11-20 shows a strongly enhanced peak at 932.5 eV with another at 931.3 eV and yet another at 933.7 eV. The low-energy satellites are stronger in Laccase, while the high-energy satellites are favored in Plastocyanin.

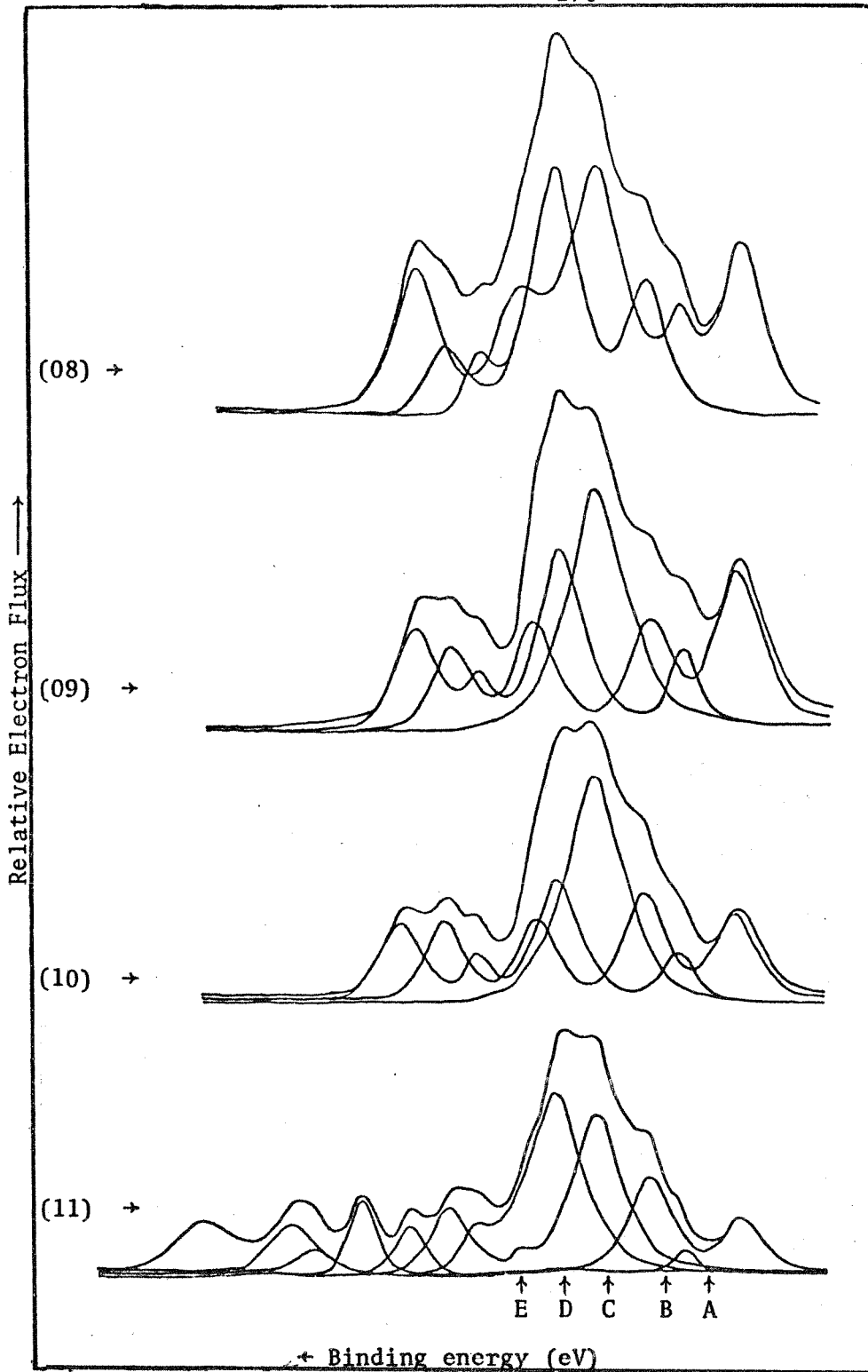


Figure 66. Deconvolved spectra of Laccase corresponding to the spectra of Fig. 62. The identification of peaks A, B, C, D, and E is indicated below the curve representing 11.

FIGURE 67 Laccase Deconvolution Peak Intensities vs. Irradiation Time

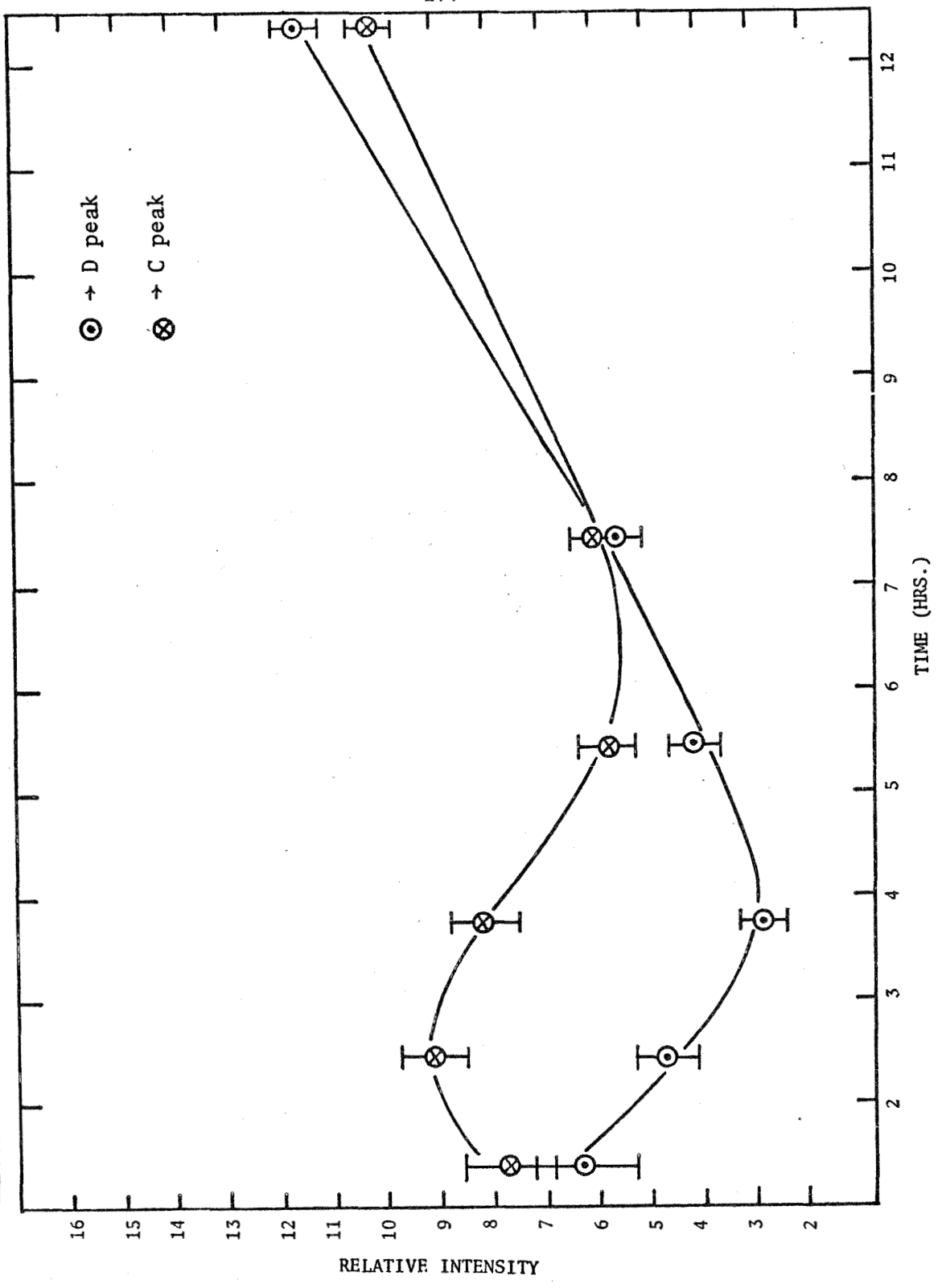


Figure 66 shows the results of curve resolution of spectra 08 through 11. The basic curve shape is described at the beginning of this chapter. These deconvolutions are the result of six different determinations for each spectrum. The position of the fitted bands was found to vary by $\pm 1.3\%$. The area of any convolution component varied by about $\pm 1.9\%$. The peaks noted A, B, C, D, and E varied in position by $+2.1\%$ to -1.2% going from 08 through 11. As has been described earlier, position, width, and height of each component were permitted to vary for best visual fit to the data. Peaks beyond E to higher binding energy and below A to lower binding energy were fit in order to compensate for changes in the baseline. The result of these experiments is plotted for peaks D & C (Fig. 67) which are the major components of the primary Cu $2p_{3/2}$ line in Laccase. Relative intensity is plotted vs. accumulated irradiation time in hours. The curve denoted C shows an increase in intensity to a maximum then falls off at about 5 to 7 hours, and increases again with extended irradiation time. The initial increase is due to photo-reduction of Cu^{II} to Cu^{I} , the subsequent decline corresponds to $\text{Cu}^{\text{I}}\text{-Cu}^{\text{O}}$ conversion, and the final rise to increased concentration of Cu^{I} because of evaporation of decomposed protein. Curve D, which corresponds to the 933.5 eV peak of the Laccase spectra, decreases because of the photoreduction $\text{Cu}^{\text{I}}\text{-Cu}^{\text{O}}$ and then increases as, again, the concentration of Cu^{I} is increased when the protein evaporates. It is seen that decomposition of the protein becomes significant after 7 to 8 hours when monochromatized $\text{AlK}\alpha_{1,2}$ radiation is used (HP 5950A model). During the experiment with Stellacyanin in the McPherson ESCA 36 instrument, total decomposition of the protein occurred already after 2

TABLE 11
Assignments of Binding Energies for Sulfur 2p_{3/2}

<u>Spectrum #</u>	<u>Compound Name</u>	<u>Sulfur Configuration</u>	<u>Binding Energy (eV)</u>
165	n-propylthiouracil Cu ^I	$\text{>C}-\text{S}^{\text{I}}-\text{Cu}^{\text{I}}$	162.8
170	Cu ^{II} bis-n-butylthioacetate	$\text{>C}-\text{S}-\text{C}=\text{C}$ Cu ^{II}	164.2
174	1,2-dibutylthioethane Cu ^{II} Cl ₂	$\text{>C}-\text{S}-\text{C}=\text{C}$ Cu ^{II}	164.3
188	di-(acetothio)ethane Cu ^{II}	$\text{>C}-\text{S}-\text{C}=\text{C}$ Cu ^{II}	164.6 164.9
193	(Cu ^I) ₂ Cu ^{II} (penicillamine) ₂	$\text{>C}-\text{S}^{\text{I}}-\text{Cu}^{\text{I}}$ $\text{>C}-\text{S}^{\text{II}}-\text{Cu}^{\text{II}}$	162.6 163.5
558	"L"Cu ₂ OC ₃ H ₇	$\phi-\text{S}^{\text{I}}-\text{Cu}^{\text{I}}$ $\phi-\text{S}^{\text{II}}-\text{Cu}^{\text{II}}$	161.9
564	"Q"Cu ₂ OC ₂ H ₅	$\text{>C}-\text{S}^{\text{I}}-\text{Cu}^{\text{I}}$ $\text{>C}-\text{S}^{\text{II}}-\text{Cu}^{\text{II}}$	162.5
711	Stellacyanin	$\text{>C}-\text{S}^{\text{I}}$ $\text{>C}-\text{S}^{\text{II}}-\text{Cu}^{\text{II}}$	161.8 163.7
		R-S-S-R	164.8
		SO ₄ ²⁻	167.7

TABLE 11, CONTINUED

Binding Energy Assignments for Sulfur $2p_{3/2}$

<u>Spectrum #</u>	<u>Compound Name</u>	<u>Sulfur Configuration</u>	<u>Binding Energy (eV)</u>
714	Laccase	$\begin{array}{c} >C-S-S-C= \\ \quad \\ I \quad Cu^I \end{array}$	161.1
		$\begin{array}{c} >C-S^{\cdot-} \cdots \cdots Cu^{II} \\ R-S-S-R \end{array}$	162.4
		R-S-S-R	165.0
		SO ₄ ²⁻	167.4
718	Hemocyanin (oxy)	$\begin{array}{c} >C-S^{\cdot-} \cdots \cdots Cu^{II} \\ R-S-S-R \end{array}$	163.9
		R-S-S-R	165.1
		SO ₄ ²⁻	167.3
732	Erythrocyuprein	S ⁻ (?)	160.9
		$\begin{array}{c} >C-S^{\cdot-} \\ >C-S^{\cdot-} \cdots \cdots Cu^I \\ >C-S^{\cdot-} \cdots \cdots Cu^{II} \end{array}$	161.8
		SO ₄ ²⁻	162.8
		SO ₄ ²⁻	163.9
		SO ₄ ²⁻	167.3
503	n-Pr ₄ N ₂ FeS ₄ (SET) ₄		161.2
			162.3
			163.7
			164.0
			164.8
			165.1
			168.7

TABLE 11, CONTINUED
 Assignments of Binding Energies for the Sulfur $2p_{3/2}$

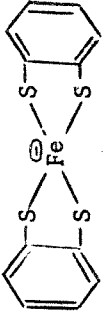
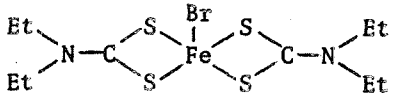
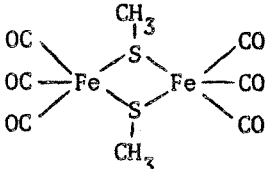
<u>Spectrum #</u>	<u>Compound Name</u>	<u>Sulfur Configuration</u>	<u>Binding Energy (eV)</u>
525	$n\text{-Bu}_4\text{N}_2\text{Fe}(\text{SCH}_2\text{CH}_2\text{S})_2$		161.2 162.4 164.8
534	$\text{Fe}(\text{SP}\phi_2\text{NC}(\text{NC}_4\text{H}_8)\text{S})_3$		161.3 162.4 162.4
538	$\text{Fe}(\text{SP}\phi_2\text{NP}\phi_2\text{S})_2$		162.1
546	$\text{Fe}(\text{SP}\phi_2\text{NP}\phi_2\text{O})_3$		160.0 161.9 163.0 163.7
572	2Fe Ferredoxin		164.0 165.2
577	4Fe Ferredoxin		160.3 161.1 161.5 163.2 164.5 165.8
736	FeS_2		161.1
737	FeS		160.3
739			161.0

TABLE 11, CONTINUED

Assignments of Binding Energies for the Sulfur 2p_{3/2}

<u>Spectrum #</u>	<u>Compound Name</u>	<u>Sulfur Configuration</u>	<u>Binding Energy (eV)</u>
742			161.0
746			161.8

hours because the x-ray flux from the MgK α source used here is about 10^3 times greater than that of the HP unit. In this case, the satellite peaks are not even observed.

In addition to the copper spectra, the sulfur spectra of the model compounds and the proteins Stellacyanin, Laccase, and Hemocyanin are compiled in Table 11, together with re-calculated data on Erythrocyprin from Jung's work^{93,94} and data discussed in Chapter VII. All sulfur spectra show considerable detail; only the prominent bands are listed in Table 11. Stellacyanin shows peak at 161.8, 163.7, 164.8, and 167.7 eV, Laccase at 161.1, 162.4, 164.1, 165.0, and 167.4 eV and Oxyhemocyanin at 163.9, 165.1, and 167.3 eV. The Varian IEE-15 spectrum reported by Jung et al. shows peaks at 160.9, 161.8, 162.8, 163.9, and 167.3 eV. All the peaks at 167.4 ± 0.3 eV can be attributed to sulfate or some other form of oxidized sulfur. The slight differences in observed binding energies represented by the 167 eV peaks could be accounted for by Madelung effects for charged species or by minor chemical shift variations.

The sulfur 2p lines at 163.9 ± 0.2 eV are assigned to metal-bound cystine sulfur while those in the region of 165.0 ± 0.2 eV are assigned as free cystine or cystine sulfur. The 161.8 eV peak in Stellacyanin and the 161.1 eV and 162.4 eV peaks in Laccase are intriguing. From the model-complex studies, the 162.4 eV peak in Laccase can be attributed to R-S⁻ bound to Cu^{II} but the 161.8 eV peak of Stellacyanin seems too low for such an explanation.

It is possible that this peak arises from R-S⁻ bound to the photo decomposition product Cu^I, but the anticipated binding energy should then be

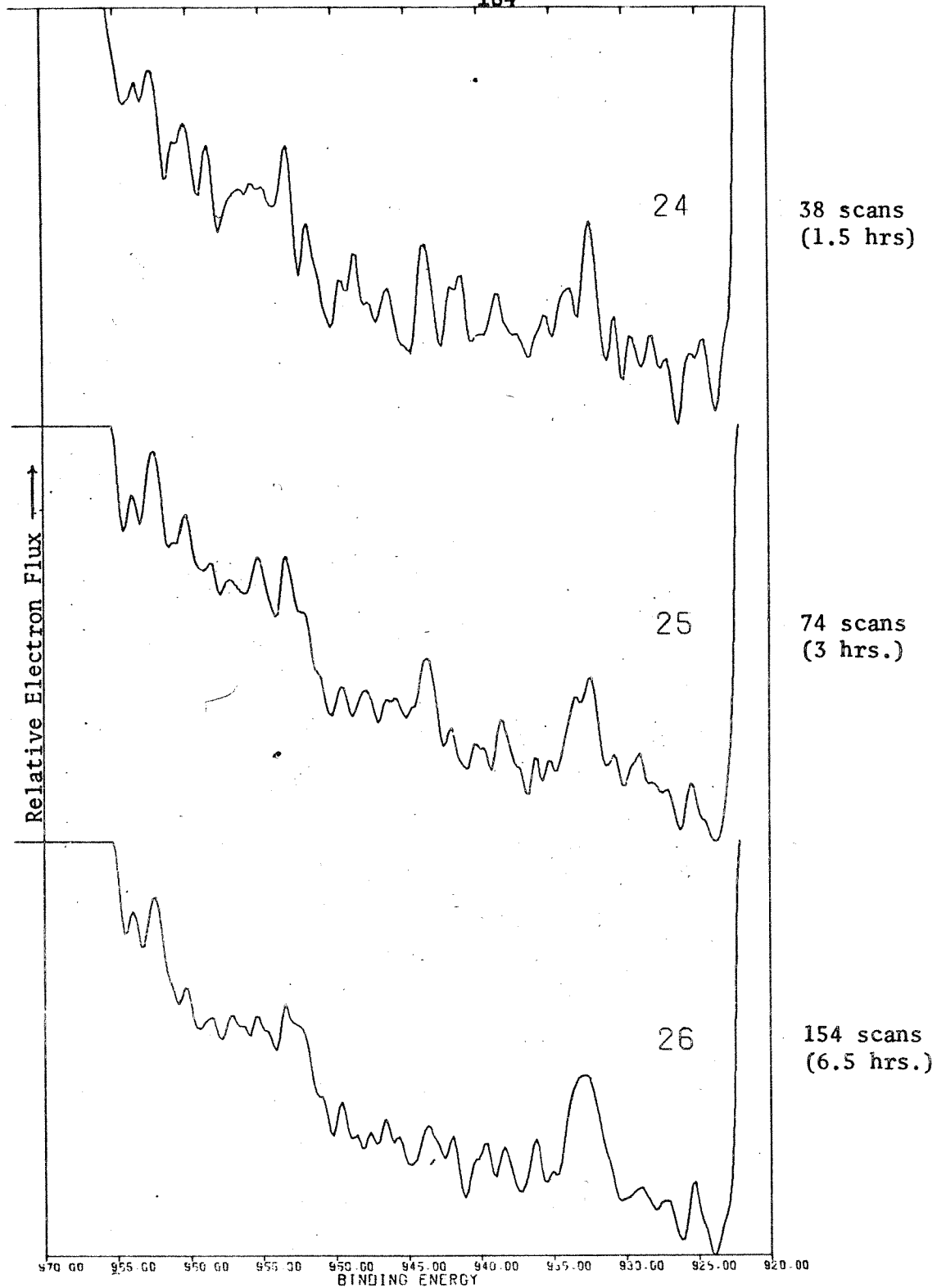


Figure 68. Copper 2p spectra of Hemocyanin listed after the data accumulation times given on the ordinate.

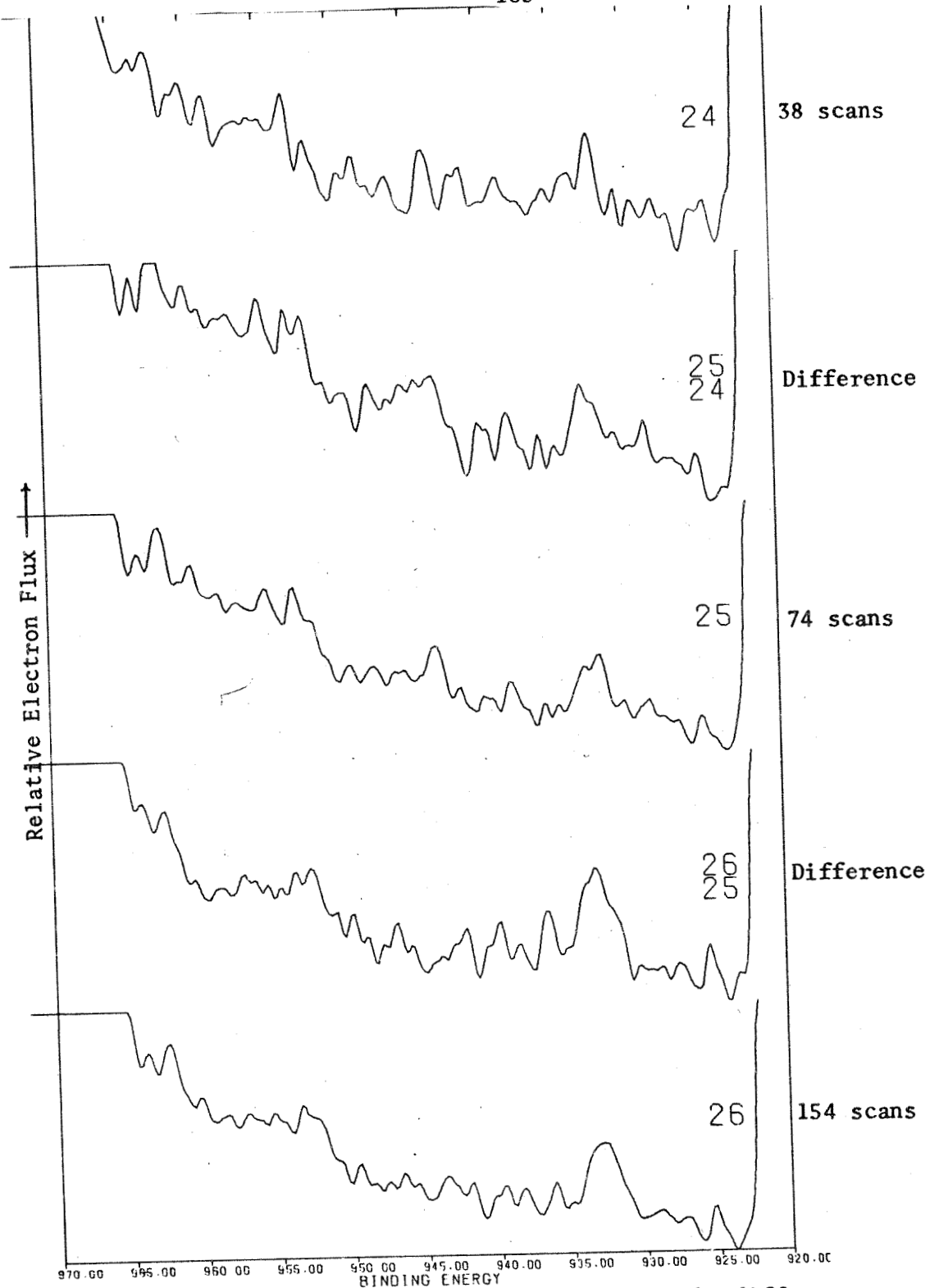


Figure 69. Copper 2p spectra of Hemocyanin and the difference spectra taken to profile the species which existed throughout the experiment.

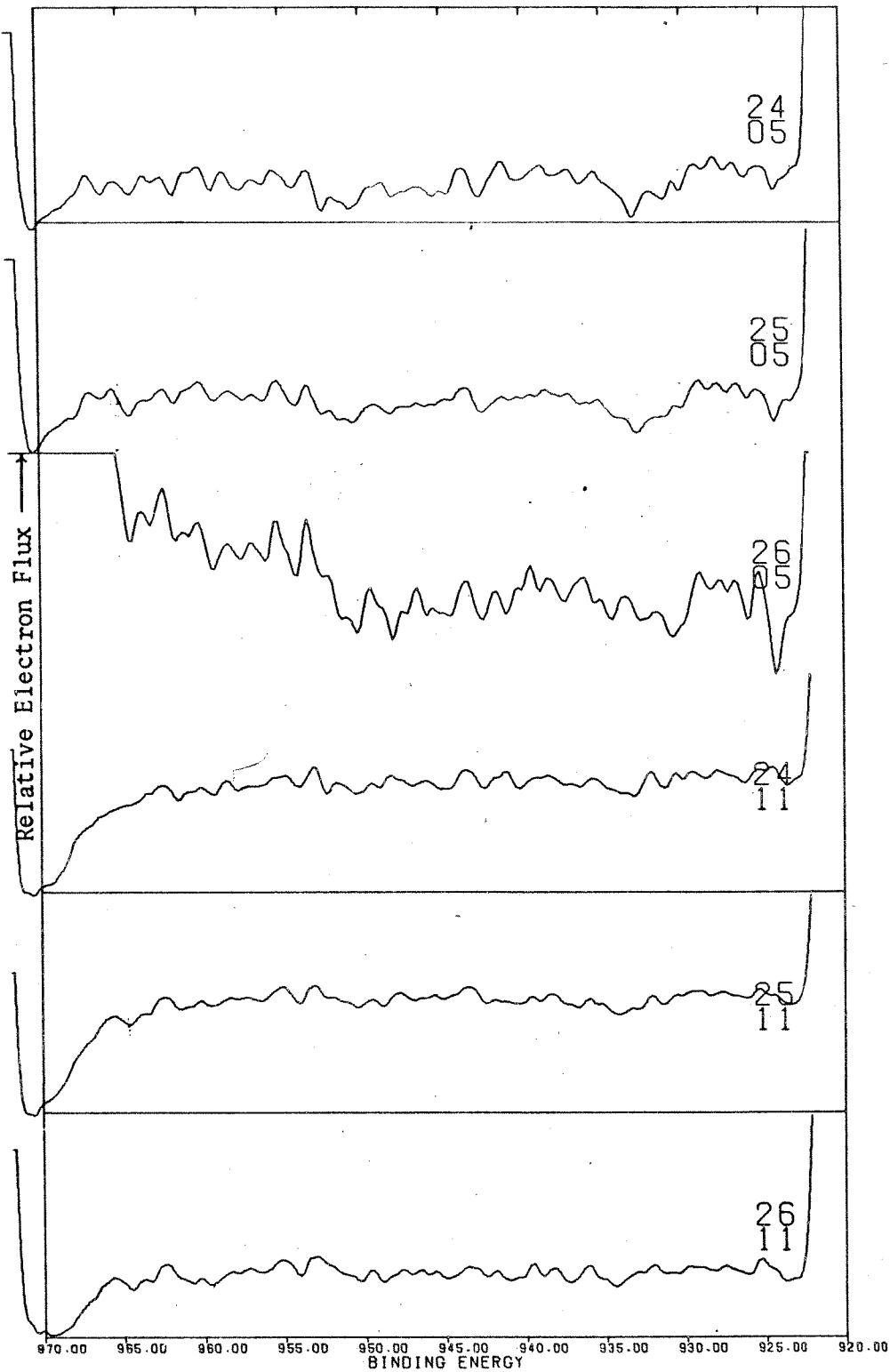


Figure 70. Difference spectra which compare the 3 Hemocyanin Cu₂p spectra of Fig. 68 with the 77 scan spectra of Stellacyanin (05) and the 5-hour spectrum of Laccase (11).

about 162.5 eV. The highly negative sulfur represented at 161.1 eV in Laccase must either be free sulfide, which is conceivable due to impurity concentration at the surface of a thin crystal, or must be assigned as a bridging disulfide as suggested in Chapter VII.

The observed difference in the low-binding energy sulfur of Laccase and that of Stellacyanin is 0.7 eV, which is intriguingly close to the values observed for differences between free sulfur ligands and those bound to copper. The author, therefore, suggests that the peak at 161.8 eV for Stellacyanin represents a precursor of the copper bound site in Laccase at 161.1 eV. Further study of sulfur in metalloproteins will attempt to make this assignment on less qualitative terms.

The sulfur spectrum of Hemocyanin is representative for sulfate or oxidized sulfur together with free (165.1 eV and 163.9 eV) cystine sulfur bound to Cu^{II} . Here, no evidence of Cu^{I} -bound sulfur was observed. The Cu 2p spectra of this protein are given in Fig. 68 as a function of time. Spectrum 24 was dumped after 38 scans (1 hr. 30 min.), 25 after 74 scans (3 hrs.), and spectrum 26 after 154 scans (6hrs, 30 min.).

Figure 69 profiles by means of difference spectra the photo decomposition. The change in relative intensities of the peaks at 933.9 eV (Cu^{II}) and 952.4 eV (Cu^{I}) is evident as is the reduction in the intensity of the satellites. A list of what are believed to be satellites is given in Table 10.

Figure 70 shows two sets of difference spectra. The first three were obtained by subtracting the Stellacyanin spectrum 05 from those of Hemocyanin 24,

25, and 26. The second set of three represents the result obtained by subtracting the Laccase spectrum 11 instead.

The Stellacyanin spectra have overcompensated the copper region and in particular the peak at 932.5 (24-05 and 25-05). In spectrum 26-05, the differences are so small that the noise dominates.

In the second set of difference spectra slight overcompensation at 935.0 eV is observed, and the satellite region appears to be dissimilar.

The relative intensities of the Cu 2p line of these proteins indicate that there are significant differences in the apparent copper concentrations. Normalized to the intensity of the oxygen Auger line at 981 eV, the relative intensities were as follows: 3.2 - Plastocyanin, 7.2 - Stellacyanin, 2.5 - Laccase, and 3.3 - Hemocyanin. The accepted values for the bulk weight percentages of copper were 0.6% (Plastocyanin), 0.4% (Stellacyanin), 0.2% (Laccase), and 0.3% (Hemocyanin) respectively. Since the observed line intensity does not correspond to these bulk concentrations, one may conclude that the intensity variation is caused by differences in the depths of the copper atoms in the proteins. The copper atoms in Plastocyanin are approximately 70% deeper than in Stellacyanin. The four copper atoms of Laccase would average 30% deeper than these in Stellacyanin and those of Hemocyanin would lie about 40% deeper.

D. Conclusions

These studies of model complexes have demonstrated that there are major differences between the spectra arising from diamagnetic d^{10} Cu(I) and paramagnetic d^9 Cu^{II}. Photoreduction of Cu^{II} to Cu^I has been observed,

the rate of which appears to be determined by the coordination. As regards the intensity and position of satellite peaks in the spectra of cupric compounds, there is again a dependence upon the coordination.

The data on all the copper proteins represent similar satellite structure. Because of the time required to accumulate good statistics, the copper in Stellacyanin and Plastocyanin underwent considerable photoreduction. The proteins appear to be more sensitive to reduction than the model complexes. This could be understood in terms of the availability of sites in Stellacyanin and Plastocyanin to stabilize the Cu^{I} photo product. Thus, the peak at 932.5 eV observed in Stellacyanin might be only partially due to decomposition product and probably indicates increased population of the Cu(I) site. This interpretation is consistent with the observation of a smaller difference in binding energy between Cu^{II} and Cu^{I} in the photoreduction doublet for the proteins than for the model complexes.

Spectral analysis of the Laccase experiments indicate that protein decomposition is extensive after 7 to 8 hours of irradiation. Further, the Cu 2p spectra indicate the intensity of one peak at 933.5 eV remains relatively constant, while the ratio of the intensities of the two peaks at 934.6 and 932.7 eV changes drastically and finally inverts. Difference spectra indicate that the doublet 934.4, 933.3 eV of Plastocyanin caused by photoreduction is similar to that of Laccase. Removal of this doublet through subtraction shows a second decomposition doublet at 933.7, 931.3 eV but does not perturb the peak at 932.5 eV. The apparent satellite structures of Plastocyanin and Laccase are very similar at the low-binding energy while at high-binding energy the Laccase and Stellacyanin satellites are very

similar. In the model complexes, this particular type of satellite structure is observed only when sulfur is coordinated to the copper. The photoreduction doublet 933.9, 932.5 eV is common to Laccase and Stellacyanin.

The line at 934.6 eV is attributed to Type 1 copper in Laccase and the line at 933.7 eV (seen in both Plastocyanin and Laccase) is assigned to Type 2 copper. Thus, the line at 933.5 eV in Laccase corresponds to a high concentration of a specific type of Cu(I) site. The binding energy is intermediate between those expected for cuprous states and cupric states in the model complexes. Upon extended irradiation, the relative intensities of this Cu(I) peak at 933.5 eV and the one at 932.7 eV corresponding to photoreduction become equal. Quantitative evaluation of Cu 2p spectra is possible only after photoreduction to Cu(I), because of the satellite problem. The assignment of 2 Cu atoms to the peak at 933.5 eV is consistent with these results. It is also suggested that the peak at 931.3 eV corresponds to a decomposition product, probably Cu metal. The reduction peak at 932.7 eV is attributed to the Type 1 copper (934.6 eV) and the anticipated decomposition product of type 2 copper was not detected at 932.7 eV.

The sulfur spectra of the copper metalloproteins is also consistent with the assignment of a $\text{Cu}^{\text{I}} \cdots \text{S}^- \text{-R}$ moiety in Laccase. A sulfur peak at uniquely low binding energy is observed in Laccase which the author assigns as a disulfide bound to Cu(I). The disulfide appears to be present in Stellacyanin as well but here, it is not bound to Cu(I).

This interpretation is consistent with the $\text{Cu(I)} \cdots \overset{\text{R}}{\text{S}} - \overset{\text{R}}{\text{S}} \cdots \text{Cu(I)}$ moiety proposed by Williams⁸⁰ and Hemmerich⁸⁷. Electron transfer from Cu(I) to the disulfide is required to explain the magnitude of the apparent negative charge on sulfur.

The appearance of a photoreduction doublet and satellite structure in hemocyanin can be explained only by a Copper II moiety. This Cu(II) site is apparently spin-spin coupled since no EPR is observed. The sulfur spectra of the protein is consistent with Cu(II) bound to sulfur.

The oxygen spectrum shows a peak at low binding energy (530.8 eV). This oxygen must have a highly negative character. Initial results indicate that a superoxide configuration is highly probable.

VII. STUDIES OF THE IRON-SULFUR MOIETY IN
2-IRON AND 4-IRON FERREDOXINS

A. Introduction

Although intensive study of iron-sulfur proteins only began within the past decade, considerable structural information is available concerning the coordination and geometry of the active sites. Since these proteins are well-characterized through x-ray crystallography, investigators have used virtually every spectroscopic tool to study the applicability of modern instrumental methods.

Biologically, the ferredoxins are involved in a large variety of electron transfer processes ranging from nitrogen fixation to photosynthesis. These proteins of relatively low-molecular weight have two to eight iron atoms at each active site and an equal number of labile (loosely bound) or inorganic sulfide ions per molecule. Analyses of the amino-acid sequences and residues of a number of plant and bacterial ferredoxins show remarkable similarities. These have led to the development of a model elucidating the evolution of the organisms which contain these proteins.

The structural chemistry of the active sites of the non-heme iron sulfur proteins has been reviewed recently¹⁰⁴. The physiochemical properties have been treated in the Tsibis and Woody review¹⁰. The structure of Rubridoxin, a one iron-0 labile sulfide protein has been given by Jensen et. al.^{105,106} who showed that the active site was comprised of a distorted

104. Mason, R., and Zubieta, J.A., Angewandte Chemie, 85, 390 (1973).

105. Herriott, J.R., Sieker, L.C., Jensen, L.H., and Lovenberg, W., J. Mol Bio., 50, 391 (1970).

106. Watenpaugh, K.D., Sieker, L.C., Herriott, J.R., and Jensen, L.H., Cold Spring Harbor Symp Quant Biol., 36, 359 (1971).

Fe-S₄ tetrahedron. High-potential iron protein (HiPIP) has been isolated from Chromatium and was refined structurally with data corresponding to 2.0 Å resolution. The results have shown the existence of a cubic Fe₄S₄ cluster in which iron and sulfur atoms are at alternate vertices^{107,108}. Carter et.al.¹⁰⁸ pointed out the structural similarity between the Fe₄S₄ cluster in reduced HiPIP and the oxidized Fe₄S₄ cluster in the four-iron ferredoxins. Recent structural results on the 8 iron-8 sulfur clostridial ferredoxin isolated from *M. aerogenes* show the presence of two Fe₄S₄ clusters separated by 12 Å. Each of these has the same cubic Fe₄S₄ structure that was found in HiPIP¹⁰⁹.

The crystallographic studies of these iron-sulfur proteins have stimulated electronic structural investigations and a series of efforts to synthesize relevant model complexes. The syntheses have proven to be very difficult. Until very recently the best models have been the dimeric and tetrameric dithiolene complexes^{110,111,112}. A new iron-sulfur cluster has been reported recently by Herskovitz et. al.¹¹³ This compound, Fe₄S₄(SCH₂R)₄²⁻, which is referred to in this work as Holm's compound, has a structure remarkably similar to that of the Fe₄S₄ group observed in HiPIP^{108,113}.

-
107. Carter, C.W., Jr., Freer, S.T., Xuong, Ng.H., Alden, R.A., and Kraut, J., Cold Spring Harbor Symp Quant Biol., 36, 381 (1971).
 108. Carter, C.W., Jr., Kraut, J., Freer, S.T., Alden, R.A., Sieker, L.C., Adman, E., and Jensen, L.H., Proc Nat Acad Sci, USA, 69, 3526 (1972).
 109. Sieker, L.C., Adman, E., and Jensen, L.H., Nature, 235, 40 (1972).
 110. Balch, A.L., J Amer Chem Soc, 91, 6962 (1969).
 111. Balch, A.L., Dance, I.G., and Holm, R.H., J Amer Chem Soc, 90, 1139 (1968).
 112. Davison, A., Howe, D.W., and Shawl, E.T., Inorg Chem, 6, 458 (1967).
 113. Herskovitz, T., Averill, B.A., Holm, R.A., Ibers, J.A., Phillips, W.D., and Weicher, J.F., Proc Natl Acad Sci, USA, 69, 2437 (1972).

A very detailed and accurate crystal-structure investigation¹¹³ indicates that the $\text{Fe}_4\text{S}_4(\text{RS})_4^{2-}$ cluster in Holm's compound contains two types of sulfur, a mercaptide and an inorganic sulfide. Although electroneutrality requires the presence of 2 Fe(II) and 2 Fe(III), the available physical data (EPR, NMR, Mossbauer, etc.) indicate that only a single species is present. The purpose of the present investigation is to determine the valence state of iron species within the time scale of photoemission and hole relaxation ($\sim 10^{-16}$ sec.). Also, a study of the electronic structure of the sulfur in the cluster needs to be re-examined to resolve the ambiguities arising from the low-resolution ESCA work reported in the literature¹¹³.

ESCA studies on iron-sulfur proteins were described by Kramer and Klein¹¹⁴ prior to the successful synthesis of Holm's cluster compound. Kramer and Klein's investigations suffered seriously because of poor instrumentation requiring choice of the weak Fe $3p_{3/2}$ line rather than the strong Fe $2p_{3/2}$ line. Nevertheless, the investigations showed that sulfur exhibited a large chemical shift.

An attempt to study the valency of iron in ferredoxins by means of ESCA was also reported by Liebfriz¹¹⁵. The stronger Fe 2p lines were investigated using several dithiolene model complexes.

Both of the above studies were carried out with the use of x-ray sources of considerable intensity not employing monochromators. Thus, considerable

114. Kramer, L.N., and Klein, M.P., in Electron Spectroscopy, ed., Shirley, D.A., (North Holland) Amsterdam, pp. 733-751 (1972).

115. Liebfriz, D., Angew Chem Int.Ed., **11**, 232 (1972).

radiation damage must have occurred in their samples.

This chapter describes ESCA experiments on iron, sulfur, carbon, nitrogen, and oxygen in 2 iron-2 sulfur spinach ferredoxin and in 4-iron - 4-sulfur high-potential iron protein. These studies are correlated with similar investigations of various model complexes including the dithiolene and Holm's Fe_4S_4 cluster compounds.

All the data relating to sulfur-containing compounds, including those taken from the literature, are discussed in Chapter VI. No similar extensive compilation of ESCA data on iron systems is available in the literature.

It has been reported that the binding energy corresponding to the $\text{Fe } 2p_{3/2}$ line varies by about 6.0 eV with changes in the chemical environment¹¹⁶.

The observed line width is governed by multiplet and shake-up effects which are determined by the spin state of the Fe core¹¹⁷. ESCA spectra of ferric and ferrous cyano complexes have been used to show the existence of two iron species with localized charge, Fe^{II} and Fe^{III} , in prussian blue¹¹⁸. Auger-electron emission spectra of iron obtained by photon and electron excitation have been described in the literature¹¹⁹. Whenever possible, valencies and binding energies given in this thesis have been standardized so as to permit comparison with published data.

116. Liebfriz, D., and Bremser, W., Chemiker-ZTG, 94, 232 (1972).

117. Fadley, C.S., and Shirley, D.A., Phys Rev A, 2, 1109 (1970).

118. Wertheim, G., and Rosencwaig, A., J Chem Phys, 54, 3235 (1971).

119. Yin, L.I., Yellin, E., and Alder, I., J Appl Phys, 42, 3595 (1971).

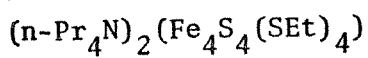
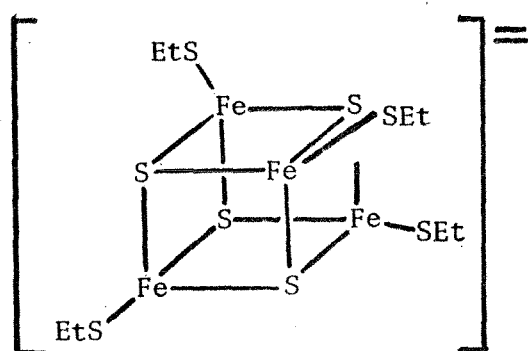
B. Experimental

J. Rawlings provided samples of the 2 Iron - 2 Labile sulfur spinach ferredoxin and the 4 Iron - 4 Sulfur high-potential iron protein from Chromatium, which were prepared according to the method of Bartsch¹²⁰. Samples of the cluster compound $(n\text{-Pr}_4\text{N})_2\text{Fe}_4\text{S}_4(\text{S Et})_4$ were provided by Dr. R. H. Holm. Dr. O. Siiman supplied samples of the dithiolene complex $(n\text{-Bu}_4\text{N})_2(\text{Fe}(\text{SCH}_2\text{CH}_2\text{S})_2)_2$ as well as $\text{Fe}(\text{SP}\phi_2\text{NP}\phi_2\text{S})_2$, $\text{Fe}(\text{SP}\phi_2\text{NP}\phi_2\text{O})_3$ and $\text{Fe}(\text{SP}\phi_2\text{NC}(\text{NC}_4\text{H}_8)\text{S})_3$. Additional iron and sulfur compounds were obtained commercially as reagent grade.

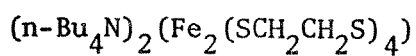
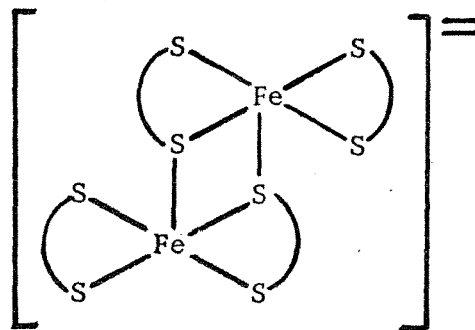
The samples were prepared for introduction into the ESCA spectrometer by the methods described previously in Chapter III and VI. Thin films of the model complexes were formed by evaporation of solutions of the tetra-alkyl ammonium salts in nitromethane and acetonitrile under dry nitrogen. The protein samples were prepared using the "frozen-solution" technique and also the thin film method. In each case, the starting materials consisted of freshly prepared aqueous solutions of the protein containing a phosphate buffer. The samples were kept under nitrogen during transport from the preparation area to the spectrometer inlet. Despite these precautions, all samples showed considerable oxidation of the surface.

Sample spectra were taken at 250°K for reasons outlined in Chapter VI. All spectra were initially referenced against the $\text{Au}4f_{7/2}$ doublet and the Fermi edge as previously described. In addition to this initial referencing, the observed spectra were corrected to give a binding energy of 285.4 eV

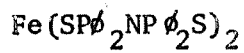
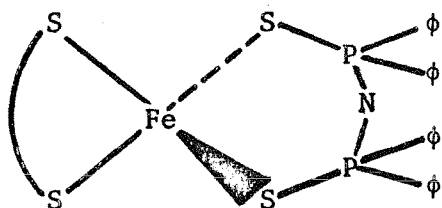
120. Bartsch, R.G., in *Bacterial Photosynthesis*, (Gest, H., San Pietro, A., and Vernon, L.P.) p. 315, Antioch, Yellow Springs, Ohio (1963).



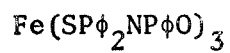
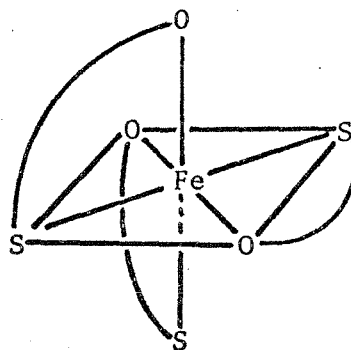
Model Complex #1



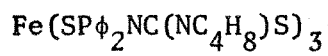
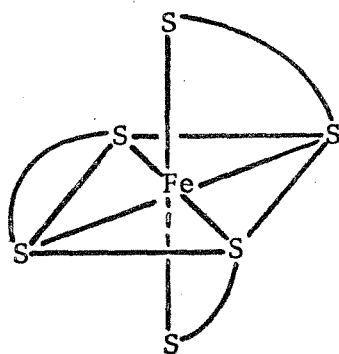
Model Complex #2



Model Complex #3



Model Complex #4



Model Complex #5

TABLE 12 Major Inflections Recorded for the Nitrogen 1s Region

Spectrum Identification Number		130	166	228	506	509	514	521	527	532	540	547	550	556	561	569	574
406.33							406.33										
406.10			406.08	406.04										406.09			405.88
405.67	405.63						405.64			405.88		405.96	405.71		405.70		405.47
	405.43	405.47		405.50		405.56							405.31	405.38			405.22
	405.08	405.10		405.01						404.91	404.86	404.95	404.88	404.80	404.86		404.80
404.83	404.80		404.85			404.62	404.90			404.76				404.48	404.40	404.41	404.42
	404.70			404.63		404.54						404.21	404.39				
404.17	404.13						404.11							404.11			403.85
	403.98	403.97	403.97			403.91				403.61	403.79		403.71		403.78		403.52
	403.78			403.69						403.45				403.53		403.52	403.44
403.50	403.57		403.39	403.38	403.32	403.28							403.19	403.03	403.12	403.10	
	403.05												403.19	403.03	403.12	403.10	402.94
402.98																	
402.67	402.73	402.66	402.72	402.78									402.49	402.69	402.64		
402.53	402.47		402.58	402.53	502.57					402.45			402.31	402.42			
			402.35	402.20									402.31	402.26			402.38
															402.07	402.18	
	401.93	401.93		401.86						402.19				401.84			401.97
										401.82					401.75	401.66	
401.47		401.40		401.57	401.51					401.66			401.78				
	401.38									401.40			401.44				
	401.08	401.02		401.36	401.26	401.34				401.36			401.26	401.33	401.20		401.13
400.93			400.84	400.96	400.80								400.83				
	400.65	400.72								400.71		400.67		400.64			400.54
	400.53	400.37		400.40						400.42			400.42				400.30
400.17			400.34	400.34						400.52				400.36	400.30	400.33	
			400.17	400.14						400.10							400.12

TABLE 12, CONTINUED

		Spectrum Identification Number →																
		130	166	228	506	509	514	521	527	532	540	547	550	556	561	569	574	
Binding Energy (eV) ↑			399.92				399.91					399.86	399.91	399.81		399.84	399.85	
					399.72	399.70			399.78		399.72		399.70		399.63			
		399.50	399.55	399.53													399.56	
			399.28					399.28	399.20	399.37	399.37				399.33		399.22	
				399.03			399.13							399.18		399.15		399.10
		398.92									398.91	398.93			398.89	398.86		
		398.70		398.62				398.61		398.65				398.68		398.66		398.76
					398.46				398.59								398.43	
			398.32				398.28				398.37	398.25	398.22	398.33				398.36
				398.12				398.03								398.19		
			397.98								397.95	397.82				397.90		397.92
			397.73						397.66							397.64	397.63	
		397.50	397.53							397.44	397.46			397.55				397.58
											397.20				397.25	397.28		397.20
							397.10											
	396.92						396.62		396.65	396.62	396.66		396.94		396.75	396.76		
															396.53			
	396.20								396.28	396.34								
											396.06			396.01				
								395.94	395.98						395.85			
														395.27				

TABLE 13

Major Inflections Recorded for the Phosphorus 2p
Region

Spectrum Identification Number →

	533	541	548
↑	136.8	136.6	
	136.3		136.3
		135.9	135.8
	135.6	135.6	
	135.0	135.1	<u>135.1</u>
	134.6	134.5	
			<u>134.3</u>
	<u>133.9</u>		<u>133.8</u>
		<u>133.6</u>	
	<u>133.3</u>		<u>133.3</u>
	<u>132.9</u>		<u>132.9</u>
	<u>132.7</u>		<u>132.6</u>
		<u>132.4</u>	
	<u>131.9</u>	<u>131.9</u>	
			131.5
	<u>131.3</u>	<u>131.2</u>	
	130.7	<u>130.6</u>	130.7
	130.3		

for aliphatic carbons, and 285.0 eV for methyl carbon centers.

All electron spectra displayed as figures in this chapter were filtered with a Weiner filter of 1.0 eV minimum width. Inflections and peak positions were assigned by derivative analysis using routines described by Savitsky⁵⁴.

The DuPont model 310 Curve Resolver was used to deconvolve the sulfur 2p spectra. The line shape used as a standard in this analysis has been described in Chapter VI.

C. Results and Discussion

The model iron complexes investigated in this thesis are represented in Fig. 70. For the sake of clarity, a number has been assigned to each of these: The tetrameric iron sulfur cluster is model #1, the dithiolene complex, $\text{Fe}_2(\text{SCH}_2\text{CH}_2\text{S})_4^{2-}$, is model #2, the tetrahedral (ferrous) complex $\text{Fe}(\text{SP}\phi_2\text{NP}\phi_2\text{S})_2$ is model #3, ferric complex species $\text{Fe}(\text{SP}\phi_2\text{NP}\phi_2\text{O})_3$ is model #4, and the ferric sulfur complex $\text{Fe}(\text{SP}\phi_2\text{NC}(\text{NC}_4\text{H}_8)\text{S})_3$ is model #5.

Each of these contain nitrogen either as the quaternary ammonium cation or as part of the ligands of complexes 3 through 5, which are composed of both aliphatic and aromatic carbons. Models 3 through 5 have two different phosphorus environments. Inflections in the spectra of the N1s region of all compounds studied here are given in Table 12. The phosphorus 2p data are given in Table 13, while the Cls data have already been given in Table 9 of Chapter VI. The inflection points for O1s are given in Table 8, Chapter VI.

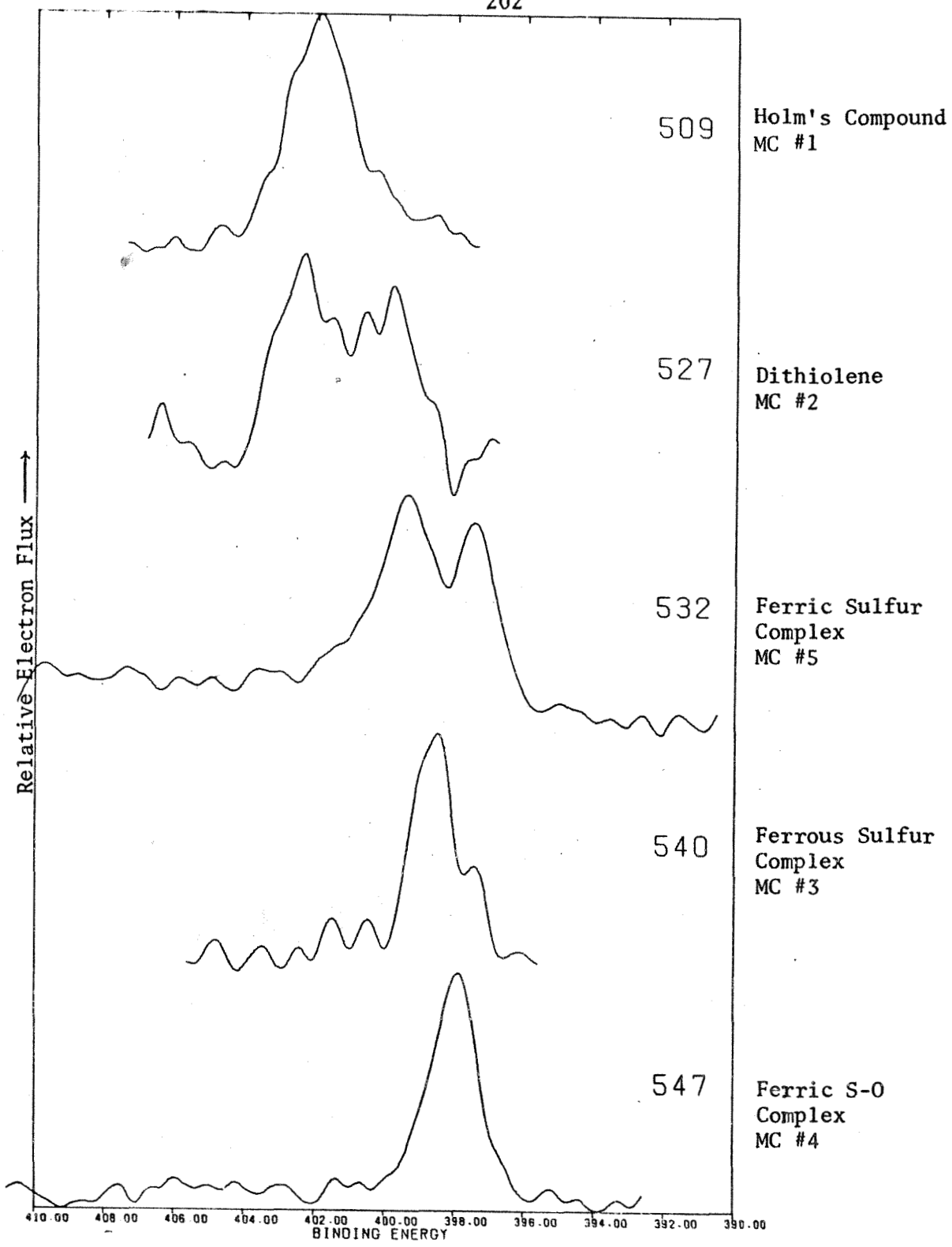


Figure 71. Nitrogen 1s Spectra of iron-sulfur model complexes.

Figure 71 shows the spectral region of nitrogen 1s representing the model complexes. The binding energy interval comprising the nitrogen 1s region ranges from 390.0 eV to 410.0 eV. Spectrum 509 shows the electron spectrum of model #1 (Holm's cluster compound). The peak corresponding to quaternary ammonium nitrogen falls at 401.9 eV. The peaks at lower binding energy probably represent photo decomposition products. Spectrum 527 corresponds to the dithiolene complex, model #2, and the peak at 402.5 eV is attributed to the quaternary nitrogen of the tetra-n-propyl ammonium cation. This spectrum also shows peaks at 399.8 eV which correspond to radiation-damage products (free amine impurities).

Spectrum 509 was taken after less than 10 minutes cumulative x-ray exposure while 527 was taken after 93 minutes. As mentioned, the photo-decomposition product of tetra alkyl ammonium nitrogens studied by the Swedish group¹ correspond to a peak which was 2 eV lower in binding energy than that of the parent species and was assigned to free amines. The group observed that this nitrogen was particularly sensitive to radiation decomposition, but a more recent report¹²⁰ makes no such statement.

In the two cases, 509 & 527, the nitrogen spectra arise from the cation in the thin film sample. No effort has been made to correct for Madelung site effects, since the crystallinity of these films has not been established. In recent work on the photoelectron spectroscopy of quaternary nitrogen compounds^{120a}, Madelung corrections were calculated for all the

120a. Jack, J.J., and Hercules, D.M., Anal Chem, 43, 729 (1971).

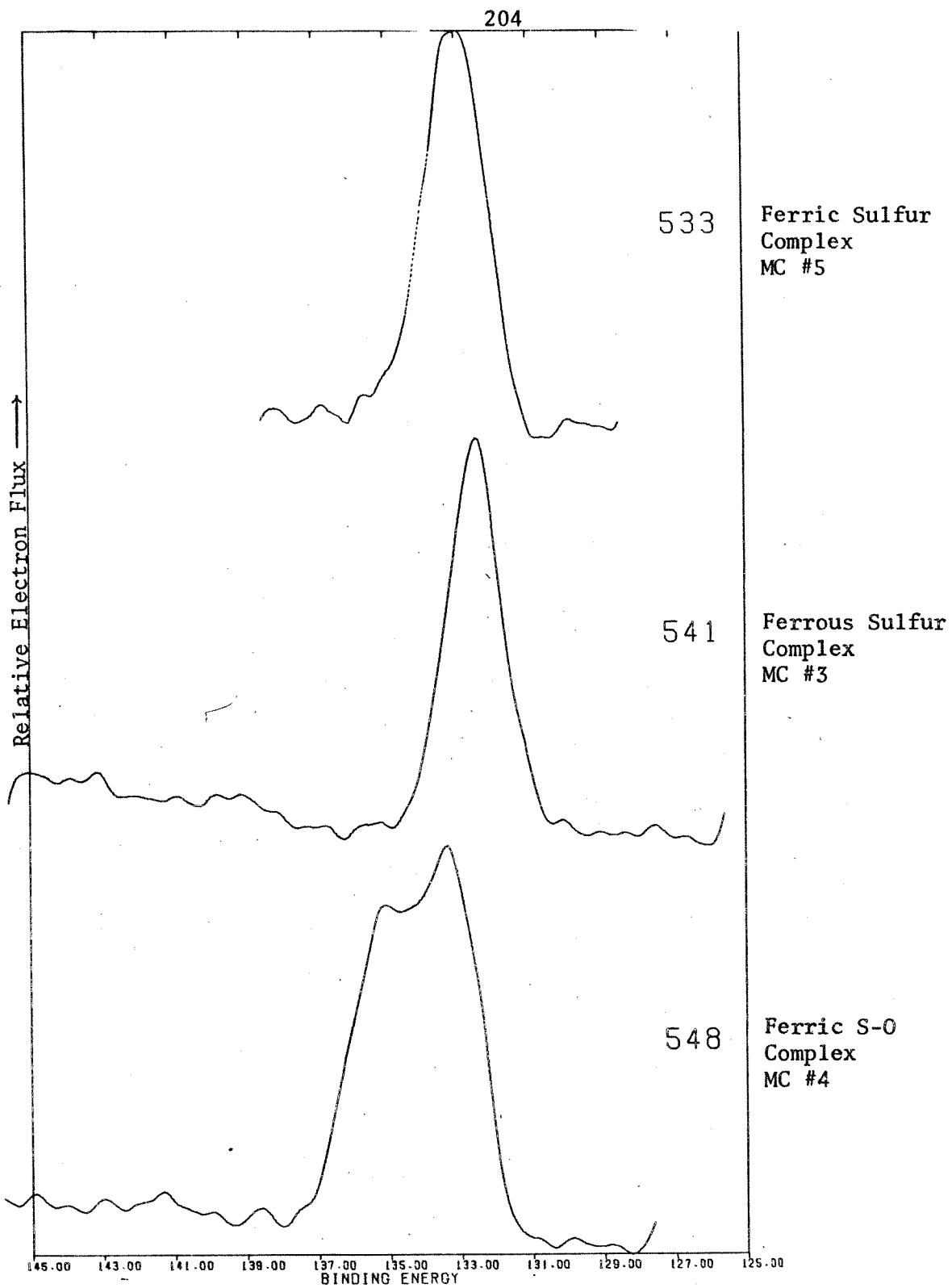


Figure 72. Phosphorus 2p spectra of the iron sulfur model complexes.

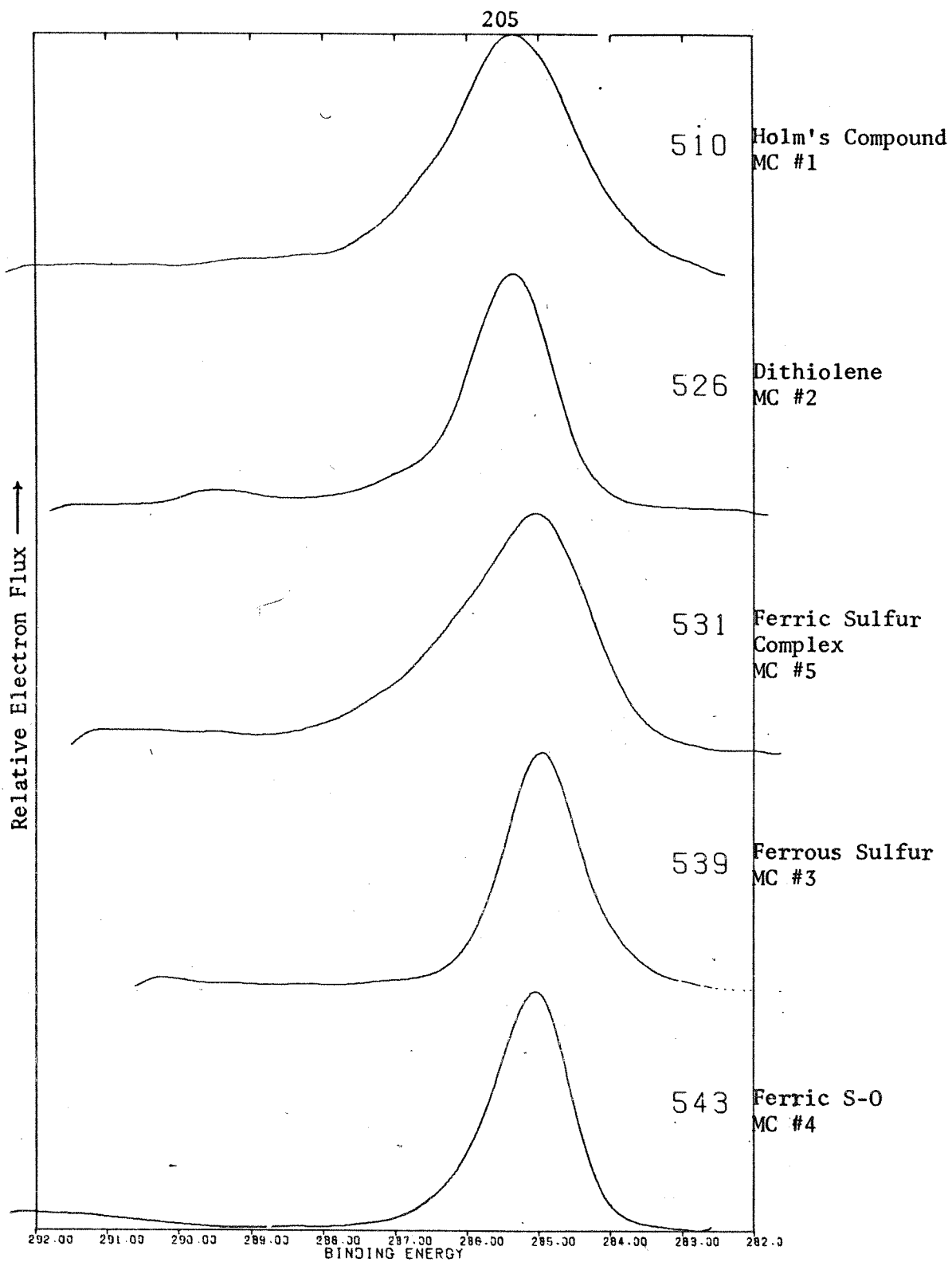


Figure 73. Carbon 1s spectra of the iron sulfur model complexes.

ammonium halides. Stabilization factors varying from 8.3 eV to 6.5 eV were calculated for all the halide anions. It is conceivable that some of the complexity of these peaks can be explained in terms of slightly different lattice sites in the crystal.

Spectrum 532 gives the N1s spectrum of model #5. Two nitrogen environments are resolved. The peak at 399.4 eV is attributed to the heterocyclic nitrogen while the peak at 397.4 eV corresponds to the nitrogen bound to diphenyl phosphine. These interpretations are consistent with those made by Nordberg et. al.¹²¹.

The spectrum of model complex #3 is given as 540. Here, the peak at 398.4 eV corresponds to the nitrogen bound to phosphine. Spectrum 547 gives the nitrogen spectrum of model #4. The major peak is observed at 397.9 eV.

The phosphorus 2p spectra of the iron sulfur complexes 3, 4, and 5 are given in Fig. 72. Spectrum 533 arises from model complex 5 and shows a maximum at 132.9 eV. The spectrum 541 with a maximum at 132.4 eV corresponds to model #3. In spectrum 548 (model complex #4) peaks are observed at 133.3 eV and 135.1 eV. In accordance with simple electronegativity consideration, the lower binding energy peak at 133.3 eV is attributed to phosphorus bound to sulfur and that at 135.1 eV to phosphine.

The carbon 1s spectra of these model complexes are given in Fig. 73. The Fe₄S₄ cluster (model #4) corresponds to spectrum 510, the dithiolene (model

121. Nordberg, R., Albridge, R.G., Bergmark, T., Ericson, U., Hedman, J., Nordling, C., Siegbahn, K., and Lindberg, B.J., Arkiv. For Kemi., 28, 19 (1967).

#2) to spectrum 526, the ferric sulfur complex (model #5) to 531, the ferrous sulfur complex (model #3) to 539, the ferric oxygen-sulfur complex (model #4) to spectrum 543. The Cls spectra of models 3 and 4 are quite similar, as was anticipated. Spectrum 543 shows a tail at high binding energy (at about 286.2 eV) which comprises 10 to 20% of the total peak intensity. The origin of the tail can be attributed to electron withdrawal from the phenyl groups.

The Cls spectrum of model 5 shows a major peak at 285.0 eV which corresponds to phenyl groups of the ligand. In view of the ligand structure, the methylene carbons of the ring system should manifest themselves in a peak at about 285.5 eV. A peak at about 286 eV would be anticipated for the nitrogen-bonded methylene carbons. The trigonal carbon bound to sulfur and nitrogen would be expected to give rise to a peak at about 287.2 eV. These three peaks apparently constitute the tail at high binding energy shown in curve #531.

The spectra arising from the cluster complex and the dithiolene compound are expected to give a primary peak at 285.4 eV characteristic for methylene carbon and a shoulder at 285.0 for methyl carbon. The peaks corresponding to the anion carbons should differ slightly from those corresponding to the cation carbons because of lattice effects. The sulfur-bound methylene groups of the cluster compound should give rise to a peak at about 286.5 eV, having about 13% of the total Cls intensity. A peak of about 25% of the total intensity should be seen in the same region in spectrum 526 representing dithiolene. However, only shoulders are observed at these energies in both spectra and well-resolved peaks occur at about 289.5 eV

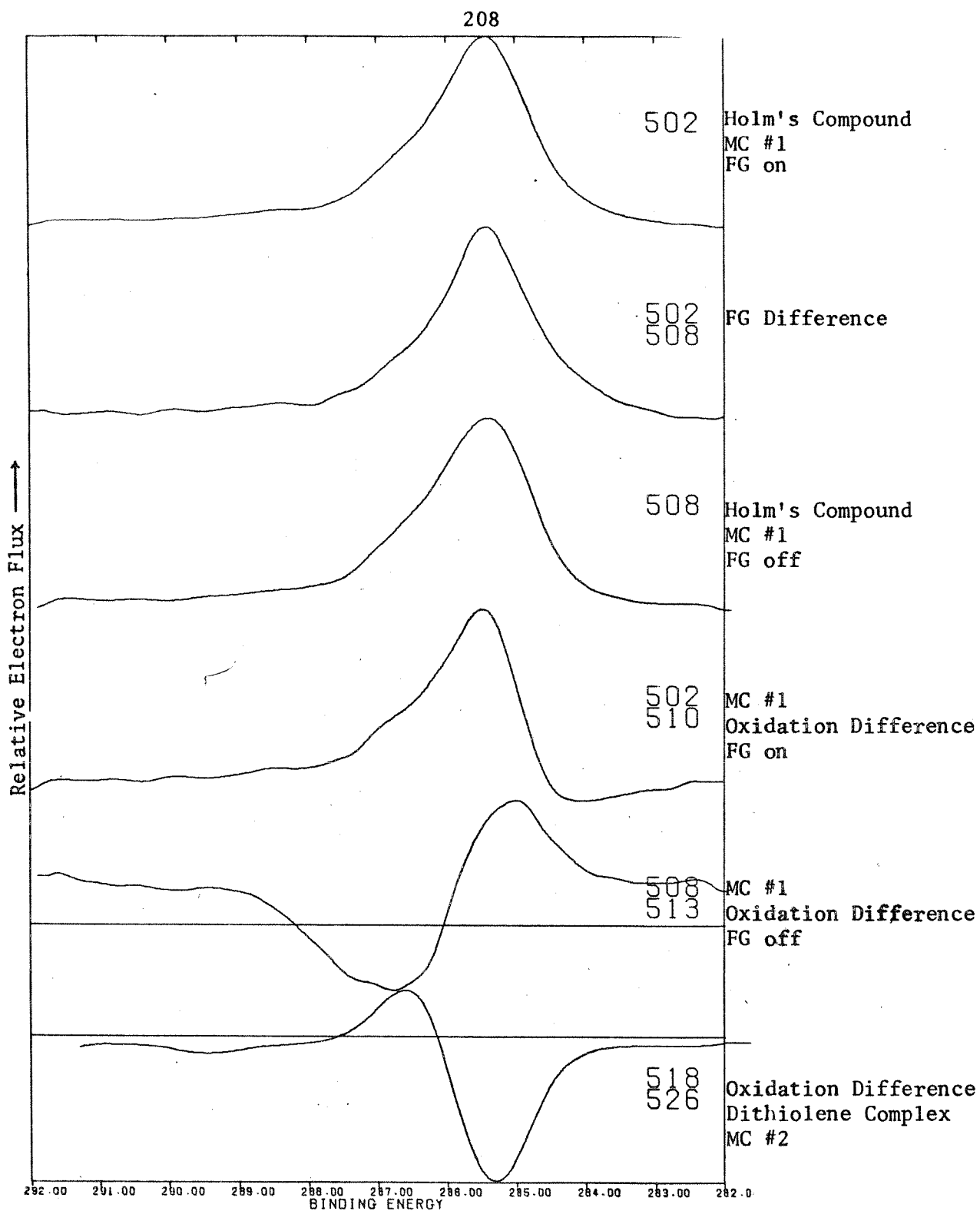


Figure 74. Carbon 1s original and difference spectra for the cluster and dithiolene complexes. 502/508 and 510/513 are FG on/off spectra of the cluster complex where the latter arise from an oxidized sample. 518 and 520 compare oxidation differences for a dithiolene sample.

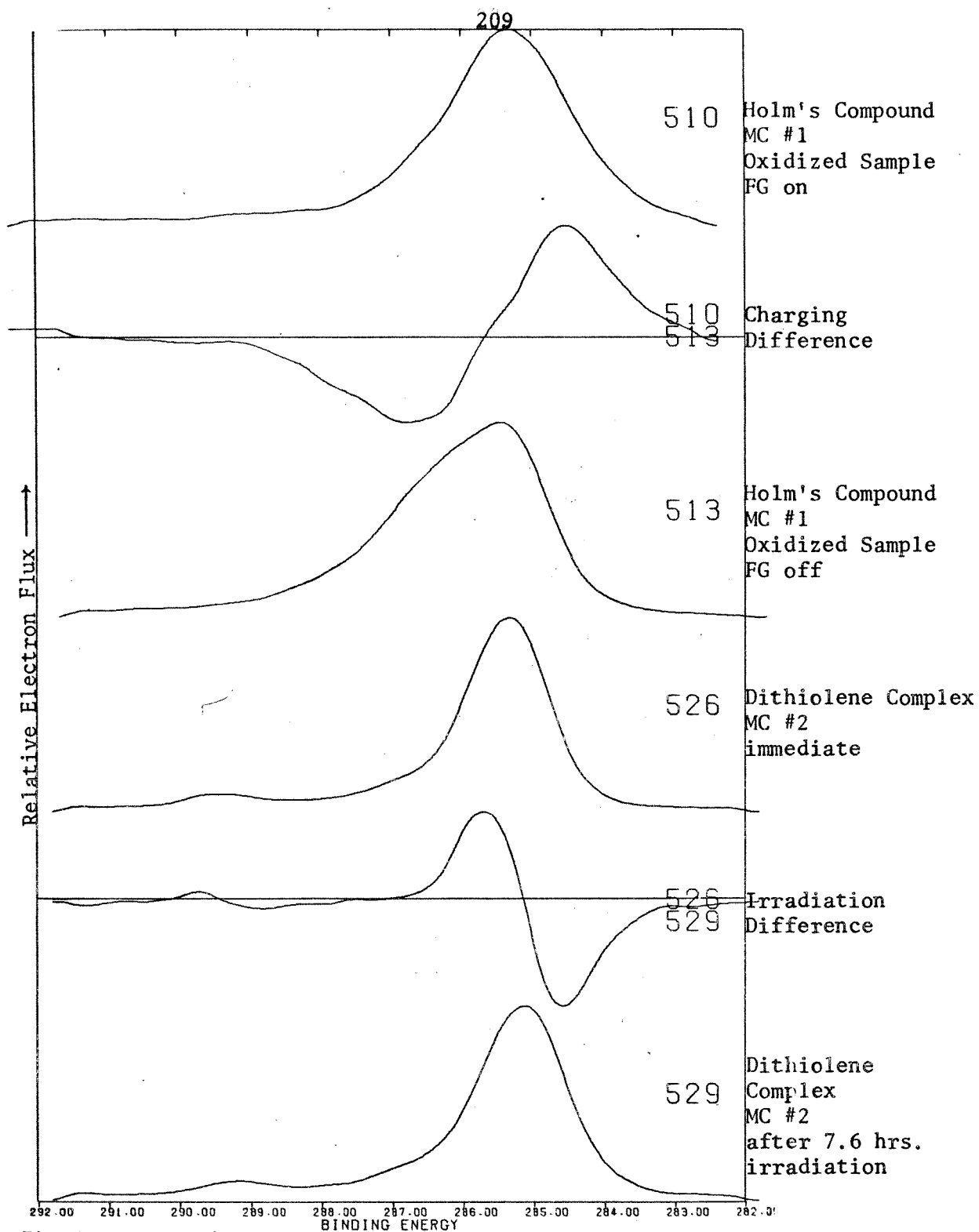


Figure 75. Carbon 1s spectra of the cluster complex (510, 513) and the dithiolene complex (526, 529).

which corresponds to carbonyl or carboxylate carbon. This indicates that the surface is significantly oxidized.

As mentioned previously, the Cls region of the spectrum is monitored to follow the progressing radiation damage. Several of these spectra are reproduced in Figure 74. Spectrum 502 gives the Cls FG-on spectrum of the cluster compound (sample slightly oxidized) and 508 gives the FG-off spectrum of the same sample. Although the band shapes differ, the charging shifts are very small.

Spectrum 510 corresponds to a highly oxidized sample of the cluster compound. The difference spectrum 510-502 emphasizes the effect of oxidization.

Spectra 508 and 513 are the FG-off counterparts of the ones just discussed (502, 510); see difference spectrum 508-513. A higher content of aliphatic carbon is reflected in 508, while 513 shows the effect of a significantly higher content of sulfur-bound carbon. The spectra of the dithiolene (oxidized, 518 and "normal", 526) exhibit the same feature.

Spectrum 513 was obtained from the same sample as 510 except that FG was off. The difference spectrum 510-513 shows a charging shift of 0.65 eV. The peak at 286.5 eV corresponding to mercaptyl sulfur is enhanced in spectrum 513. Also, a peak representing a positively charged carbon has shifted about 2 volts.

Spectrum 526 (Fig. 75) gives the Cls spectrum corresponding to the dithiolene complex and was taken immediately after insertion into the spectrometer. Spectrum 529 corresponds to the same sample but was taken after 7.6 hrs. of irradiation at 300°K. Both are FG-on spectra and the difference

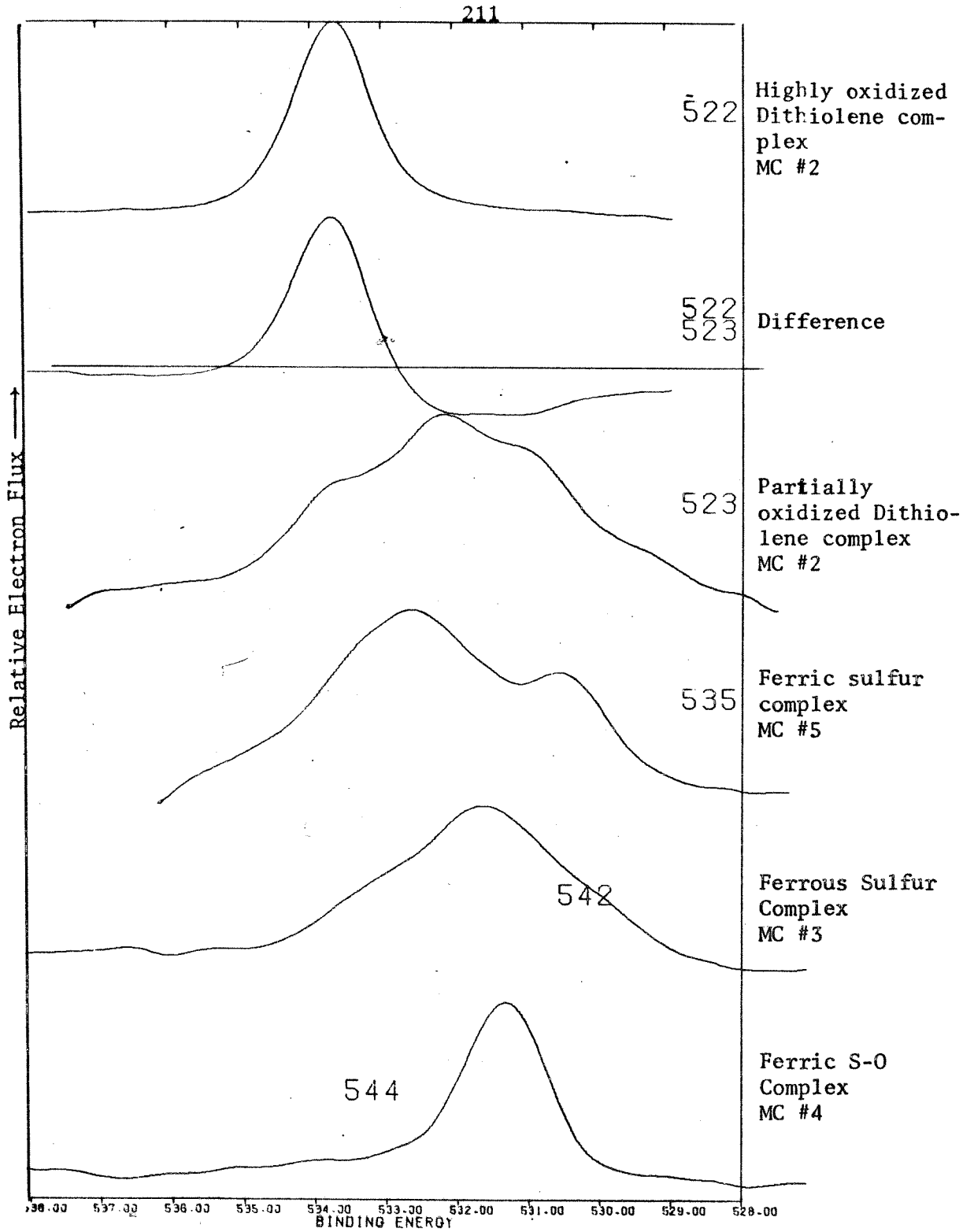


Figure 76. Oxygen 1s spectra showing the effects of aerobic oxidation of the Iron-Sulfur complexes.

spectrum (526-529) profiles the radiation damage. The aliphatic carbon attributable to the tetra-n-butyl groups of the quaternary ammonium cation appears to decompose to a negatively charged carbon species. Precise determination of the decomposition product is beyond the scope of this thesis, since a choice between negative free radicals, simple free amines and elemental carbon cannot be made without additional and extensive experimental work. The N1s spectrum (527) of dithiolene is given in Fig. 71. Again, negative free radicals cannot be distinguished from other possible reaction products.

The effects of aerobic oxidation of the iron-sulfur complexes is apparent in Fig. 76, which shows the oxygen 1s spectra. Spectrum 522 corresponds to highly oxidized dithiolene, 523 to less oxidized sample, and 522-523 is the difference spectrum. Both spectra show a peak at 533.6 eV. Spectrum 523 also contains maxima at 532.2 eV and 530.9 eV. The latter can be attributed to oxide but carboxylate oxygen should occur at about 531.6 eV; see Chapter VI. The region of 532.2 eV \pm 0.3 eV corresponds to sulfoxide species. Lindberg et.al.³⁷ have demonstrated that aliphatic sulfate esters give peaks at about 532.5 eV and 533.8 eV \pm 0.3 eV, whereas sulfite esters show transitions at 533.2 eV and 533.6 eV \pm 0.2 eV. Thus, the peak at 533.6 eV in the spectrum of oxidized dithiolene can be attributed to a sulfite ester. Spectrum 523 arises from a partially aerobically oxidized sample. One may speculate that the oxidation begins with formation of sulfoxide which oxidizes further to sulfite, the bonds to aliphatic carbon remaining intact. Some metal oxide is observed on the surface after oxidation, although sulfur oxides are the main constituents.

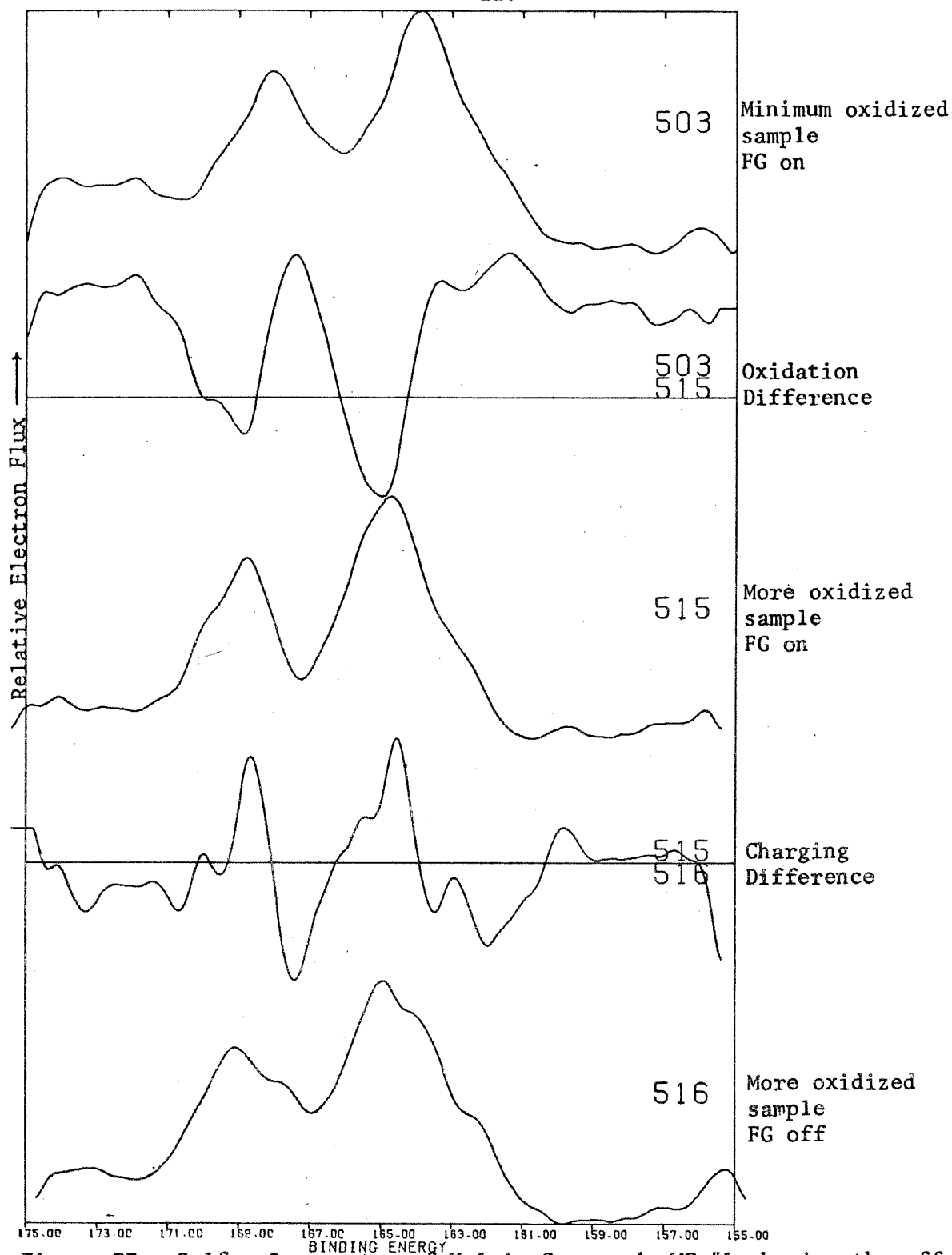


Figure 77. Sulfur 2p spectra of Holm's Compound, MC #1 showing the effects of increased oxidation.

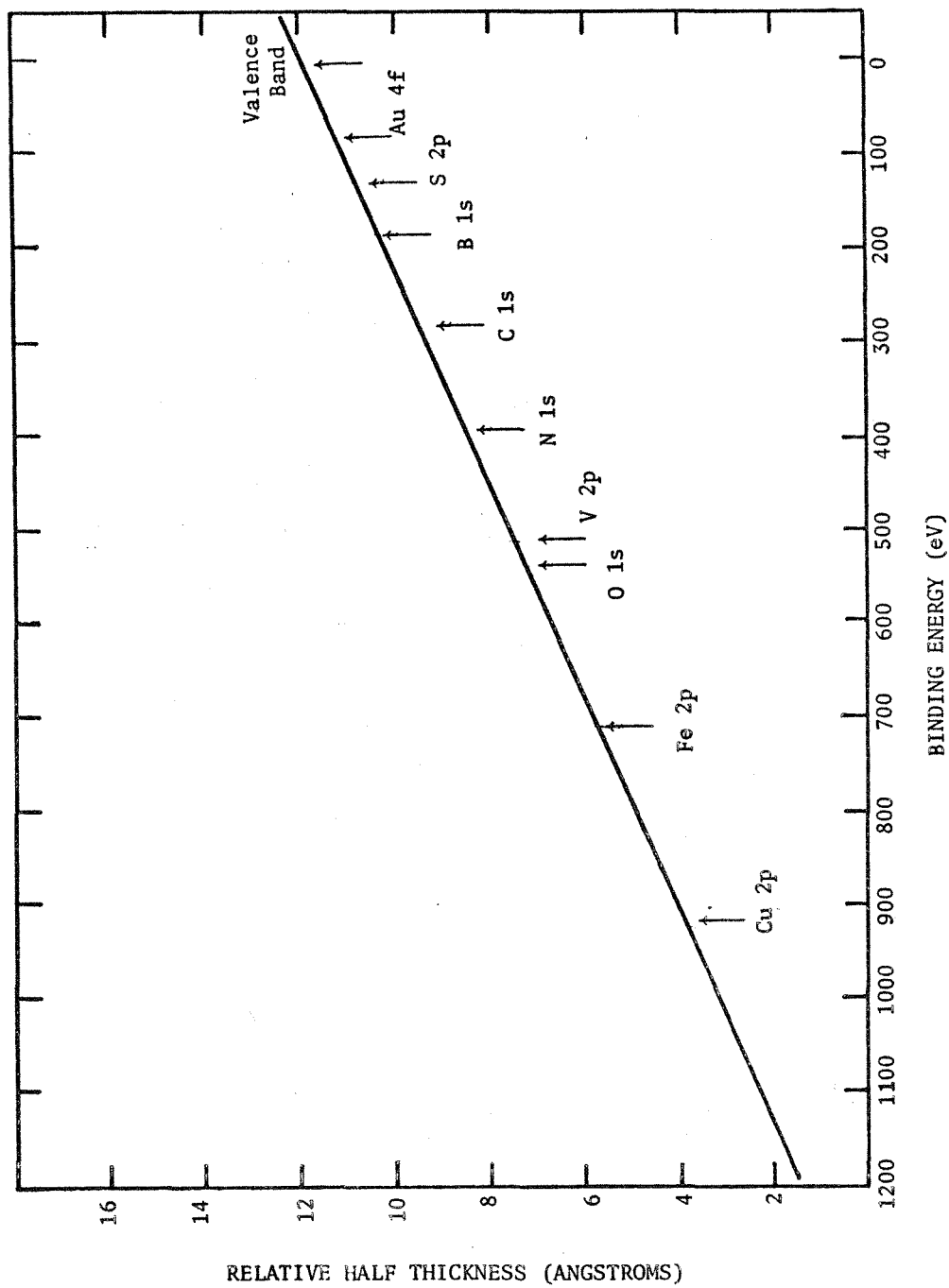
Spectrum 535, Fig. 76, gives the O1s spectrum for model complex #5.

Again, the spectra can be attributed to oxide, sulfoxide, and sulfite oxygens. No evidence of phosphorus oxides was found in the corresponding P2p spectra. The peak at 531.5 eV in spectrum 542 (model complex 3) can be attributed to oxygen bound to phosphorus. The extended tail toward low binding energy is indicative of metal oxides and that toward high binding energy would indicate the presence of some sulfoxides. The spectrum of model complex 4 shows the metal and phosphorus bound oxygen together with small amounts of an unknown oxidation product. The number of counts above background for the maxima in the spectra of Fig. 76, are 7K for 522, 2K per 523, 1K for 542 and 3K for 544. Thus, the oxidation of the dithiolene sample (522) has proceeded extensively when compared to that of the samples corresponding to 523 and 535. Oxidation is virtually negligible in the sample of the ferrous complex (542).

Figure 77 illustrates S2p spectra of Holm's cluster complex. As the cluster complex is oxidized, the relative amount of mercaptyl carbon increases. Similar conclusions can be reached by inspection of 503 and 515. 503 arises from a sample showing the least oxidation of the cluster complex observed in this work, while that corresponding to 515 is extensively reacted. The difference spectrum 503-515 shows an increase in the unresolved sulfoxide-sulfite peak at $168.0 \text{ eV} \pm 0.5 \text{ eV}$, and the peak arising from mercaptyl sulfur.

Spectrum 516 gives the FG-off case of 515 and the difference spectrum shows the charging of one sulfur species, but also permits increased resolution (in 516) of the mercaptyl and other low binding energy components of the

FIGURE 77a OBSERVATION DEPTH LAYER VERSUS BINDING ENERGY



164.0 eV \pm 0.8 eV peak. Reduced charging shifts should result for species lying at some depth below the surface. Thus, surface-oxidation products should show a charging effect but the unreacted complex (underneath) should not.

As mentioned in Chapter III, the effective sampling depths in this spectroscopy have been studied¹²² by means of carbon deposition. Fig. 77a shows a plot of these results, where thickness of the investigated layer is compared to the observed binding energy referenced to AlK α . This data appears to give observation depths within an error of 200 to 300%. The effective sampling depths for the major peaks have been indicated in the figure.

When taking into account the difference between the mean free paths of the electrons in proteins and amorphous graphite, the sampling depths should be 30 Å for S2p, 21 Å for O1s, 18 Å for Fe 2p, and 27 Å for C1s. Thus, the carbon and sulfur spectra will be more representative of the bulk and unoxidized material than the oxygen 1s spectra, and the iron spectra should be least representative of unreacted bulk material.

The photoemitted electrons come from an irradiated area of 1 x 5 mm².

This means that the examined volume of the specimen is about $1 \cdot 10^7 \times 5 \cdot 10^7 \times 50 = 2.5 \cdot 10^{16}$ Å³. Considering an irradiated, examined segment to be a cube 50 Å on a side, then the experimental observation would comprise 10^{11} sampling cells, which corresponds to a surface-to-

122. Steinhardt, R.G., Hudis, J., and Perlman, M.L., Phys Rev B., 5, 1016 (1972).

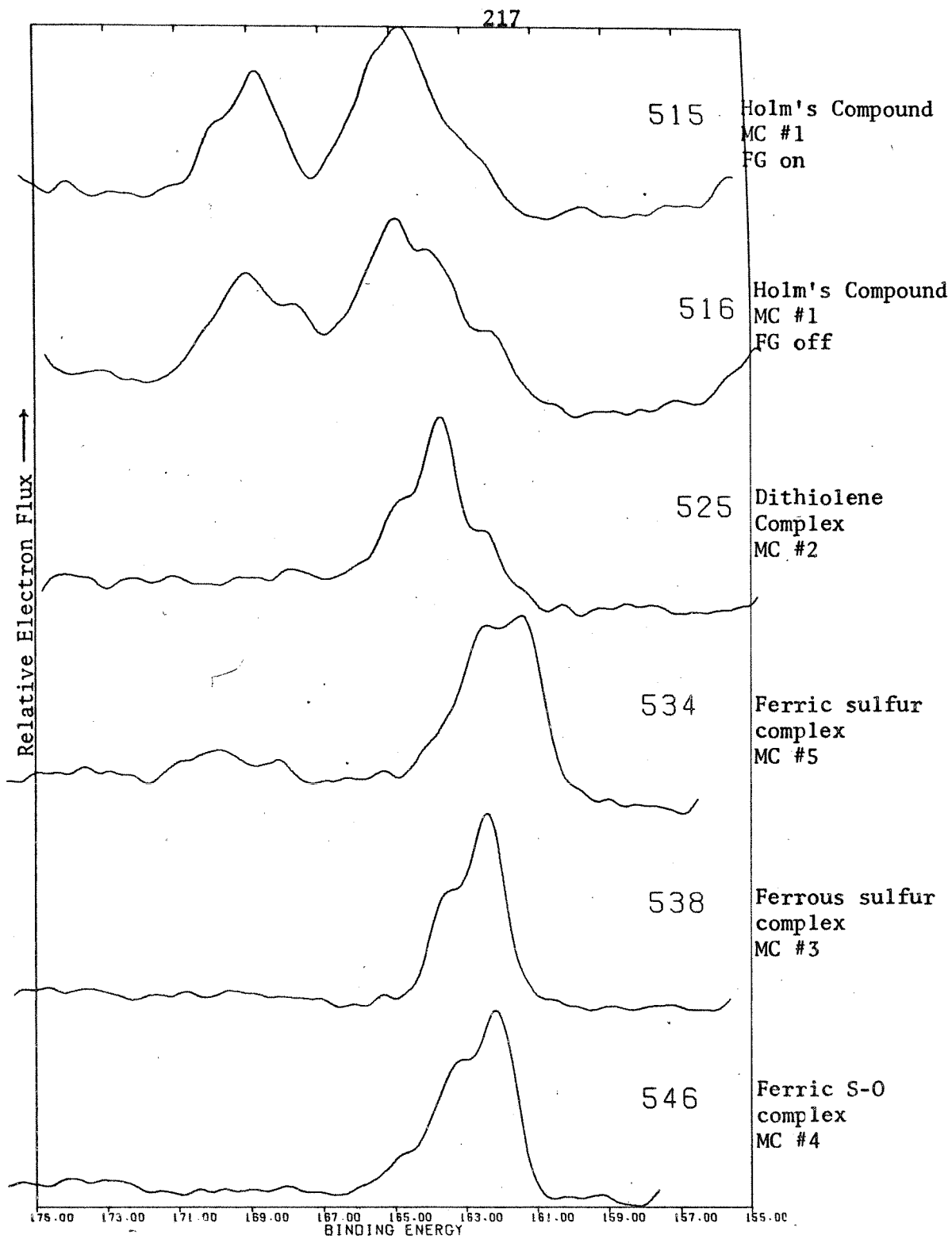


Figure 78. Sulfur 2p spectra of the iron sulfur model complexes.

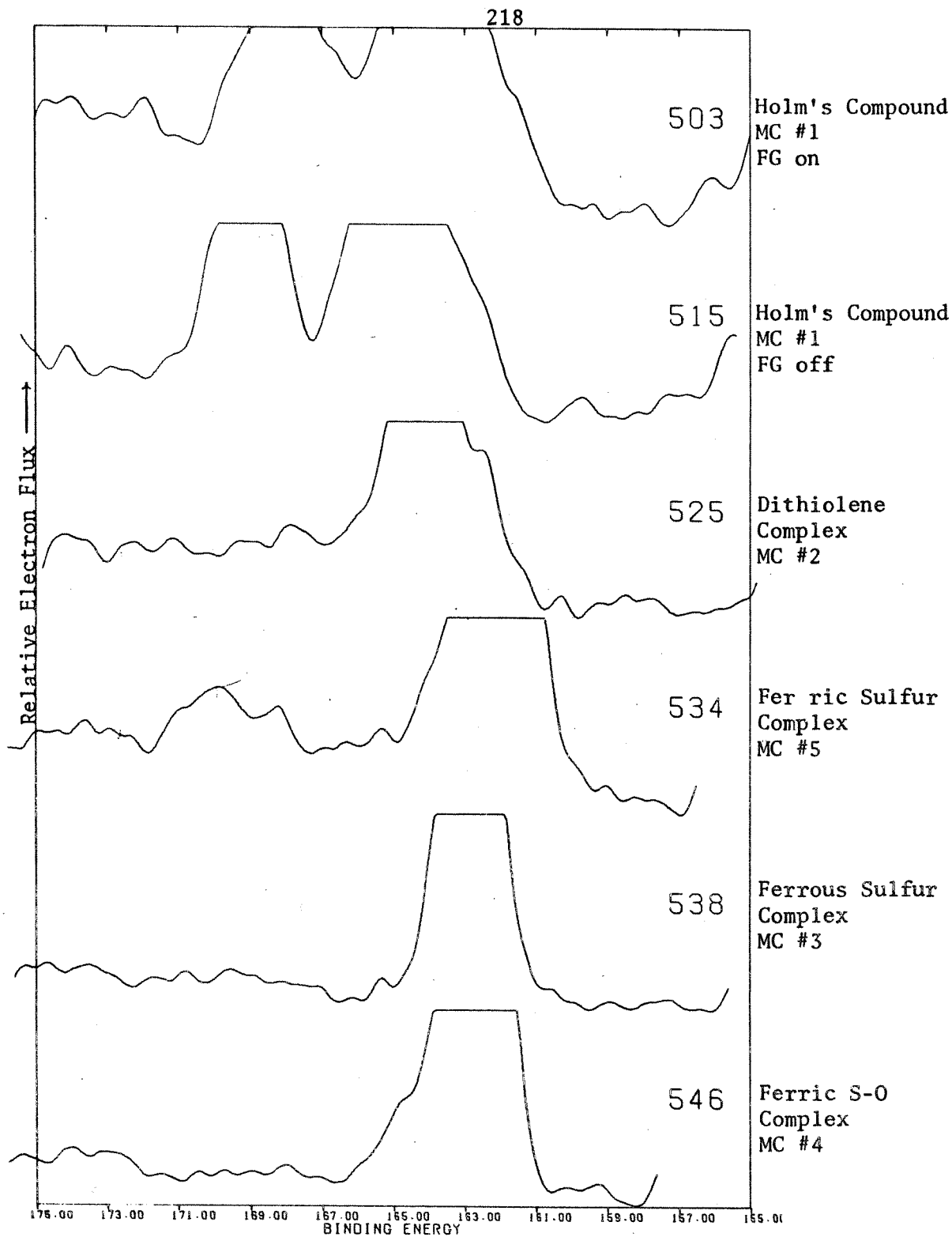


Figure 79. Duplication of the S 2p spectra of Fig. 78 with multiplications by 2X on the ordinate.

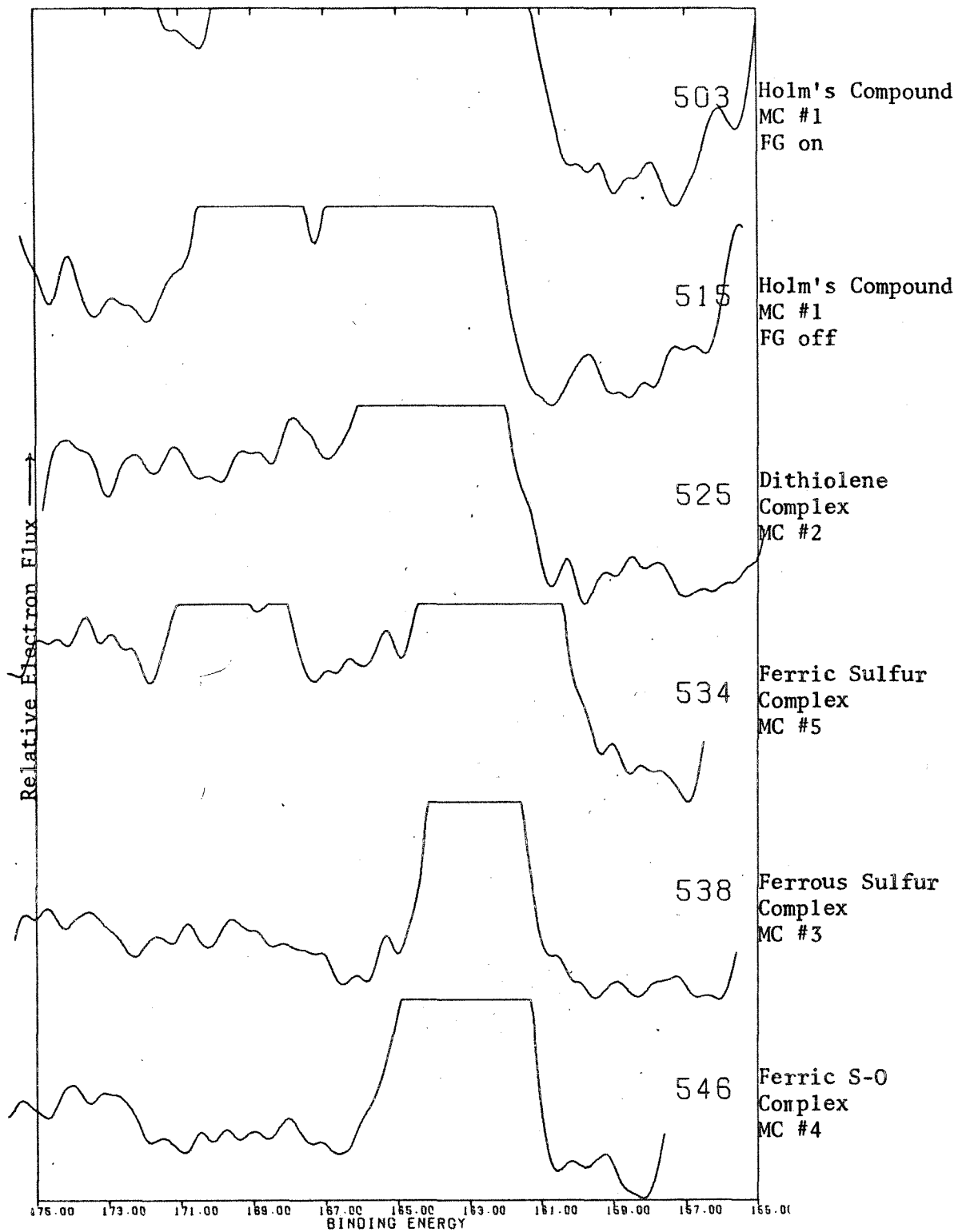


Figure 80. Duplication of S 2p spectra of Fig. 78 with multiplication of 4X on ordinate.

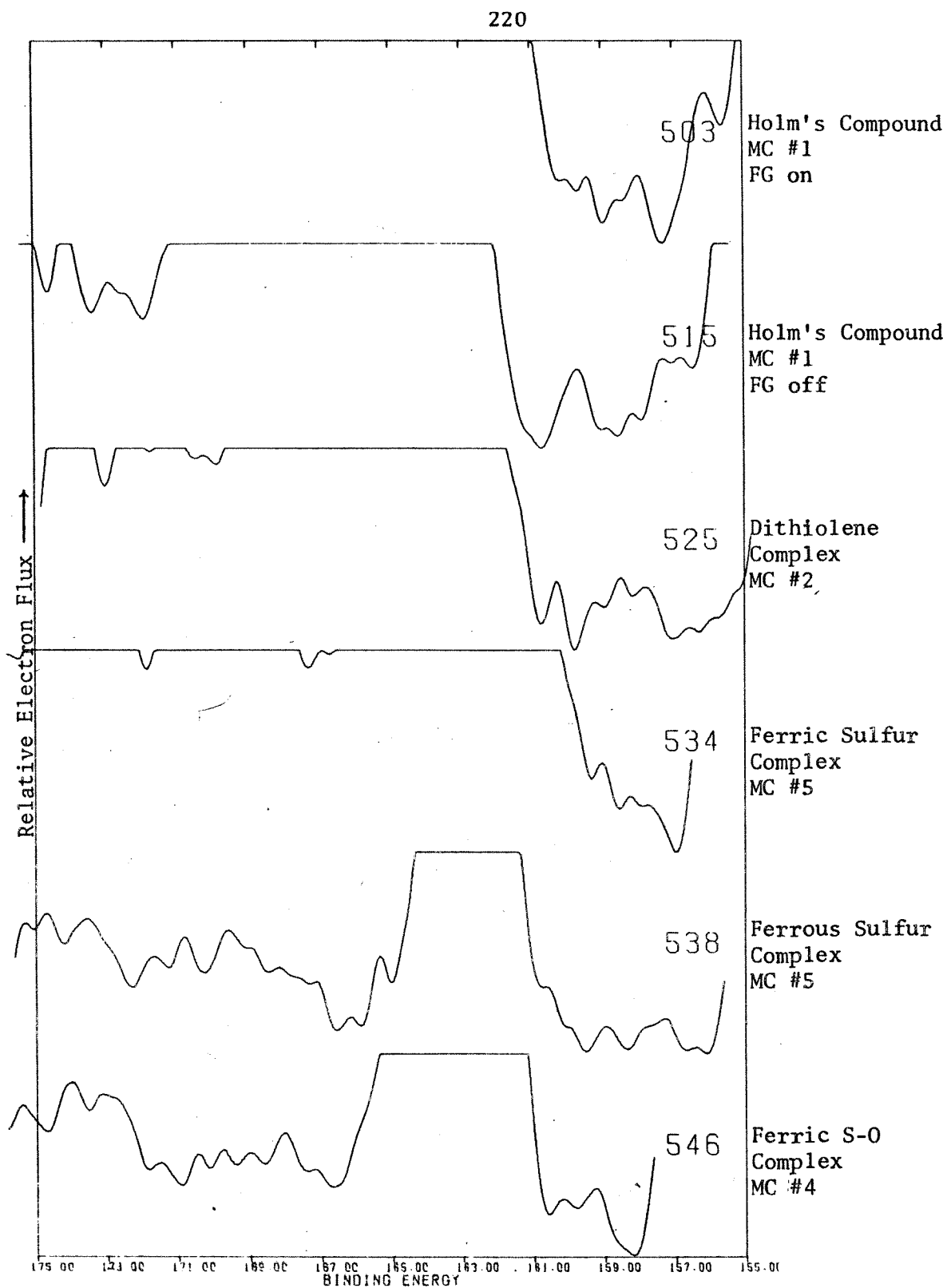


Figure 81. Duplication of the S 2p spectra of Fig. 78 with multiplication of 6X on ordinate.

TABLE II

Assignments of Binding Energies for Sulfur 2p_{3/2}

Spectrum #	Compound Name	Sulfur Configuration	Binding Energy (eV)
165	n-propylthiouracil Cu ^I	$\text{>C}-\text{S}^{\text{I}}-\text{Cu}^{\text{I}}$	162.8
170	Cu ^{II} bis-n-butylthioacetate	$\text{>C}-\text{S}-\text{C} \begin{array}{l} \\ \text{Cu}^{\text{II}} \end{array}$	164.2
174	1,2-dibutylthioethane Cu ^{II} Cl ₂	$\text{>C}-\text{S}-\text{C} \begin{array}{l} \\ \text{Cu}^{\text{II}} \end{array}$	164.3
188	di-(acetothio)ethane Cu ^{II}	$\text{>C}-\text{S}-\text{C} \begin{array}{l} \\ \text{Cu}^{\text{II}} \end{array}$	164.6 164.9
193	(Cu ^I) ₂ Cu ^{II} (penicillamine) ₂	$\text{>C}-\text{S}^{\text{I}}-\text{Cu}^{\text{I}}$ $\text{>C}-\text{S}^{\text{I}}-\text{Cu}^{\text{I}}$ $\phi-\text{S}^{\text{II}}-\text{Cu}^{\text{II}}$	162.6 163.5
558	"L"Cu ₂ OC ₃ H ₇	$\text{>C}-\text{S}^{\text{I}}-\text{Cu}^{\text{I}}$ $\phi-\text{S}^{\text{II}}-\text{Cu}^{\text{II}}$	161.9
564	"Q"Cu ₂ OC ₂ H ₅	$\text{>C}-\text{S}^{\text{I}}-\text{Cu}^{\text{I}}$ $\text{>C}-\text{S}^{\text{I}}$	162.5
711	Stellacyanin	$\text{>C}-\text{S}^{\text{I}}$ $\text{>C}-\text{S}^{\text{I}}-\text{Cu}^{\text{II}}$ R-S-S-R SO ₄ ²⁻	161.8 163.7 164.8 167.7

TABLE 11, CONTINUED.

Binding Energy Assignments for Sulfur $2p_{3/2}$

<u>Spectrum #</u>	<u>Compound Name</u>	<u>Sulfur Configuration</u>	<u>Binding Energy (eV)</u>
714	Laccase	$\begin{array}{c} \text{>C--S--S--C=} \\ \quad \\ \text{I} \quad \text{I} \\ \text{Cu} \quad \text{Cu} \end{array}$	161.1
		$\begin{array}{c} \text{>C--S}^{\ominus}\text{---Cu}^{\text{II}} \\ \\ \text{R--S--S--R} \end{array}$	162.4
		$\begin{array}{c} \text{SO}_4^{2-} \\ \\ \text{>C--S}^{\ominus}\text{---Cu}^{\text{II}} \\ \\ \text{R--S--S--R} \end{array}$	165.0
718	Hemocyanin (oxy)	$\begin{array}{c} \text{>C--S}^{\ominus}\text{---Cu}^{\text{II}} \\ \\ \text{R--S--S--R} \end{array}$	167.4
		$\begin{array}{c} \text{SO}_4^{2-} \\ \\ \text{>C--S}^{\ominus}\text{---Cu}^{\text{II}} \\ \\ \text{R--S--S--R} \end{array}$	163.9
		$\begin{array}{c} \text{SO}_4^{2-} \\ \\ \text{S}^{\ominus} (?) \end{array}$	165.1
732	Erythrocyuprein	$\begin{array}{c} \text{>C--S}^{\ominus} \\ \\ \text{>C--S}^{\ominus}\text{---Cu}^{\text{I}} \\ \\ \text{>C--S}^{\ominus}\text{---Cu}^{\text{II}} \\ \\ \text{SO}_4^{2-} \end{array}$	167.3
		$\begin{array}{c} \text{SO}_4^{2-} \\ \\ \text{S}^{\ominus} (?) \end{array}$	160.9
		$\begin{array}{c} \text{>C--S}^{\ominus} \\ \\ \text{>C--S}^{\ominus}\text{---Cu}^{\text{I}} \\ \\ \text{>C--S}^{\ominus}\text{---Cu}^{\text{II}} \\ \\ \text{SO}_4^{2-} \end{array}$	161.8
		$\begin{array}{c} \text{SO}_4^{2-} \\ \\ \text{S}^{\ominus} (?) \end{array}$	162.8
		$\begin{array}{c} \text{SO}_4^{2-} \\ \\ \text{S}^{\ominus} (?) \end{array}$	163.9
		$\begin{array}{c} \text{SO}_4^{2-} \\ \\ \text{S}^{\ominus} (?) \end{array}$	167.3
503	n-Pr ₄ N ₂ Fe ₄ S ₄ (SEt) ₄	$\begin{array}{c} \text{SO}_4^{2-} \\ \\ \text{S}^{\ominus} (?) \end{array}$	161.2
		$\begin{array}{c} \text{SO}_4^{2-} \\ \\ \text{S}^{\ominus} (?) \end{array}$	162.3
		$\begin{array}{c} \text{SO}_4^{2-} \\ \\ \text{S}^{\ominus} (?) \end{array}$	163.7
		$\begin{array}{c} \text{SO}_4^{2-} \\ \\ \text{S}^{\ominus} (?) \end{array}$	164.0
		$\begin{array}{c} \text{SO}_4^{2-} \\ \\ \text{S}^{\ominus} (?) \end{array}$	164.8
		$\begin{array}{c} \text{SO}_4^{2-} \\ \\ \text{S}^{\ominus} (?) \end{array}$	165.1
		$\begin{array}{c} \text{SO}_4^{2-} \\ \\ \text{S}^{\ominus} (?) \end{array}$	168.7

TABLE 11, CONTINUED Assignments of Binding Energies for the Sulfur $2p_{3/2}$

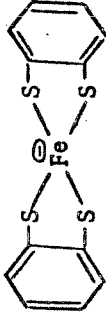
<u>Spectrum #</u>	<u>Compound Name</u>	<u>Sulfur Configuration</u>	<u>Binding Energy (eV)</u>
525	$n\text{-Bu}_4\text{N}_2\text{Fe}(\text{SCH}_2\text{CH}_2\text{S})_2$		161.2 162.4 164.8
534	$\text{Fe}(\text{SP}\phi_2\text{NC}(\text{NC}_4\text{H}_8)\text{S})_3$		161.3 162.4
538	$\text{Fe}(\text{SP}\phi_2\text{NP}\phi_2\text{S})_2$		162.4
546	$\text{Fe}(\text{SP}\phi_2\text{NP}\phi_2\text{O})_3$		162.1
572	2Fe Ferredoxin		160.0 161.9 163.0 163.7 164.0 165.2
577	4Fe Ferredoxin		160.3 161.1 161.5 163.2 164.5 165.8
736	FeS_2		161.1
737	FeS		160.3
739			161.0

TABLE 11, CONTINUED Assignments of Binding Energies for the Sulfur 2p_{3/2} Binding Energy (eV)

<u>Spectrum #</u>	<u>Compound Name</u>	<u>Sulfur Configuration</u>	<u>Binding Energy (eV)</u>
742			161.0
746			161.8

depth ratio of 10^{11} .

Figure 78 gives the S2p spectra for the set of iron-sulfur model complexes. Spectra 515/516 are the FG on/off set for the cluster model. The dithiolene complex gives spectrum 525, model complex 5 gives spectrum 534, spectrum 538 represents model complex 3, and spectrum 546 arises from model compound #4.

The peaks observed in these spectra together with assignments of the sulfur environments corresponding to these lines are given in Table 11.

Divalent sulfur (S^{2+}) and sulfide (S^{2-}) give rise to peaks in the region 166.0 eV to 160.0 eV, while oxidized sulfur, e.g., sulfate, sulfite esters, and sulfoxides, give peaks corresponding to higher binding energies (167.0 eV to 171.0 eV).

Oxidized sulfur is observed in samples corresponding to spectra 515, 516, 525, and 534. In order to emphasize the presence of weak peaks which probably correspond to unoxidized compound, the spectra of Fig. 78 are reproduced in subsequent figures. Figure 79 represents multiplication on the y-axis of Fig. 78 by a factor of 2, Fig. 80 by a factor of 4, and Fig. 81 by a factor of 6. In each case, the spectra are plotted from the minimum value and the curves are blanked off after reaching the upper plot limit.

The oxidation products in Spectrum 534 are more pronounced as shown in Figure 79 while the change in the shape of the background is accentuated in Figs. 80 and 81 for spectra 525 and 534. The binding energies indicated by the peaks corresponding to these oxidized components are similar for model complexes 3 through 5. The spectra of the oxidized components of the

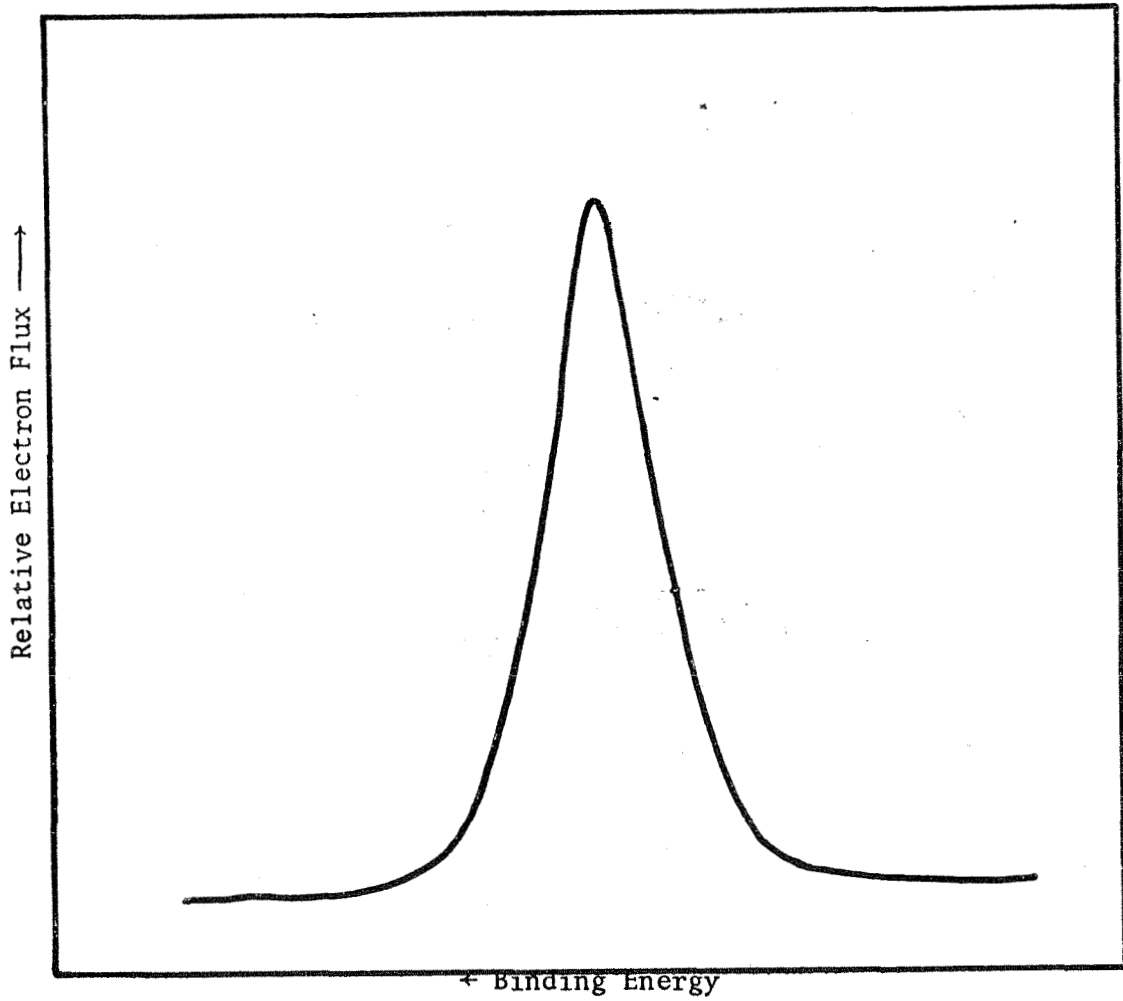


Figure 82a. Basic line shape used in deconvolution of S 2p spectra with Dupont 310 Curve Resolver.

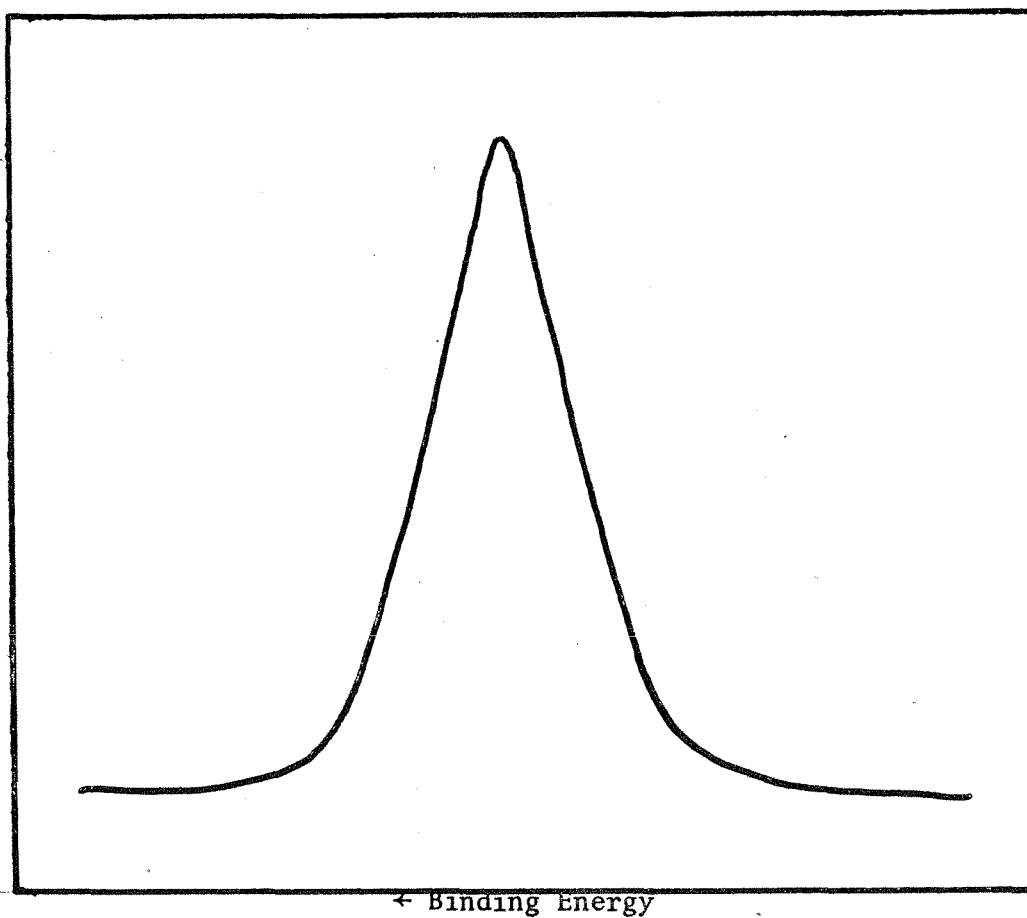


Figure 82b. Spectral line shape used in deconvolution with Dupont 310 Curve Resolver, when a skewed background is used in the resolution.

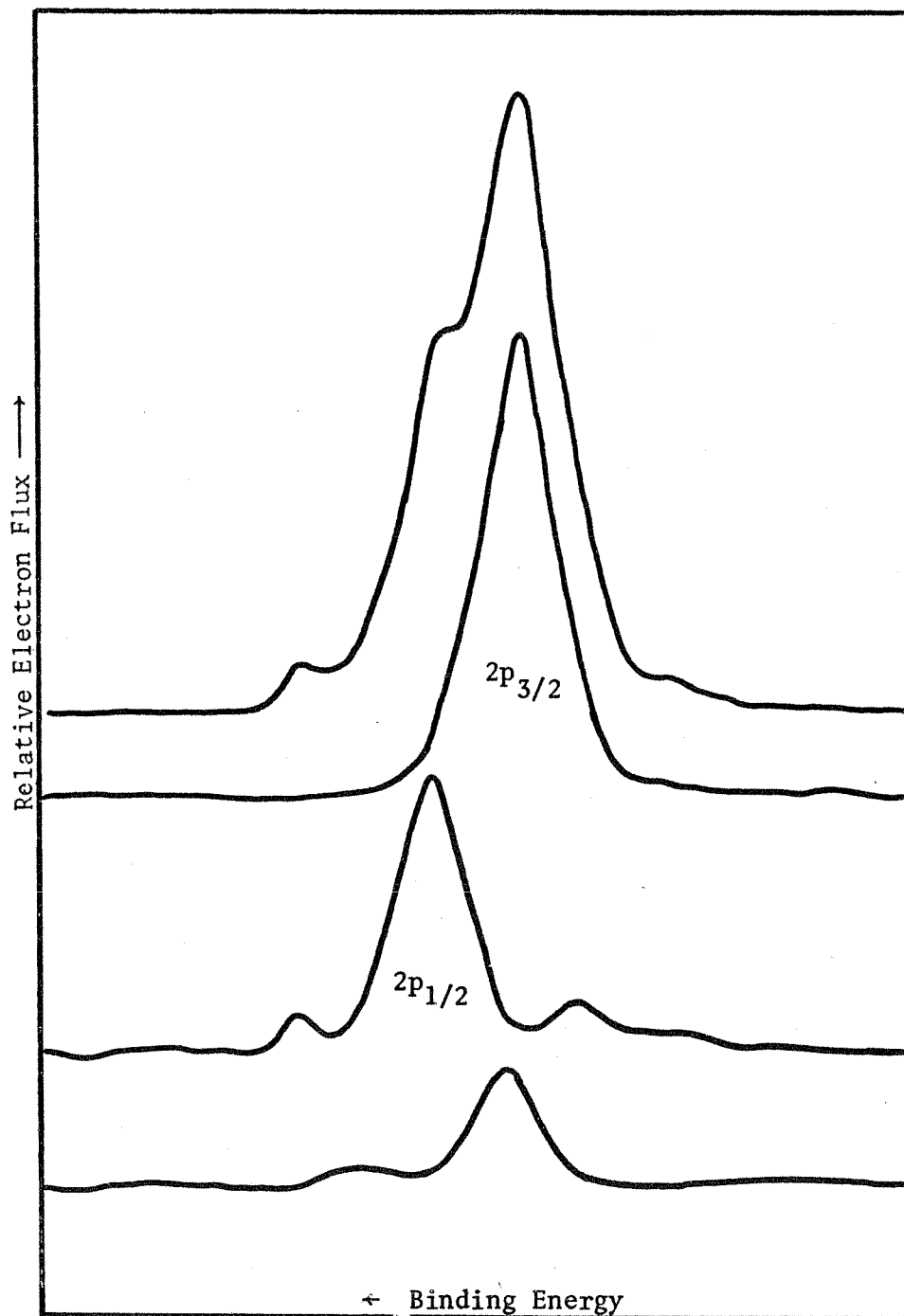


Figure 83. Deconvolution of spectrum 538 corresponding to the Ferrous Sulfur complex (MC #3).

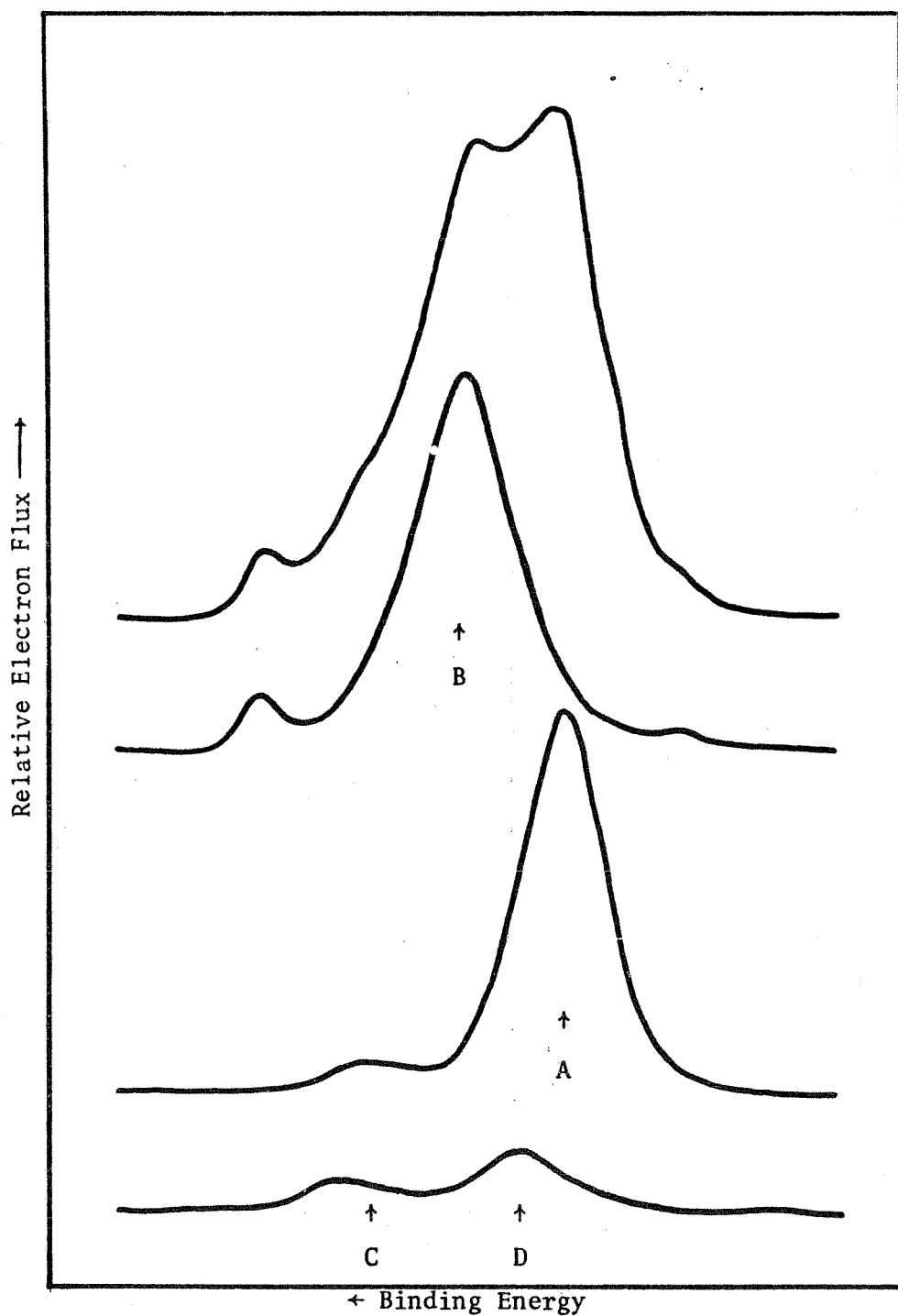


Figure 84. Deconvolution of S 2p spectrum 534, corresponding to the Ferric sulfur complex (MC #5).

dithiolene and cluster compounds differ drastically from those of complexes 3 through 5.

Complicated structure is observed in the region corresponding to S^{2+} through S^{2-} . As mentioned, in this work the spin orbit doublet of the sulfur 2p level has been resolved. Consequently, each sulfur environment gives rise to two lines, with an intensity ratio of 2:1, separated by 1.2 electron volts. The curve-resolving methods for deconvolution developed in Chapter VI were used to determine the intensity ratios of these peaks and their corresponding binding energies.

The basic line shape used in deconvolution was described in Chapter VI. A representative line shape is given in Fig. 82a. Figure 82b gives the line shape when a skewed background is used to approximate the discrete loss region of the spectrum.

The least complicated of the sulfur spectra is given in spectrum 538 (model complex 3). The major peak of spectrum 538, 163.0 eV is shown deconvolved in Figure 83. Two major lines are found at relative intensities of approximately 2:1 with a splitting of 1.16 eV. Several additional peaks are found, the largest of which has an intensity of 7% of the total. This peak is located beneath the strongest peak but has been shifted 0.3 eV toward the high binding energy. Its intensity and location varied over the 4 attempted deconvolutions suggesting an error in the line shape. The small peaks at low binding energy consistently give the same position and intensity and can be attributed to electron-induced radiation damage.

Spectrum 534, (model compound 5) is shown deconvolved in Fig. 84. In

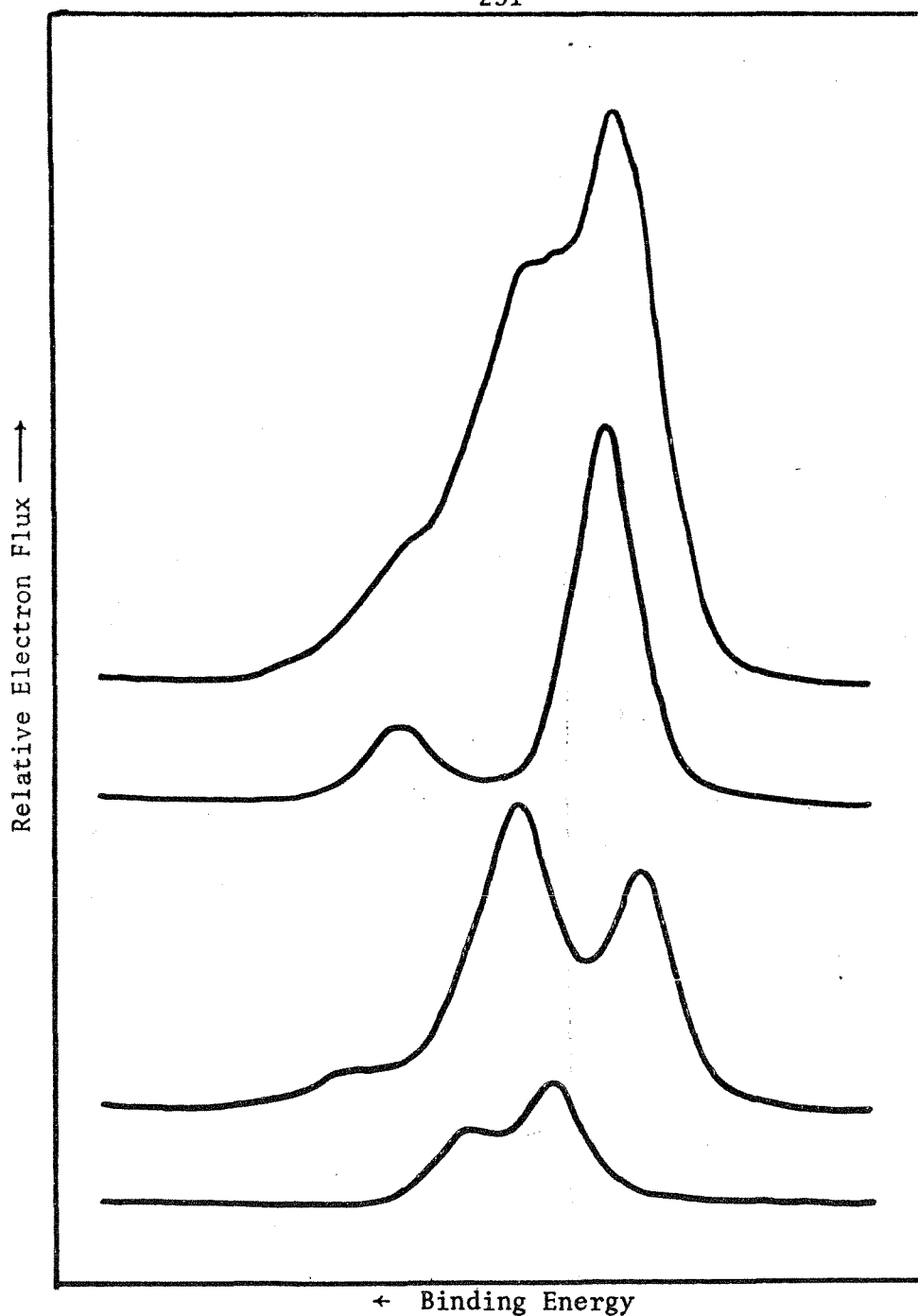


Figure 84a. Deconvolution of spectrum 546, corresponding to the Ferric sulfur-oxygen complex (MC #4).

addition to the minor peaks as found in Fig. 83, two major peaks of equal intensity separated by 1.2 eV are observed. If the low binding energy peak is treated as a composite of the $2p_{1/2}$ line from the first state and the $2p_{3/2}$ line from a second state, results consistent with the observed structure can be obtained. A 35% relative intensity is observed for the first peak and the intensity of the high binding peak becomes $37\% - \frac{1}{2} (35\%)$ or 20%. This suggests a doublet component at 10% relative intensity and 1.0 to 1.2 eV higher binding energy. The deconvolution gives two coincident peaks at a point 1.2 eV higher binding energy of 4% and 5% relative intensity for a total of 9% which is within the realm of accuracy of the method. For six deconvolutions, the width of the second, high binding energy peak (B) and the position and intensity of the peaks in the region of C were observed to vary by $\pm 7\%$.

The best observed fit to the data of spectrum 546 (model compound 4) is displayed in Fig. 84a. The peak structure which resulted from the deconvolution was reproducible in position, width and intensity to within 3%, for 3 deconvolutions. This set of peaks can be duplicated by three spin-orbit doublets with the intensity ratios 3:2:1 at 162.1 eV, 161.7 eV, and 163.5 eV, respectively. The doublet at 162.1 eV is attributed to the primary sulfur species. The doublet at 161.7 eV could arise from electronic effects within the complex, e.g., oxidation-reduction, or it could correspond to decomposition product as previously noted. The peak at 163.5 eV, however, corresponds to impurities containing sulfur bound to carbon and iron.

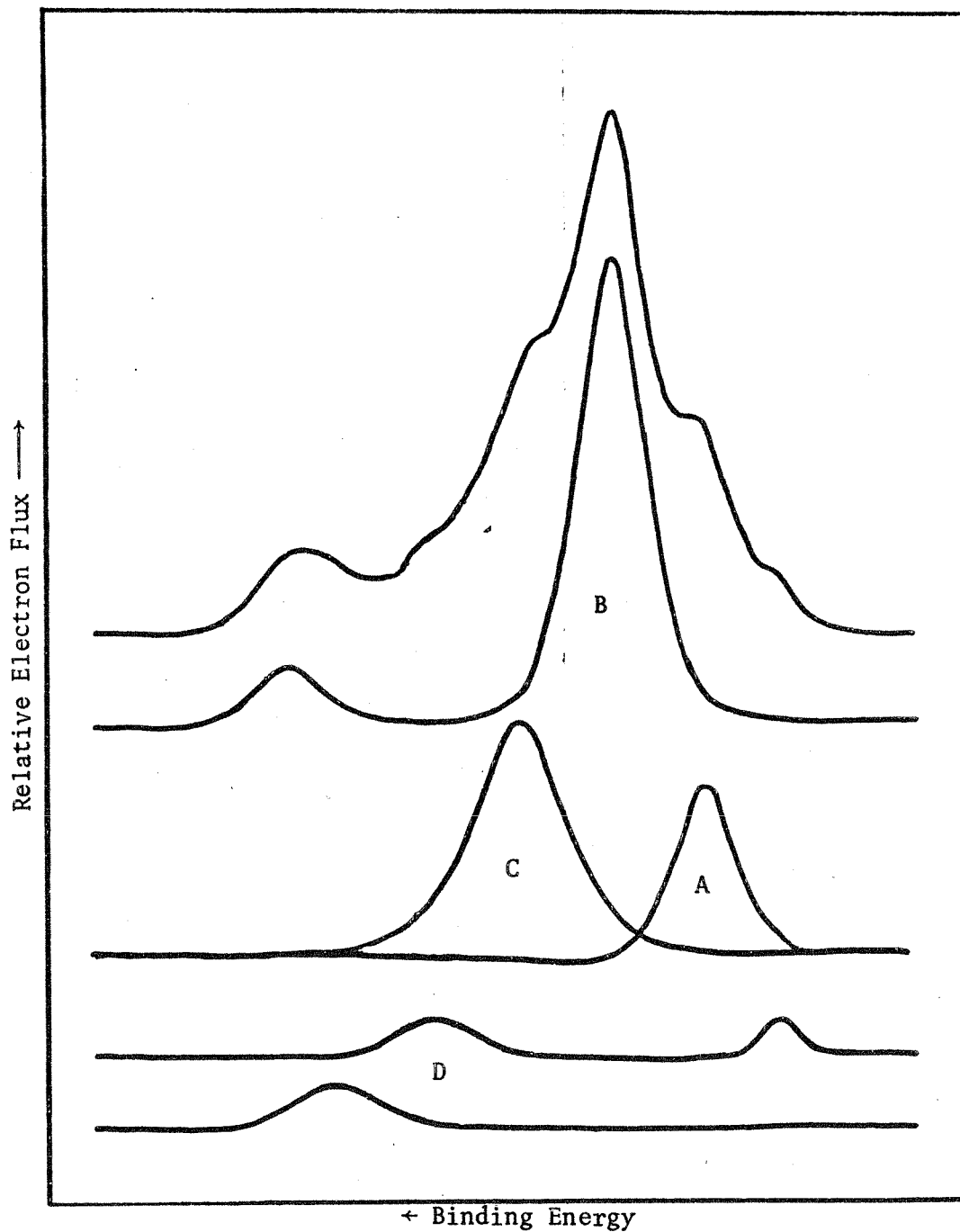


Figure 85. Deconvolution of Spectrum 525 corresponding to the dithiolene complex (MC #2).

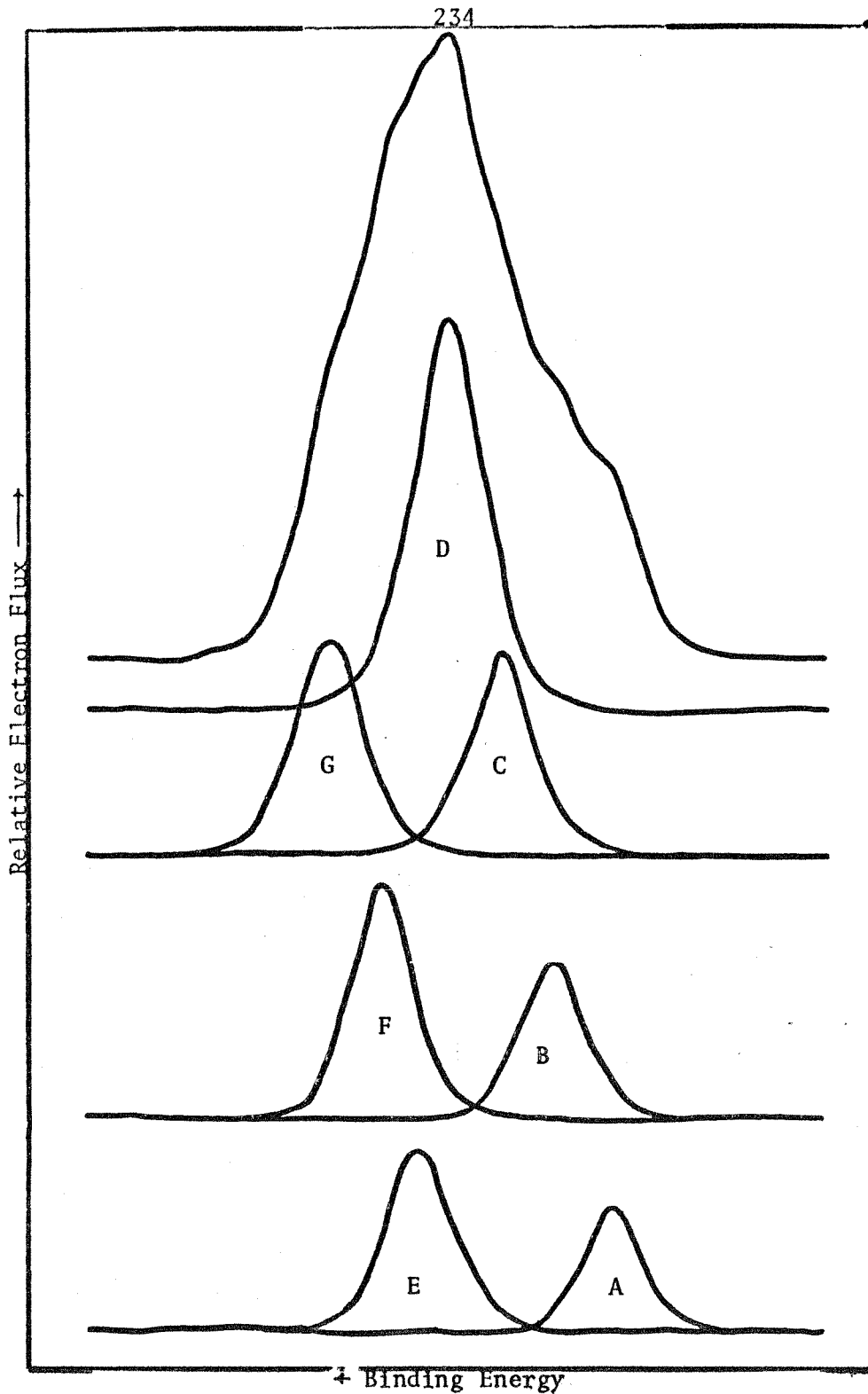


Figure 86. Deconvolution of Spectrum 515 corresponding to Holm's Compound (Cluster - MC #5).

The spectrum 525 (dithiolene complex) is shown deconvolved in Fig. 85.

The best fit observed for this spectrum results in 3 major peaks noted A, B, and C, with relative intensities of 12%, 48%, and 25% respectively of the total. Proceeding from right to left A occurs at 162.3 eV, B at 163.6 eV and C at 164.9 eV. Each of the deconvolved peaks falls within 1.2 eV of the nearest neighbor. The peak at A (12% relative intensity) reduces the observed peak intensity of B to 42% (with a spin-orbit doublet assignment) which in turn requires a peak of 21% at the energy of C. The difference of 4% in the observed intensity of C could arise from error in the method or alternatively, the smaller peaks at D might indicate the presence of another low-level component with a $2p_{3/2}$ line at 164.7 eV.

The primary features of the spectrum can be accounted for by $2p_{3/2}$ lines at 162.3 eV and 163.6 eV having an intensity ratio of about 1:3.5.

Intriguingly, the structure of the dithiolene complex indicates a 3 to 1 distribution of sulfur environments where 6 of the sulfur atoms are bound to one aliphatic carbon and to one iron, while the other two sulfur atoms are bound to one aliphatic carbon and two iron centers. Thus, the 162.3 eV peak is attributed to the two-iron bound sulfur, while the peak at 163.6 eV corresponds to the one-iron sulfur.

Holm's model compound gives the most complicated of these spectra (515).

Seven deconvolutions of these data were completed, and the composite of the best fits to the peaks is given in Fig. 86. The areas, peak positions and widths of the deconvolved components varied within a range of $\pm 1.4\%$. The positions and relative intensities of the component peaks are given as follows:

<u>Peak</u>	<u>Position</u>	<u>Rel. Intensity</u>
A	162.5 eV	8%
B	163.3 eV	8%
C	164.0 eV	15%
D	164.7 eV	26%
E	165.1 eV	10%
F	165.5 eV	12%
G	166.3 eV	12%

The DuPont model 310 Curve Resolver used in these deconvolutions can generate 9 peaks for synthesis of the observed line shape. Each of the peaks is controlled by a separate channel, and gives a symmetrical line shape. It is not possible to fix the relative heights and positions of a set of two channels and then move them as set or unit for curve fitting. The sulfur 2p spectra consist of spin orbit doublets which are separated by 1.2 eV and related in intensity (2:1). Thus, this interrelation reduces the number of degrees of freedom in the system. To take advantage of this relationship, the intensity of the deconvoluted peaks must be reduced to the doublet components.

Consequently, the peak noted A requires a corresponding peak at about 163.7 eV of about 4% relative intensity. The primary intensity of C is corrected to 11%. Further, the peak at B requires a doublet at 164.5 eV of 4% relative intensity. This reduces the peak at D to 22%. The primary peak at C requires a line at 165.2 eV of intensity 5.5%. Within the error of approximation, this can be assigned to the peak at E, thereby reducing its primary intensity to 4.5%. The primary intensity of D requires a line at 165.9 eV of intensity 11%. The peak at E requires a line at 166.3 eV of about 2%. Since 165.9 eV falls about midway between F and G, the required intensity will be proportionally split and therefore F reduces to

6% while G reduces to 5%.

The positions and relative intensities of the primary sulfur $2p_{3/2}$ peaks (neglecting doublet intensity) inferred from this analysis of spectrum 515 can be listed as:

<u>Peak</u>	<u>Position</u>	<u>Rel. Intensity</u>
A'	162.5 eV	8%
B'	163.3 eV	8%
C'	164.0 eV	11%
D'	164.7 eV	22%
E'	165.1 eV	4.5%
F'	165.5 eV	6%
G'	166.3 eV	5%

The peaks at A' and B' would be attributed to sulfide, while C', D', E', F', and G' would be attributed to sulfur bound to aliphatic carbon. The ratio of the two forms is approximately 14%/48% or about 1:3.5. Planimeter analysis of the full spectrum (515) indicates that the oxidized sulfur peak is related to the low binding peak by the ratio 1:1.93. The overall ratios of the three regions, i.e., oxidized, aliphatic divalent, and sulfide sulfur, occur in the ratio of 2.4:3.5:1. These area assessments indicate that the intensity of the peak corresponding to aliphatic divalent sulfur is nearly equal to the observed sum of oxidized sulfur and sulfide.

Sulfide and divalent sulfur occur in the ratio 1 to 1 in the complex. Thus, it appears that the oxidized sulfur results from the oxidation of sulfide and not mercaptyl sulfur.

The peak at 162.5 eV ± 0.2 eV is attributed to the bridging sulfur. The peak at 163.3 eV probably arises from bound sulfide as well, but the higher binding energy (0.8 eV) requires that this sulfur is bonded to a

more electron-withdrawing system. The approximately one to one ratio of A to B sulfur will be discussed later in this section.

The sulfur peak at 164.0 eV of 11% intensity (C sulfur) shows a negligible charging shift; see spectrum 516. This peak is attributed to the mercaptyl sulfur of the cluster complex. The assignment of the D sulfur (164.0 eV) must take into account its intensity. As mentioned, the relative intensity of the three major forms of sulfur is in the ratio of 2.4:3.5:1. The ratio of oxidized sulfur to sulfide is larger than 2:1. Consequently, consideration must be made of the nature of the oxidized sulfur species contributing to the peak at 168.7 eV. From Lindberg's work³⁷, we can see that the S^{6+} in sulfate gives a peak at about 168.5 eV, while the S^{4+} in sulfite esters occurs at 167.3 eV and inorganic sulfite occurs at 166.3 eV. Oxidized cystine sulfoxide was found at 166.1 eV and dioxo sulfur of oxidized cystine occurred at 168.4 eV.

The observed sulfur oxides then fall right in the neighborhood of sulfate or other higher oxides of sulfur. Little evidence is found for sulfite esters, however, the peak at G and the shoulder at 168.0 eV in 515 falls in the region of bound sulfur oxides. The oxidation giving rise to sulfate should also destroy the complex and lead to free or unbound mercaptide ligands. The mercaptides should be expected to evaporate in the spectrometer vacuum, but could possibly be trapped in the sample surface because of the low temperature (250°K), or the formation of sulfo polymers. The peak at 164.7 eV is therefore assigned as divalent sulfur bound to carbon but not to iron.

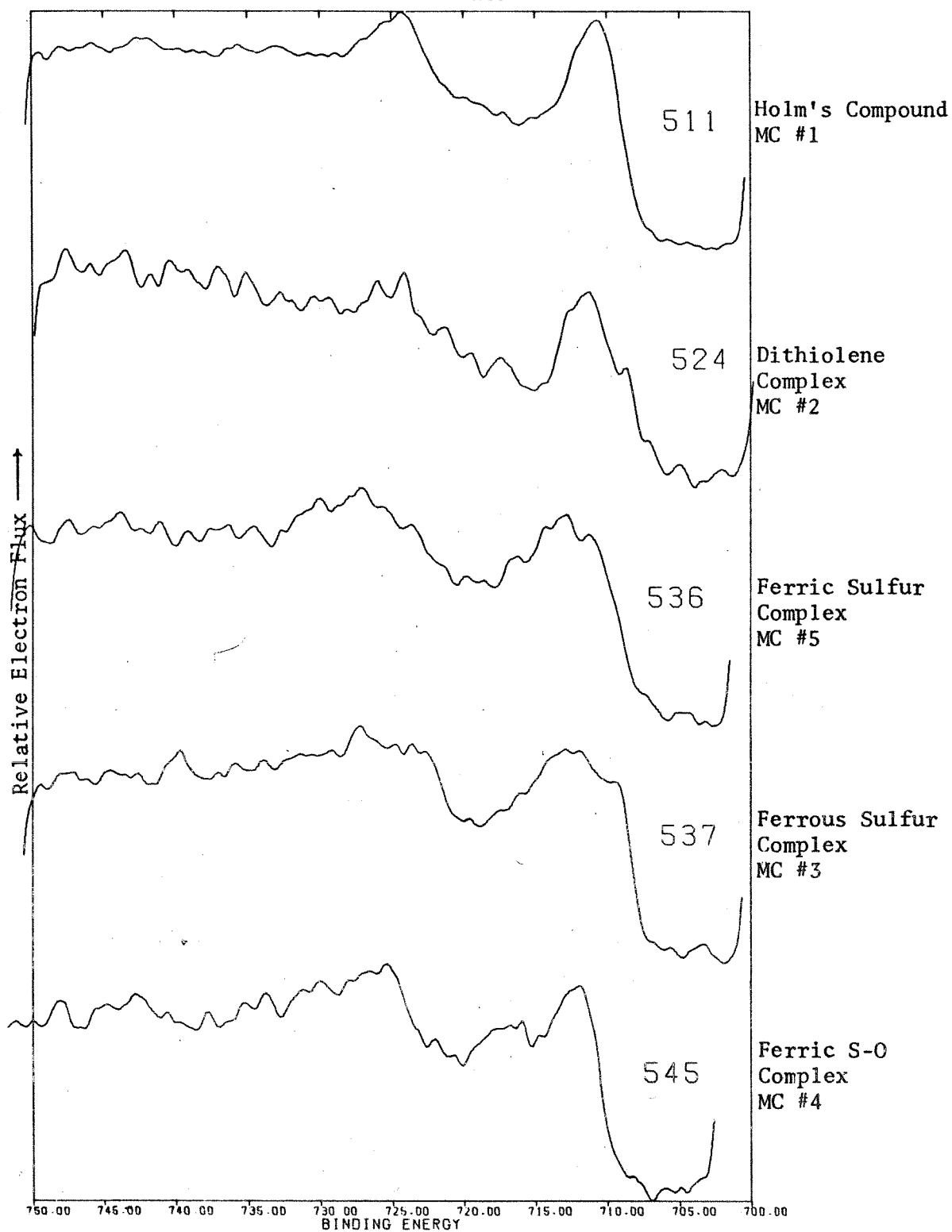


Figure 87. Iron 2p spectra of the iron-sulfur model complexes.

TABLE 14 Major Inflections Recorded for the Iron 2p Region

Spectrum Identification Number →		512	524	536	537	545	568	576
					748.0	750.0		748.8
			<u>743.5</u>	<u>743.2</u>	<u>743.5</u>	<u>742.7</u>		<u>743.2</u>
			741.6	742.4	742.5	742.1	<u>741.2</u>	742.7
			<u>740.2</u>	741.0	<u>740.4</u>	740.5	740.5	
					<u>739.6</u>	739.6	739.2	739.5
			739.1	739.1	<u>739.6</u>			737.9
						737.7		
			737.0	737.5	<u>737.0</u>			
			736.4	<u>736.3</u>		736.4	736.5	
		<u>736.0</u>			<u>735.8</u>	735.2	734.8	<u>735.7</u>
<u>735.6</u>		<u>734.7</u>	<u>735.0</u>					<u>734.8</u>
		<u>733.6</u>		<u>734.6</u>	733.9	733.7		
		<u>733.0</u>	732.7	<u>733.0</u>			732.7	732.8
<u>732.2</u>			731.9	731.3	731.3	731.8		
		731.6				<u>731.1</u>		<u>730.7</u>
730.6		730.8	730.3	730.0				
729.6		729.8	<u>729.2</u>		<u>729.1</u>	<u>729.2</u>		<u>729.5</u>
728.8		728.7		<u>728.7</u>			<u>728.5</u>	
			727.8	<u>727.2</u>		727.2		<u>727.2</u>
727.1		727.4	726.8	<u>727.0</u>	<u>727.2</u>	<u>726.7</u>		
		<u>726.5</u>					<u>726.6</u>	
		<u>726.0</u>	<u>725.2</u>		725.2	725.3		
<u>725.4</u>				<u>725.4</u>	<u>724.7</u>	<u>724.7</u>		<u>725.6</u>
		<u>724.9</u>						

TABLE 14, CONTINUED

Spectrum Identification Number		→												
511	512	524	536	537	545	568	576							
<u>724.2</u>	<u>723.2</u>	<u>724.1</u>	<u>724.6</u>			<u>723.8</u>	<u>724.5</u>							
<u>723.5</u>		<u>723.0</u>		<u>723.5</u>	<u>712.1</u>	<u>722.2</u>	<u>722.9</u>							
<u>721.4</u>	<u>721.6</u>	<u>721.3</u>	<u>721.3</u>	<u>722.6</u>	<u>721.9</u>	<u>721.4</u>	<u>721.5</u>							
<u>719.8</u>	<u>720.0</u>		<u>719.7</u>	<u>719.6</u>		<u>720.3</u>								
<u>718.6</u>	<u>718.6</u>		<u>718.6</u>		<u>719.0</u>	<u>718.8</u>	<u>718.9</u>							
<u>717.2</u>	<u>717.3</u>	<u>717.4</u>		<u>717.4</u>	<u>717.7</u>	<u>717.4</u>	<u>717.9</u>							
	<u>716.6</u>	<u>716.7</u>			<u>716.7</u>	<u>716.3</u>	<u>716.2</u>							
<u>715.2</u>	<u>715.7</u>		<u>716.3</u>	<u>715.8</u>	<u>715.9</u>	<u>715.2</u>	<u>715.0</u>							
<u>714.0</u>	<u>714.7</u>	<u>714.4</u>		<u>715.0</u>	<u>714.6</u>	<u>714.2</u>	<u>714.4</u>							
	<u>713.8</u>					<u>713.5</u>	<u>714.4</u>							
<u>711.2</u>	<u>711.7</u>	<u>712.2</u>	<u>712.2</u>	<u>712.9</u>	<u>712.7</u>	<u>711.6</u>	<u>712.6</u>							
	<u>711.2</u>	<u>711.3</u>	<u>711.2</u>	<u>711.8</u>	<u>711.8</u>	<u>710.7</u>	<u>711.7</u>							
<u>710.6</u>			<u>709.6</u>	<u>709.4</u>	<u>710.2</u>	<u>709.8</u>	<u>709.8</u>							
		<u>708.6</u>												

↑ Binding Energy (eV)

The postulated presence of sulfoxide in the ESCA samples leads to several possible explanations of the two different (by 0.8 eV) iron-bound sulfide peaks in 515. One possibility is partial oxidative attack on the cluster resulting in S-O species still bound to the metal. This would require electron transfer from the cluster and (in terms of a delocalized model) should result in higher charges on the unoxidized sulfide. The sulfoxide sulfur should also shift to lowered binding energy because of electron delocalization in the cluster. A second possibility arises if irradiation of the sample with low-energy electrons produces a slight amount of reduced cluster compound, which should give rise to S2p peaks at lowered binding energy as compared to the parent compound.

These arguments suggest that the A sulfur corresponds to the reduced state of the cluster sulfide and the B sulfur to the oxidized state.

Turning to the Fe 2p region of the photoelectron spectrum, Fig. 87 gives the spectra of the model complexes in the range of 750 to 700 eV. Spectrum 511 is that of Holm's compound, 524 represents the dithiolene complex, 536 the Model #5, 537 the Model #3, and 545 the Model #4.

Because of the aerobic oxidation manifested in the O1s and S2p spectra of these complexes, it can be concluded that the Fe2p spectra contain contributions from the reaction products as well as from the parent compound which remain in the observation layer.

The inflection points observed in these spectra are listed in Table 14. The spectra of Fig. 87 lack the fine structure produced by the d^9 Cu(II) complexes described in Chapter VI. In general, d^5 Fe^{III} and d^6 Fe^{II} complexes are high spin and undergo several multiplet and shake up processes.

The low spin complexes show shake up structure but still give narrow lines (~ 2 eV FWHM) as compared to the high spin cases where the spectrum becomes an indistinct broad band ($\sim 6-7$ eV FWHM). The superior performance of the HP 5950A permits resolution of structure superimposed on these bands.

Present theory cannot cope with the variety of states which give rise to the large number of multiplet and shake up peaks comprising these spectra.

In all spectra of Fig. 87, initial background (from low binding energy to high) is relatively flat but the background at binding energies greater than those corresponding to the $2p_{1/2}$ components is nearly as great (electron flux) as the observed photoelectron peaks. The region between the $2p_{3/2}$ and the $2p_{1/2}$ peaks never returns to the initial background. The shape of the background should be dependent on the cross-section for electron scattering and therefore be sample dependent.

In each spectrum, the curve shows structure at binding energies which are slightly lower than the $2p_{1/2}$ line. This structure falls in the range of observed multiplets^{116,117,118}.

Spectrum 537, ferrous model #3, shows a sharp line at 709.4 eV and a broad peak at 712.7 eV. Model #5, the ferric sulfur complex, shows (spectrum 536) a peak at 711.2 eV with structure at 712.9 eV. Spectrum 545 of model #4, ferric sulfur, oxygen complex shows a peak at 711.8 eV with additional structure at 716.7 eV.

The dithiolene complex (MC #2) gives rise to spectrum 524, which shows a peak at 708.6 eV with a major peak at 711.3 eV. Finally, the cluster complex gives rise to a peak (spectrum 511) at 710.6 eV with a shoulder at

711.9 eV. Throughout those spectra, broad peaks are found at 711.8 \pm 0.2 eV. Previous investigators have assigned the Fe 2p_{3/2} from Fe₂O₃ at 712.0 eV \pm 0.2 eV, and the 2p_{3/2} peak from FePO₄ at 712.8 eV \pm 0.2 eV^{116,123}. Thus, each of these samples apparently contains an iron oxide contaminant in addition to the starting compound. Since none of the model compound spectra are due to a totally oxidized species, no oxide curve is available for difference analysis.

The spectrum of the dithiolene complex shows peaks at ferrous (708.6 eV) and ferric (711.3 eV) positions. These are comparable to those reported by Liebfritz¹¹⁵ for reduced and oxidized dithiolene complexes. If the peak at 708.6 eV arises from reduced complex and that at 711.3 eV from oxidized dithiolene, the remaining component at 712.5 eV must arise from the metal oxide.

The peak at 709.4 eV in spectrum 537 corresponds to the parent compound. The broad structure at high binding energy can be attributed to oxidized ferric components. Similarly, the parent compound (model #5) gives rise to the peak at 711.2 eV in spectrum 536 and the structure at 712.9 eV corresponds to metal oxide or shake-up transitions. However, as noted in Table 14, a small inflection is observed in this spectrum at 709.6 eV which could be attributed to reduced species arising from mechanisms discussed in Chapter VI.

The peak at 711.8 eV in spectrum 545 is assigned to the parent ferric compound (model #4). Those peaks centered at 716.7 eV can be assigned to shake-up processes. The sharpness of the peak may be related to the

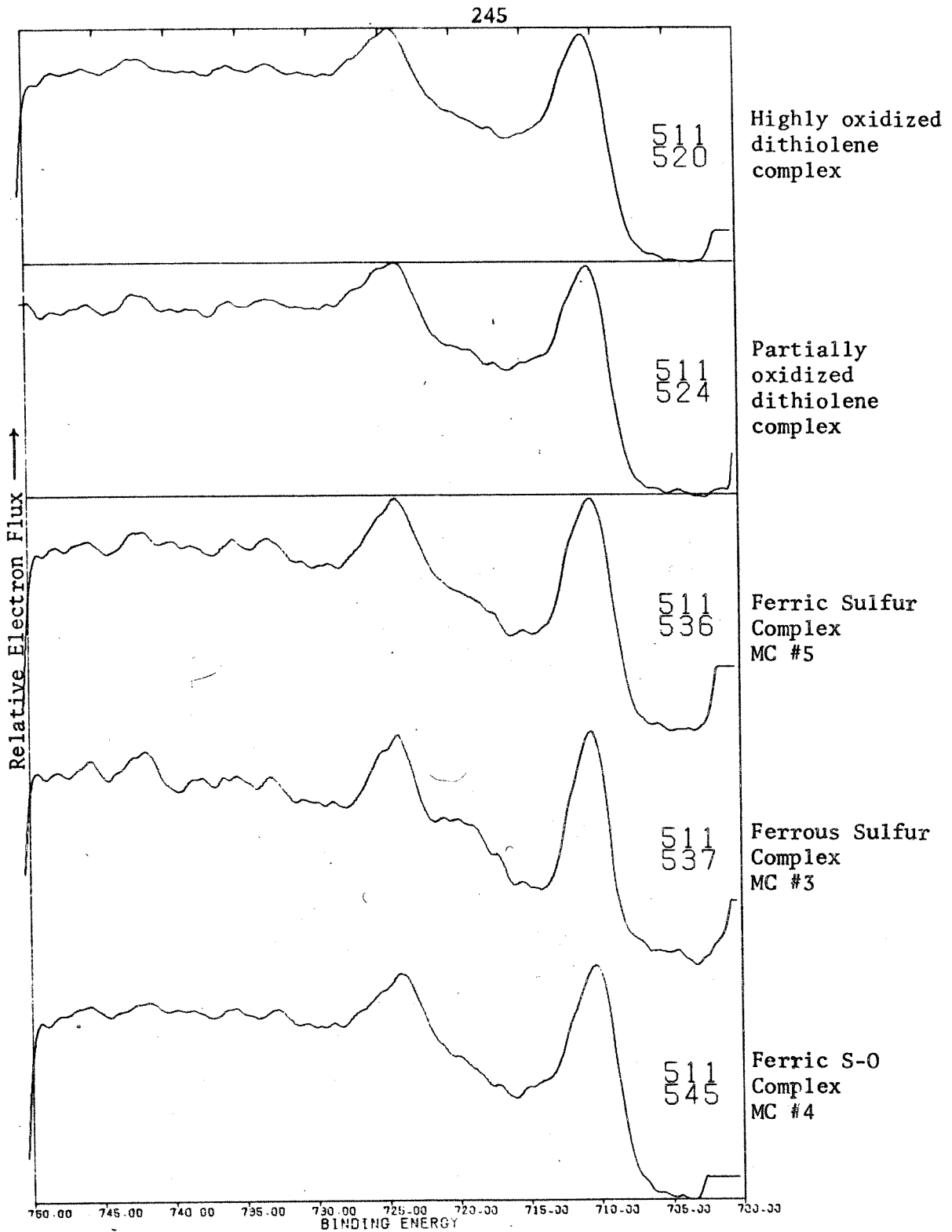


Figure 88. Difference spectra comparing spectrum (511) of Holm's cluster compound (MC #1) with that of the other complexes listed on the ordinate.

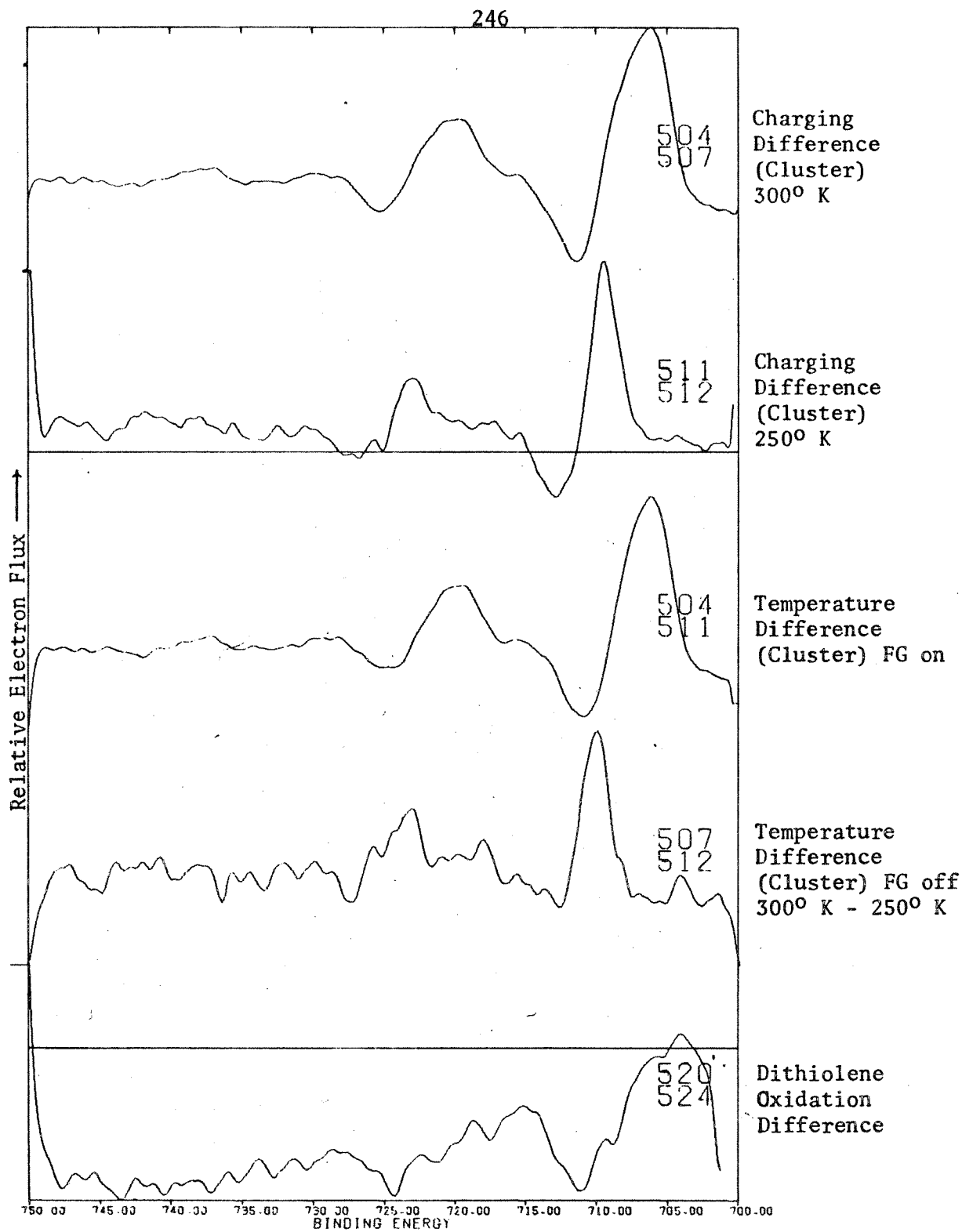


Figure 89. Difference spectra comparing spectra arising from the cluster complex (MC #1)

presence of oxygen in the inner ligating sphere.

Figure 88 gives difference spectra in which spectrum 511 (Holm's compound) is compared with the spectra of the other model complexes. The difference spectrum 511-520 compares the spectrum of the cluster with that of the highly oxidized dithiolene sample. 511-524 gives this comparison with the spectrum of a less oxidized dithiolene sample. The contrasting of spectra 536 and 537 shows a sharpening of detail in the 511 spectrum and enhancement of the structure at about 720 eV.

As has been mentioned, both spectrum 536 (MC # 5) and spectrum 537 (MC #3) are dominated by structure at 712 eV which has been attributed to metal oxides. However, the major enhancement in the spectrum of the cluster complex through this difference analysis occurs at 716 eV which should arise primarily from multiplet structure.

Spectrum 537 shows evidence of ferrous components and the 511-537 difference spectrum has sharpened the low binding energy side of the Fe $2p_{3/2}$ peak of 511. This spectrum of predominately ferric species (536) has enhanced the shoulder at lower binding energy in the difference spectrum 511-536. These difference spectra indicate that the cluster compound contains a small amount of ferrous iron. The Fe(II) species are probably contained in the reduced state of the cluster complex which was suggested in the sulfur spectra.

Figure 89 shows a set of flood gun experiments. 511 is the FG on spectrum of the cluster complex and 512 the FG off case. Their difference spectrum (511-512) shows a peak centered in the ferrous region which

shifts to high binding energy. This is consistent with charging experiments using the S2p spectra of this complex. The reduced state appears to shift more than the normal (electron oxidized) state.

Spectrum 507 is that of the cluster complex at 300^oK (FG off) and is compared to its 250^oK counterpart (512) in the difference spectrum 507-512. This curve suggests that the amount of ferrous material in the sample of the cluster complex is much greater at room temperature than at reduced temperatures. Again, as observed in the copper problem, reduction appears to be inhibited by going to lower temperatures.

This analysis of the spectra of Holm's compound indicates that some reduced species are present and ferric decomposition products are observed in the sample, but the Fe 2p photoelectron spectra are consistent with a delocalized model of the cluster. No evidence is found for equal amounts of localized charge Fe(III) and Fe(II) species, and the observed line width is consistent with the low spin magnetic states.

Since the time scale of the relaxation processes which dominate this experiment is 10^{-16} sec and these spectra probe atomic or core states, this observation of low spin iron is not consistent with the antiferromagnetically coupled (spin-paired) state which Herskovitz et.al.¹¹³ have used to describe the complex.

If additional data from other methods should conclusively show that the iron centers are high-spin antiferromagnetically coupled, then new concepts of magnetic effects on ESCA line shapes must be developed.

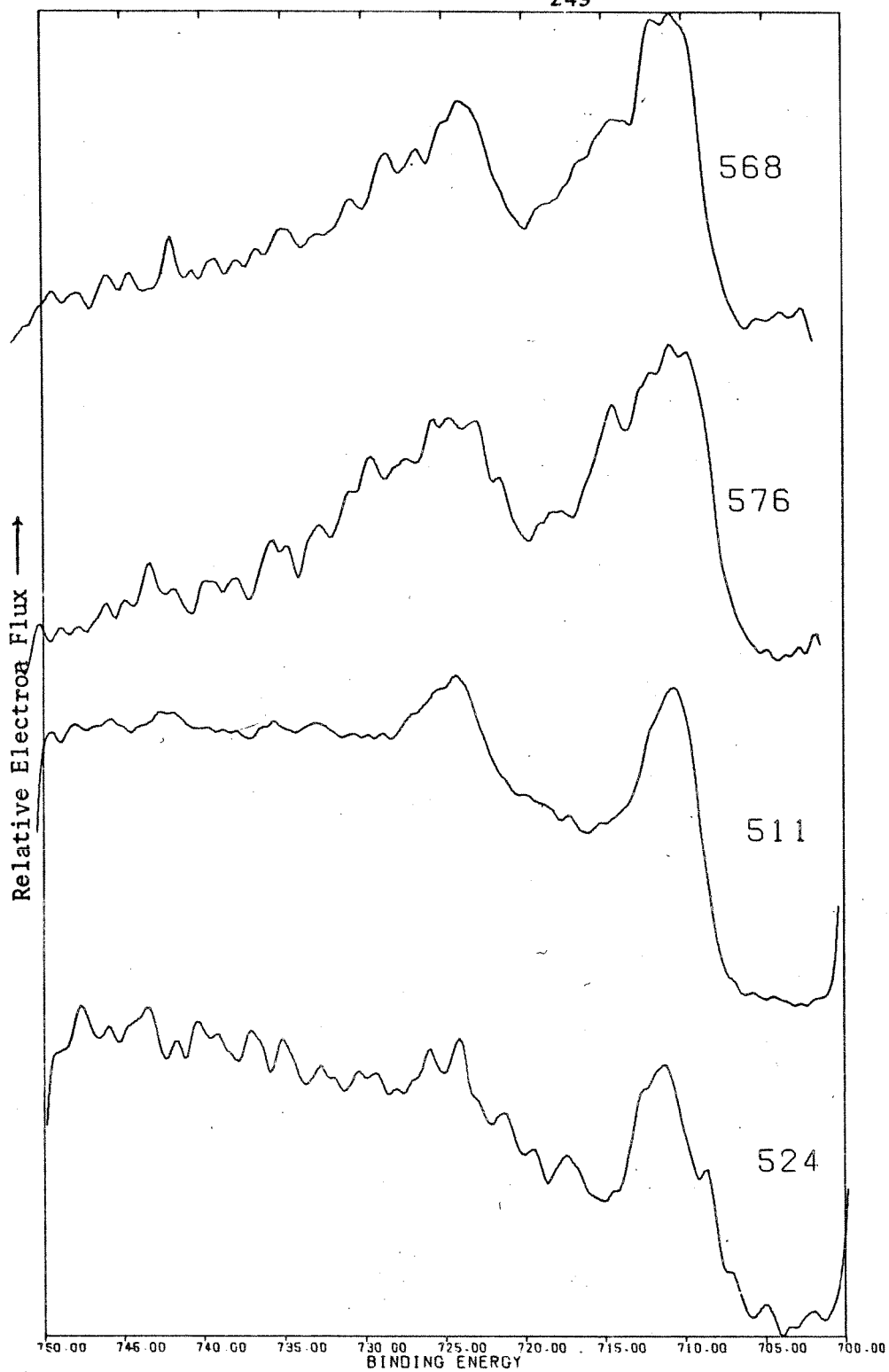


Figure 90. Iron 2p spectra of 2 Iron (568) and 4 Iron (576) ferredoxin proteins. The Fe 2p spectra of the cluster (571) and the dithiolene (524) complexes are also plotted for comparison.

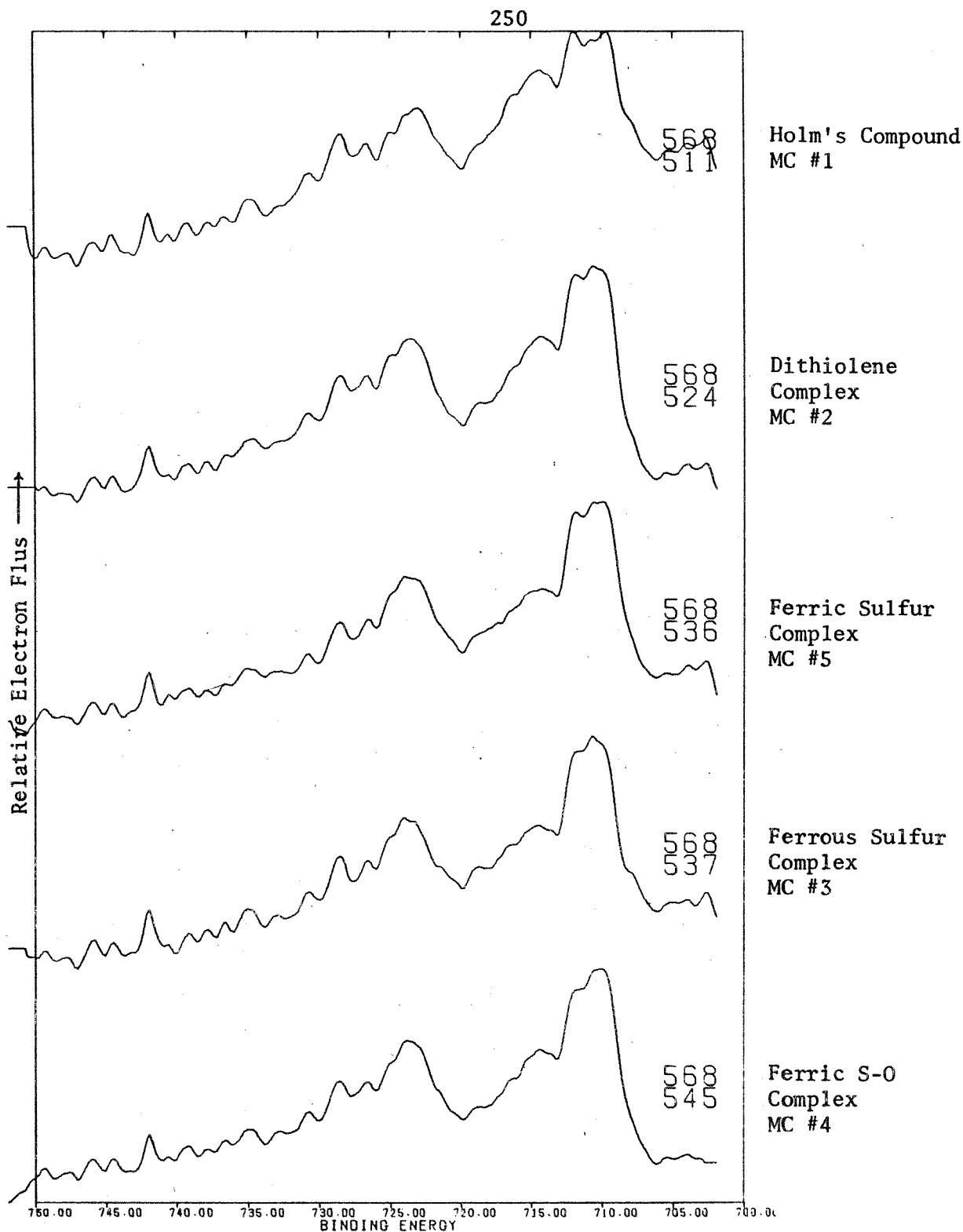
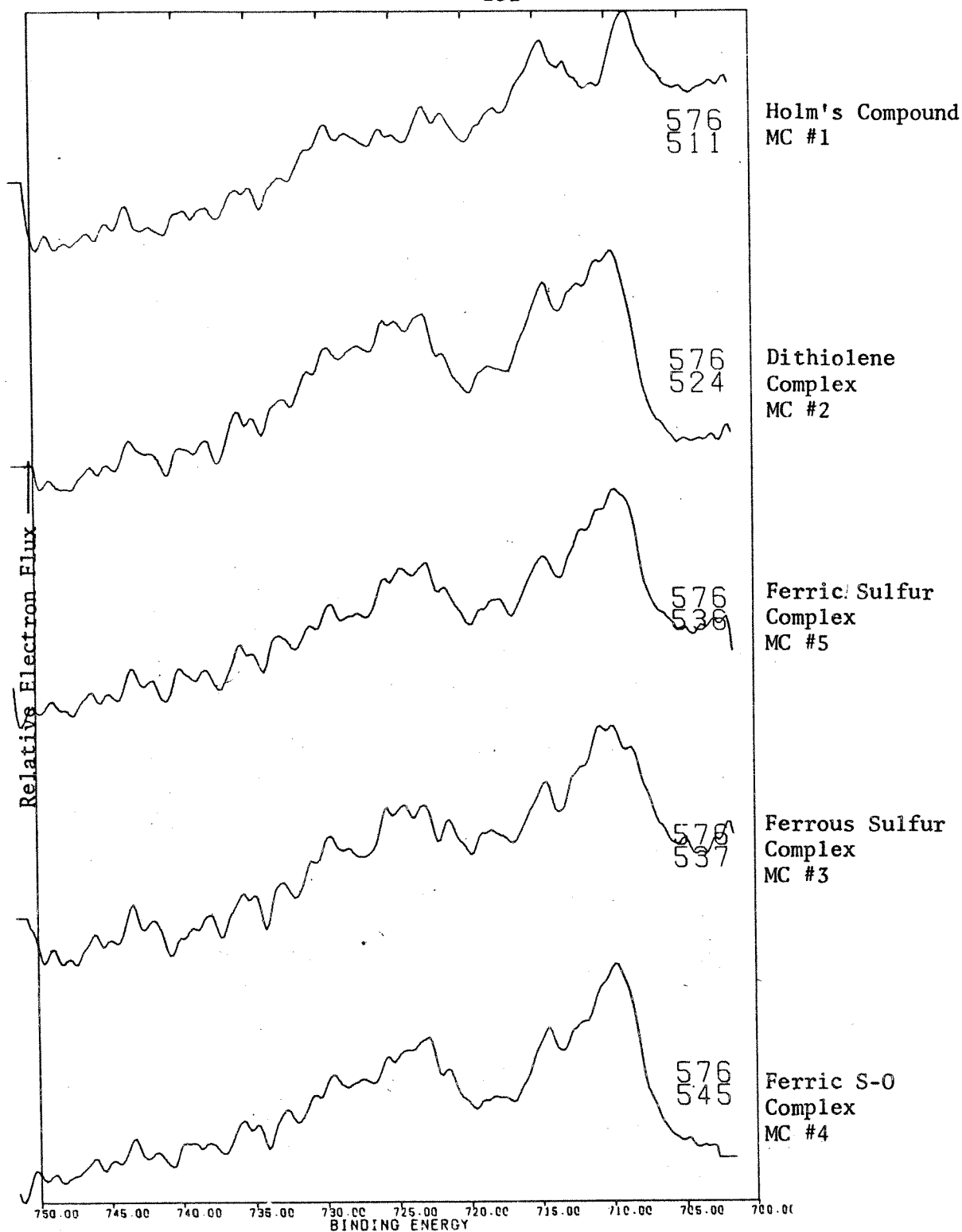


Figure 91. Difference spectra comparing the Fe 2p spectrum of the 2 Fe-2S Ferredoxin with the spectra of the iron sulfur model complexes.



(Figure 92. Difference spectra comparing the Fe 2p spectrum of the 4 Iron Ferredoxin (576) with that of the iron-sulfur Model Complexes.

Now turning to an analysis of the 2 Iron and 4 Iron ferredoxins, Fig. 90 gives their Fe 2p spectra. Spinach ferredoxin (2 Fe, 2 labile S) corresponds to spectrum 568, and spectrum 576 arises from the high potential iron protein (4 Fe, 4S) from Chromatium. The Fe 2p spectra of the cluster complex (511) and the dithiolene complex (524) are also shown in this figure for comparison.

A difference in the structure of the background at high binding energy is apparent in the protein spectra. This change can be attributed to sample-related differences in the electron-scattering cross-sections. In the case of the protein, the average Z of the scattering atom will be much lower than that of the model complexes which have a higher concentration of iron.

The spectrum (568) of the two-iron spinach ferredoxin shows a major peak at 710.7 eV which is intriguingly similar to that of the cluster complex (710.6 eV). It also shows a second peak at 714.2 eV. The HiPIP spectrum (576) shows a major peak at 711.8 eV, a shoulder at 709.7 eV, and another peak at 714.3 eV.

Figure 91 gives the difference spectra which compare the 2 Fe ferredoxin with the model complexes and Fig. 92 contains similar comparisons for the 4 Fe case.

From Figure 91, it appears that while the cluster complex is an excellent model for the major Fe 2p line of spectrum 568, it gives an inadequate representation of the satellite peak at 714.2 eV. The spectrum arising from the oxidized (ferric) contaminant has little effect on the overall shape of the protein spectrum. In the case of the ferrous model complex

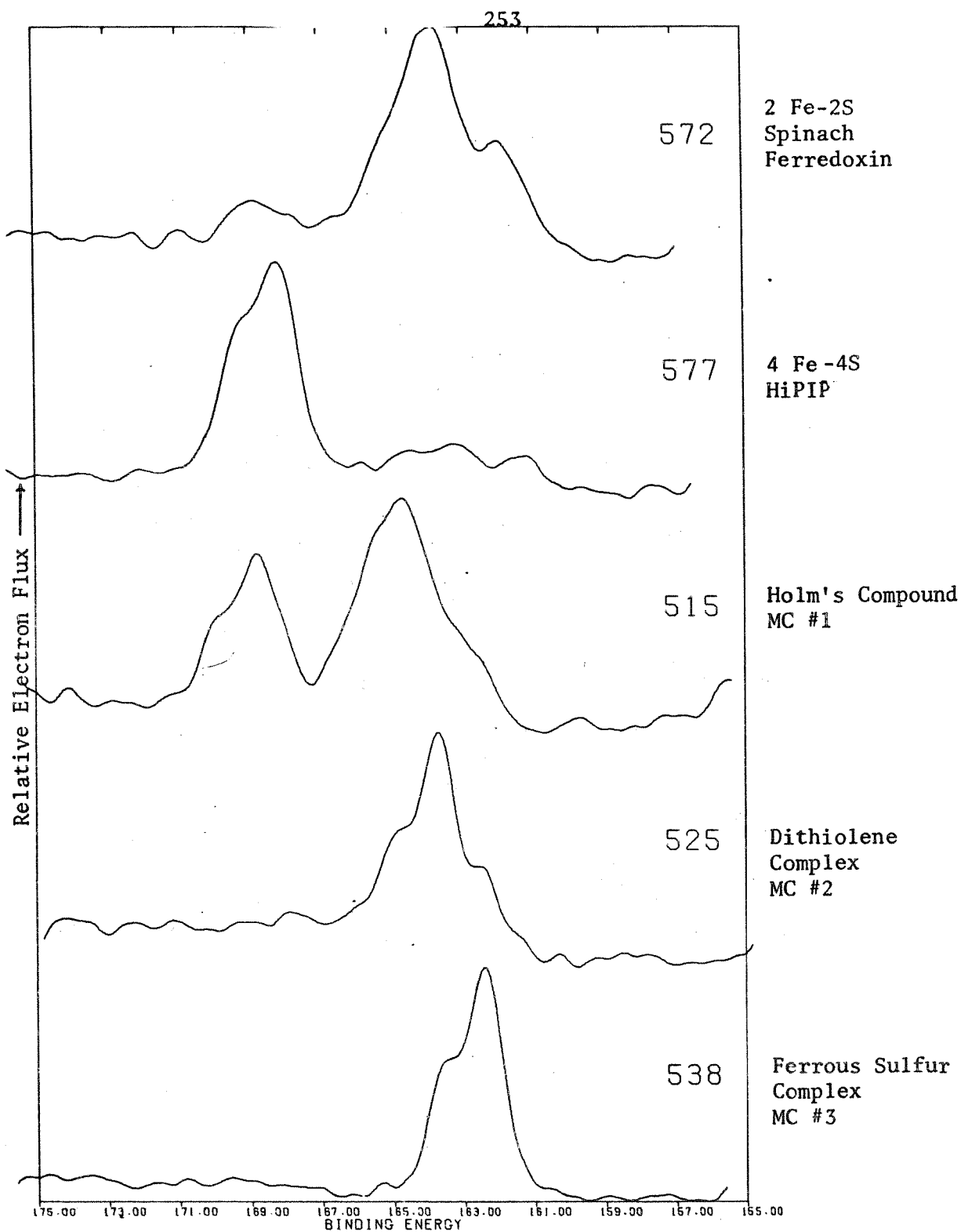


Figure 93. Sulfur 2p spectra of the Ferredoxin proteins. The spectra corresponding to several of the model complexes is also plotted for reference.

(568-537), the low binding energy side of the main peak is sharpened. This indicates that some reduced species are present in the spinach ferredoxin sample.

The difference spectra using the spectrum of 4 Fe-HiPIP are quite different from those using that of the 2 Fe protein. Comparison with the cluster complex (576-511) demonstrates that more reduced iron is present in the HiPIP sample. Nonetheless, the spectra of the cluster complex is still the best model for that of the protein in every regard except for the peak at 714.3 eV. This peak occurs in both protein spectra and could arise from a satellite transition unique to the proteins and the nearest neighbors around the active site.

Comparison with the spectrum of the dithiolene complex also emphasizes the presence of some reduced iron in the protein sample. The difference spectrum with 536 enhances this low binding energy peak, while 576-537 appears to emphasize the ferric component of the protein. The shape of the curve resulting from 576-545 (MC #4) shows the enhancement of a low binding energy peak, and a symmetrical peak midway between the ferric and ferrous parts of the spectrum.

The sulfur 2p spectra for these proteins are given in Figure 93. Spectrum 572 arises from spinach ferredoxin and spectrum 577 corresponds to a four iron HiPIP sample. The S2p spectra arising from the cluster complex, the dithiolene complex and the ferrous model complex (MC #3) are included in the figure for comparison. Differences between the protein spectra are immediately evident. HiPIP (577) shows significantly more sulfate

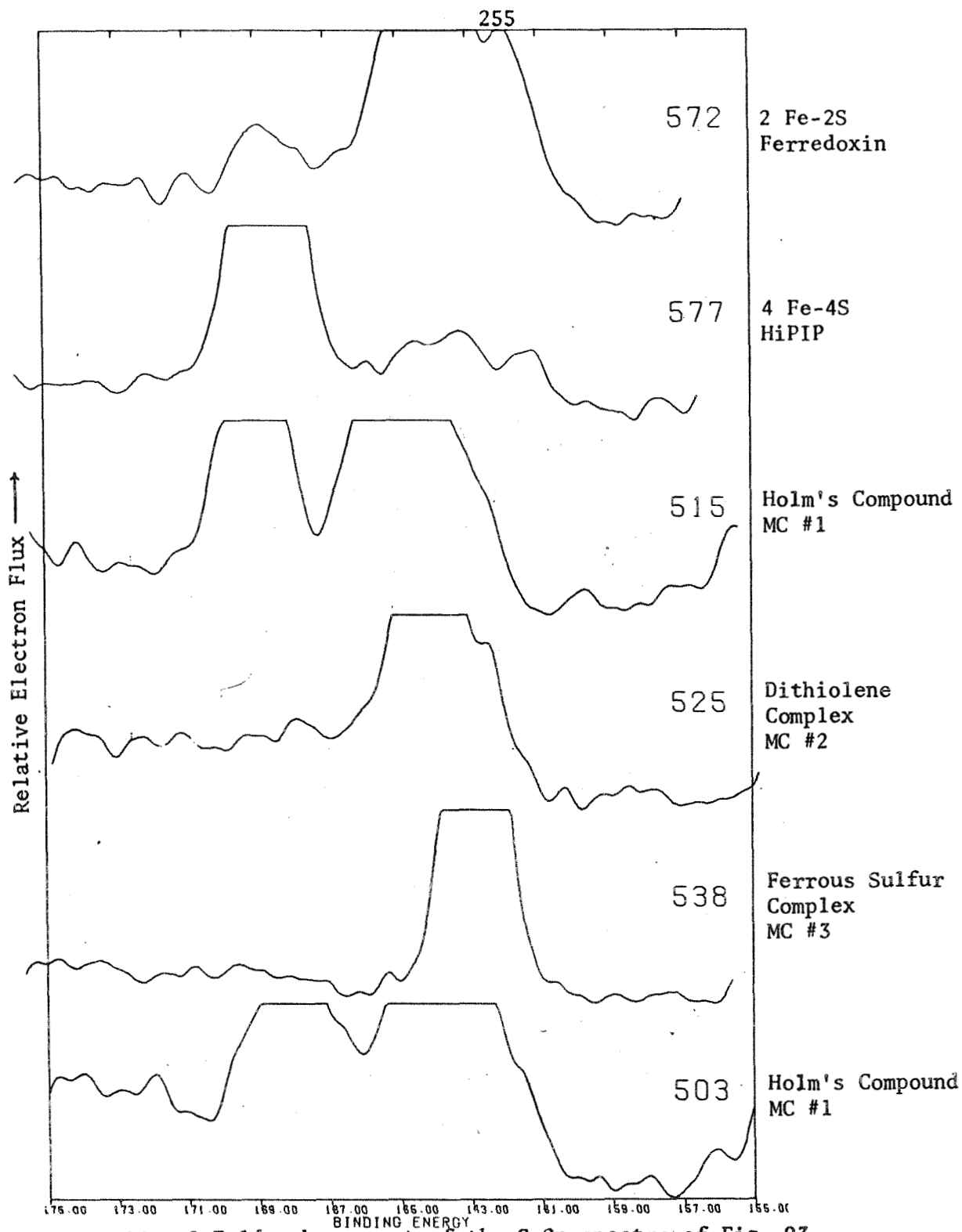


Figure 94. 2-Fold enhancement of the S 2p spectra of Fig. 93.

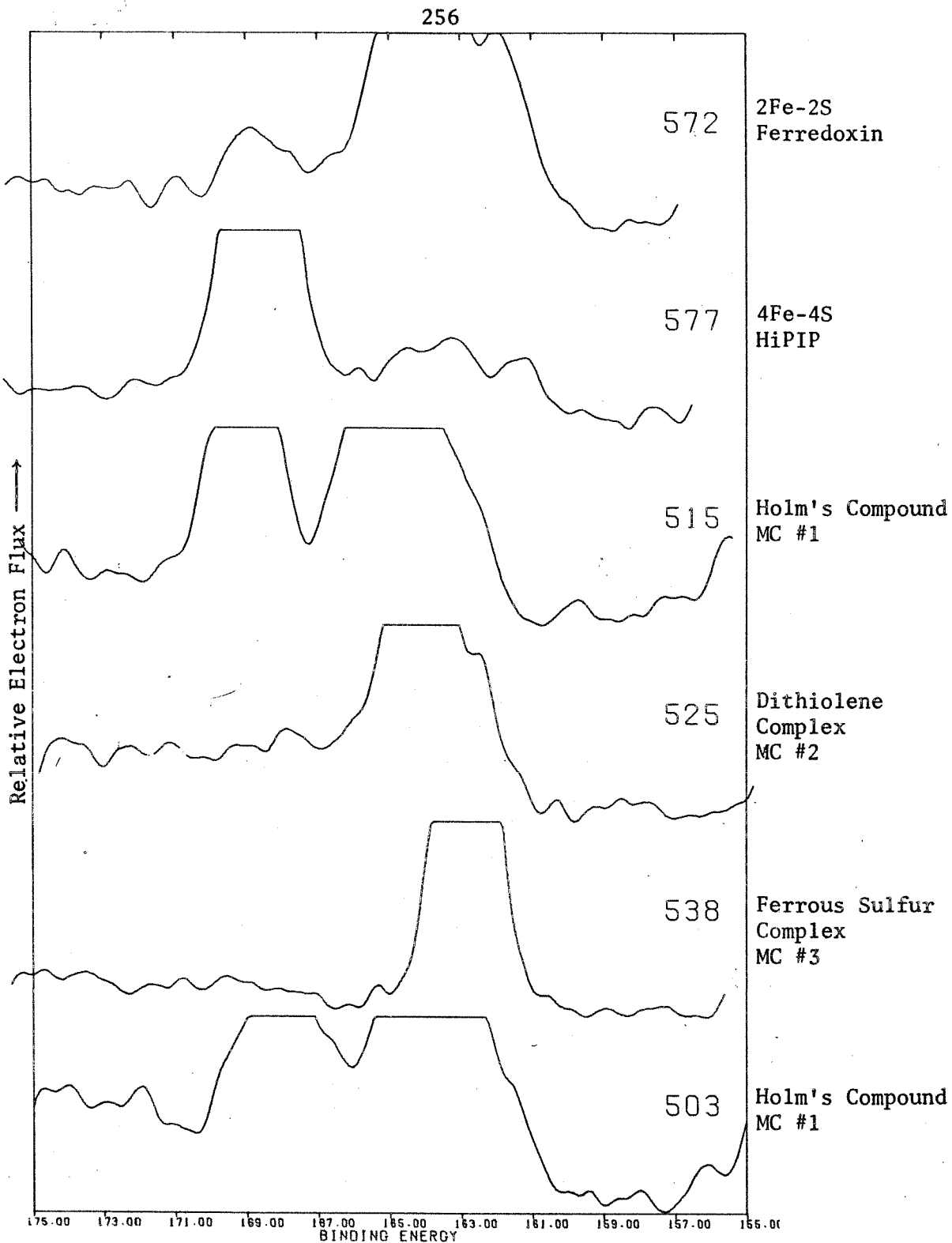
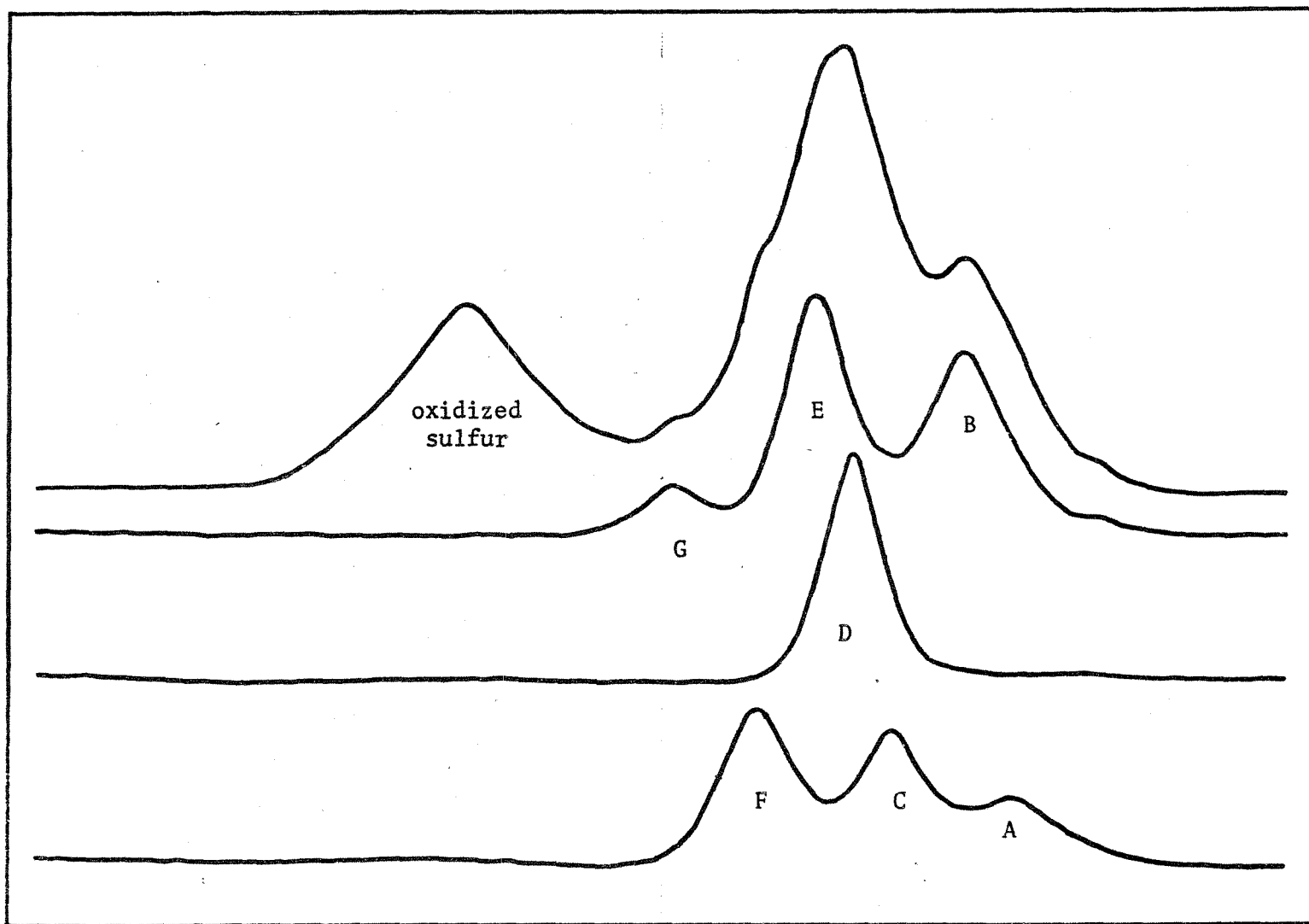


Figure 95. 4-Fold enhancement (y-axis) of the spectra of Fig. 93.



257

← Binding Energy

Figure 96. Deconvolution of the S2p spectrum (572) corresponding to 2Fe-2S Spinach Ferredoxin.

than does spinach ferredoxin, as evidenced by the intensity of the sulfur peaks at 168.1 eV and 168.3 eV. This difference was consistently observed during all work with these proteins (4 samples of HiPIP and 7 of spinach ferredoxin). Similar results were reported by Kramer and Klein¹¹⁴.

Apparently, sulfate is more tightly bound to HiPIP than to spinach ferredoxin even though both proteins had been extensively desalted. The strong oxidized sulfur peak in HiPIP has prompted the use of magnification of the y-axis to better resolve the divalent sulfur region.

Correspondingly, Fig. 94 shows 2-fold enhancement of Fig. 93 and Fig. 95, 4-fold. The observed positions of the major peaks are catalogued in Table 11 for comparison with other S2p data.

Figure 96 gives the deconvolution spectrum of S2p spectrum 572 for spinach ferredoxin. The deconvolved peaks with their positions and intensities are given as follows:

<u>Peak</u>	<u>Position</u>	<u>Rel. Intensity</u>
A	161.2 eV	6%
B	162.0 eV	24%
C	163.1 eV	11%
D	163.7 eV	16%
E	164.3 eV	20%
F	165.2 eV	14%
G	166.5 eV	4.5%

Proceeding from low binding energy to high, and assigning positions which correspond to the S2p_{3/2} line, we find that the peak at 161.2 eV requires a component at 162.4 eV of 3% relative intensity. Reducing B by 3% to 21%, this peak suggests a line at 163.2 eV of about 11%. C is therefore assigned as the spin-orbit component of B. If D is a primary component

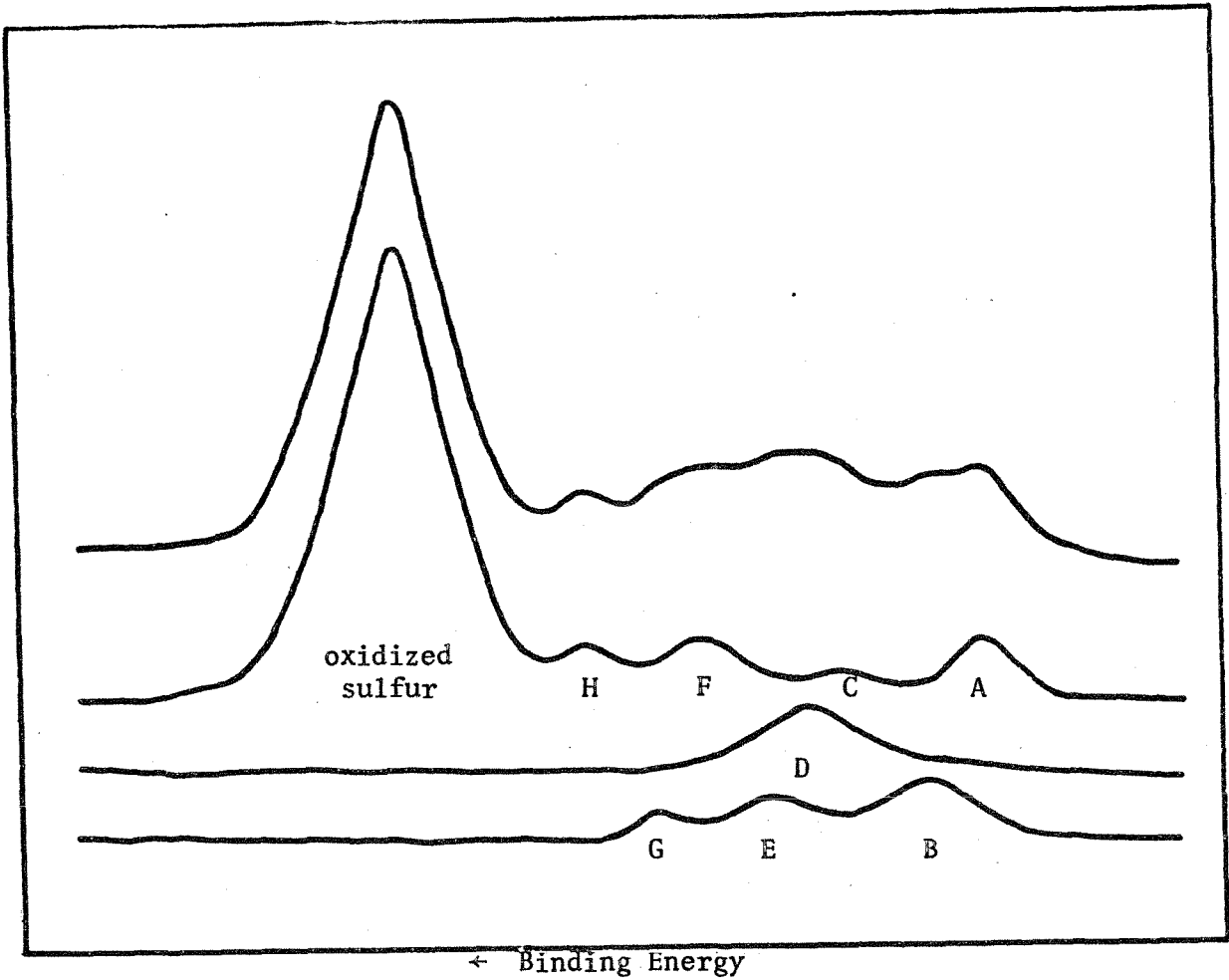


Figure 97. Deconvolution of spectrum 576 corresponding to 4Fe-4S High Potential Iron Protein (HiPIP)

(16%) intensity, a line is required at 164.9 eV with 8% relative intensity. The peak at 164.3 eV with 20% primary intensity requires a peak at 165.5 eV with 10% relative intensity. These two spin-orbit requirements could be attributed to the broad line at 165.2 eV (F).

The reduced intensities, showing only the $S2p_{3/2}$ peak position and intensity, are as follows:

<u>Peak</u>	<u>Position</u>	<u>Rel. Intensity</u>
A'	161.2 eV	6%
B'	162.0 eV	21%
D'	163.7 eV	16%
E'	164.3 eV	20%
G'	166.5 eV	4%

Through comparison with the assignments of the sulfur spectra of the cluster compound, A' sulfur is attributed to bridging sulfur at a reduced site and B' as its oxidized counterpart. The ratio of these sites is about 4:1 (oxidized:reduced). D' sulfur is attributed to cystine bound to metal, whereas E' is assigned as free cystine (not coordinated to metal). The intensity ratio indicates that the concentration of bound cystine is nearly equal to that of the unbound.

The labile (sulfide) $S2p$ assignments for spinach ferredoxin are 1.3 eV (for both peaks) lower than the corresponding assignment in the cluster compound. The peaks corresponding to aliphatic divalent sulfur differ by 0.4 eV. Thus, about 0.4 eV of these differences can be attributed to localized site differences.

The deconvolution of spectrum 576 is given as Figure 97. The spectrum of Fig. 92 was used in this work and not the magnified traces of Fig. 93.

The errors in intensity and position are much greater than in the previous deconvolutions. A summary of the data follows:

<u>Peak</u>	<u>Position</u>	<u>Rel. Intensity</u>
A	161.1 eV	16.5 %
B	161.8 eV	15.0 %
C	162.9 eV	6.0 %
D	163.3 eV	24.0 %
E	163.7 eV	9.0 %
F	164.6 eV	16.5 %
G	165.0 eV	5.0 %
H	165.9 eV	10.0 %

We then proceed from low binding energy to high to construct a set of $S2p_{3/2}$ lines. A should give rise to a peak at 162.3 eV with 8% rel. intensity. This lies part-way between C and D and, as before, they are reduced by 4%. B (161.8 eV) requires a spin-orbit component at 163.0 eV with 5% rel. intensity. This eliminates the intensity of the peak at C (now attributed to $S2p_{1/2}$ components).

D requires a spin-orbit component at 164.5 eV with 12% rel. intensity and E requires one at 164.9 eV with 4.5 % relative intensity. G (165.0 eV) can be attributed to spin-orbit components, and F is reduced to 5% relative intensity.

The net intensities and the positions of the $S2p_{3/2}$ lines estimated from the deconvolution are given below:

<u>Peak</u>	<u>Position</u>	<u>Rel. Intensity</u>
A'	161.1 eV	16%
B'	161.8 eV	10%
D'	163.3 eV	24%
E'	163.7 eV	9%
F'	164.6 eV	5%
H'	165.9 eV	6%

As before, the peak at 161.1 eV is assigned as sulfide in the reduced state and at 161.8 eV to sulfide in the oxidized state of the cluster. D' corresponds to cystine sulfur coordinated to a metal and E' is attributed to the unbound cystine. The ratio of oxidized to reduced active site (deduced from the labile sulfur assignments) is about 2:3 and the ratio of bound to unbound cystine is 2.5:1.

Throughout this work, the low binding energy part of the spectrum has been reducible to two $2p_{3/2}$ peaks with 0.7 eV \pm 0.1 eV separation. The author has attributed this difference to the charge difference observed on the delocalized cluster between the oxidized and the reduced states. In the case of HiPIP, the sulfide photoelectron peaks lie 1.4 eV to lower binding energy than do the sulfide peaks of the cluster complex. The aliphatic bound divalent sulfur lies at about 0.8 eV lower binding energy when comparing HiPIP to the cluster complex.

These deviations can be explained in terms of site variations and are consistent with observations of the sulfur spectra of spinach ferredoxin. The apparent charge on the sulfur atoms, comparing bound cystine to labile sulfur, is not equal and varies for the two cluster cases (model and HiPIP).

These conclusions concerning oxidized and reduced states of the cluster effecting the S2p spectra requires re-examination of the Fe 2p spectra (Fig. 90, 91, 92). Spectrum 568 showed contributions from a small amount of reduced component. Some multiplet structure at 713.5 eV is observed, and a major line is evident at 710.7 eV which is similar to that found for Holm's cluster compound. Spectrum 576 shows line shapes characteristic of

paramagnetic structures and a peak similar to that arising from a reduced species is apparent at lower binding energies (form and shape are similar to that of the cluster compound). Both proteins show a satellite transition at 714.3 eV in their Fe 2p spectra.

These data suggest that the spinach ferredoxin sample contains a small amount of paramagnetic species (seen in the spectra at Fe(II) binding energies). Also, the HiPIP Fe 2p spectrum contains significant contributions from a ferric paramagnetic state.

Finally, the unique satellite structure observed for the proteins suggests that another electron transfer pathway is available in which is provided by nearest neighbors (to the active site) and which has not been approximated by the model complexes studied thus far.

These interpretations are consistent with recent proposals by Carter et al.¹⁰⁶ suggesting that the active site of reduced HiPIP and oxidized 4-iron ferredoxin could both be described as a spin-paired state. Oxidized HiPIP and reduced Ferredoxin would be paramagnetic.

D. Conclusions

This chapter has been devoted to discussion of the ESCA spectra of compounds which are well defined crystallographically. Most of this work has emphasized the cluster model complex synthesized by Holm and co-workers.

Comparison of the electron spectra of this model with the 2Fe and 4Fe ferredoxins has been based on the Fe 2p and S2p spectra.

This complex has been shown to provide an excellent model for the photo-

electron spectra of the active sites of these proteins. In addition to the similarities in the ESCA spectra, several intriguing differences exist. Specifically, the labile sulfur and the mercaptyl or cystine sulfur have been detected in the spectra of the model. Only this complex, Holm's compound, provides a reasonable model for the sulfur spectra of the proteins. The Fe 2p spectra of the cluster model and the native proteins are also strikingly similar. However, the relative charge on the mercaptyl (cystine) and labile sulfur is apparently different for the proteins as compared to the cluster. Also, the Fe 2p spectra of the proteins show a well-resolved satellite transition which is not present in the spectra of the model complexes.

The S2p spectra in low binding energy region can be attributed to the presence of oxidized and reduced states of the Fe-S clusters as regards both the proteins and the cluster model. Spin-paired states have been observed in the oxidized ferredoxin and reduced HiPIP, and paramagnetic states have been found in oxidized HiPIP and reduced ferredoxin. These results have been interpreted in terms of a three-point oxidation cycle where HiPIP and the ferredoxin share a structurally-similar intermediate.

The magnetic environment of the iron centers studied in this thesis has been assigned and these results appear to conflict with data from other physical methods. Specifically, the iron sites in the cluster complex appear to be diamagnetic at an atomic level (10^{-16} sec. relaxation time) rather than low spin at a molecular level (through spin-spin coupling).

These experiments have only solved some of the preliminary problems

pertaining to the study of metalloproteins through ESCA. Again, it appears that oxidized and reduced sites can be prepared "in situ". The possibility of electron titration or electrochemistry in vacuum must be explored further.

This work has demonstrated that proteins can be studied under these experimental conditions. Although decomposition occurs, the parent material can be followed for considerable periods of time. Low temperature capability is essential to the study of decomposable materials, and much attention must be given to sample preparation for reproducible results.

VIII. CONCLUSIONS

This work was initiated after an extensive effort to study the electronic structure of transition metal complexes through low temperature radiation methods proved to be unsuccessful. At this time, the pioneering work of the Uppsala group came to my attention. After a review of the existing literature, I became involved in a program of instrumental design and experimentation which forced a detailed restudy of the fundamental aspects of this work.

The experimental work was first directed at signal detection, then at the physics of x-ray tube design in an effort to generate more signal.

Additional signal demonstrated the poor resolution of our system and the cycle was reiterated. Finally, the instrumentation was under such control that consideration could be given to the samples used in the experiment.

In an effort to solve the engineering problems encountered in the construction of the JPL-USU spectrometer, the author closely examined commercial design practice. In the course of the study of these instruments, experiments were designed to study radiation damage and sample handling techniques. Much difficulty was encountered when attempting to compare results from different laboratories.

The desire to obtain "hard" numbers and control the variations in the charging shift, led the author to develop the experiments described in Chapter III on V_C effects. A conductive sample with insulating oxide layers permitted the measurement of charging shifts relative to an internal standard. The first flood gun on/off experiments with the HP 5950A led to

bias-potential experiments. These stimulated new concepts about the physics of electron capture on the sample surface.

This work demonstrated that charging potentials are primarily neutralized by low-energy electrons and that 95% of these electrons had kinetic energies of less than 6 eV. The bias-potential experiments suggested that models could be developed for the electronic interaction of molecules. Significant chemical properties could be linked to differences in the surface conductivity. This led to the use of a through-bond conduction model to explain these results.

The charging-effect experiments led to the steady-state model for vacuum-electron emission and replenishment. This steady-state determined the observed surface potential of the insulating material.

The work on the VB_2 -passivation reaction was stimulated by the desire to understand these differences in the properties of the surface.

Throughout this work, a prejudice was developing which held that ESCA contained significant quantitative and qualitative information which might be focused to solve practical chemical problems.

The key to the quantitative problem came with Wagner's publication of relative sensitivities of the elements which he had observed through considerable research. The regression analysis of his data led directly to the observations of adsorptive reactivity in Chapter V. This may lead to significant new understanding in studies of catalysis.

The variation in the VB_2 spectra by sample forced the author to examine critically the techniques of handling samples. These studies demonstrated

the necessity of clean vacuum systems which are free of major hydrocarbon impurities. This permits the use of internal reference standards based on methyl or aliphatic carbons which can be used to compensate for lattice and other site effects.

The use of double-stick tape was soon abandoned and the thin film and thin crystal techniques were developed.

The study of metalloproteins required an extension of the sensitivity of the method **by** one order of magnitude beyond levels previously reported. This resulted in development of optimum-resolution filters to remove the noise in the data.

A knowledge of radiation photo-processes led the author to devise the time/temperature experiments reported in Chapter VI. Here, Dr. Gray's continuing interest in copper metalloproteins stimulated the author to go beyond the disappointment of overlapping chemical shifts of Cu(I) and Cu(II).

Experiments were developed which used the satellite structure of the photoelectron lines of transition metal ions and the observed photo-reduction of cupric ion; see Chapter VI. These experiments led to the proposal of a $\text{Cu}^{\text{I}}\text{-S-S-Cu}^{\text{I}}$ identity for the diamagnetic type 3 copper site in Laccase. Similar experiments led to a Cu(II) model for the copper-oxygen site in oxy-hemocyanin.

The sulfur spectra of proteins and model complexes were also studied. The observation of disulfide coordinated to metal reinforced the model proposed for Laccase. The enhanced rate of photoreduction in proteins led to the suggestion that both oxidized and reduced forms could be studied "in situ"

in the photoelectron experiment. A smaller difference in binding energy between Cu(I) and Cu(II) at similar sites was observed in the proteins as compared to the model complexes. This should lead to models of the coordination in the biological state, since the difference in energy between the oxidized and the reduced state is uniquely low.

Much of this work was speculative because no definitive structural evidence was available.

In Chapter VII, a study of iron-sulfur (non-heme) proteins is reported. Here, complicated iron and sulfur spectra are analyzed using internal referencing, variable temperature control, charging differences and electron reactions to develop an electronic structural model of the active sites of these electron-transfer proteins. The recent synthesis of a cluster complex which effectively modeled the active site of the iron sulfur protein provided an opportunity for the application of the previous experiments to a well-characterized system.

Chapter VII details the analysis of the structural aspects of iron-sulfur model systems and gives a discussion of the properties of the delocalized Fe-S cluster. The labile sulfur which is bound to iron in the cluster appears to be found in two forms, one corresponding to the oxidized electronic state of the cluster, the other corresponding to the reduced form. Free cystine sulfur has been observed as well as its metal-coordinated equivalent.

The magnetic state of the iron centers have been examined. A delocalized model of the iron sulfur moiety is consistent with the data. As observed

in the copper-protein experiments, both oxidized and reduced forms of the proteins have contributed to the ESCA spectrum. Only one iron environment and valence is observed in the Fe-S clusters (model and protein).

A major difference in the Fe 2p spectrum of the proteins as compared to the model complex has led to the speculation of the existence of an additional environment in the protein capable of electron transfer from the cluster. The possible correlation of shake-up transitions with detailed analysis of the valence band of the photoelectron spectrum and the far UV adsorption spectrum might lead to new insight into electron transfer mechanisms in proteins.

REFERENCES

1. Siegbahn, Kai; Nordling, Carl; Fahlman, Anders; Nordberg, Ragnar; Hamrin, Kjell; Hedman, Jan; Johansson, Gunnilla; Bergmark, Torsten; Karlsson, Sven; Lindgren, Ingvar; Lindberg, Bernt; Electron Spectroscopy for Chemical Analysis-Atomic, Molecular, and Solid State Studies by Means of Electron Spectroscopy, Almqvist & Wiksells Boktryckeri AB, Stockholm, Sweden, 1967.
2. Hollander, J.M., and Shirley, D.A., Ann. Rev. Nucl. Sci., 20, 435 (1970).
3. Siegbahn, et. al., ESCA Applied to Free Molecules, North Holland, Amsterdam, 1969.
4. Gelius, U., Molecular Orbitals and Line Intensities in ESCA Spectra, Uppsala University, Institute of Physics, Publication #753, November, 1971.
5. Fadley, C.S., Thesis, University of California, Berkeley, 1970.
6. Pollak, R.A., Thesis, University of California, Berkeley, 1972.
7. Bremser, W., X-ray Photoelectron Spectroscopy in Topics in Current Chemistry, 36, Springer-Verlag, Berlin 1973.
8. Hercules, D.M., Analytical Chemistry, 42, 20A, 1970.
9. Gray, H.B., Structural Models for Iron and Copper Proteins Based on Spectroscopic and Magnetic Properties in Bioinorganic Chemistry, Advances in Chemistry, 100, American Chemical Society, Washington, D.C., 1971.
10. Tsibris, J.C.M., and Woody, R.W., Coordination Chemistry Reviews, Elsevier Publishing, Amsterdam, 1970.
11. Williams, R.J.P., Role of Transition Metal Ions in Biological Processes, RIC Reviews, 1, 13 (1968).
12. Fadley, C.S., Theoretical Aspects of Electron Spectroscopy, NATO Conference on Electron Emission, Ghent, 1973.
13. Kittel, C.K., Solid State Physics, Wiley, (1968); 2nd Edition 1973.
14. Fadley, C.S., Hagstrom, S.M.M., Klein, M.P., and Shirley, D.A., J. Chem. Phys., 48, 3779 (1968).

15. Pauling, L., The Nature of Chemical Bond, Ithaca, New York, Cornell Univ. Press, 3rd edition, 1960.
16. Bagus, P.S., and Liw, B., Phys. Rev., 148, 79 (1966).
17. Kraus, M.O., Vestal, M.L., Johnston, W.H., and Carlson, T.A., Phys. Rev., 133, A385 (1964).
18. Carlson, T.A., and Kraus, M.O., Phys. Rev., 137, A1655 (1965).
19. Kraus, M.O., Carlson, T.A., and Desmukes, R.D., Phys. Rev., 170, 37 (1968).
20. Hedin, L., and Lundqvist, S., Solid State Physics, 23, 1 (1969).
21. Doniact, S., Phys. Rev., B2, 3898 (1970).
22. Wagner, C.D., Anal. Chem., 44, 967 (1972).
23. Henke, B.L., X-ray Optics and X-ray Microanalysis, Academic Press, New York, 1963, pp. 157-172.
24. Wagner, C.D., Anal. Chem., 44, 1050 (1972).
- 24a. Jorgensen, C.K., and Berthou, H., Farad. Disc. Chem. Soc., 54, 269, (1972).
- 24b. Nefedov, V.I., Sergushin, N.P., Bond, I.M., and Trzhaskovskaya, M.B., J. Elec. Spec., 2, 383, (1973).
25. Riggs, W.M., Private Communication.
- 25a. Brundle, C.R., and Roberts, M.W., Proc. R Soc. Lond., A 331, 383 (1972).
26. Luccesi, C.A., and Lester, J.E., J. Chem. Ed., 50, A205 (1973).
27. Purcell, E.M., Phys. Rev., 54, 818 (1938).
28. Rendina, J., American Laboratory, 6, 27 (1972).
29. Wood, J.K., and Grunthaner, F.J., unpublished results.
30. Siegbahn, K., Hammond, D., Fellner-Feldigg, H., Barnett, E.F., Science, 176, 245 (1972).
31. Bremser, W., Lennemann, F., Chemiker-Ztg, 95, 1011 (1972).
32. Olgilvie, J.L., and Wolberg, A., Applied Spectroscopy, 26, 401 (1972).

33. Brundle, C.R., Applied Spectroscopy, 25, 8 (1971).
34. Jorgensen, C.K., Chimia, 25, 213 (1971).
35. Hnatowich, P.J., Hudis, J., Perlman, M.L., Ragaini, R.C., J. Appl. Phys., 42, 4883 (1971).
36. Uebbing, J.J., Private Communication.
37. Lindberg, B.J., Hamrin, K., Johansson, G., Gelius, U., Fahlman, A., Nordling, C., Siegbahn, K., Physica Scripta, 1, 286 (1970).
38. Gelius, U., Hedin, P.F., Hedman, J., Lindberg, B.J., Manne, R., Nordberg, R., Nordling, C., Siegbahn, K., Physica Scripta, 2, 70 (1970).
39. Mandelung, E., Z. Physik, 19, 528 (1918).
40. Huchital, D.A., and McKeon, R.T., Appl. Phys. Lett., 20, 158 (1972).
41. Melera, A., and Kelly, M., Private Communication.
- 41a. Riggs, Wm., and Wendt, R., Private Communication.
- 41b. Brundle, C.R., J. Vac. Sci. Technol., 11, 212 (1974).
42. Swartz, W.E., Watts, P.H., Watts, J.C., Brasch, J.W., Lippincott, E.R., Analyt. Chem., 44, 2001 (1972).
43. Diamis, W.P., Lester, J.E., Analyt. Chem., 45, 1416 (1973).
44. Cowman, C., Thesis, California Institute of Technology, 1974.
45. Siegbahn, H., Physica Scripta, 4, 164 (1973).
46. Kramer, L., Klein, M., J. Chem. Phys., 57, 3620 (1969).
47. Liebfriz, D., Angew Chem, 84, 156 (1972).
48. Butler, M.A., Wertheim, G.K., Rousseau, D.L., and Hufner, S., Chem. Phys. Lett., 13, 374 (1972).
49. Figure from HP 5950A manual.
50. Ernst, R.C., Sensitivity Enhancement in Magnetic Resonance, in Advances in Magnetic Resonance, J. Waugh, ed., Vol. 2, 1966.
51. Moore, L., Brit. J. Appl. Phys. (J. Phys D)1 (2), 237 (1968).

52. Morrison, J.D., J. Chem. Phys., 39, 200 (1963).
53. Petersson, G.A., Thesis, California Institute of Technology, 1970.
54. Savitsky, A., and Golay, M.J.E., Anal. Chem., 36, 1627 (1964).
55. Castleman, K.R., and Welch, A.J., Feature Extraction in Visual Evoked Potential Analysis, TR 72, Biomedical Research Laboratory, Univ. of Texas, Austin (1969).
56. Bracewell, R., The Fourier Transform and its Applications, McGraw-Hill, New York (1965).
57. Papoulis, A., The Fourier Integral and its Applications, McGraw-Hill, New York (1962).
58. Wiener, N., The Fourier Integral and Certain of its Applications, Dover, New York (1960).
59. Davenport, W.B., and Root, W.L., An Introduction to the Theory of Random Signals and Noise, McGraw-Hill, New York, 1958.
60. This program was developed and implemented by L.K. Scheffer. The functional filter relationships were provided by K. Castleman and F. Grunthaner.
- 60a. Jansson, Peter A., J. Opt. Soc. Am., 60, 184 (1970).
- 60b. Jansson, Peter A., and Hunt, R.H., Optical Spectra, Sept., 1972, p. 36.
61. Greenwood, N.N., Parish, R.V., and Thornton, P., J. Chem. Soc. (A), 320, (1966).
62. Clendening, P., and Powers, D.P., unpublished results.
63. Larrson, R., and Nunziata, G., Acta. Chem. Scand., 24, 1 (1970).
64. Lavison, R., Acta. Chem. Scand., 26, 549 (1972).
65. Goodenough, J.B., in Progress in Solid State Chem., ed., H. Reiss, Pergamon, Oxford, Vol. 5, 155 (1971).
66. Hamrin, K., Nordling, C., and Kihlberg, L., Ann. Acad. Reg. Sci. Upsaliensis, 14, 1 (1970).
67. Honig, J.M., Van Zandt, L.L., Board, R.D., and Weaver, H.E., Phys. Rev. B., 6, 1323 (1972).

68. Fiermans, L., and Vennik, J., Surface Science, 35, 42 (1973).
69. Calpaert, M.N., Clauws, P., Fiermans, L., Vennik, J., Surface Science, 36, 513 (1973).
70. Wertheim, G.K., Rosencwaig, A., Gallagher, P.K., and Buchanan, D.N.E., Bull. Am. Phys. Soc., 16, 322 (1971).
71. Larsson, R., Falkesson, B., and Schon, G., Chemica Scripta, 3, 88 (1973).
72. The term flood gun refers to the low energy irradiating device described in Chapter III. The reproducibility and magnitude of the flood gun or voltaic potential experiments are described in Chapter III - Section C.
73. Hendrickson, D.N., Hollander, J.M., and Jolly, W.L., Inorg. Chem., 9, 612 (1969).
74. Mavel, G., Escard, J., Costa, P., and Costaing, J., Surface Science, 35, 109 (1973).
75. Allison, D.A., Johansson, G., Allan, C.J., Gelius, U., Siegbahn, H., Allison, J., and Siegbahn, K., Journal of Electron Spectroscopy and Related Phenomenon, 1, 269 (1973).
76. Hamrin, K., Johansson, G., Gelius, U., and Nordling, C., J. Chem. Phys. Solids, 32, 2669 (1970).
77. The flood gun accessory is a relatively new development in the field of electron spectroscopy having only been available in December, 1972 on the H.P. SID spectrometer. Previous work on this instrument would give results reported in this thesis as FG off data. Discrepancies between this and data from other spectrometers were often relegated as spurious.
78. Malkin, R., and Malmstrom, B.G., Adv. In Enzymology, 33, 177 (1970).
79. Vallee, B.L., and Wachter, W.E.C., "The Proteins", H. Neurath, ed., Val, V., Metalloproteins, 2nd ed., Academic Press, New York (1970).
80. Byers, W., Curzon, G., Gorbett, K., Speyer, B.E., Young, S.N., and Williams, R.J.P., Biochem. & Biophys. Acta., 210, 38 (1973).
81. Omura, T., J. Biochem. (Tokyo), 50, 264, and 389 (1961).
82. Katoh, S., Nature, 186, 533 (1960).

83. Katoh, S., Shiratori, I., and Takamiya, A., J. Biochem (Tokyo), 51, 32 (1962).
84. Blumberg, W.E., and Peisach, J., Biochem Biophys Acta, 126, 269 (1966).
85. Mosbach, R., Biochem. Biophys. Acta., 73, 204 (1963).
86. Reinhammer, B., Biochem. Biophys. Acta., 205, 35 (1970).
87. Hemmerich, P., in Oxidases and Related Redox Systems, King, T.E., Mason, H.S., and Morrison, M., eds., p. 216, Wiley, New York (1964).
88. Boas, J.F., Pilbrow, J.R., Troup, G.J., Moore, C., and Smith, T.D., J. Chem. Soc. A 1969, 965 (1969).
89. Ghiretti, F., ed., Physiology and Biochemistry of Hemocyanin, Academic, New York (1968).
90. Van Holde, K.E., Biochemistry, 6, 93 (1967).
91. Frost, D.C., Ishitani, A., and McDowell, C.A., Molecular Physics, 24, 77 (1973).
92. Jung, G., Ottnad, M., Bohnenkamp, W., Bremser, W., and Weser, U., Biochem Biophys Acta, 295, 77 (1973).
93. Jung, G., Ottnad, M., Bohnenkamp, W., and Weser, U., FEBS Lett, 25, 346 (1972).
94. Jung, G., Voelter, W., and Weser, U., Z Physiol Chem, 353, 720 (1972).
- 94a. Holwerda, R., Thesis, California Institute of Technology, 1974.
95. Novakov, T., Phys. Rev., B3, 2693 (1971).
96. Novakov, T., and Prins, R., Solid State Comm, 9, 1975 (1971).
97. Robert, T., Bartel, M., and Offergeld, G., Surface Science, 33, 123, (1972).
98. Castle, J.E., Nature Physical Science, 234, 93 (1971).
99. Schon, G., Surface Science, 35, 96 (1973).
100. Rosencwaig, A., and Werthein, G.K., J. Electron Spec. and Rel. Phen., 1, 493 (1973).
101. Schugar, H.J., Private Communication.

102. Klein, M., and Kramer, L., "Proceedings of the Symposium on Improving Plant Protein by Nuclear Techniques".
103. Wurzbach, J., Private Communication.
104. Mason, R., and Zubieta, J.A., Angewandte Chemie, 85, 390 (1973).
105. Herriott, J.R., Sieker, L.C., Jensen, L.H., and Lovenberg, W., J. Mol. Bio., 50, 391 (1970).
106. Watenpaugh, K.D., Sieker, L.C., Herriott, J.R., and Jensen, L.H., Cold Spring Harbor Symp. Quant. Biol., 36, 359 (1971).
107. Carter, C.W., Jr., Freer, S.T., Xuong, Ng H., Alden, R.A., and Kraut, J., Cold Spring Harbor Symp. Quant. Biol., 36, 381 (1971).
108. Carter, C.W., Jr., Kraut, J., Freer, S.T., Alden, R.A., Sieker, L.C., Adman, E., and Jensen, L.H., Proc.Natl.Acad.Sci. USA, 69, 3526 (1972).
109. Sieker, L.C., Adman, E., and Jensen, L.H., Nature, 235, 40 (1972).
110. Balch, A.L., J. Amer. Chem. Soc., 91, 6962 (1969).
111. Balch, A.L., Dance, I.G., and Holm, R.H., J. Amer. Chem. Soc., 90, 1139 (1968).
112. Davison, A., Howe, D.W., and Shawl, E.T., Inorg. Chem., 6, 458 (1967).
113. Herskovitz, T., Averill, B.A., Holm, R.A., Ibers, J.A., Phillips, W.D., and Weicher, J.F., Proc.Natl.Acad.Sci. USA, 69, 2437 (1972).
114. Kramer, L.N., and Klein, M.P., in Electron Spectroscopy, ed., Shirley, D.A., (North Holland) Amsterdam, pp. 733-751 (1972).
115. Liebfritz, D., Angew Chem Int Ed, 11, 232 (1972).
116. Liebfritz, D., and Bremser, W., Chemiker-Ztg, 94, 232 (1970).
117. Fadley, C.S., and Shirley, D.A., Phys.Rev.A, 2, 1109 (1970).
118. Wertheim, G., Rosencwaig, A., J. Chem. Phys., 54, 3235 (1971).
119. Yin, L.I., Yellin, E., and Alder, I., J. Appl. Phys, 42, 3595 (1971).
120. Bartsch, R.G., in Bacterial Photosynthesis, (Gest, H., San Pietro, A., and Vernon, L.P.) p. 315, Antioch, Yellow Springs, Ohio (1963).
- 120a. Jack, J.J., and Hercules, D.M., Anal. Chem., 43, 729 (1971).

121. Nordberg, R., Albridge, R.G., Bergmark, T., Ericson, U., Hedman, J., Nordling, C., Seigbahn, K., and Lindberg, B.J., Arkiv Kemi, 28, 257, (1968).
122. Steinhardt, R.G., Hudis, J., and Perlman, M.L., Phys Rev B., 5, 1016 (1972).
123. Yin, L.I., Ghose, S., and Alder, I., Appl. Spectry., 26, 355 (1972).

IX. APPENDICES

A. Index of Spectra

SPECTRA INDEX

VOSO ₄	109, 128
VB ₂	44, 74, 98, 99, 100, 102, 104, 105, 106, 107, 113, 114, 116, 118, 120, 121, 123, 124
V ₂ O ₅	106, 109, 111, 114, 116, 120, 121, 123, 124, 126, 127, 128
V ₂ O ₃	106, 109, 111, 114, 116, 120, 121, 123, 124, 126, 127, 128
V	109, 111, 114, 116, 120, 121, 123, 124, 126, 127, 128
VN	109, 126
Na ₃ VO ₄	109, 128
Na ₂ B ₄ O ₇ · 10H ₂ O	109
Au	73, 151, 152
Laccase	194, 196, 197, 199
Stellacyanin	76, 187, 190, 197, 210
Plastocyanin	187, 190, 197, 210
Hemocyanin	207, 209, 210
Cu(BuSCH ₂ CO ₂) ₂	167, 174, 176, 177, 182
Cu ₃ (SC(CH ₃) ₂ CH(NH ₂)CO ₂) ₂	167, 174, 176, 177, 179, 181, 182
Cu(O ₂ CCH ₂ S(CH ₂) ₂ SCH ₂ CO ₂)	167, 174, 176, 177, 182
CuCl ₂ (n-BuS(CH ₂) ₂ S-(n-Bu))	167, 174, 176, 177, 182
Cu(n-Pr(C ₄ H ₄ N ₂ OH)S)	167, 174, 176, 177, 181, 182, 183
Cu(Tetra phenyl phorphrin)	169, 174, 176, 183
Spinach Ferredoxin	80, 280, 282-5
HIPIF	280, 282-5

$\text{Fe}_4\text{S}_4(\text{SEt})_4^{2-}$	79, 81, 227, 232, 234, 236, 238, 241, 246-9, 272, 275, 277, 280, 282-5
$\text{Fe}_2(\text{SCH}_2\text{CH}_2\text{S})_4^{2-}$	227, 232, 236, 238, 246-9, 272, 275, 280, 282-5
$\text{Fe}(\text{SP}\emptyset_2\text{NP}\emptyset\text{S})_2$	227, 231, 232, 238, 246-9, 272, 275, 282-5
$\text{Fe}(\text{SP}\emptyset_2\text{NP}\emptyset_2\text{O})_3$	227, 231, 232, 238, 246-9, 272, 275, 282-5
$\text{Fe}(\text{SP}\emptyset\text{NC}(\text{NC}_4\text{H}_8)\text{S})_3$	227, 231, 232, 238, 246-9, 272, 275, 282-5
Bremstrahlung From Mg Target	29, 30
RGA Spectrum	36

B. Electron Energy Diagrams

PHOTOELECTRON AND AUGER LINES

(Al Xrays)

(A = Auger line; 1 = sub 1/2; 3 = sub 3/2; 5 = sub 5/2; 7 = sub 7/2)

18	*	Hf4f	63	*	Na2s	110		Te4p	180	*	Tm4d	271		Gd4p3
26	*	Ta4f	65		Hf5s	111	*	Be1s	181		Ge4s	273	*	Os4d5
29	*	Ge3d	66		Pt5p1	111	*	Rb3d	182	*	Br3p3	274		Re4d3
31		Hf5p3	66		V3s	111	*	Ce4d	182		Th5p3	279	*	Ru3d5
32	*	Sb4d	67		Cd4p	112		Ni3s	183		Zr3d3	280		Sr3p1
34		K3s	68	*	Ni3p	114	*	Pr4d	184	*	Yb4d5	284		Ru3d3
34	*	W4f7	70	*	Br3d	118	*	Al2s	186		I4s	284		Eu4p1
35		W5p3	71	*	Pt4f7	118	*	Nd4d	118	*	B1s	284	*	Cl1s
37		W4f5	71		Ta5s	118		Bi5p1	189	*	P2s	289		Gd4p1
37		Ta5p3	72		Au5p1	118	*	Tl4f7	189		Br3p1	290		Ce4s
38		Hf5p1	73	*	Al2p	120		Cu3s	192		Ba4p1	290		Os4d3
38	*	V3p	74		Pt4f5	120		Hg5s	193		La4p3	290		Th5s
38		Sr4s	74		Cr3s	122		In4s	195	*	Lu4d5	294	*	K2p3
40	*	Te4d	74	*	Cu3p	122	*	Ge3p3	197		Yb4d3	295	*	Ir4d5
41	*	As3d	75		Ru4s	122		Tl4f5	200	*	C12p	297		K2p1
43	*	Cr3p	76		Tl5p3	123		I4p	204		As3s	301	*	T3p3
43		Ru4p	77		W5s	129		Ge3p1	205		Lu4d3	305		Pr4s
44		Ca3s	77		In4p	130	*	Sm4d	205	*	Nb3d5	306		Ho4p3
45		Ta5p1	78	*	Cs4d	134	*	Sr3d	206		La4p1	307	*	Rh3d5
46	*	Re4f	81		Rh4s	134	*	Eu4d	208		Nb3d3	311		Tb4p1
46		Y4s	81		Hg5p1	135	*	P2p	208		Ce4p3	312		Rh3d3
46		W5p1	83		Re5s	137		Zn3s	214	*	Hf4d5	312		Ir4d3
46		Re5p3	84		Os5s	137		Sn4s	218		Pr4p3	313		Y3p1
48		Rh4p	84	*	Au4f7	137		Tl5s	224		Ce4p1	314	*	Pt4d5
49	*	Mn3p	84		Mn3s	138	*	Pb4f7	224		Hf4d3	316		Nd4s
50	*	I4d	86		Pd4s	141	*	Gd4d	225		Nd4p3	320		Er4p3
51	*	Os4f	86		Pb5p3	141	*	As3p3	227	*	Mo3d5	322		Rb3s
51		Os5p3	87		Au4f5	143		Pb4f5	229	*	S2s	322		GeA
51		Pt5p3	87	*	Zn3p	147		As3p1	229		Th5p1	324		U5s
51		Pd4p	89	*	Mg2s	148	*	Tb4d	230		Mo3d3	331	*	Zr3p3
52	*	Mg2p	89		Sn4p	148		Pb5s	230	*	Ta4d5	331		Pt4d3
52		Zr4s	90	*	Ba4d5	149	*	Si2s	231		Cs4s	332		Dy4p1
52		Ir5p3	93		Ba4d3	152		Sb4s	232		Se3s	334	*	Au4d5
54		Sc3s	93		Bi5p1	154	*	Dy4d	237		Pr4p1	335	*	Th4f7
54		Au5p3	95		Fe3s	158		Ga3s	239	*	Rb3p3	335	*	Pd3d5
55	*	Lil1s	95		Ag4s	158	*	Bi4f7	242		Ta4d3	337		Tm4p3
56	*	Fe3p	96		Ir5s	159	*	Y3d	224		Nd4p1	340		Pd3d3
56		Ag4p3	99		Sb4p	160		Bi5s	246	*	W4d5	343		Ho4p1
57	*	Se3d	99	*	La4d	161	*	Ho4d	248		Rb3p1	343		Yb4p3
58		Nb4s	99	*	Hg4f7	162	*	Se3p3	249		Sm4p3	344		Th4f5
58		Re5p1	100	*	Si2p	162		Cs4p3	253		Ba4s	345		Zr3p1
58		Hg5p3	100		Tl5p1	163		Bi4f5	257		Br3s	347		Sm4s
59		Ti3s	101		Co3s	165	*	S2p	257		Eu4p3	347	*	Ca2p3
60	*	Co3p	102		Pt5s	168		Se3p1	259		W4d3	350		Ca2p1
60	*	Ir4f7	103	*	Ga3p3	168		Te4s	260		U5p1	352		Au4d3
62		MO4s	103		Hg4f5	168	*	Er4d5	260	*	Re4d5	354	*	GeA
62		Ag4p1	105		Pb5p1	172		Cs4p1	267		Sm4p1	358		Sr3s
63		Ir4f5	107		Ga3p1	177		Er4d3	269	*	Sr3p3	359		Lu4p3
63		Os5p1	108		Cd4s	180	*	Zr3d5	270	*	C12s	360		Eu4s
63		Ir5p1	108		Au5s	180		Ba4p3	271		La4s	360	*	Hg4d5

TABLE 1

PHOTOELECTRON AND AUGER LINES (CONTINUED)

363 *	Nb3p3	469	Os4p3	608	Pt4p1	779 *	CO2p3	978 *	Nd3d5
366	Er4p1	472	Tm4s	609	Tl4p3	780	U4d3	981 *	CA
367 *	Ag3d5	479	CuA	617 *	Cd3p3	781 *	Ba3d5	984 *	IA
374	Ag3d3	480	ZnA	620 *	I3d5	782	CoA	998	Cs3p3
376	Gd4s	483	Ru3p1	625	Re4s	784	FeA	1000	Nd3d3
377 *	K2s	485 *	Sn3d5	627	Rh3s	794	Co2p1	1001	OA
379	Nb3p1	487	Yb4s	628	V2s	796	Ba3d3	1005 *	TeA
379	Hg4d3	492	W4p1	629	CuA	797 *	PrA	1006	Te3s
380	Hf4p3	493	GaA	631	I3d3	800	Hg4s	1007	CrA
381 *	U4f7	494	Sn3d3	632	La4d	806	Bi4p1	1007	Ni2s
386	Tm4p1	495	Ir4p3	640	CuA	812	Sb3p1	1015 *	TeA
386 *	Tl4d5	496 *	Rh3p3	640 *	NiA	819	Te3p3	1020	Va
392	V4f5	500 *	Sc2s	641 *	Mn2p3	826	In3s	1021 *	Zn2p3
393 *	Mo3p3	500 *	NaA	644	Au4p1	827 *	CeA	1032	Sba
395	Y3s	503 *	ZnA	645	Pb4p3	832 *	La3d5	1040 *	Sba
396	Yb4p1	505	Mo3s	648	CuA	835 *	FA	1044	Zn2p1
398	Tb4s	506	Lu4s	651	Cd3p1	838	CoA	1045	U4p3
399 *	N1s	511	GaA	652	Mn2p1	843	CoA	1055	SnA
400	GaA	513 *	V2p3	655	Os4s	845	Tl4s	1060 *	VA
402 *	Sc2p3	518	Re4p1	664 *	In3p3	845 *	FeA	1063 *	SnA
404 *	Cd3d5	519	Pt4p3	670	Pd3s	846	Fe2s	1063	Ba3p3
405	Ta4p3	520	V2p1	675 *	SmA	848	La3d3	1065	Cs2p1
407	Sc2p1	521	Rh3p1	677	Hg4p1	855 *	Ni2p3	1072	I3s
407	Tl4d3	522	GaA	677 *	Th4d5	861	FA	1072 *	Nals
410	Mo3p1	528 *	Sb3d5	679	Bi4p3	865 *	LaA	1077	TiA
410	Lu4p1	531 *	Pd3p3	686 *	F1s	870	Te3p1	1080	InA
411	Cd3d3	532 *	O1s	690	Ir4s	873	Ni2p1	1081 *	Sm3d5
413 *	Pb4d5	537	Sb3d3	695	Cr2s	875	I3p3	1087 *	InA
416	Dy4s	538	Hf4s	702	In3p1	884	Sn3s	1096	Cu2s
423	GeA	540	NaA	710 *	Fe2p3	884 *	Ce3d5	1107	Sm3d3
426	W4p3	546	Au4p3	712	CuA	890	BaA	1107 *	Na
427 *	GaA	547	Os4p1	712	NiA	894	Pb4s	1109	CdA
431	Zr3s	547	CuA	714	Th4d3	896	FeA	1113 *	TiA
435	Pb4d3	559	Pd3p1	715 *	Sn3p3	902	Ce3d3	1116 *	CdA
436	Ho4s	564 *	Ti2s	715	CoA	903 *	BaA	1116 *	Ga2p3
437	Hf4p1	566	Ta4s	717	Ag3s	908 *	MnA	1124	La3p3
438 *	Ca2s	567	ZnA	722	Tl4p1	915	CsA	1131	AgA
440 *	Bi4d5	568 *	CuA	723	Fe2p1	926	Co2s	1131 *	Eu3d5
443 *	In3d5	571	Hg4p3	724	Pt4s	927 *	CsA	1136 *	AgA
444	GeA	571 *	Ag3p3	726 *	Cs3d5	931	I3p1	1137	Ba3p1
445	Re4p3	572 *	Te3d5	738 *	U4d5	931 *	Pr3d5	1143	Ga2p1
449	Er4s	575 *	Cr2p3	740	Cs3d3	931 *	Cu2p3	1157 *	ScA*
451	In3d3	577	Ir4p1	755 *	NdA	939	Bi4s	1158 *	PdA
454	GeA	581	ZnA	757	Sn3p1	944	Sb3s	1190 *	RhA
455 *	Ti2p3	582	Te3d3	759	Au4s	951	Cu2p1	1198 *	CaA
461	Ti2p1	584	Cr2p1	764	Pb4p1	951	Pr3d3	1215 *	RuA
461 *	Ru3p3	585	Ru3s	766	Sb3p3	952	MnA	1230 *	CA
464	Bi4d3	590	ZnA	769	Mn2s	967 *	CrA	1239 *	KA
465	Ta4p1	595	W4s	770	Cd3s	968	Th4p3	1307 *	C1A
469	Nb3s	602	Ag3p1	778	NiA	972	IA	1315 *	BA
								1333 *	SA

* Strongest Auger Line or one of the two strongest photoelectron lines in the element spectrum, not including minor lines of spin doublets.

Figure 3 Relative Intensities of the Photoelectron Lines

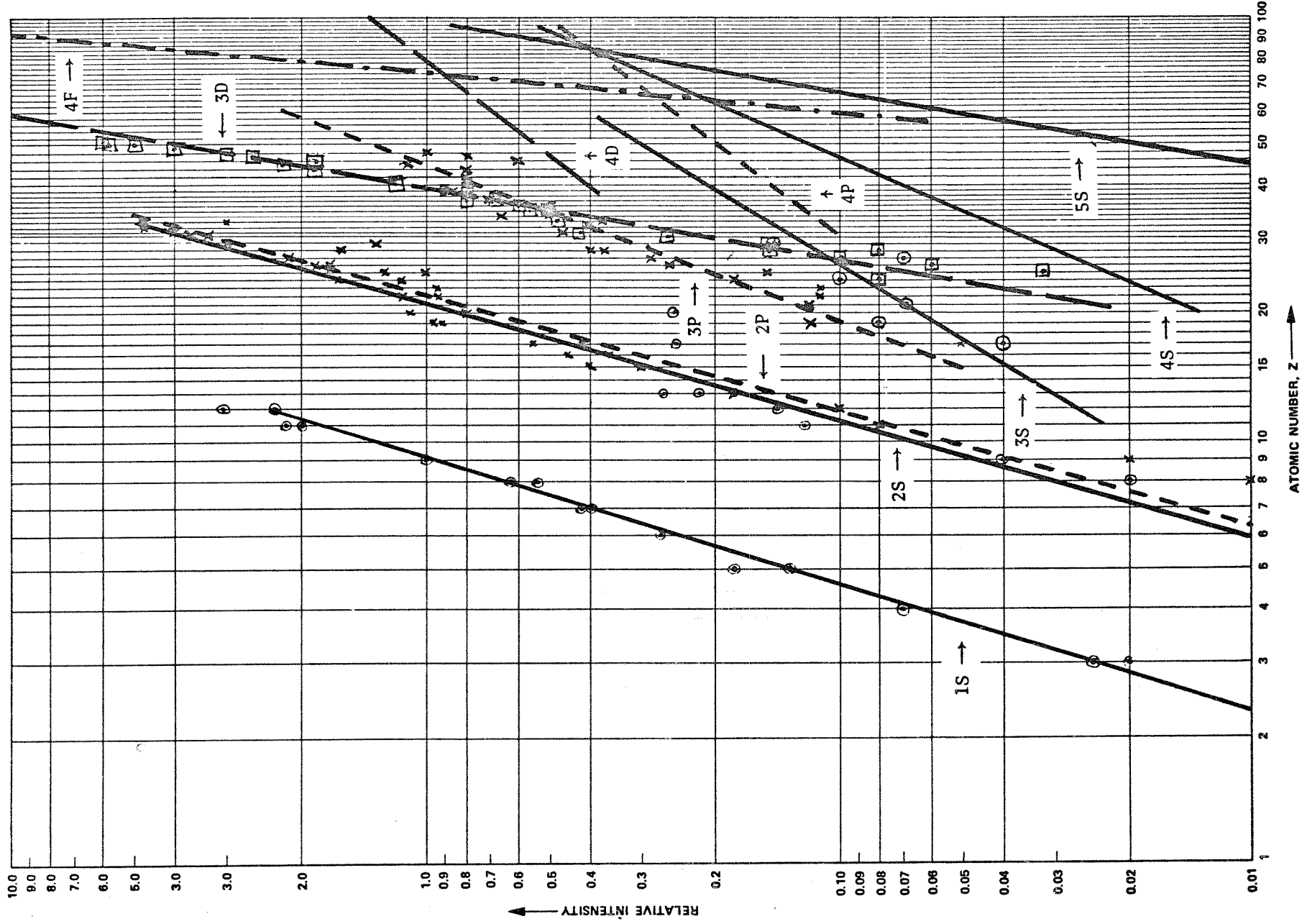


Figure 2k PRINCIPAL PHOTO ELECTRON ENERGIES

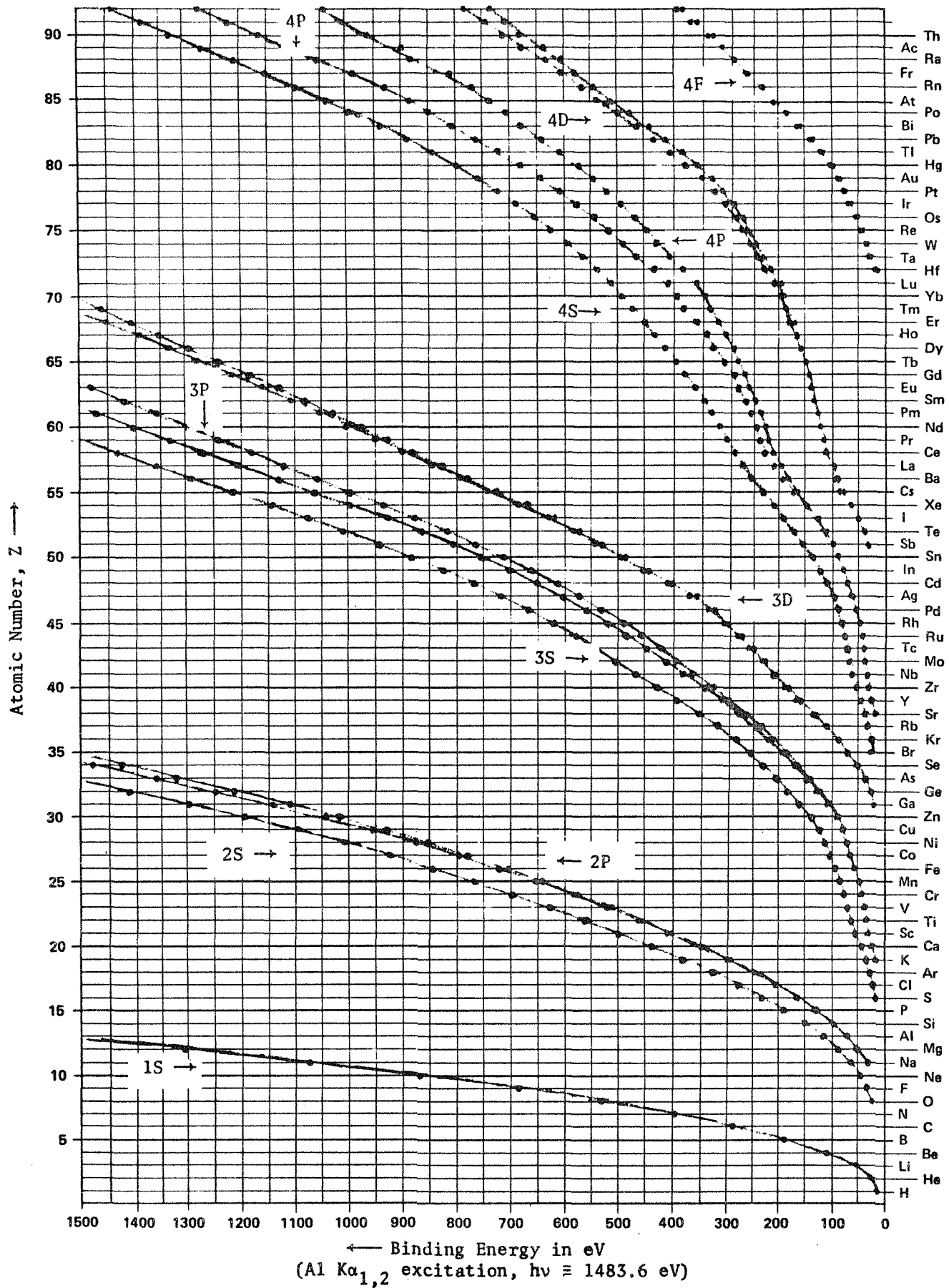
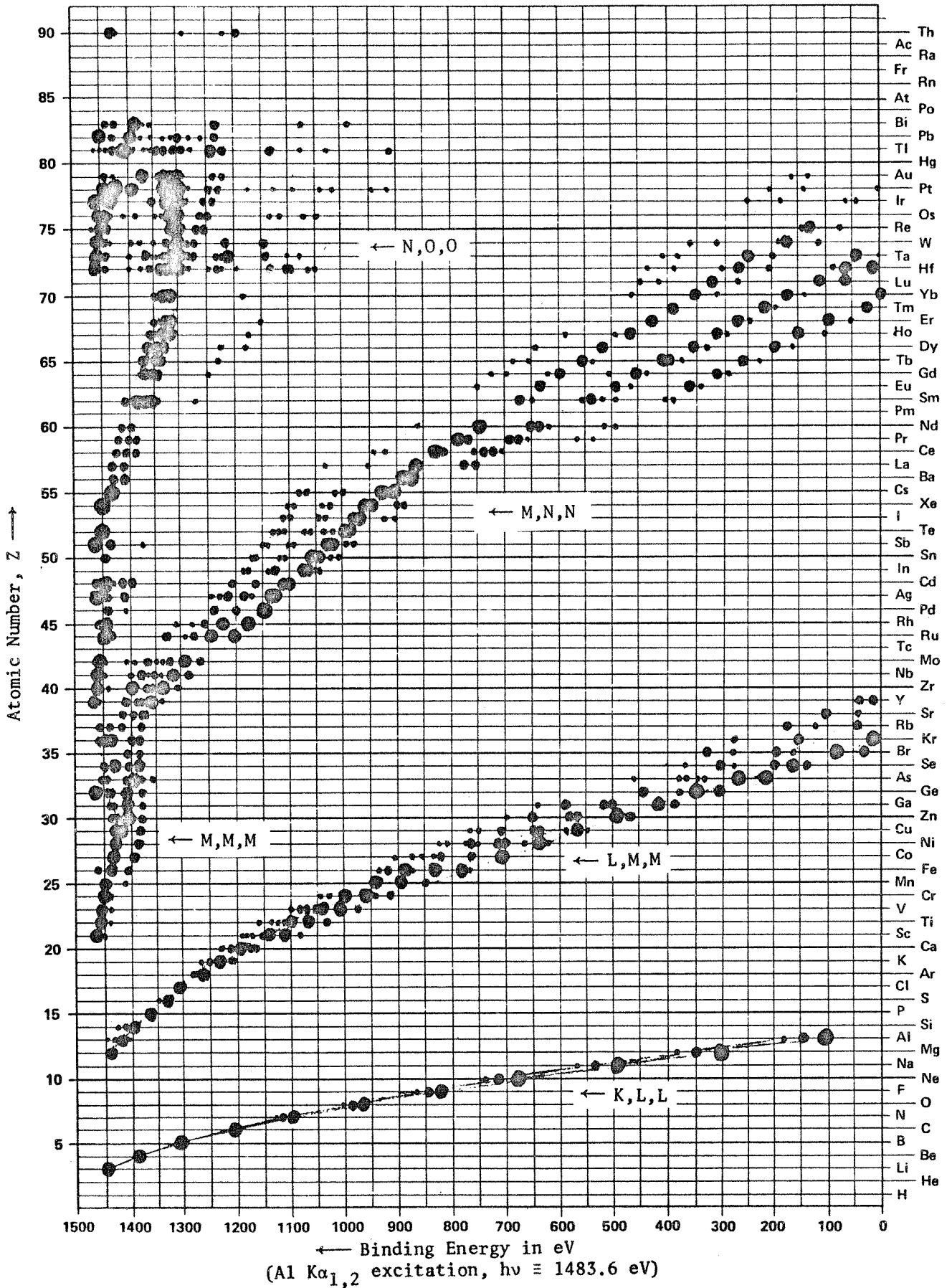


Figure 2b PRINCIPAL AUGER ELECTRON ENERGIES



C. General ESCA Data Analysis Program

```
@RUN LKS,JJ6A3R,ESCA,2,30/50000
@MSG LOAD SEQ 1909
@SYM,SC PUNCH$,,69300A
@FOR,IS PLOTR
```

```
SUBROUTINE PLOTR(ARRAY,N,AMAX,SIZE,PLEN)
```

```
-----
C THIS SUBROUTINE PLOTS AN ARRAY OF N POINTS, SCALED FROM 0.0 TO
C AMAX, ON A GRAPH OF HEIGHT 'SIZE', AND LENGTH 'PLEN' .
C-----
```

```
DIMENSION ARRAY(1)
COMMON FS(1024)
S=SIZE
Y=ARRAY(1)/AMAX*S
IF(Y.GT.S)Y=S
CALL PLOT(-Y,0.0,3)
DO 1 I=2,N
X=PLEN*(I-1)/(N-1)
Y=S*ARRAY(I)/AMAX
IF(Y.GT.S)Y=S
1 CALL PLOT(-Y,X,2)
END
```

```
@FCF,I FORT
```

```
SUBROUTINE FORT(A,M,S,IFS,IFERR)
```

```
FORT0001
```

```
-----
C FORT, ONE-DIMENSIONAL FINITE COMPLEX FOURIER TRANSFORM.
C-----
```

```
FORT0002
```

```
FORT0003
```

```
FORT0004
```

```
FORT0005
```

```
FORT0006
```

```
FORT0016
```

```
FORT0007
```

```
DOES EITHER FOURIER SYNTHESIS, I.E., COMPUTES COMPLEX FOURIER SERIES FORT0008
```

```
GIVEN A VECTOR OF N COMPLEX FOURIER AMPLITUDES, OR, GIVEN A VECTOR FORT0009
```

```
OF COMPLEX DATA X DOES FOURIER ANALYSIS, COMPUTING AMPLITUDES. FORT0010
```

```
A IS A COMPLEX VECTOR OF LENGTH N=2**M COMPLEX NOS. OR 2*N REAL FORT0011
```

```
M IS AN INTEGER 0.LT.M.LE.13, SET BY USER. FORT0012
```

```
S IS A VECTOR S(J)= SIN(2*PI*J/NF ), J=1,2,.....,NP/4-1, FORT0013
```

```
COMPUTED BY PROGRAM. FORT0014
```

```
IFS IS A PARAMETER TO BE SET BY USER AS FOLLOWS- FORT0015
```

```
IFS=1 TO SET N=NP=2**M, SET UP SIN TABLE, AND DO FOURIER FORT0017
```

```
SYNTHESIS, REPLACING THE VECTOR A BY FORT0018
```

```
X(J)= SUM OVER K=0,N-1 OF A(K)*EXP(2*PI*I/N)**(J*K), FORT0019
```

```
J=0,N-1, WHERE I=SQRT(-1) FORT0021
```

```
THE X'S ARE STORED WITH RE X(J) IN CELL 2*J+1 FORT0023
```

```
AND IM X(J) IN CELL 2*J+2 FOR J=0,1,2,.....,N-1. FORT0024
```

```
THE A'S ARE STORED IN THE SAME MANNER. FORT0025
```

```
IFS=-1 TO SET N=NP=2**M, SET UP SIN TABLE, AND DO FOURIER FORT0027
```

```
ANALYSIS, TAKING THE INPUT VECTOR A AS X AND FORT0028
```

```
REPLACING IT BY THE A SATISFYING THE ABOVE FOURIER SERIES. FORT0029
```

```
IFS=+2 TO DO FOURIER SYNTHESIS ONLY, WITH A PRE-COMPUTED S. FORT0030
```

```
IFS=-2 TO DO FOURIER ANALYSIS ONLY, WITH A PRE-COMPUTED S. FORT0031
```

```
IFERR IS SET BY PROGRAM TO- FORT0032
```

```
=0 IF NO ERROR DETECTED. FORT0033
```

=1 IF M IS OUT OF RANGE., OR, WHEN IFS=+2,-2, THE
 PRE-COMPUTED S TABLE IS NOT LARGE ENOUGH.
 =-1 WHEN IFS =+1,-1, MEANS ONE IS RECOMPUTING S TABLE
 UNNECESSARILY.

NOTE- AS STATED ABOVE, THE MAXIMUM VALUE OF M FOR THIS PROGRAM
 IS 13. ONE MAY INCREASE THIS LIMIT BY REPLACING 13 IN
 STATEMENT 3 BELOW BY LOG2 N, WHERE N IS THE MAX. NO. OF
 COMPLEX NUMBERS ONE CAN STORE IN HIGH-SPEED CORE. ONE MUST
 ALSO ADD MORE DO STATEMENTS TO THE BINARY SORT ROUTINE
 FOLLOWING STATEMENT 24 AND CHANGE THE EQUIVALENCE STATEMENTS
 FOR THE K'S.

```

DIMENSION A(1), S(1), K(14)
EQUIVALENCE (K(13),K1),(K(12),K2),(K(11),K3),(K(10),K4)
EQUIVALENCE (K( 9),K5),(K( 8),K6),(K(7),K7),(K( 6),K8)
EQUIVALENCE (K( 5),K9 ),(K( 4),K10),(K( 3),K11),(K( 2),K12)
EQUIVALENCE (K( 1),K13),( K(1),K2)
IF(M)2,2,3
3 IF(M-13) 5,5,2
2 IFERR=1
1 RETURN
5 IFERR=0
  N=2**M
  NP=N
  MP=M
  NT=N/4
  MT=M-2
  IF( IABS(IFS) - 1 ) 200,200,20
  SCRAMBLE A, BY SANDE'S METHOD
20 K(1)=2*N
  DO 22 L=2,M
22 K(L)=K(L-1)/2
  DO 24 L=M,12
24 K(L+1)=2
  NOTE EQUIVALENCE OF KL AND K(14-L)
  BINARY SORT-
  IJ=2
  DO 30 J1=2,K1,2
  DO 30 J2=J1,K2,K1
  DO 30 J3=J2,K3,K2
  DO 30 J4=J3,K4,K3
  DO 30 J5=J4,K5,K4
  DO 30 J6=J5,K6,K5
  DO 30 J7=J6,K7,K6
  DO 30 J8=J7,K8,K7
  DO 30 J9=J8,K9,K8
  DO 30 J10=J9,K10,K9
  DO 30 J11=J10,K11,K10
  DO 30 J12=J11,K12,K11
  DO 30 JI=J12,K13,K12
  IF(I,-JI)28,30,30
28 T=A(IJ-1 )
  A(IJ-1)=A(JI-1)
  A(JI-1)=T

```

FORT0034
 FORT0035
 FORT0036
 FORT0037
 FORT0038
 FORT0039
 FORT0040
 FORT0041
 FORT0042
 FORT0043
 FORT0044
 FORT0045
 FORT0046
 FORT0047
 FORT0048
 FORT0049
 FORT0050
 FORT0051
 FORT0052
 FORT0053
 FORT0054
 FORT0055
 FORT0056
 FORT0057
 FORT0058
 FORT0059
 FORT0060
 FORT0061
 FORT0062
 FORT0063
 FORT0064
 FORT0065
 FORT0066
 FORT0067
 FORT0068
 FORT0069
 FORT0070
 FORT0071
 FORT0072
 FORT0073
 FORT0074
 FORT0075
 FORT0076
 FORT0077
 FORT0078
 FORT0079
 FORT0080
 FORT0081
 FORT0082
 FORT0083
 FORT0084
 FORT0085
 FORT0086
 FORT0087
 FORT0088

```

T=A(IJ)
A(IJ)=A(JI)
A(JI)=T
30 IJ=IJ+2
IF(IFS)32,2,36
C DOING FOURIER ANALYSIS,SO DIV. BY N AND CONJUGATE.
32 FN = N
DO 34 I=1,N
A(2*I-1) = A(2*I-1)/FN
34 A(2*I)=-A(2*I)/FN
C SPECIAL CASE- L=1
36 DO 40 I=1,N*2
T = A(2*I-1)
A(2*I-1) =T + A(2*I+1)
A(2*I+1)=T-A(2*I+1)
T=A(2*I)
A(2*I) = T + A(2*I+2)
40 A(2*I+2)= T - A(2*I+2)
IF(M-1) 2,1 ,50
C SET FOR L=2
50 LEXP1=2
C LEXP1=2**(L-1)
LEXP=8
C LEXP=2**(L+1)
NPL= 2**MT
C NPL = NP* 2**-L
60 DO 130 L=2,M
C SFECIAL CASE- J=0
DO 80 I=2,N2,LEXP
I1=I + LEXP1
I2=I1+ LEXP1
I3 =I2+LEXP1
T=A(I-1)
A(I-1) = T +A(I2-1)
A(I2-1) = T-A(I2-1)
T =A(I)
A(I) = T+A(I2)
A(I2) = T-A(I2)
T= -A(I3)
TI = A(I3-1)
A(I3-1) = A(I1-1) - T
A(I3 ) = A(I1 ) - TI
A(I1-1) = A(I1-1) +T
80 A(I1 ) = A(I1 ) +TI
IF(L-2) 120,120,90
90 KLAST=N2-LEXP
JJ=NPL
DO 110 J=4,LEXP1,2
NPJJ=NT-JJ
UP=S(NPJJ)
UI=S(JJ)
ILAST=J+KLAST
DO 100 I= J,ILAST,LEXP
I1=I+LEXP1
I2=I1+LEXP1

```

FORT0089
FORT0090
FORT0091
FORT0092
FORT0093
FORT0094
FORT0095
FORT0096
FORT0097
FORT0098
FORT0099
FORT0100
FORT0101
FORT0102
FORT0103
FORT0104
FORT0105
FORT0106
FORT0107
FORT0108
FORT0109
FORT0110
FORT0111
FORT0112
FORT0113
FORT0114
FORT0115
FORT0116
FORT0117
FORT0118
FORT0119
FORT0120
FORT0121
FORT0122
FORT0123
FORT0124
FORT0125
FORT0126
FORT0127
FORT0128
FORT0129
FORT0130
FORT0131
FORT0132
FORT0133
FORT0134
FORT0135
FORT0136
FORT0137
FORT0138
FORT0139
FORT0140
FORT0141
FORT0142
FORT0143

```

I3=I2+LEXP1
T=A(I2-1)*UR-A(I2)*UI
TI=A(I2-1)*UI+A(I2)*UR
A(I2-1)=A(I-1)-T
A(I2 )=A(I ) - TI
A(I-1) =A(I-1)+T
A(I)   =A(I)+TI
T=-A(I3-1)*UI-A(I3)*UP
TI=A(I3-1)*UR-A(I3)*UI
A(I3-1)=A(I1-1)-T
A(I3)   =A(I1 )-TI
A(I1-1)=A(I1-1)+T
100 A(I1)   =A(I1)   +TI
C   END OF I LOOP
110 JJ=JJ+NPL
C   END OF J LOOP
120 LEXP1=2*LEXP1
LEXP = 2*LEXP
130 NPL=NPL/2
C   END OF L LOOP
140 IF(IFS)145,2,1
C   DOING FOURIER ANALYSIS. REPLACE A BY CONJUGATE.
145 DO 150 I=1,N
150 A(2*I) =-A(2*I)
160 GO TO 1
C   RETURN
C   MAKE TABLE OF S(J)=SIN(2*PI*J/NP), J=1,2,...,NT-1, NT=NP/4
200 CONTINUE
IF(MT) 260,260,205
205 THETA=.7853981634
C   THETA=PI/2**((L+1)   FOR L=1
210 JSTEP = NT
C   JSTEP = 2**(( MT-L+1 ) FOR L=1
JDIF = NT/2
C   JDIF = 2**((MT-L)   FOR L=1
S(JDIF) = SIN(THETA)
IF (MT-2)260,220,220
220 DO 250 L=2,MT
THETA = THETA/2.
JSTEP2 = JSTEP
JSTEP = JDIF
JDIF = JDIF/2
S(JDIF)=SIN(THETA)
JC1=NT-JDIF
S(JC1)=COS(THETA)
JLAST=NT-JSTEP2
IF(JLAST-JSTEP)250,230,230
230 DO 240 J=JSTEP,JLAST,JSTEP
JC=NT-J
JD=J+JDIF
240 S(JD)=S(J)*S(JC1)+S(JDIF)*S(JC)
250 CONTINUE
260 IF(IFS)20,1,20
END
@FOR,IS MAIN

```

FORTO144
FORTO145
FORTO146
FORTO147
FORTO148
FORTO149
FORTO150
FORTO151
FORTO152
FORTO153
FORTO154
FORTO155
FORTO156
FORTO157
FORTO158
FORTO159
FORTO160
FORTO161
FORTO162
FORTO163
FORTO164
FORTO165
FORTO166
FORTO167
FORTO168
FORTO169
FORTO170
FORTO171
FORTO172
FORTO173
FORTO174
FORTO175
FORTO176
FORTO177
FORTO178
FORTO179
FORTO180
FORTO181
FORTO182
FORTO183
FORTO184
FORTO185
FORTO186
FORTO187
FORTO188
FORTO189
FORTO190
FORTO191
FORTO192
FORTO193
FORTO194
FORTO195

DECK SETUP IS AS FOLLOWS:

AN ARBITRARY NUMBER OF GROUPS MAY BE PLOTTED
FOR EACH GROUP, TWO GROUP CONTROL CARDS ARE REQUIRED, FOLLOWED BY
THE SPECTRA NEEDED FOR THAT GROUP

THE FORMAT OF THE GROUP CONTROL CARDS IS:

CARD 1 COL. 1- 2 NUMBER OF PLOTS IN THE GROUP

CARD 1 COL 3-38 TITLE OF THE GROUP

CARD 2 COL. 1-10 INITIAL BINDING ENERGY OF THE GROUP PLOT

COL 11-20 FINAL BINDING ENERGY

COL 21-30 WIDTH OF WEINER IN EV

AT THIS POINT COME THE SPECTRA. EACH OF THE SPECTRA ALSO HAS TWO
CONTROL CARDS. THE FORMAT OF THESE IS:

CARD 1 COL 1- 6 TITLE

COL 7- 9 STORAGE NUMBER

COL 10-11 AMOUNT THE NUMBER OF POINTS IS TO BE REDUCED

COL 12-20 NUMBER OF SCANS

CARD 2 COL 1-10 INITIAL BINDING ENERGY

COL 11-20 FINAL BINDING ENERGY

COL 21-29 CORRECTION FACTOR

COL 30 NORMALIZATION INDICATOR

COL 31 SUBTRACTION INDICATOR

COL 32-41 MAGNIFICATION FACTOR

THIS IS FOLLOWED BY THE DATA IN A (4X,10I7) FORMAY

GENERAL NOTES

WHEN SUBTRACTING SPECTRA, THE PLOT IS OF THE FIRST MINUS THE
SECOND

THE SUBTRACTION INDICATOR OCCURS ON THE SUBTRAHEND, THE NORMAL-
IZATION INDICATOR ON THE MINUEND.

IF THE STORAGE NUMBER IS NOT EQUAL TO ZERO, THE SPECTRA WILL BE STORED
IN THAT LOCATION.

IF THE SPECTRUM NAME IS 'STORED', THE SPECTRA STORED IN THE LOCATION
INDICATED BY STORAGE NUMBER WILL BE RETRIEVED AND NO DATA CARDS
ARE NECESSARY. THE SECOND SPECTRUM CONTROL CARD IS STILL NECESSARY
HOWEVER.

IF THE REDUCTION FACTOR IS OMITTED, IT IS SET TO 1

IF THE NUMBER OF SCANS IS OMITTED, IT IS SET TO 10.0

IF THE WEINER WIDTH IS OMITTED, IT IS SET TO 1.0 VOLTS

IF THE MAGNIFICATION FACTOR IS OMITTED, IT IS ASSUMED NOT TO CHANGE

DEFINE ARRAYS USED, TEMPORARY STORAGE, AND PERFORM INITIALIZATION

DIMENSION TITLE(6),DAT(1024),OS(1024)

DIMENSION S(256)

COMPLEX DATA(1024),TEMP(1024)

COMMON FS(1024)

DEFINE FILE 40(30,1030,U,IFILE)

CALL PLOTS

FMAG=1.0

READ IN THE GROUP CONTROL CARDS

NG= NUMBER OF GRAPHS IN THE GROUP

TITLE= TITLE OF THE GROUP

EMAX= MAXIMUM BINDING ENERGY TO BE DISPLAYED

```

C   EMIN   MINIMUM BINDING ENERGY TO BE DISPLAYED
C   W=     WIDTH OF THE SMOOTHING WEINER, IN VOLTS

```

```

C-----
C   21 READ(5,100,END=99)NG,TITLE,EMAX,EMIN,W
C   100 FORMAT(I2,6A6,/,3F10.0)

```

```

C-----
C   PLOT THE FRAME.  DIF= THE SIZE OF ONE GRAPH
C-----

```

```

C   IF(W.EQ.0.0)W=1.0
C   CALL SYMBOL(-.1,C.0,C.28,TITLE,9C.0,36)
C   CALL PLOT(0.0,10.0,3)
C   DO 1 I=1,10
C   Y=10-I
C   CALL PLOT(0.0,Y,2)
C   CALL PLOT(0.1,Y,2)
C   1 CALL PLOT(0.0,Y,2)
C   DIF=17.0/NG
C   CALL PLOT(17.0,0.0,2)
C   CALL AXIS(17.0,0.0,'BINDING ENERGY',-14,10.0,90.0,EMAX,(EMIN-EMAX)
C   */10.0)
C   CALL PLOT(17.0,10.0,3)
C   CALL PLOT(0.0,10.0,2)
C   WRITE(6,303)
C   303 FORMAT(////////)

```

```

C-----
C   MAIN LOOP.  PROGRAM GOES THROUGH THIS ONCE FOR EACH GRAPH OF A GROUP
C-----

```

```

C   DO 20 JJ=1,NG

```

```

C   READ A SPECTRA INTO ARRAY DAT

```

```

C   CALL READIN(DAT,NAM,E1,E2)
C   IFLAG=0
C   IF(IFSUB.EQ.0)GO TO 10

```

```

C   IF A SUBTRACTION IS TO BE DONE, READ IN THE OTHER SPECTRA TO
C   ARRAY OS

```

```

C   IFLAG=1
C   CALL READIN(OS,NAM2,E3,E4)
C   DO 151 I=1,N
C   151 FS(I)=DAT(I)

```

```

C   CALCULATE THE SHIFT IN POINTS

```

```

C   ISH=(E3-E1)*N/(E1-E2)+IDISP+C.5
C   WRITE(6,199)ISH
C   199 FORMAT(' RELATIVE SHIFT OF ',I7)
C   302 CONTINUE

```

```

C   DO THE SUBTRACTION

```

```

C   DO 2 I=1,N
C   J=I+ISH
C   IF(J.GT.0)GO TO 7

```

```

DAT(I)=DAT(1-ISH)-OS(1)
GO TO 2
7 IF(J.LE.N) GO TO 8
  DAT(I)=DAT(I-1)
  GO TO 2
8 DAT(I)=DAT(I)-OS(J)
2 CONTINUE

```

C FIND THE MAXIMUM AND MINIMUM OF THE DATA
C -----

```

10 AMAX=-1.0E6
  AMIN=1.0E6
  DO 11 I=1,N
    X=DAT(I)
    IF(X.GT.AMAX)AMAX=X
    IF(X.LT.AMIN)AMIN=X
11 CONTINUE
  WRITE(6,203)AMIN,AMAX
203 FORMAT(2F15.3)

```

C IF THE MINIMUM IS GREATER THAN ZERO, AND/OR NORMALIZATION IS NOT
C WANTED, SKIP THE NORMALIZATION SECTION
C -----

```

IF(AMIN.GT.0.0.OR.INORM.EQ.0)GO TO 152

```

C OTHERWISE, NORMALIZE THE RESULT OF THE SUBTRACTION
C -----

```

DO 153 I=1,N
  IF(DAT(I).EQ.AMIN)GO TO 154
153 CONTINUE
154 S1=FS(I)
  S2=S1-AMIN
  FNOR=S1/S2
  WRITE(6,401)FNOR
401 FORMAT(' THE NORMALIZATION FACTOR IS ',F8.5)
  DO 155 I=1,N
    OS(I)=OS(I)*FNOR
155 DAT(I)=FS(I)
  INORM=0
  GO TO 302
152 CONTINUE

```

C MAKE ALL DATA POSITIVE FOR ROUTINE PLOTR
C -----

```

DO 12 I=1,N
12 DAT(I)=DAT(I)-AMIN

```

C CALCULATE THE SHIFT OF THE ORIGIN NECESSARY, AND COMPUTE THE
C LENGTH OF THE PLOT
C -----

```

SHIFT=(EMAX-E1)/(EMAX-EMIN)*10.0
ALEN=(E1-E2)/(EMAX-EMIN)*10.0

```

C IF THE PLOT IS WITHIN THE PLOTTED LIMITS, SKIP THE TRUNCATION SEC-
C TION.
C -----

```

C-----
C      IF (SHIFT.GT.(-0.4).AND.(SHIFT+ALEN).LT.10.4) GO TO 15
C-----

```

```

C      TRUNCATE THE DATA SO IT FITS ON THE GRAPH
C-----

```

```

      DISP=ALEN/(N-1)
      IF (SHIFT.GT.0.0) GO TO 200
      NS=(-0.4-SHIFT)/DISP+1
      SHIFT=SHIFT+NS*DISP
      DO 201 I=1,N
201  DAT(I)=DAT(I+NS)
      N=N-NS
      GO TO 202
200  NS=(SHIFT-(10.4-ALEN))/DISP+1
      N=N-NS
202  ALEN=ALEN-NS*DISP

```

```

C-----
C      RESET THE ORIGIN AND CALCULATE THE POSITION OF THE ZERO LINE
C-----

```

```

15  CALL PLOT(DIF,SHIFT,-3)
     H=DIF*(-AMIN)/(AMAX-AMIN)

```

```

C-----
C      PLOT THE DATA AND WRITE THE TITLES
C-----

```

```

      AMAX=AMAX-AMIN
      AMAX=AMAX/FMAG
      WRITE(6,405)FMAG
405  FORMAT(' MULTIPLICATION FACTOR IS',F10.2)
      CALL PLOT(DAT,N,AMAX,DIF,ALEN)
      VER=8.88-SHIFT
      IF (H.GT.0.DIF.OR.H.LT.0.0) GO TO 127
      CALL PLOT(-H,10.0-SHIFT,3)
      CALL PLOT(-H,-SHIFT,2)
127  CONTINUE
      CALL SYMBOL(-DIF/2.0,VER,0.28,NAM,90.0,5)
      IF (IFLAG.GT.0) CALL SYMBOL(-DIF/2.+0.32,VER,0.28,NAM2,90.0,6)
20  CALL PLOT(0.0,-SHIFT,-3)

```

```

C-----
C      SHIFT THE ORIGIN AND RETURN FOR A NEW GROUP
C-----

```

```

      CALL PLOT(5.0,0.0,-3)
      GO TO 21
99  CALL PLOT(10.0,0.0,999)
     STOP

```

```

C-----
C      THIS SUBROUTINE READS IN AND STORES THE RAW DATA FROM THE
C      SPECTROMETER.  PARAMETERS ARE:
C      IQ      A REAL ARRAY CONTAINING THE DATA WHEN THE SUBROUTINE
C              IS DONE
C      NAM     THE NAME OF THE SPECTRA
C      E1     THE BINDING ENERGY START OF THE SPECTRA
C      E2     THE BINDING ENERGY AT THE END OF THE SPECTRA
C-----

```

```

SUBROUTINE READIN(IQ,NAM,E1,E2)
REAL IQ(1)

```

```

C-----
C      IF(SHIFT.GT.(-0.4).AND.(SHIFT+ALEN).LT.10.4)GO TO 15
C-----

```

```

C      TRUNCATE THE DATA SO IT FITS ON THE GRAPH
C-----

```

```

      DISP=ALEN/(N-1)
      IF(SHIFT.GT.0.0)GO TO 200
      NS=(-0.4-SHIFT)/DISP+1
      SHIFT=SHIFT+NS*DISP
      DO 201 I=1,N
201  DAT(I)=DAT(I+NS)
      N=N-NS
      GO TO 202
200  NS=(SHIFT-(10.4-ALEN))/DISP+1
      N=N-NS
202  ALEN=ALEN-NS*DISP

```

```

C-----
C      RESET THE ORIGIN AND CALCULATE THE POSITION OF THE ZERO LINE
C-----

```

```

15  CALL PLOT(DIF,SHIFT,-3)
     H=DIF*(-AMIN)/(AMAX-AMIN)

```

```

C-----
C      PLOT THE DATA AND WRITE THE TITLES
C-----

```

```

      AMAX=AMAX-AMIN
      AMAX=AMAX/FMAG
      WRITE(6,405)FMAG
405  FORMAT(' MULTIPLICATION FACTOR IS ',F10.2)
      CALL PLOT(DAT,N,AMAX,DIF,ALEN)
      VER=8.88-SHIFT
      IF(H.GT.DIF.OR.H.LT.0.0)GO TO 127
      CALL PLOT(-H,10.0-SHIFT,3)
      CALL PLOT(-H,-SHIFT,2)
127  CONTINUE
      CALL SYMBOL(-DIF/2.0,VER,0.28,NAM,90.0,6)
      IF(IFLAG.GT.0)CALL SYMBOL(-DIF/2.+0.32,VER,0.28,NAM2,90.0,6)
20  CALL PLOT(0.0,-SHIFT,-3)

```

```

C-----
C      SHIFT THE ORIGIN AND RETURN FOR A NEW GROUP
C-----

```

```

      CALL PLOT(5.0,0.0,-3)
      GO TO 21
99  CALL PLOT(10.0,0.0,999)
     STOP

```

```

C-----
C      THIS SUBROUTINE READS IN AND STORES THE RAW DATA FROM THE
C      SPECTROMETER.  PARAMETERS ARE:
C      IG      A REAL ARRAY CONTAINING THE DATA WHEN THE SUBROUTINE
C              IS DONE
C      NAM     THE NAME OF THE SPECTRA
C      E1     THE BINDING ENERGY START OF THE SPECTRA
C      E2     THE BINDING ENERGY AT THE END OF THE SPECTRA
C-----

```

```

SUBROUTINE READIN(IG,NAM,E1,E2)
REAL IG(1)

```

```

DIMENSION ISTOP(30)
COMMON FT(1024)
DIMENSION IN(10)
DATA ISTOP/'STORED'/

```

```

-----
C READ IN THE FOLLOWING VARIABLES:

```

```

C NAM THE NAME OF THE SPECTRA
C INU THE LOCATION THE SPECTRA IS TO BE STORED IN OR RETRIEVED
C FROM
C NRED THE FACTOR THE NUMBER OF POINTS SHOULD BE REDUCED BY
C SCANS THE NUMBER OF SCANS TAKEN IN THE SPECTRA
C E1 THE INITIAL BINDING ENERGY OF THE SPECTRA
C E2 THE FINAL BINDING ENERGY OF THE SPECTRA
C CF THE CORRECTION FACTOR FOR THE ENERGIES OF THE SPECTRA
C INORM A VARIABLE EQUAL TO 1 IF THE SPECTRA IS TO BE NORMALIZED
C IFSUB A VARIABLE EQUAL TO ONE IF THE SPECTRA IS THE FIRST OF
C TWO SPECTRA THAT ARE TO BE SUBTRACTED
C IDISP AN ADDITIONAL DISPLACEMENT THAT MAY BE USED FOR SUBTRACTION
C FMAG A MAGNIFICATION FACTOR FOR THE FINAL GRAPH

```

```

-----
C READ(5,101)NAM,INU,NRED,SCANS
101 FORMAT(A6,I3,I2,F9.0)
IF(SCANS.EQ.0.0)SCANS=10.0
FA=10.0/SCANS
FSAV=FMAG
READ(5,103)E1,E2,CF,INORM,IFSUB,IDISP,FMAG
103 FORMAT(2F10.0,F9.0,2I1,I4,F10.0)
IF(FMAG.EQ.0.0)FMAG=FSAV

```

```

-----
C IF RETRIEVING A PREVIOUSLY STORED SPECTRUM, GO TO THE READ SECTION

```

```

C IF(NAM.EQ.ISTOP)GO TO 45

```

```

-----
C OTHERWISE, READ IN A SPECTRA FROM THE CARDS

```

```

-----
C MM=0
C E1=E1+CF
C E2=E2+CF
C N=0
1 READ(5,100)IN
100 FORMAT(4X,10I7)
DO 2 I=1,10
IF(IN(I).EQ.0)GO TO 3
N=N+1
IO(N)=IN(I)
GO TO 2
3 IF(N.GT.10)GO TO 4
2 CONTINUE
GO TO 1

```

```

-----
C IF THE NUMBER OF POINTS IS TO BE REDUCED, DO IT HERE

```

```

-----
C 4 IF(NRED.EQ.0)GO TO 14
C N=N/NRED
C M=0

```

```

DO 60 I=1,N
SUM=0.0
DO 61 J=1,NRED
M=M+1
61 SUM=SUM+IQ(M)
60 IQ(I)=SUM/NRED

```

C CALCULATE THE MAXIMUM AND MINIMUM OF THE DATA
C-----

```

14 BMAX=-1.0E6
BMIN=1.0E6
DO 50 I=1,N
X=IQ(I)*FA
IF(X.GT.BMAX)BMAX=X
IF(X.LT.BMIN)BMIN=X
50 DATA(I)=X
75 AMAX=BMAX-BMIN

```

C FIND M , WHERE M= A NUMBER SUCH THAT 2**M=NUMBER OF POINTS IN THE
C SPECTRUM
C-----

```

J=2
DO 51 M=1,12
IF(J.GE.N)GO TO 52
51 J=J*2

```

C IF NECESSARY, ADD 1 POINT TO THE SPECTRA
C-----

```

52 IF(J.EQ.N)GO TO 53
N=N+1
IQ(N)=IQ(N-1)
DATA(N)=DATA(N-1)

```

C NOW DO THE WEINER
C-----

```

53 CALL FORT(DATA,M,S,-1,IFERR)
WRITE(6,102)NAM,E1,E2,CF ,BMIN,BMAX,N,M
102 FORMAT(1X,A6,5F10.1,2I7)

```

C CALCULATE A LORENTZIAN OF THE CORRECT WIDTH
C-----

```

WIDE=W/2.*N/(ABS(E1-E2))
HIGH=AMAX/3.0
DO 30 J=1,N
X=(J-N/2-0.5)/WIDE
MM=J+N/2
IF(MM.GT.N)MM=MM-N
30 TEMP(J)=HIGH/(1.0+X**2)
CALL FORT(TEMP,M,S,-1,IFERR)

```

C FIND THE AVERAGE NOISE VALUE
C-----

```

SUM=0.0
L1=N/4
L2=N/2

```

```

DO 20 I=L1,L2
20 SUM=SUM+CABS(DATA(I))
AV=SUM*4/N

```

```

-----
C DO THE ACTUAL WEINER FILTERING
-----

```

```

DO 35 J=1,N
G=CABS(TEMP(J))
FAC=G/(G+AV)
FT(J)=FAC
35 TEMP(J)=DATA(J)*FAC
CALL FORT(TEMP,M,S,1,IFERR)
FA=0.0
DO 40 I=1,N
40 IQ(I)=REAL(TEMP(I))+FA

```

```

-----
C IF THE SPECTRA IS NOT TO BE STORED, RETURN. OTHERWISE, STORE IT
C AND TRY TO READ IT BACK AGAIN
-----

```

```

IF(INU.EQ.0)RETURN
ISTOR(INU)=N
WRITE(6,147)N,INU
MM=0
97 WRITE(40*INU)NAM,E1,E2,(IQ(I),I=1,N)
READ(40*INU,ERR=99)NA,F1,F2,(FT(I),I=1,N)
WRITE(6,115)NAM,INU
115 FORMAT(' SPECTRA ',A6,' STORED IN LOCATION ',I4)
RETURN

```

```

-----
C UP TO FIVE RETRIES ALLOWED
-----

```

```

99 MM=MM+1
IF(MM.GT.5)STOP
WRITE(6,118)
118 FORMAT(' ERROR IN WRITE SECTION')
GO TO 97

```

```

-----
C READ A SPECTRA FROM THE FILES. IF AN ERROR OCCURS, RETRY UP TO
C FIVE TIMES.
-----

```

```

45 N=ISTOR(INU)
WRITE(6,147)N,INU
147 FORMAT(2I10)
READ(40*INU,ERR=98)NAM,E1,E2,(IQ(I),I=1,N)
WRITE(6,116)NAM,INU
116 FORMAT(' SPECTRA ',A6,' RETRIEVED FROM LOCATION ',I4)
RETURN
98 WRITE(6,119)
119 FORMAT(' READ ERROR')
MM=MM+1
IF(MM.GT.5)STOP
GO TO 45
END

```


DISTRIBUTED FEEDBACK NEON $K\alpha$ X-RAY LASERPROPOSITION

It is proposed that an x-ray laser could be constructed employing electron pumping of Neon gas, for excitation of K shell fluorescence, in a distributed feedback laser cavity formed by a synthetic zeolite crystal.

INTRODUCTION

Throughout this worker's investigations in X-ray photoelectron spectroscopy, the need for an x-ray photon source of usable energy, reasonable intensity, and narrow width has been consistently apparent. Present raw x-ray sources of $AlK\alpha_{1,2}$ (~1.1 eV wide) and $Mg\alpha K_{1,2}$ (~0.9 eV wide) radiation are too broad for high resolution work and offer spectral complications in the form of satellite transitions.

The monochromatized $Al K\alpha_{1,2}$ radiation system employed in this thesis has removed the satellite problem and narrowed the line shape to 0.5 eV at the expense of x-ray intensity, and instrumental complexity. He(I) (21.0 eV) and He(II) (40.8 eV) photon sources, though quite narrow, have limited utility because of their low energies.

This worker embarked on an attempt to fabricate a narrow line source for use in electron spectroscopy with limited success. A sodium $K\alpha$ source was constructed by the simple expedient of evaporating NaCl onto a cold Cu target and bombarding the thin NaCl film with 5 KEV electrons. The Na K line at (1041 eV) had an apparent width of ~0.7 eV but the source was quite erratic, and could be operated at very low intensities. A Fluorine $K\alpha$ source was fabricated by fluoridating a copper target, then

X. PROPOSITIONS

exciting K shell fluorescence by electron bombardment. The F $K\alpha$ line was observed to be weak and quite broad (~ 2.0 eV).

Effort then focused on fabricating a Neon K x-ray source. Employing a directed beam of electrons, Neon gas was introduced into the electron path from a capillary under pressure. The resultant spectra were very weak and plagued with satellite structure.

An ongoing project in EM Theory of distributed feedback laser cavity at JPL/CIT was brought to my attention at this time, and¹ it was noted that the EM Theory appeared to apply to the x-ray region of the spectrum as well as the optical. At this time, the possibility of fabricating an x-ray laser based on Neon K-Shell fluorescence and a distributed feedback laser cavity prepared from synthetic zeolite crystals was developed.

NEON $K\alpha$

A number of papers have recently appeared treating the line shape and satellite intensity distribution in the K fluorescence of Neon. The most notable of these are the direct electron excitation work of LaVilla² and $CrK\alpha$ x-ray photon excitation work of Keski-Rahkonen³. Both of these experimenters employed double crystal spectrometers in their work and show line widths for the $K\alpha$ transition which are significantly broadened by instrumental contribution.

In general, the $K\alpha$ x-ray fluorescence line denotes the transition of an

-
1. Evans, G., and Elachi, C., Private Communication
 2. LaVilla, R.E., Phys Rev., A4, 476 (1971)
 3. Keski-Rahkonen, O., Physica Scripta, 7, 151 (1973).

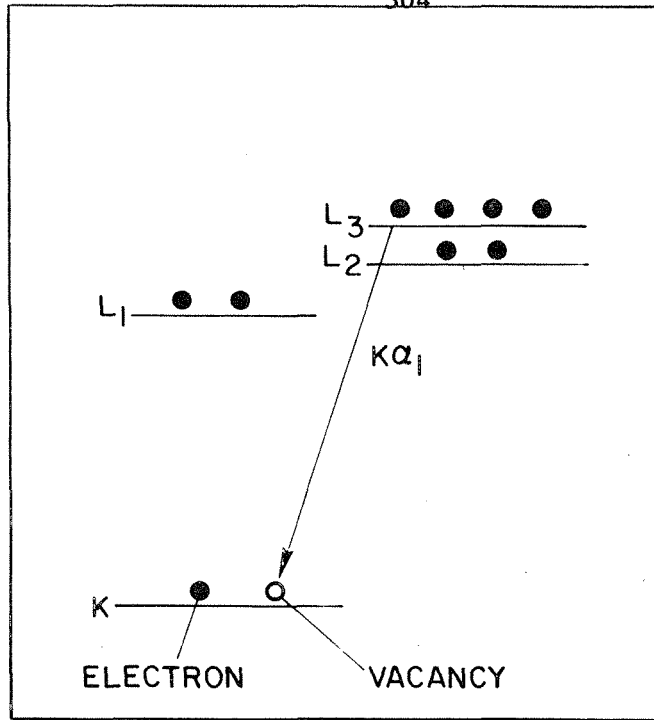


FIG. 1 K α_1 TRANSITION

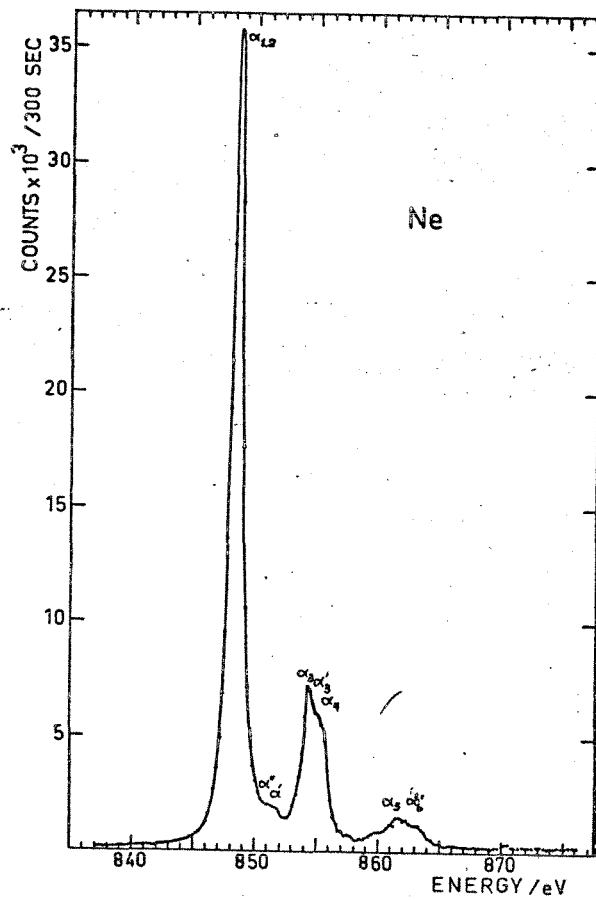
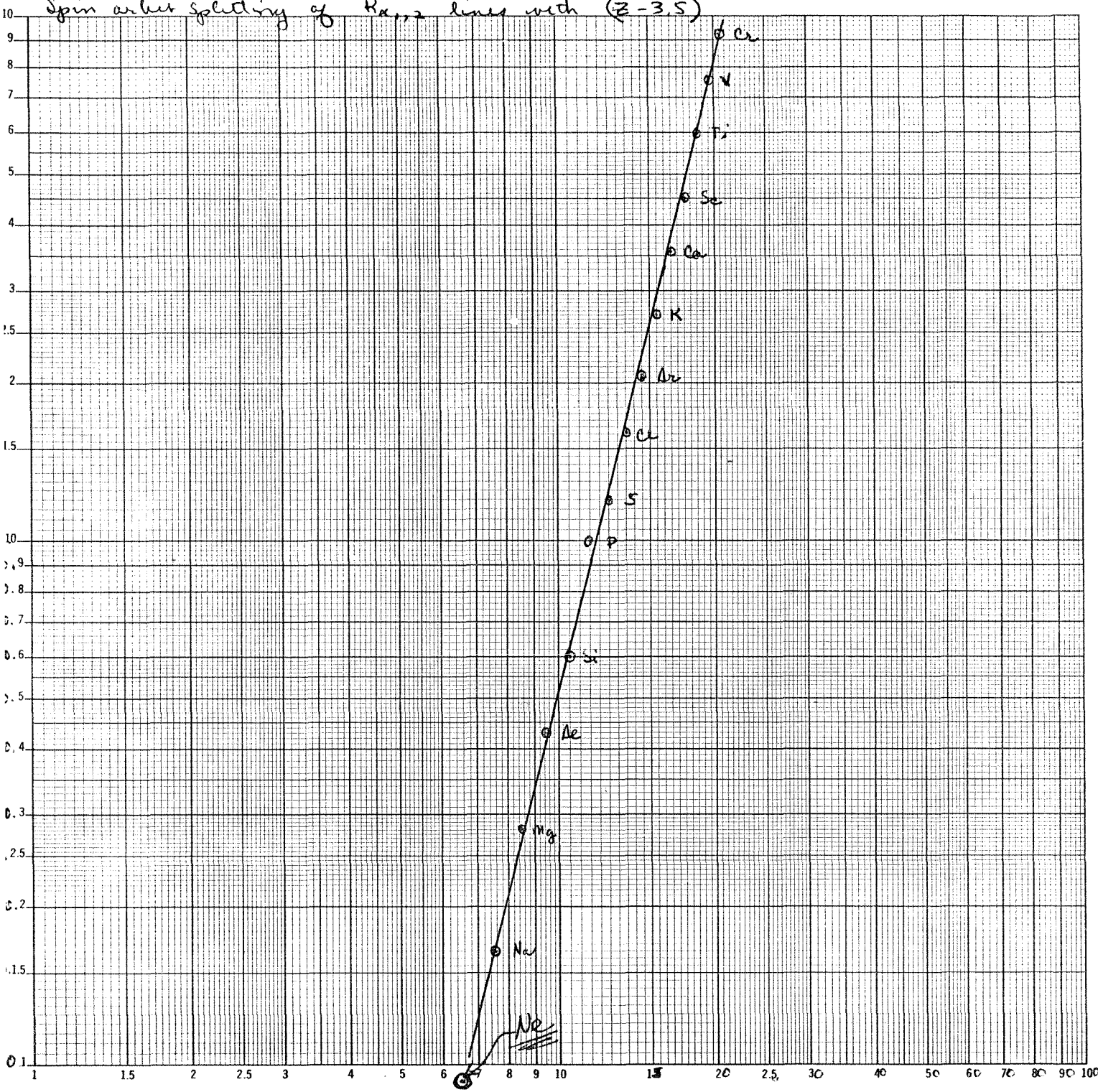


FIG. 2. Ne K α EMISSION SPECTRUM

Fig. 3

Spin orbit splitting of $H_{\alpha,2}$ lines with $(z-3.5)$



electron from the 2p shell to a 1s vacancy, and relaxation of the resultant high energy state with the emission of an x-ray quanta. This process is diagrammed in Fig. 1. Strictly, 2 $K\alpha$ transitions are possible, one from the L_3 level and one from the L_2 level. The observed $K\alpha$ line should have twice the intensity of the $K\alpha_2$ line as given by the statistical weights of the levels.

The observed energy separation between the $K\alpha_1$ and the $K\alpha_2$ lines is largely determined by the spin orbit splitting of the 2p level. In Fig. 3, the spin-orbit splitting observed is plotted vs. atomic number for the elements below Cr in the periodic table. From the figure it is evident that the spin orbit splitting of Ne should be less than 100 meV.

The observed spectrum of K shell fluorescence in Ne is given in Fig. 2. As predicted from the spin-orbit extrapolation in Fig. 3, the $K\alpha_{1,2}$ doublet of Al and Mg has coalesced into a single $K\alpha$ transition within the instrumental resolution. Note, however, that more than 40% of the available x-ray fluorescence has been partitioned in the satellite lines³.

Recent Auger electron studies of Neon^{4,5} give linewidths which indicate that the raw $K\alpha$ neon line should be between 100 and 200 meV wide with inherent state linewidths of the order of 1.0 meV. K shell emission cross-sections for neon are given at $\sim 10^{-22}$ cm²/atom while the K shell

-
4. Johansson, G., Hedman, J., Berndtsson, A., Klasson, M., and Nilsson, R., UUIP-769, March 1972.
 5. Gelius, U., Basilier, E. Svensson, S., Bergmark, T., and Seigbahn, K., UUIP-817, April 1973.

ionization cross-section is of the order of $\sim 10^{-21}$ cm²/atom^{6,8,10}.

Studies of the total Auger and x-ray rates for occupation of a K shell vacancy in Ne give a K lifetime of about 15-80 or 10^{-15} seconds^{7,8,9,11}.

X-RAY LASERS

Following the skeptically received announcement of the observation of lasing in x-rays produced upon superradiant excitation of CuSO₄ in gelatin¹², much work has been devoted in private and governmental laboratories to an attempt to reproduce the original data (unsuccessful) and to fabricate an x-ray laser¹³.

This activity is based in part on the fact that substantial gain/atom are possible with allowed x-ray transitions. The cross-section for stimulated emission has the value at the center of the line of,

$$\sigma_s = \frac{\lambda^2}{4\pi^2} \frac{\tau_{u \rightarrow l}^{-1}}{\Delta\nu} \quad , \quad 1$$

where,

λ \equiv the wavelength

$\Delta\nu$ \equiv the natural linewidth

$\tau_{u \rightarrow l}$ \equiv the radiative transition probability for u to l.

-
6. Harrison, K.G., Tawara, H., and DeHeer, F.J., Physica, 66, 16 (1973)
 7. Bhalla, C.P., Falland, N.O., and Hein, M.A., Phys Rev A, 8, 649 (1973)
 8. Kraus, M.O., Stenie, F.A., Lewis, L.J., Carlson, T.A., and Moddeman, W.E., Phys Lett A., 31, 81 (1970)
 9. Heinz, J., Z. Phys., 143, 153 (1955)
 10. Mehlharn, W., and Asaad, W.N., Z. Phys., 191, 231 (1966)
 11. Bhalla, C.P., and Hein, M., Phys Rev Lett, 30, 39 (1973)
 12. Kepros, J.G., Erying, E.M., and Coyle, F.W., Jr., Proc Nat Acad Sci USA, 69, 1744 (1972)
 13. Mallozzi, P.J., Epstein, H.M., Jung, R.G., Applebaum, D.C., Fairland, B.P., and Gallagher, W.J., 'Fundamental and Applied Laser Physics, Proceedings of the Esfahan Symposium'. Javan, A., and Feld, M.S., ed. Wiley, 1973)

For the Cu $K\alpha_1$ line, subject of the initial work, σ_s is $8.0 \times 10^{-18} \text{ cm}^2$. This cross-section is 2 orders of magnitude greater than that for the Nd-Glass laser at $\lambda=1.06\mu\text{m}$ ¹⁴.

Similarly, for Cu, the atomic adsorption corss-section, σ_a , at $\text{Cu}K\alpha_1$, $h\nu=8.0 \text{ KEV}$) is of the order of $5.0 \times 10^{-21} \text{ cm}^2$, at $h\nu= 8\text{KEV}$. These comparative emission and adsorption cross-sections require that about 0.1% of all Cu atoms would have to be in the upper state at a given moment for lasing to occur. These terms when correlated with K shell lifetimes require a power flux of $10^{19} \text{ watts/cm}^2$, or nearly 6 orders of magnitude above present state of art¹⁵.

For the soft x-ray case of $\text{Al}K\alpha$, σ_s is $\sim 1.8 \times 10^{-17} \text{ cm}^2$, $\sigma_a = 1.4 \times 10^{-20} \text{ cm}^2$, and the minimum threshold power is $1.1 \times 10^{15} \text{ watts/cm}^2$ which has already been achieved at Battelle Memorial Institute¹³. Substituting available numbers as cited previously, for the Neon case, we have for $K\alpha= 848 \text{ eV}$, $\sigma_s \sim 10^{-15} \text{ cm}^2$, $\tau_u \sim 20 \text{ fs}$, and a $P_m(\text{Ne}) \approx 10^{12}-10^{13} \text{ watts/cm}^2$, without cavity based gain.

DISTRIBUTED FEEDBACK LASERS

Laser cavities based on periodic changes in the operative index of refraction per unit cavity length permit the elimination of mirrors as a fundamental constraint. Total transmission of the laser photon is then possible.

-
14. Dugnay, M.A., and Rentzepis, P.M., Appl Phys Lett., 10, 350 (1967)
 15. Stankevich, Yu. L., Dokl Akad Nauk SSSR, 191, 805 (1970).

Such a periodic cavity is most effective when the periodicity Δ is such that

$$\Delta = \lambda/2 \quad 2$$

where λ is the wavelength of the x-ray wave. Neon $X\alpha$ emission at 14.61\AA would, therefore, require periodicities in a laser cavity at 7.305\AA for greatest effect in the distributed feedback mode.

Simplifying the development of the DFB mode, a cubic crystal of period Δ and atomic backscattering cross-section σ , the coupling coefficient, C , between the forward and feedback mode is given by,

$$C = \eta \frac{\sigma}{\Delta^2} \frac{L}{\lambda} \quad 3$$

where L is the length of the laser.

If the predicated laser gain is

$$\text{gain} \times \text{length} = 1.2 \quad 4$$

then the coupling required is about

$$C \approx 1.$$

For wavelengths in the region of $\text{NeK}\alpha$ requirements, σ must be greater than 0.1\AA .

ZEOLITE CAVITY

The key term of this proposition is the utilization of naturally occurring minerals and new synthetic analogues of the zeolite class as distributed feedback laser cavities. The requirements of long channels with periodic matter waves with periodicity at 7 to 8 \AA is consistent with presently available zeolite structures. The porosity of these structures to the inert gases such as Ne presents the possibility of channeling the x-ray emitter in the cavity by diffusion.

Following the advent of successful synthetic methods, a large number of zeolites have been fabricated which show at least one open channel with periodicity and pore size in the specification needed to form a distributed feedback laser cavity for x-ray emission. However, existent structural data^{16,17} describes these dimensions within 0.1 Å due to experimental difficulties and material variation. Dehydrating natural and synthetic zeolites induces changes in the framework structure¹⁸. Exchanged forms, with cation replacement by hydrogen, similarly exhibit structural changes. It appears, however, that Linde L¹⁹, Mordenite²⁰, and Faujasite²¹ offer general zeolite classes in which a suitable cavity may be found. Since a number of questions remain unresolved about the proper cavity use of zeolites as well as the pumping levels required for Ne x-ray lasing, such should be resolved in the experimental sequence.

EXPERIMENT

It is the general design of the experiment to excite Ne K α x-rays in the confines of a naturally determined cavity and to detect the generation, intensity and angular distribution of such. The physical placement of Neon gas in the cavity would be accomplished as indicated in Fig. 4.

-
16. Breck, D.W., "Advances in Zeolite Science" in Advances in Chem, 101, Flanigen, E.M., and Sand, L.B., ed., ACS, Washington, D.C. (1971) 1-19.
 17. Meier, W.M., and Olson, D.H., "Zeolite Frameworks" in Advances in Chem 101, Flanigen, E.M., and Sand, L.B., ed., ACS, Washington, D.C. (1971) pp. 155-170.
 18. Balgard, W.D., and Ray, R., "Crystal Chemical Relationships in the Analcite Family", Advances in Chem, 121, Meier, W.M., and Uytterhaeven, J.B., ed., ACS, Washington, D.C., (1973), pp. 189-199.
 19. Barrer, R.M., Villiger, H., Z Krist, 128, 352 (1969).
 20. Meier, W.M., Z Krist, 115, 439 (1961).
 21. Baur, W.H., Am Mineralogist, 49, 697 (1964).

TITLE:

SOFT X-RAY LASER USING CRYSTAL CHANNELS AS DISTRIBUTED FEEDBACK CAVITIES

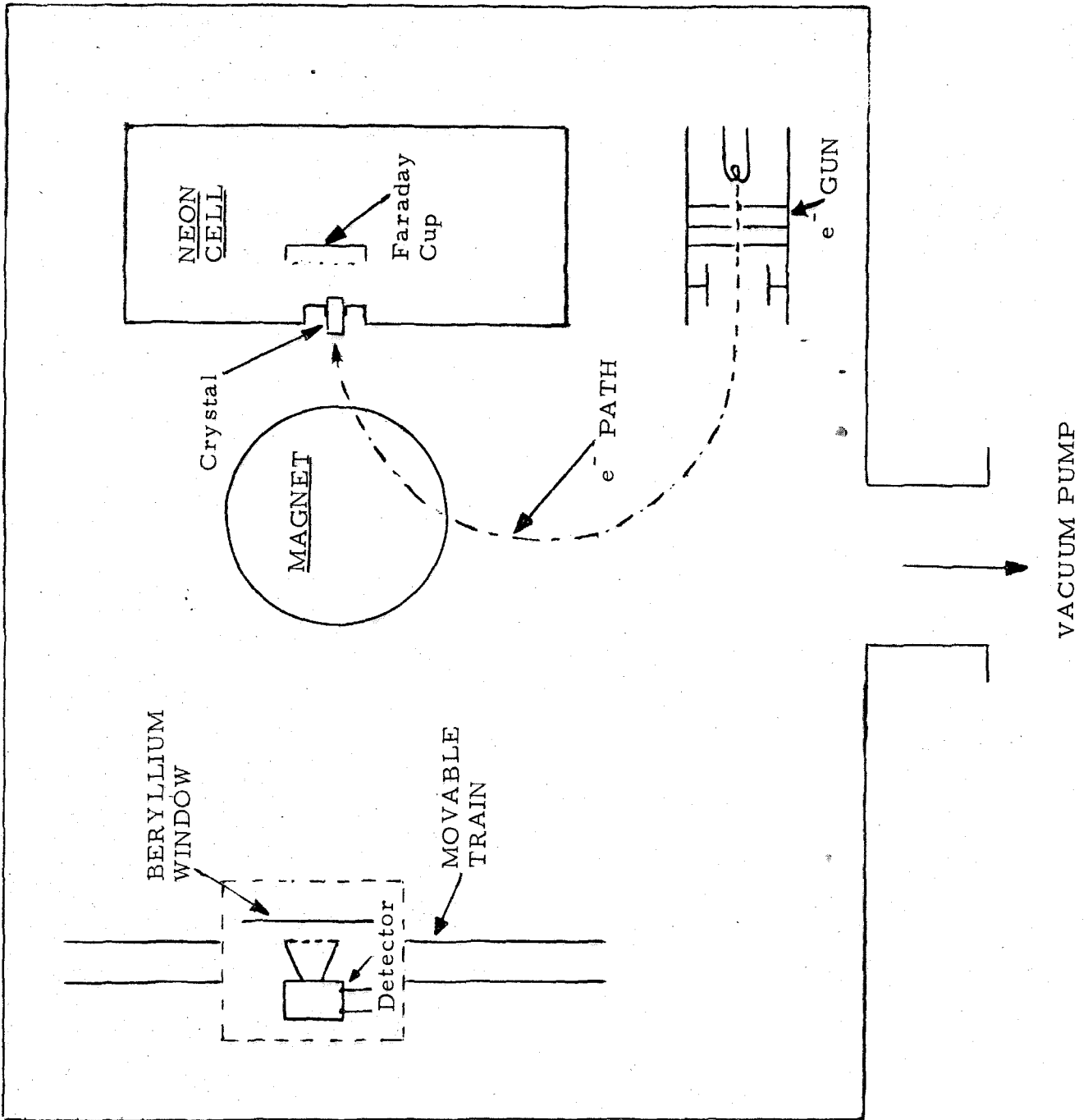


Fig. 5

Here a section of zeolite crystal is sealed in the wall of the experimental chamber; on the outward side of the crystal is a high vacuum environment; on the inward side of the crystal is a chamber of liquid Neon, which is permitted to diffuse through the crystal to the outside vacuum chamber. Presumably the flow of Neon should be through the channels in the zeolite crystal.

In the vacuum chamber is mounted an electron gun capable of high intensity and x-y raster. Perpendicular to the plane of the crystal and parallel to the plane of the electron beam is mounted a magnet with externally variable field. Also in the vacuum chamber is mounted a movable photon counter. A Beryllium shield is placed between the detector (photon counter) and the source (the crystal).

Given the experimental apparatus, the general experiment can be described as follows:

1. With faraday cup in Neon chamber, align electron optics for maximum channeling with both chambers at high vacuum.
2. Admit increasing amounts of He gas into the primary neon chamber and repeat the measurements of 1.
3. Admit liquid neon, He mixture and irradiate in maximum channeling modes while observing angular photon distribution.
4. Iterate crystal choice.

In this experimental scheme, it is anticipated that electron irradiation

in the zeolite field will cause plasma generation in the gas mixture and avalanche currents for Ne ionization. The addition of He gas should provide He^+ for neutralization of space charge build-up. Variation of e^- gun power and Ne temperature should provide an adjustable parameter to vary the lattice plane spacing for empirical adjustment for lasing condition.

CONCLUSION

Initial calculations on this system indicate that the crystal plane spacing is critical and should be maintained to $\pm 0.01\text{\AA}$. Actual Ne $K\alpha$ line widths of the order of 1 meV or less are anticipated. The lack of information about cell parameters and internal electrical fields of many of the synthetic zeolites indicate necessity for considerable crystal research.

314
REFERENCES

DISTRIBUTED FEEDBACK NEON K α X-RAY LASER

1. Evans, G., and Elachi, C., Private Communications.
2. LaVilla, R.E., Phys Rev., A4, 476 (1971).
3. Keski-Rahkoven, O, Physica Scripta, 7, 151 (1973).
4. Johansson, G., Hedman, J., Berndtsson, A., Klasson, M., and Nilsson, R., UUIP-769, March 1972.
5. Gelius, U., Basilier, E., Svensson, S., Bergmark, T., and Seigbahn, K., UUIP-817, April, 1973.
6. Harrison, K.G., Tawara, H., and DeHeer, F.J., Physica, 66, 16 (1973).
7. Bhalla, C.P., Falland, N.O., and Hein, M.A., Phys Rev A., 8, 649 (1973).
8. Kraus, M.O., Stevie, F.A., Lewis, L.J., Carlson, T.A., and Moddeman, W.E., Phys Lett A., 31, 81 (1970).
9. Heinz, J., Z Phys, 143, 153 (1955).
10. Meihorn, W., and Asaad, W.N., Z Phys, 191, 231 (1966).
11. Bhalla, C.P., and Hein, M., Phys Rev Lett, 30, 39 (1973).
12. Kepros, J.G., Erying, E.M., and Coyle, F.W., Jr., Proc Nat Acad Sci, USA, 69, 1744 (1972).
13. Mallozzi, P.J., Epstein, H.M., Jung, R.G., Applebaum, D.C., Fairland, B.P., and Gallagher, W.J., "Fundamental and Applied Laser Physics, Proceedings of the Esfahan Symposium". Javan, A. and Feld, M.S., ed., Wiley (1973).
14. Dugnay, M.A., and Rentzepes, P.M., Appl Phys Lett, 10, 350 (1967).
15. Stankevich, Yu. L., Dokl Akad Nauk SSSR, 191, 805 (1970).
16. Breck, D.W., "Advances in Zeolite Science" in Advances in Chem, 101, Flanigen, E.M., and Sand, L.B., ed., ACS, Washington, D.C. (1971) pp. 1-19.

17. Meier, W.M., and Olson, D.H., "Zeolite Frameworks" in Advances in Chem 101, Flanigen, E.M., and Sand, L.B., ed., ACS, Washington, D.C., (1971) pp. 155-170.
18. Balgard, W.D., and Roy, R., "Crystal Chemical Relationships in the Analcite Family" in Advances in Chem 121, Meier, W.M. and Uytterhaeven, J.B., ed., ACS, Washington, D.C., (1973) pp. 189-199.
19. Barrer, R.M., Villiger, H., Z Krist, 128, 352 (1969).
20. Meier, W.M., Z Krist, 115, 439 (1961).
21. Baur, W.H., Am. Minerologist, 49, 697 (1964).

CHARACTERIZATION OF METAL SURFACES AND ADSORBATES BY
INTERMOLECULAR AUGER ELECTRON PROCESSESPROPOSITION

It is proposed that significant new information pertaining to the identity and characterization of metal adsorbate bonds could be obtained through a study of interelectronic Auger processes, in such systems.

INTRODUCTION

The application of surface state spectroscopies such as infrared reflectance spectroscopy¹, electron impact spectroscopy², low energy electron diffraction³, auger electron spectroscopy⁴, and x-ray photoelectron spectroscopy⁵ to the study of metal surfaces and adsorbates has yielded considerable information about chemical bonding in this system. Each of the cited spectroscopies have been major research efforts in the past few years, however XPS and AES are now at the forefront of interest because of the unique data available.

A prediction is developed in this thesis that of the latter two spectroscopies, XPS perturbs the system of metal-metal surface-adsorbate less than does AES and further it is speculated that the XPS spectrum can study the Adsorbate-metal surface bond in detail.

-
1. Yates, J.T., Jr., and King, D.A., Surface Science, **30**, 601, (1972).
 2. Newsham, I.G., and Sandstrom, D.R., J Vac Sci and Tech., **10**, 39, (1973).
 3. Duke, C.B., Paper, 20th Natl Symposium American Vacuum Soc., 1973.
 4. Tracy, J.C., and Palmburg, P.W., J Chem Phys, **51**, 4852 (1969).
 5. Madey, T.E., Yates, J.T., and Erickson, N.E., Chem Phys Lett., **19**, 487 (1973).

To date, however, the electron emission spectroscopies have emphasized absolute and relative electron kinetic and binding energies as the relevant interpretable data. This approach has neglected the possibility of significant information in the band shapes of the observed $N(E)$ distributions. Recently, however, with the advent of high resolution AES and XPS spectrometers, the instrumental and experimental contributions to the observed line structures have become minimal and quantified. These developments pose the possibility of interrogating the observed line shapes and thereby accruing data on the chemical effects on the hole-state lifetimes which govern these transitions.

HOLE STATE LIFETIMES

It has been shown that the lifetime of core holes in solids⁶ and gases⁷, which decay primarily through non-radiative Auger transitions involving valence electrons on the hole state atom, depend on the chemical state of that atom. The experimental observation of this effect was based on XPS measurements where higher oxidation states of a given element gave rise to narrower core electron line widths. This was interpreted in terms of the decreased number of valence electrons available for filling the photoelectron vacancy.

These processes can be explained in terms of intra-atomic considerations. Recently, however, Citrin⁸ has observed and described an inter-atomic Auger process which he describes as generally dominant in photoemission spectroscopy.

6. Friedman, R.M., Hudis, J., and Perlman, M.L., Phys Rev Lett, 29, 692 (1972).
7. Shaw, R.W., Jr., and Thomas, T.D., Phys Rev Lett, 29, 689, (1972).
8. Citrin, P.H., Phys Rev Lett, 31, 1164 (1973).

The matrix element describing an Auger transition may be expressed as

$$\langle \rho_A(1)\psi(2) | \frac{1}{|\vec{r}_1 - \vec{r}_2|} | \Phi_{A,B}(1)\Phi_{A,B}(2) \rangle \quad 1$$

where ρ_A is the initial hold state on site A, $\psi(2)$ is the continuum state of the Auger electron, and $\Phi(1)$ and $\Phi(2)$ are the initial bound states of the hold-filling and photo ejected electrons, respectively. One can now treat a number of specific cases in terms of the Auger annihilation of the hole state. The bound state wave functions can be localized either on site A (the hold state atom) or site B (inner sphere ligand to A), or the various combinations of these sites.

Considering the decay of the photo-vacancy in terms of an Auger mechanism, one can distinguish the various possibilities by the notation group AA, BB, AB, and BA, where the first letter refers to the site from which the hole filling electron originates and the second letter denotes the source of the emitted Auger electron.

The AA mechanism is straight-forward and has been described in intra-atomic terms. Line shape characteristics should be solely determined by the chemical state of the hole state center. The BB mechanism, in contradistinction, must be described as a intermolecular process where electrons are donated from the ligand to the central metal ion vacancy followed by ligand Auger emission.

The existence of such processes in Na2p linewidths is demonstrated⁸ upon consideration of the 2p spectra of NaOH and Na metal. The 2p core hole in Na metal decays by means of Auger mechanisms based on the Na 3s conduction electrons. On the basis of intra-molecular arguments (AA relaxation mechanisms) the 2p core hole of Na⁺ in NaOH should be considerably narrower than the Na metal case. Experimentally after subtraction

of the instrumental broadening terms, the 2p line in NaOH was observed to be five times the width of the line in the metal case. This lifetime broadening has been attributed⁹ to the availability of hydroxyl valence electrons for filling the photo hole.

From Eq. 1, the magnitude of the interatomic transition rate depends on the spatial distribution or density of the ligand electrons available for hole-filling and/or Auger ejection by virtue of their overlap with or proximity to the hole state. The effective total valence electron density available to the hole state by the inner sphere ligand system (AVED) has been correlated with the observed linewidth of core electrons in a variety of compounds.

Of the above mentioned hole state decay mechanisms, the AB system is most interesting. Here the intra-atomic or inter-atomic effects can be varied. The very efficient Coster-Kronig (intra-atomic) terms can be kept essentially constant over a series of central metals by judicious choice of core electron level studied, consequently emphasizing ligand effects.

A method therefore exists to follow the consequence of nearest neighbor interactions upon hole state effects and correlate same with the nature of the operative bonding. This represents a hitherto unexplored aspect of AES, XPS and X-ray adsorption spectroscopies.

EXPERIMENTAL

The central consideration of this proposal entails the study of hole-state

9. Citrin, P.H., Phys Rev A, to be published.

decay processes in a variety of transition metal-ligand situations as primary objective.

As noted in the introduction, a significant number of experimental investigations are underway studying various metal substrates, eg., Pt, Ir, Pd, Ni, etc., together with various adsorbates, eg., CO, OH, O₂, N₂, etc., in an effort to study the catalytic effect of such surfaces.

This proposal, therefore, suggests the study of metal and adsorbate line width of various core levels as a function of metal and adsorbate identity. This information, however, would be inconclusive without modeling studies of transition metal complexes. By study of gas and solid phase photoelectron spectra of transition metal carbonyls, for example, significant bonding variations and metal ligand interactions could be established for the adsorbate CO.

Additional studies of transition metal aquo and amino complexes, trans-fixed in thin solid films or clathrate glasses should provide correlative information for H₂O and NH₃ adsorption modes. Variation of glass media or relative composition should give information concerning outer sphere interactions on the femtosecond time scale.

CONCLUSION

The lifetimes of core hole states depend on both intra-atomic and inter-atomic electron contributions. The latter ligand to metal Auger relaxation mechanisms offer a low resolution observation of the delocalization of Metal ligand bonding. The monitoring of observed lifetimes through XPS and AES linewidth determinations offers significant neglected information from the spectroscopies.

The study of linewidths of core electron lines in both ligand and metal for the ligand CO, H₂O, and NH₃ is proposed for a series of central transition metals for correlation with metal ligand bond information accrued from electronic adsorption spectroscopy. The extension of this data to the interpretations of observed core linewidths in the XPS, AES studies of the adsorbates CO, H₂O, and NH₃ on single crystal transition metals is proposed to study the adsorbate-metal surface bonding characterization.

REFERENCESCHARACTERIZATION OF METAL SURFACES AND ADSORBATES BY
INTER-MOLECULAR AUGER ELECTRON PROCESSES

1. Yates, J.T., Jr., and King, D.A., Surface Science, 30, 601, (1972).
2. Newsham, I.G., and Sandstrom, D.R., J Vac Sci and Tech, 10, 39 (1973).
3. Duke, C.B., Paper, 20th Natl Symposium, American Vacuum Society, 1973.
4. Tracy, J.C., and Palmburg, P.W., J. Chem Phys, 51, 4852 (1969).
5. Madey, T.E., Yates, J.T., and Erickson, N.E., Chem Phys Lett., 19, 487 (1973).
6. Friedman, R.M., Hudis, J., and Perlman, M.L., Phys Rev Lett., 29, 689 (1972).
7. Shaw, R.W., Jr., and Thomas, T.D., Phys Rev Lett., 29, 689 (1972).
8. Citrin, P.H., Phys Rev Lett, 31, 1164 (1973)
9. Citrin, P.H., Phys Rev A., to be published.

CHEMISTRY AND PHYSICS OF ELECTRONIC CONDUCTION IN
AMORPHOUS SiO_2 FILMS BY X-RAY PHOTOELECTRON SPECTROSCOPYPROPOSITION

It is proposed that a vacuum level low energy electron irradiation device can substitute for a metal for the purposes of studying the dynamics of conduction-material interaction in metal-oxide-semiconductor field effect devices by means of x-ray photoelectron spectroscopy.

INTRODUCTION

The electronic component technology of the semiconductor industry is directly tied to large-scale integrated circuit design. The fundamental operative technology of transistors in integrated circuits will emphasize MOSFET (metal-oxide-semiconductor-field-effect-transistor) devices. Substantial research efforts are devoted to understanding the fundamental material parameters of the operation of such devices. A significant aspect of this work involves the attempt to understand the chemical and physical mechanisms which incite these devices through a comprehension of the fundamental chemical and physical aspects of electronic conduction. To date, there has existed no method of probing the fundamental aspects of the electronic structure of such devices while undergoing reasonable operative modes. The data of photoemission spectroscopy, namely occupied electronic densities of states, chemical environment and surface state interactions has offered promise as a tool for studying the active materials of such devices. This experimental probe has been largely ineffective in such studies in near time because of its limited observa-

tional depth, poor resolution and serious charging problems involved in the study of non-conductive materials.

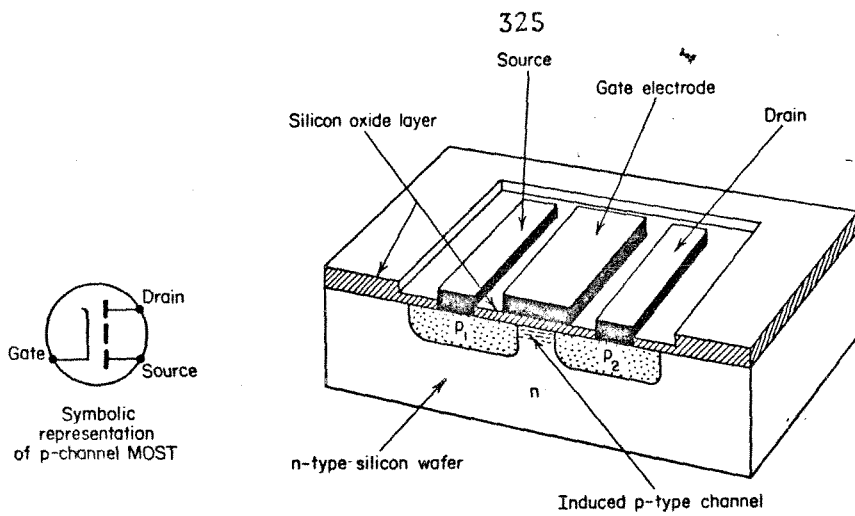
This thesis has developed a concept of an electron steady state, involving a balance of photoemission and replenishment currents in the experiment, which promises to solve charging and spectral reproducibility problems. This steady state experiment, however, offers no intrinsic charge standard to facilitate absolute V_C potential measurements and subsequent compensation.

This proposition suggests that the Flood Gun device¹ described in the thesis can be employed as a metal layer substitution and consequently would permit the preparation of simulated MOS device experiments. These experiments should lead to understanding of the conduction process on an atomistic scale and should permit comprehensive study of the SiO_2 -Si interface.

SEMICONDUCTOR DEVICES

A number of excellent texts exist which offer detailed treatment of semiconductor device design, theory, utilization and processing technology^{2,3,4}. The most common industrial transistor technology is based upon the bipolar junction device where two types of conductors are involved in operation, the free-electron and the positive-hole. This discussion, however, centers

-
1. Huchital, D.A., and McKeon, R.T., Appl Phys Lett, 20, 158 (1972).
 2. Grove, A.S., Physics & Technology of Semiconductor Devices, Wiley, N.Y., (1967).
 3. Holland, L., ed., Thin Film Microelectronics, Wiley, N.Y., (1965).
 4. Penney, W.M., and Lau, L., ed., MOS Integrated Circuits, Van Nostrand Reinhold, N.Y., (1972).



Basic structure of an MOS transistor.

FIG. 1

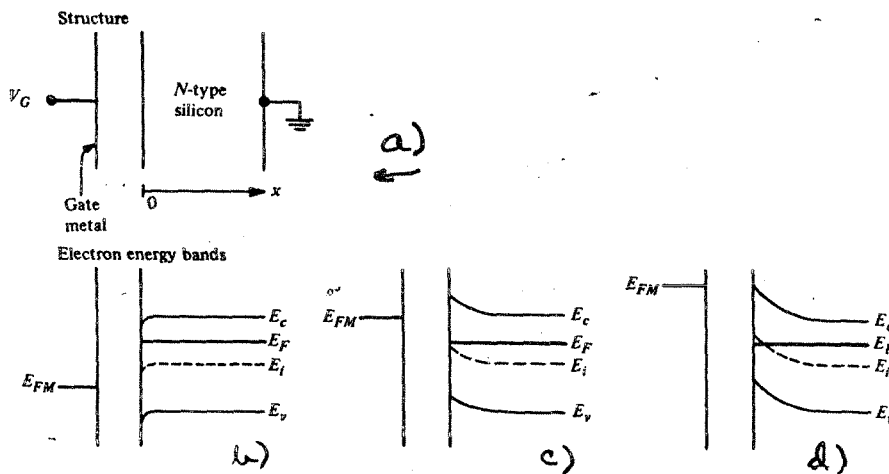


FIG. 2

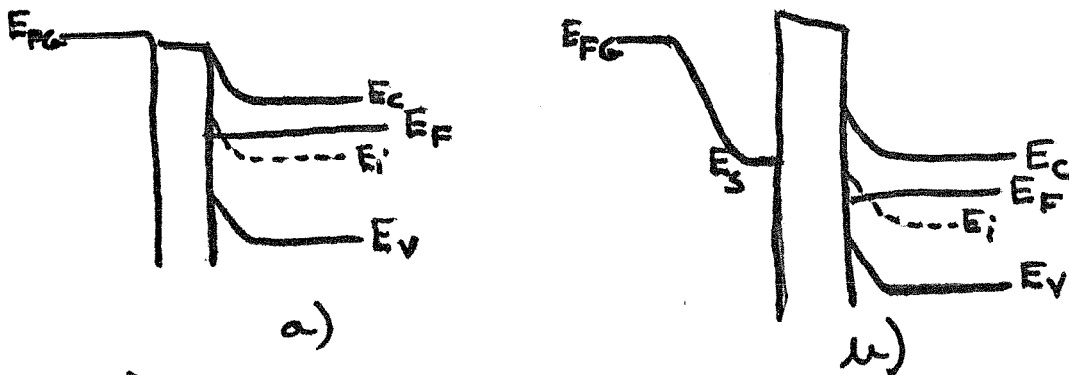


FIG. 3

about a more recently developed device, the MOS transistor, which is of major importance in integrated circuit technology.

In the MOS transistor, a conducting channel is induced between two very closely spaced electrode regions by increasing the electric field at the surface of the semiconductor between the electrodes. The basic structure is shown in Fig. 1.

The two electrode regions, called the source and drain, are formed by a p-type diffusion into an n-type silicon wafer. Between the source and the drain are two p-n junctions back to back, $p_1 n$ and np_2 . With a voltage V_{DS} applied between the source (positive) and the drain (negative) the np_2 junction is reverse-biased, and therefore no current will flow from source to drain. If then, the gate electrode over the space between source and drain is made sufficiently negative with respect to the source, holes are attracted to the surface of the n-type region and cause it to change to p-type. One then has two p-type electrodes with a p-channel joining them and consequently a current can flow.

The thickness of pure oxide under the gate electrode is of the order of 1000\AA , however, the actual effectiveness of the device is determined by the Si-SiO₂ interface and the first 30 to 40 \AA of the SiO₂ oxide film on the Si surface. As the field or charge on the oxide is changed, the bands of the silicon substrate move in energy or bend in response. Hence, the field observed by the Si substrate interface is an extremely accurate representation of the charge on the oxide. Further, the Si interface communicates directly with the first 20 to 30 \AA of SiO₂ from the interface. SiO₂ beyond 40 \AA from the interface is effectively a bulk dielectric medium.

The effect on the internal energy levels of the Si-semiconductor of charge in the interfacial oxide is represented in Fig. 2. Here Fig. 2a diagrams the effective circuit in an experimental device. The electron energy levels for various potential effects are given in Fig. 2b, c and d. Accumulation of charge at the Si surface brought about by applying a suitable external electric field orientated to attract electrons toward the surface is diagrammed in Fig. 2b. Raising the apparent fermi level of the metal by external bias will bring the bands of the semiconductor into the depletion region (Fig. 2c) and with continued bias increase into the inversion region (Fig. 2d). Here the density of holes becomes greater than that of electrons and the substrate interface resembles p-type material.

EXPERIMENT

As developed in this thesis, the actual escape depth of unperturbed electrons in the range of kinetic energies employed in X-ray photoelectron spectroscopy have been established to be in the region 4-100 Å over the range of observed materials. For insulators (SiO_2) and semiconductors (Si) the range 15-80Å seems more appropriate.

For thin oxides on semiconductors (20-40Å thickness) it would appear that the oxide, the interface, and the proximate bulk semiconductor could be examined in the XPS spectrum. Variation of the electron steady state parameters at constant Flood Gun energies should permit the establishment of actual electron flux parameters and a profiling of the core and valence levels of the SiO_2 - Si system.

This proposition suggests that the low energy electron irradiating device can be substituted for the biasing metal electrode in the fabrication of a simulated MOS device. This experiment is diagrammed in Fig. 3a.

If the Flood Gun directly substitutes for the metal, the net effect of conduction would be charge injection into the Si conduction band. This case is represented as Fig. 3b. If, however, as is indicated in recent inelastic electron tunneling experiments on this system⁵, surface states abound on the oxide, then, these states could set up a pseudo-metal boundary on the oxide. This would enable biasing by the electron steady state and access to the charge accumulation region of the band bending experiment.

Finally, if a preponderance of surface states is observed, the low energy electron device offers the possibility of taking inelastic electron tunneling spectra of the surface states simultaneously with the acquisition of the photoelectron spectrum.

CONCLUSION

This proposition suggests the fabrication of an experimental program on the XPS study of the surface and interface states of the SiO₂-Si system operating under active electronic conduction. The program should include investigation of different surface preparations, dopants and thermal modes in order to profile the operational mechanics of MOS devices. Correlation with electrical measurements and processing technology should enable conclusions concerning conduction mechanisms in oxide semiconductor materials.

5. Lewis, B.F., Private Communication.

REFERENCESCHEMISTRY AND PHYSICS OF ELECTRONIC CONDUCTION IN AMORPHOUS SiO₂
FILMS BY X-RAY PHOTOELECTRON SPECTROSCOPY

1. Huchital, D.A., and McKeon, R.T., Appl Phys Lett, 20, 158 (1972).
2. Grove, A.S., Physics and Technology of Semiconductor Devices, Wiley, New York, (1967).
3. Holland, L., ed., Thin Film Microelectronics, Wiley, New York (1965).
4. Penney, W.M., and Lau, L., ed., MOS Integrated Circuits, Van Nostrand Reinhold, New York (1972).
5. Lewis, B.F., Private Communication.

THIN FILM ELECTRO-OPTICAL SPECTROSCOPY OF
 d^6 , d^8 , AND d^{10} , TRANSITION METAL COMPLEXES

PROPOSITION

It is proposed that a thin film spectroscopic method be investigated in order to study high electric field coupling effects on ligand field and charge transfer transitions in well-characterized d^6 , d^8 , and d^{10} transition metal complexes.

INTRODUCTION

Recent progress in the field of integrated optics has emphasized the development of thin-film lasers¹ and modulators². This work has in turn stimulated development of thin films as wave guides to trap the component light trains.

Studies of these thin film light guides have mainly been devoted to synthetic problems. The use of thin single crystal garnet films as optical wave-guides has been described³. Recent work in Tien's group^{4,5,6} has been devoted to the study of a series of thin organosilicon films prepared in RF discharge.

-
1. Kogelnik, H., and Shank, C.V., Appl Phys Lett, 18, 152 (1971).
 2. Tien, P.K., Martin, R.J., Wolfe, R., LeCraw, R.C., and Blank, S.L., Appl Phys Lett, 21, 394 (1972).
 3. Tien, P.K., Martin, R.J., Blank, S.L., Wemple, S.H., and Varnerin, L.J., Appl Phys Lett, 21, 207 (1972).
 4. Tien, P.K., Smolinsky, G., and Martin, R.J., Appl Optics, 11, 637 (1972).
 5. Vosile, M.J., and Smolinsky, G., J Electrochem Soc, 119, 451 (1972).
 6. Tien, P.K., Martin, R.J., Smolinsky, G., Appl Optics, 12, 1909 (1972).

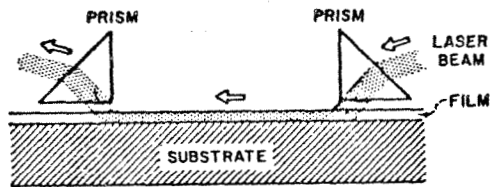


Fig. 1

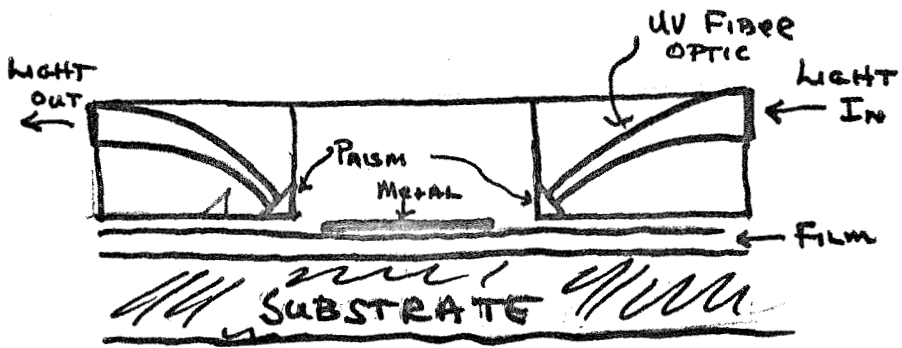


Fig. 2

guide medium to another medium of differing refractive index providing that the transition between the two guides is gradual.

Similarly, technical development of fiber optics for effective transmittance of UV and visible light in the range 280 to 1300 nm has progressed to a marketable stage⁹. The use of tapered fibers permits concentration and expansion of incident light intensities.

A spectral device is consequently proposed to permit the study of electronic adsorption spectroscopy in thin fabricated films and is represented in Fig. 2. Here prismatic coupling to the films is provided by tapered UV light guides bonded to superasil prisms. The prism system on the right of Fig. 2 excites a light wave into a film and a few centimeters away the same light wave is coupled out of the film by the system on the left.

This spectrographic device would permit thermal modulation of the observed spectra by thermal variations of the substrate. Deposition of a masked Au film above the medium and the use of a metal substrate permits the application of high AC and DC electric fields across the sample. This facilitates study of the coupling of electronic transitions with electric fields up to the film breakdown limit.

Should the substrate upon which the medium is grown be of optically transparent material, tuneable dye lasers could be used to excite particular transitions within the film while observing the electronic spectrum at normal incidence in an optical double resonance experiment.

9. Dislich, H., and Jacobsen, A., Angew Chem Int Ed, 12, 439 (1973).

EXPERIMENT

This worker's investigations as well as those of C.Cowman¹⁰ indicate that a large number of transition metal complexes form thin single crystals under appropriate conditions when crystallized as tetra-alkylammonium salts. This proposal, then, suggests that a study of the changes in the electronic adsorption spectrum as a function of the state and applied DC fields near breakdown potential be undertaken for a series of thin film samples of transition metal complexes . This study should encompass simple halo complexes of octahedral d^6 (Ir^{III}, Pt^{IV}), square planer d^8 (Pt^{II}, Au^{III}) and tetrahedral d^{10} (Hg^{II}, Tl^{III}) transition metals.

CONCLUSION

A thin film spectroscopy involving optical coupling mechanics into thin materials is proposed in order to enable electro optical, and optical double resonant studies of model transition metal complexes.

10. Cowman, C., Thesis, California Institute of Technology, 1973.

REFERENCESTHIN FILM ELECTRO-OPTICAL SPECTROSCOPY OF
 d^6 , d^8 , AND d^{10} TRANSITION METAL COMPLEXES

1. Kogelnik, H., and Shank, C.V., Appl Phys Lett, 18, 152 (1971).
2. Tien, P.K., Martin, R.J., Wolfe, R., LeCraw, R.C., and Blank S.L., Appl Phys Lett, 21, 394 (1972).
3. Tien, P.K., Martin, R.J., Blank, S.L., Wemple, S.H., and Varnerin, L.J., Appl Phys Lett, 21, 207 (1972).
4. Tien, P.K., Smolinsky, G., and Martin, R.J., Appl Optics, 11, 637 (1972).
5. Vasile, M.J., and Smolinsky, G., J. Electrochem Soc., 119, 451 (1972).
6. Tien, P.K., Martin, R.J., Smolinsky, G., Appl Optics, 12, 1909 (1973).
7. Smolinsky, G., Paper, 20th National Symposium, American Vacuum Society, October 1973.
8. Ulrich, R., and Martin, R.J., Appl Optics, 10, 2077 (1971).
9. Dislich, H., and Jacobsen, A., Angew Chem Int Ed., 12, 439 (1973).
10. Cowman, C., Thesis, California Institute of Technology, 1973.

PREPARATION OF DAMAGE FREE SILICON SURFACES
BY PSEUDO-CHEMICAL MECHANICAL ION POLISHING PROCESSES

PROPOSITION

It is proposed that chemical mechanical polishing systems employing discreet oxidative and complexing mechanisms should be studied as a preparative method for the synthesis of damage free silicon substrates.

INTRODUCTION

Silicon and its oxides provide excellent substrates for such diverse applications as catalytic modeling studies on semiconductors and as substrates for electronic devices. One of the most important considerations in the utility of silicon is the high chemical purity in which it is readily available. Additionally, its oxides are well behaved, and the thermally grown amorphous SiO_2 has excellent adhesion and contact stability to the semiconductor substrate.

Studies of Si and SiO_2 -Si as catalytic and electronic substrates rely on the ability to prepare a reproducible surface structure with minimum defectation and which images the structural parameters of the bulk state as exactly as possible.

Silicon is generally supplied as polished wafers. These polished wafers are cut from Silicon ingots by diamond saws which leave damage fields on the surface to a depth of about 100 microns^{1,2}. Mechanical abrasive

1. Buck, T.M., in Surface Chemistry of Metals and Semiconductors, Gatos, H.C., ed., p. 107, Wiley, N.Y., (1960).
2. Meek, R.L., and Huffstutler, M.C., Jr., J Electrochem Soc., 116, 893 (1969).

polishing systems leave this damage structure in the surface profile. Chemical etchants polish by removing the damage zone, but leave an undulating surface behind³.

Because of the demanding surface quality required by the electronics industry, a series of polishing systems were devised which combined the optimum parameters of chemical and mechanical systems. The two preeminent systems still in use utilize discreet two-stage reaction processes. These processes can be described as oxidation of the silicon followed by solvation of the resultant species.

It has been reported⁴, however, that high resolution studies of Si surfaces show extensive microsplit damage. The microsplits have dimensions of the order of μm and the density of the splits is of the order of $10^6/\text{cm}^2$. It appears that these micro-cracks in the surface are residual saw damage and are propagated by mechanical strain of the surface during the polishing operation. It was shown by the IBM workers that simple chemical etchants could remove the splits but would degrade the surface. This proposition emphasizes a new approach to chemical mechanical polishing which may lead to virtually damage free surfaces for electronic and chemical application.

CHEMICAL MECHANICAL METHODS

Two processes are in wide-spread use in the industry as noted. One of

3. Rai-Choudhury, P., J. Electrochem Soc., 118, 1183 (1971).

4. Schwuttke, G.H., IBM Technical Report, TR 22.1588, Jan, 1973.

these is termed copper ion polishing⁵ and relies on cupric oxidation of the Silicon substrate to deposit a layer of Cu metal over the fresh oxide. The ambient solution consists of basic fluoride buffer which can effect solvation and subsequent removal of the silicon oxide if it comes in contact with the oxide. The inhibitory effect of the Cu metal layer is mechanically wiped away by means of a lapping polishing cloth. This has the net effect of emphasizing reaction at the topologically higher elevations and reducing reaction rate at lower elevations. Therefore, comes the description of the process as hybrid, chemical-mechanical polishing. This worker's extensive analysis of this system led to the postulation of a mechanism for the heterogeneous reaction⁶ and the following proposal for its substitution by a new process technology. It was first proposed that the function of the metal buffer layer could more effectively be served by the substitution of long chain surfactants for the metal. These long chain surfactants were presupposed to adsorb to the oxide surface, only to be removed by the mechanical intervention of the wiping element. Eliminating the need for the metal coating lead to the proposal that the Iron HEDTA clathrate complex be employed in the oxidation couple with elementary silicon. The process would then become:

1. Iron HEDTA oxidation $4\text{Fe}^{\text{III}} + \text{Si}^{\text{O}} \rightarrow \text{Si}^{\text{IV}} + 4\text{Fe}^{\text{II}}$
2. Surfactant oxide barrier coating
3. Fluoride solvation and removal of the Si Oxide by complexation.

5. Regh, J., and Silvey, G.A., Electrochem Tech, 6, 155 (1968).
 6. Grunthaler, F.J., NASA Technical Memorandum, June, 1973.

EXPERIMENTAL

In view of the recent IBM surface studies of silicon substrate, the possibility of damage free surfaces has become a major objective in system design. The proposed Fe-HEDTA/Surfactant system eliminated a number of serious problems inherent in the Cu-ion polishing technique including the imbedding of metal ion and metal clusters in the surface. The mechanical lapping system could, however, reintroduce the microsplit situation.

It is, therefore, suggested in this proposition that agitation of the surfactant layer for complexation/removal be accomplished by laminar wiping of the substrate face. Here, the substrate and the wiping wheel are separated several hundreds or thousands of microns but totally submerged in the polishing solution. The net effect of wiper movement is a laminar flow removal of the occupied surfactant states. The energy imparted to the surface by the mechanical aspect of the process should now be trivial with respect to that required for micro-split formation.

Studies of the rate of material removal as a function of oxidant concentration, surfactant length, and solution pH are likewise suggested in an effort to better understand the heterogeneous reaction mechanism.

CONCLUSION

A new surface pretreatment technology is proposed which should facilitate the preparation of damage free, optical quality surfaces for chemical and electronic studies involving elemental Silicon.

REFERENCESPREPARATION OF DAMAGE FREE SILICON SURFACES BY
PSEUDO-CHEMICAL-MECHANICAL ION POLISHING PROCESSES

1. Buck, T.M., in Surface Chemistry of Metals and Semiconductors, Gatos, H.C., ed., p. 107, Wiley, N.Y., (1960).
2. Meek, R.L., Huffstutler, M.C., Jr., J Electrochem Soc., 116, 893 (1969).
3. Rai-Choudhury, P., J. Electrochem Soc., 118, 1183 (1971).
4. Schwuttke, G.H., IBM Technical Report, TR 22.1588, Jan. 1973.
5. Regh, J., and Silvey, G.A., Electrochem Tech., 6, 155 (1968).
6. Grunthaner, F.J., NASA Technical Memorandum, June, 1973.